CNWRA 94-007

EFFECTIVE HYDRAULIC PROPERTY CALCULATIONS FOR UNSATURATED, FRACTURED ROCK WITH SEMI-ANALYTICAL AND DIRECT NUMERICAL TECHNIQUES: REVIEW AND APPLICATIONS

Prepared for

Nuclear Regulatory Commission
Contract NRC-02-93-005

Prepared by

Center for Nuclear Waste Regulatory Analyses
San Antonio, Texas

March 1994

2.2 --- T199403300051
Effective Hydraulic Property
Calculations for
Unsaturated, Fractured Rock

CNWRA 94-007

EFFECTIVE HYDRAULIC PROPERTY CALCULATIONS FOR UNSATURATED, FRACTURED ROCK WITH SEMI-ANALYTICAL AND DIRECT NUMERICAL TECHNIQUES: REVIEW AND APPLICATIONS

Prepared for

Nuclear Regulatory Commission
Contract NRC-02-93-005

Prepared by

Amvrossios C. Bagtzoglou, Sitakanta Mohanty,
Ashok Nedungadi, Tian-Chyi Jim Yeh, and Rachid Ababou

Center for Nuclear Waste Regulatory Analyses
San Antonio, Texas

March 1994

ABSTRACT

This report consists of an extensive, yet not exhaustive, literature review on the subjects of effective property calculations, fracture network generation with stochastic approaches, and modeling approaches for fluid flow simulation in fractured rock. It also presents visualization, statistical, and connectivity analyses of realistic networks at the Apache Leap Tuff Site, Arizona; the development and verification of a two-dimensional fracture network generator; the theoretical background, assumptions, and algorithm implementation of the Real Space Renormalization Group (RSRG) approach for calculation of effective properties; the verification of the RSRG approach for binary and nonbinary matrix-fracture systems; a study of effective property calculations with direct numerical simulation using the MMOC2 and BIGFLOW numerical codes; and a parametric study and analysis of limitations of the RSRG approach. In this report, a modeling approach which addresses the issue of modeling flow in unsaturated, heterogeneous, fractured rock is advocated. This approach models explicitly all important geological features as persistent discontinuities, and lumps together the remaining heterogeneity, composed either of fractures or matrix heterogeneity, under a regionalized effective and/or stochastic continuum approach.

CONTENTS

Section		Page
FIGURES		viii
TABLES		xii
ACKNOWLEDGMENTS		xiii
EXECUTIVE SUMMARY		xiv
1	FLUID FLOW IN FRACTURED ROCKS AND THE NEED FOR EFFECTIVE PROPERTY CALCULATIONS	1-1
1.1	MOTIVATION FOR EMPLOYING EFFECTIVE PROPERTIES IN THE SIMULATION OF LARGE-SCALE FLOW IN FRACTURED ROCK	1-1
1.2	FRACTURES AND THEIR CHARACTERISTICS	1-2
1.2.1	Fracture Orientation and Inclination	1-7
1.2.2	Fracture Aperture	1-7
1.2.3	Fracture Trace Length	1-7
1.2.4	Fracture Mineralization and Alterations	1-8
1.2.5	Fracture Conceptual Model	1-8
1.3	MODELING APPROACHES FOR FLOW IN FRACTURED ROCK	1-9
1.3.1	Single Continuum Models	1-10
1.3.2	Dual Porosity Models	1-13
1.3.3	Discrete Fracture Network Models	1-14
1.3.4	Discrete Fracture Equilibrium Models	1-15
1.3.5	Discrete Fracture Nonequilibrium Models	1-15
1.3.6	Stochastic Fracture Continuum Models	1-15
1.4	REGIONALIZATION OF FRACTURE PARAMETERS	1-16
2	VISUALIZATION AND NUMERICAL GENERATION OF REALISTIC FRACTURE SETS	2-1
2.1	STATISTICAL STUDY OF FRACTURE SETS	2-1
2.1.1	Orientation of Fracture Sets	2-1
2.1.2	Probability Distributions for Directional Data	2-2
2.1.2.1	Univariate Fisher Distribution	2-2
2.1.2.2	Bivariate Fisher Distribution	2-3
2.1.2.3	Bivariate Normal Distribution	2-3
2.1.2.4	Bivariate Bingham Distribution	2-4
2.1.3	Fracture Density and Spacing	2-4
2.1.4	Trace Length	2-5
2.1.5	Aperture and Thickness	2-6
2.1.6	Probability Distributions for Scalar Data	2-6
2.1.6.1	Uniform Distribution	2-6
2.1.6.2	Exponential Distribution	2-6
2.1.6.3	Normal Distribution	2-7
2.1.6.4	Lognormal Distribution	2-7
2.1.6.5	Power-Law Distribution	2-8

CONTENTS (Cont'd)

Section		Page
2.2	VISUALIZATION, STATISTICAL, AND CONNECTIVITY ANALYSES OF APACHE LEAP TUFF SITE FRACTURE SETS	2-9
2.2.1	Visualization and Statistical Analyses	2-9
2.2.2	Connectivity Analyses	2-13
2.3	NUMERICAL GENERATION OF REALISTIC FRACTURE NETWORK SETS	2-22
2.4	APPLICATION AND VERIFICATION OF A TWO-DIMENSIONAL FRACTURE NETWORK GENERATOR	2-27
3	METHODS FOR ESTIMATING EFFECTIVE UNSATURATED HYDRAULIC PROPERTIES	3-1
3.1	EFFECTIVE PROPERTY CALCULATIONS BASED ON ADDITIVE VOLUME FRACTIONS	3-1
3.2	EFFECTIVE PROPERTY CALCULATIONS BASED ON DIRECT NUMERICAL SIMULATIONS	3-7
3.3	EFFECTIVE PROPERTY CALCULATIONS BASED ON HOMOGENIZATION AND RENORMALIZATION METHODS	3-9
3.4	EFFECTIVE PROPERTY CALCULATIONS BASED ON POWER AVERAGING	3-10
4	SEMI-ANALYTICAL PREDICTION OF EFFECTIVE HYDRAULIC PROPERTIES WITH THE REAL SPACE RENORMALIZATION GROUP METHOD	4-1
4.1	REAL SPACE RENORMALIZATION GROUP METHOD	4-2
4.2	DETERMINING EFFECTIVE HYDRAULIC CONDUCTIVITY WITH THE REAL SPACE RENORMALIZATION GROUP METHOD	4-7
4.2.1	Assumptions	4-7
4.2.2	Algorithm	4-9
4.3	VERIFICATION RESULTS AND DISCUSSION	4-10
5	CALCULATION OF EFFECTIVE HYDRAULIC PROPERTIES WITH DIRECT NUMERICAL SIMULATIONS	5-1
5.1	APPROACH	5-1
5.2	ANALYSIS AND RESULTS	5-1
5.2.1	Case 1—Flow Perpendicular and Parallel to Unidirectional Fully Connecting Fractures	5-1
5.2.1.1	Flow Perpendicular to Fractures	5-2
5.2.1.2	Flow Parallel to Fractures	5-2
5.2.2	Case 2—Flow Through Orthogonal Fracture Sets Embedded in Homogeneous Rock Matrix	5-4
5.2.2.1	Fracture Sets with Equal Density in Horizontal and Vertical Directions	5-4
5.2.2.2	Fracture Sets with Different Density in Horizontal and Vertical Directions	5-6
5.2.3	Case 3—Flow Through a Random Network of Fractures Embedded in Homogeneous Rock Matrix	5-6
5.2.3.1	Flow Through Short Fractures	5-9
5.2.3.2	Flow Through Long Fractures	5-20

CONTENTS (Cont'd)

Section		Page
5.2.4	Case 4—Flow Through a Random Network of Fractures Embedded in Heterogeneous Rock Matrix	5-20
5.2.4.1	Flow Through Short Fractures	5-20
5.2.4.2	Flow Through Long Fractures	5-20
5.3	ANISOTROPIC EFFECTIVE HYDRAULIC CONDUCTIVITY FOR ROCKS WITH PARALLEL, INCLINED FRACTURES	5-21
5.4	DISCUSSION	5-30
6	PARAMETRIC STUDY FOR THE CALCULATION OF EFFECTIVE PROPERTIES AND LIMITATIONS OF THE REAL SPACE RENORMALIZATION GROUP METHOD	6-1
6.1	DESIGN OF EXPERIMENTS	6-1
6.2	SUMMARY OF PARAMETRIC STUDY RESULTS	6-6
6.2.1	Fractured Matrix (f=7 percent)	6-6
6.2.1.1	Effect of Matrix Standard Deviation σ	6-6
6.2.1.2	Effect of Matrix Mean	6-6
6.2.1.3	Effect of Matrix Correlation Length λ	6-6
6.2.1.4	Effect of Increasing Fracture Volume	6-7
6.2.1.5	Effect of Anisotropy in Fracture Length, and Matrix Correlation Length	6-8
6.2.2	Nonfractured Matrix	6-10
6.2.2.1	Effect of Matrix Spatial Structure	6-10
6.2.2.2	Effect of Anisotropy in Matrix Correlation Length	6-11
6.2.2.3	Effect of Matrix Standard Deviation	6-11
6.3	SUMMARY OF MULTIPLE REALIZATION STUDY RESULTS	6-12
6.3.1	Effect of Variability in Fracture Network for Fixed Fracture Volume	6-12
6.3.2	Effect of Variability in Matrix for a Fixed Fracture Network	6-14
6.4	SUMMARY OF REAL SPACE RENORMALIZATION GROUP VERIFICATION RESULTS FOR NONBINARY SYSTEMS	6-15
6.5	DISCUSSION	6-21
7	SUMMARY AND CONCLUSIONS	7-1
8	REFERENCES	8-1

FIGURES

Figures		Page
1-1	Different hydrogeological conceptual models for the representation of a stratified, highly fractured rock	1-3
1-2	Schematic of a 2D fractured system to be used in flow simulations with a large-scale flow simulator	1-4
1-3	Distinction among fractures based on their mechanism of formation	1-6
1-4	Schematic of a fault zone and variability in the fracture density around the fault offset	1-6
1-5	Determination of the pole of fracture plane Π on a lower-hemisphere stereographic projection diagram	1-8
1-6	Permeability characteristic curve for three types of fractures	1-10
1-7	Schematic of fracture conceptual model and the corresponding continuum approximation	1-11
1-8	Photograph of rock sample showing vein filled with angular clasts of host rock and calcite mineralization	1-12
2-1	Pole analysis and contouring of the stereographic projection diagram	2-2
2-2	Borehole configuration at the ALTS: (a) plan view; and (b) profile view	2-10
2-3	Lower-hemisphere stereonet projection of fracture pole orientations observed at the ALTS	2-12
2-4	Fracture plane strike (A) and dip (B) distribution at the ALTS	2-13
2-5	Line interpretation of structural lineaments in the ALTS	2-14
2-6	Histogram of strike azimuth for the dominant fracture set and normal distribution honoring the first two moments	2-15
2-7	3D representation of inventory of observed fracture traces obtained from oriented cores along the boreholes of the ALTS	2-16
2-8	3D representation of 224 fracture planes at the ALTS. The fractures are assumed to be of infinite extent	2-17
2-9	Outcropping traces for the fractures of Figure 2-8	2-18
2-10	Schematic of three intersecting fracture planes and associated fracture plane intersections	2-19
2-11	3D representation of 56 fracture planes and their 845 fracture plane intersections	2-20
2-12	X-Z projection of 6,309 identified connections between fracture plane intersections	2-21
2-13	X-Y projection of 6,309 identified connections between fracture plane intersections	2-21
2-14	Synthetic 2D fracture network in a 100×100 m domain, where each 10×10 m subdomain was generated independently	2-25
2-15	Conceptualization of fracture set appearance at the ALTS	2-28
2-16	Fracture network generator flowchart	2-29
2-17	Set of vertical fractures used for network generator verification	2-29
2-18	Horizontal (dashed) and vertical (solid) variograms for the fracture pattern of Figure 2-17	2-30
2-19	Vertical variogram for the fracture pattern of Figure 2-17 and fitted theoretical variogram models	2-31
2-20	Trace length variogram and fitted theoretical variogram models	2-31

FIGURES (Cont'd)

Figures		Page
2-21	Highly fractured, heterogeneous structures for a binary matrix-fracture system	2-32
2-22	Highly fractured, heterogeneous structures for a stochastic matrix-fracture system	2-32
4-1	Effect of fracture half-length on the effective saturated conductivity of a 2D fracture network	4-6
4-2	Schematic of RSRG transformation	4-8
4-3	Schematic of algorithm for the determination of effective unsaturated conductivity	4-10
4-4	Schematic of a fully connected fracture network with anisotropic fracture density	4-11
4-5	Comparison between RSRG and direct numerical simulation results for saturated flow in a network of fully connecting fractures	4-13
4-6	Semi-variogram of uncorrelated saturated conductivity at successive steps of the real space renormalization group process	4-14
4-7	Comparison of effective unsaturated hydraulic conductivity between a fracture system with fully connecting fractures and a system with a random binary distribution of fracture and matrix pixels	4-14
4-8	Comparison of effective unsaturated hydraulic conductivity between a fracture system with fully connecting fractures and a system with a random binary distribution of fracture and matrix pixels	4-15
4-9	Comparison of effective unsaturated hydraulic conductivity for real space renormalization group and direct numerical simulation results for a system with fractures of finite length	4-15
5-1	Comparison of effective hydraulic conductivity from numerical simulations and the weighted harmonic mean for flow perpendicular to a set of fully connecting fractures in homogeneous matrix	5-3
5-2	Comparison of effective hydraulic conductivity from numerical simulations and the weighted arithmetic mean for flow parallel to a set of fully connecting fractures in homogeneous matrix	5-5
5-3	Comparison of effective hydraulic conductivity from numerical simulations and the weighted mean of Eq. (5-2) for flow in two orthogonal sets of fractures with isotropic densities and uniform spacing in homogeneous matrix	5-7
5-4	Comparison of effective hydraulic conductivity from numerical simulations and the weighted mean of Eq. (5-2) for flow in two orthogonal sets of fractures with anisotropic densities and random spacing in homogeneous matrix	5-8
5-5	Schematic illustrating the two types of numerical simulations conducted for the calculation of effective hydraulic conductivities	5-9
5-6	Schematic showing the location of fractures and the finite element discretization used for the MMOC2 numerical simulations of flow through a randomly generated set of short fractures	5-10
5-7	Pressure head distribution for flow through a randomly generated set of short fractures in homogeneous matrix. The average suction in the domain is $\Psi=60$ cm.	5-11
5-8	Pressure head distribution for flow through a randomly generated set of short fractures in homogeneous matrix. The average suction in the domain is $\Psi=200$ cm.	5-12

FIGURES (Cont'd)

Figures		Page
5-9	Comparison of effective hydraulic conductivity from numerical simulations and the arithmetic, geometric, and harmonic means for flow through a randomly generated set of short fractures in homogeneous matrix	5-13
5-10	Pressure head distribution for flow through a randomly generated set of short fractures in homogeneous matrix. The average suction in the domain is $\Psi = 10$ cm.	5-14
5-11	Pressure head distribution for flow through a randomly generated set of short fractures in homogeneous matrix. The average suction in the domain is $\Psi = 200$ cm.	5-15
5-12	Streamlines corresponding to the pressure head field of Figure 5-10	5-16
5-13	Streamlines corresponding to the pressure head field of Figure 5-11	5-17
5-14	Typical equipotential lines and streamlines for flow around an intruding fracture	5-18
5-15	Comparison of effective hydraulic conductivity from numerical simulations and the arithmetic, geometric, and harmonic means for flow through a randomly generated set of short fractures in homogeneous matrix. Contrast between fracture and matrix saturated hydraulic conductivity was reduced by a factor of 100	5-19
5-16	Schematic showing the location of fractures and the finite element discretization used for the MMOC2 numerical simulations of flow through a randomly generated set of long fractures	5-21
5-17	Comparison of effective hydraulic conductivity from numerical simulations and the arithmetic, geometric, and harmonic means for flow through a randomly generated set of long fractures in homogeneous matrix. Contrast between fracture and matrix saturated hydraulic conductivity was reduced by a factor of 100.	5-22
5-18	Comparison of effective hydraulic conductivity from numerical simulations and the arithmetic, geometric, and harmonic means for flow through a randomly generated set of short fractures in heterogeneous matrix	5-23
5-19	Comparison of effective hydraulic conductivity from numerical simulations and the arithmetic, geometric, and harmonic means for flow through a randomly generated set of long fractures in heterogeneous matrix	5-24
5-20	Schematic showing one of a set of infinite, parallel, inclined fractures	5-25
5-21	Comparison of analytical and semi-analytical solutions for the effective unsaturated conductivity of a 45° inclined set of parallel and infinitely extensive fractures	5-28
5-22	Anisotropy ratio (K_{zz}/K_{xx}) as a function of suction head for various angles of inclination	5-29
6-1	Effect of matrix standard deviation on the effective hydraulic conductivity of a fractured medium.	6-7
6-2	Effect of the mean value for the matrix saturated conductivity on the effective conductivity of the combined fracture-matrix system	6-8
6-3	Effect of matrix isotropic correlation length on the effective conductivity of a fractured medium	6-9
6-4	Effect of increasing fracture volume on the effective conductivity of a fractured medium.	6-10
6-5	Effect of fracture length anisotropy on the effective conductivity of a fractured medium.	6-11

6-6 Effect of anisotropy in correlation length on the effective conductivity of a fractured medium. 6-12
6-7 Effect of matrix spatial structure on the effective conductivity of an unfractured medium. 6-13
6-8 Effect of anisotropy in correlation length on the effective conductivity of an unfractured medium. 6-14
6-9 Effect of matrix standard deviation on the effective conductivity of an unfractured matrix. 6-15
6-10 Mean (solid) and standard deviation (dashed) of the 24 realizations of fracture networks superimposed on the fixed matrix of Experiment 16 6-16
6-11 Relative variability of the effective conductivity for 24 fracture network realizations on the fixed matrix of Experiment 16 6-16
6-12 Mean (solid) and standard deviation (dashed) of the 24 realizations of fracture networks superimposed on the fixed matrix of Experiment 17 6-17
6-13 Relative variability of the effective conductivity for 24 fracture network realizations on the fixed matrix of Experiment 17 6-17
6-14 Mean (solid) and standard deviation (dashed) of a fixed fracture network superimposed on 24 realizations of the matrix of Experiment 17 6-18
6-15 Relative variability of the effective conductivity for a single fracture network superimposed on 24 realizations of the matrix of Experiment 17 6-18
6-16 Mean (solid) and standard deviation (dashed) of a fixed fracture network superimposed on 24 realizations of the matrix of Experiment 18 6-19
6-17 Relative variability of the effective conductivity for a single fracture network superimposed on 24 realizations of the matrix of Experiment 18 6-19
6-18 Comparison of Real Space Renormalization Group and BIGFLOW results for a heterogeneous, anisotropic, nonfractured matrix field with $K^m{}_G$ = 0.01 cm/s 6-20
6-19 Comparison of Real Space Renormalization Group and BIGFLOW results for a heterogeneous, anisotropic, nonfractured matrix field with $K^m{}_G$ = 0.001 cm/s 6-20
6-20 Comparison of Real Space Renormalization Group and BIGFLOW results for a heterogeneous, isotropic, fractured matrix field with $K^m{}_G$ = 0.01 cm/s 6-22
6-21 Comparison of Real Space Renormalization Group and BIGFLOW results for a heterogeneous, isotropic, fractured matrix field with $K^m{}_G$ = 0.0001 cm/s 6-22

TABLES

Table		Page
3-1	Equivalence between the stochastic perturbation and power average approaches $\rho \neq 0$	3-16
3-2	Equivalence between the stochastic perturbation and power average approaches $\rho = 0$	3-16
4-1	Possible configurations of conductivity for a binary system and associated effective conductivity	4-4
4-2	Execution time comparison between numerical simulation and RSRG method for the determination of effective saturated conductivity	4-12
4-3	Execution time comparison between numerical simulation and RSRG method for the determination of effective unsaturated conductivity	4-12
6-1	List of experiments to study the effect of several parameters on effective conductivity of a stochastic matrix-fracture composite	6-3

ACKNOWLEDGMENTS

This report was prepared to document work performed by the Center for Nuclear Waste Regulatory Analyses (CNWRA) for the Nuclear Regulatory Commission (NRC) under Contract No. NRC-02-93-005. The activities reported here were performed on behalf of the NRC Office of Nuclear Regulatory Research, Division of Regulatory Applications under FIN B6664. The report is an independent product of the CNWRA and does not necessarily reflect the views or regulatory position of the NRC.

Expert technical assistance for the fracture network visualization and connectivity analyses was provided by M. Muller (Southwest Research Institute). A critical review of Section 5.3 was conducted by Dr. V. Kapoor. Able editorial and secretarial support was provided by C. Cudd, T. Fischer, B. Ford, C. Gray, M. Gruhlke, and A. Ramos. The authors thank Ms. R. Sanchez for her format review, Drs. D. Ferrill, S. Stothoff, and G. Wittmeyer for their technical reviews, and Dr. W. Patrick for his programmatic review. The reviewers were very generous with their time and effort, and their suggestions and comments have made this voluminous report a much more enjoyable product. The authors gratefully acknowledge the contributions of Mr. T.J. Nicholson, the NRC Project Officer.

EXECUTIVE SUMMARY

The technical objective of the Stochastic Analysis of Unsaturated Flow and Transport Research Project, hereafter called Stochastic Project, is to provide and document the methods and tools necessary for realistic modeling and analysis of the complex, heterogeneous flow and transport processes anticipated or hypothesized to occur in the far-field of the proposed high-level waste (HLW) repository at Yucca Mountain, Nevada. These models and analyses will be necessary to predict the performance of the overall system (10 CFR 60.112), the Geologic Setting (10 CFR 60.113), and to evaluate compliance with siting criteria (10 CFR 60.122). The spatial variability of many processes and parameters affecting the long-term behavior of the flow system at the scale of the Yucca Mountain site is poorly known. More specifically, there is a lack of acceptable hydrogeologic parameters, theories, and conceptual and mathematical models that are considered applicable or computationally feasible for the conditions prevailing at Yucca Mountain. Even if such models are developed, there will be a variety of fundamental questions regarding their applicability over the spatial scales of the subregional and regional hydrologic systems. Moreover, some uncertainty will always remain in the value of hydrogeologic parameters because realistically, only a limited amount of data will be collected. One must also keep in mind that this information is provided at vastly different scales, ranging from the millimeter or centimeter laboratory scale, to the meter laboratory or field scale, all the way up to the tens or thousands of meters field scale. Making these measurements compatible with each other so that they all play an integral role in building a conceptual and mathematical model of a site at the kilometer scale is a formidable task.

The Stochastic Project aims to address issues related to the quantitative characterization of large-scale flow and transport in unsaturated, highly-fractured, heterogeneous rock. Information, methodologies, and numerical tools developed within this project will be used to support specific portions of the License Application Review Plan (LARP). Specifically, review plans that deal with "Assessment of Compliance with the Groundwater Travel Time Performance Objective" and "Potentially Adverse Condition: Perched Water Bodies," which have been judged to require a Type 5 review, and thus require independent research to resolve the following key technical uncertainties (KTUs): (i) determining effective hydrologic characteristics (e.g., effective porosity, effective hydraulic conductivity) as a function of scale for the saturated and unsaturated zone, (ii) developing a conceptual groundwater flow model that is representative of the Yucca Mountain flow system, and (iii) uncertainties associated with determining characterization parameters.

This first of two final reports addresses the issue of effective hydraulic property calculations with semi-analytical and direct numerical techniques and summarizes one possible methodology for the accurate and efficient simulation of large-scale flow processes in unsaturated, highly-fractured, heterogeneous rock. It is organized as follows. Chapter 1 introduces fractures and discusses their characteristics. The chapter presents a discussion on the need for effective hydraulic properties and the presentation of an approach for large-scale flow modeling in fractured rock. This approach consists of: (i) lumping all micro- and macro-scale fractures under one equivalent, spatially variable, hydraulic property and (ii) preserving the discrete nature of dominant stratification and/or linear features under the "persistent discontinuity" concept. Examples of such features are fault zones and highly-fractured rock zones. It continues with a brief literature review of several modeling approaches for studying flow in fractured rock. It then presents the concept of describing fracture characteristics as regionalized variables, which is integral to the modeling approach presented herein. Chapter 2 deals with the visualization and numerical generation of realistic fracture sets. The chapter introduces some concepts for the statistical description of fractures and their characteristics. Then it continues with the study of the Apache Leap Tuff Site (ALTS) in Arizona,

one of the Nuclear Regulatory Commission (NRC) sponsored hydrology research field sites. The application of visualization and connectivity analysis tools, developed under the Stochastic Project, for the ALTS is the next part of the chapter. An extensive literature review on the subject of numerical generation of realistic fracture networks is also presented. Finally, Chapter 2 concludes with the development and verification of a simple, yet realistic and efficient, fracture network generator. Chapter 3 of this report constitutes a thorough, yet not exhaustive, literature review on the subject of effective property estimation. This literature review is grouped under the following broad categories: (i) calculations based on additive volume fractions, (ii) calculations with direct numerical simulations, (iii) calculations based on homogenization and renormalization methods, and (iv) calculations based on power averaging and its variants. Chapter 4 presents a detailed description of one of the renormalization methods, the Real Space Renormalization Group (RSRG) method. The assumptions used and the algorithmic implementation of the RSRG method for unsaturated, fractured media are also presented. Finally, Chapter 4 concludes with some verification results for the case of binary matrix-fracture systems. Chapter 5 presents a detailed direct numerical simulation study. A variety of cases are studied, and two numerical codes, the Modified Method of Characteristics 2 (MMOC2) and BIGFLOW codes are used to explore the dependence of the effective hydraulic conductivity on several matrix and fracture characteristics. Chapter 5 concludes with a study of the anisotropic, tensorial nature of the fracture network, comprising parallel, inclined fractures of infinite extent. Chapter 6 presents a parametric study of the RSRG method. A comprehensive suite of numerical experiments was conducted, and the importance of various parameters, such as the degree of fracturing, the heterogeneity of the matrix, the spatial structure of the matrix, the fracture length, etc., was studied. This chapter also presents a study of the effect of variability in the fracture networks on the effective properties. This chapter concludes with some further verification of the RSRG method in the case of nonbinary matrix-fracture systems and identifies some of the limitations of the method. Chapter 7 of this report summarizes the findings, and presents some conclusions.

This work showed that any modeling effort must be site-specific. For example, at the ALTS, an equivalent continuum approach could be valid for a relatively shallow part of the rock only. At greater depths, this approach would most probably neglect the existence of elongated, highly connected features. This work has reviewed some pertinent literature on methods for effective property calculations and introduced the RSRG method, which was found to be extremely accurate for binary matrix-fracture systems.

A variety of numerical experiments was conducted with the help of the MMOC2 and BIGFLOW codes and comparisons between the two codes and the RSRG solution were made. Finally, a detailed parametric study of the RSRG method showed that it provides a viable alternative to direct numerical simulation techniques, especially since it is typically two to three orders of magnitude faster. However, it has to be noted that the RSRG method is not a panacea since it suffers from limitations, especially in cases where the underlying matrix rock is heterogeneous with very long, isotropic correlation structures.

1 FLUID FLOW IN FRACTURED ROCKS AND THE NEED FOR EFFECTIVE PROPERTY CALCULATIONS

1.1 MOTIVATION FOR EMPLOYING EFFECTIVE PROPERTIES IN THE SIMULATION OF LARGE-SCALE FLOW IN FRACTURED ROCK

Assessing the performance of the potential high-level waste (HLW) repository at Yucca Mountain, Nevada, requires the determination of the rate of radionuclide transport via groundwater through the unsaturated and/or saturated zones to the accessible environment. The unsaturated zone extends over approximately 500 m of interbedded welded and nonwelded ash flow tuffs. This tuffaceous rock exhibits a large variation in petrophysical properties due to the post-depositional fracturing, faulting, and erosion (Flint et al., 1993). It has been postulated (Nitao and Buscheck, 1991) that as the water infiltrates down from the surface, it may, at first, flow mainly through the fractures in the rock. As this filtration occurs, water may also imbibe into the matrix blocks. The rate at which imbibition takes place determines whether or not the water from a precipitation event can reach the repository level. The accessibility is also strongly governed by the fracture characteristics such as density (i.e., inverse of spacing), connectivity, and orientation. Explicit representation of individual fractures in numerical models is not considered feasible, except possibly for small volumes of rock, and unless some simplifying assumptions are made concerning fracture network geometry. However, that would be almost impossible for the Yucca Mountain site since, if the Topopah Spring welded unit has a mean fracture density of 20 fractures/m^3 and a mean thickness of 300 m over the approximately 7×10^6 m^2 area of the central Yucca Mountain block, one would have to consider flow in approximately 4×10^{10} discrete fractures (U.S. Geological Survey, 1993). As it is virtually impossible to describe the exact fracture topology in a deterministic fashion to conduct a full-scale simulation, it is worthwhile to investigate an alternative approach. This approach consists of stochastically generating several fracture realizations to estimate the most likely flow behavior of the fractured composite. These realizations may be conditioned on experimental data. To stochastically generate and analyze many realizations in a reasonable amount of time, it is required that the simulation of flow using each realization of the stochastic field be able to be conducted relatively quickly. A minimum requirement is to be able to determine the essential or dominant flow behavior by using fewer discretized flow units without sacrificing the important contributions from features smaller than the grid block scale.

One approach to modeling variably saturated fractured rock has been to explicitly represent a single fracture in the computational mesh, and invoke the symmetry of highly idealized fracture-network geometries, such as parallel fracture systems, to predict network behavior (Nitao and Buscheck, 1991; Pruess et al., 1990a,b). This approach has provided useful insights regarding how fluids are exchanged between fractures and intact matrix, but has ignored potentially important issues such as network connectivity and the dispersive effects on flow due to intersecting fractures. Additionally, relatively infrequent, potentially highly transmissive and areally extensive fractures (e.g., fault zones) may be represented as distinct entities in the models. Small-aperture fractures or microfractures, or less extensive features, are lumped into the fracture continuum and treated as a single continuum. This approach captures some of the flow irregularity which is characteristic of fractured environments, yet reduces the number of fractures that need to be considered as discrete entities by the model. The objective of models to be developed by this study is to create an artificial system that displays flow and transport behavior approximately equivalent to the real system.

In fact, this indirect approach to heterogeneous flow modeling can be used in combination with explicit modeling of certain types of heterogeneities that are too important to be treated implicitly (Ababou, 1991). Besides explicit modeling of site-specific large-scale geologic discontinuities and trends, auxiliary models such as the ones presented above would be used to deal with smaller scale heterogeneity in a simplified manner. Therefore, when indirect modeling methods are implemented with a view to obtain representative field-scale simulations of site-specific processes, direct representation of heterogeneities is still needed to capture essential features. Clemo (1989) advocated a similar method which he calls the "dual permeability" approach. This term should not be confused with the dual porosity continuum models, as it refers to an approach that addresses the simulation of fractures at two levels. Under this approach, the larger and, therefore, more important fractures are modeled discretely, whereas the smaller (but abundant) fractures are lumped in a continuum with representative properties. According to Clemo (1989), this approach lies between the concepts of REV and discrete fracture modeling. Figure 1-1 depicts a schematic, adapted from Mazurek et al. (1993), of the process involved in representing reality with three different conceptual models. Under this conceptualization, the highly fractured rock at the left could be described by: (i) an equivalent porous medium which honors stratification, (ii) the hybrid or dual permeability approach, and (iii) a discrete fracture approach.

The methodology advocated in this report is very much consistent with such an approach. Important geologic features, also called persistent discontinuities, must be modeled explicitly. This could be accomplished with the help of several techniques, but a continuum approach is, in our opinion, fully justified, especially under conditions of uncertain data. The remaining heterogeneity in the rock mass can be lumped together under a single continuum approach. This is precisely the point of interest here. It is necessary to somehow account for the fracturing over different parts of the domain under study, and assign representative effective properties to the grid blocks of a large-scale flow simulator. This concept is demonstrated in Figure 1-2. As indicated in this figure, one may want to conduct a flow simulation on a 5×5 computational cell domain. This can be accomplished only if some representative hydraulic property is assigned to each of the grid blocks. There is nothing in this approach that precludes the implementation of a stochastic continuum approach. In fact, this could well be a very realistic representation of field conditions. A model, therefore, is necessary that is independent of distributional assumptions and hydraulic conductivity contrasts, imposes minimal computer memory space requirements, and is fast enough in its numerical implementation for repeated use. Models based on the theory of renormalization seem to be powerful enough to overcome these constraints, at least for saturated flow systems. As it will be demonstrated later in this report, these methods have been extended and applied for unsaturated fractured rock systems.

The object of this work is to study the effective flow behavior of an ensemble of fractures in the presence of matrix-fracture interaction. Presented in this work are salient features of a fracture network visualization and statistical analysis tool, and a simple, but efficient, two-dimensional (2D) fracture network generator code developed at the Center for Nuclear Waste Regulatory Analyses (CNWRA). Then, the implementation of the Real Space Renormalization Group (RSRG) method to upscale petrophysical and flow properties from the scale of measurements to the large-scale simulation grid block scale is discussed, together with results from direct numerical simulations.

1.2 FRACTURES AND THEIR CHARACTERISTICS

Fractures are abundant in all types of rocks and soils. Fractures are the result of shear and tensile stresses which develop within rock masses under the influence of various forces, such as

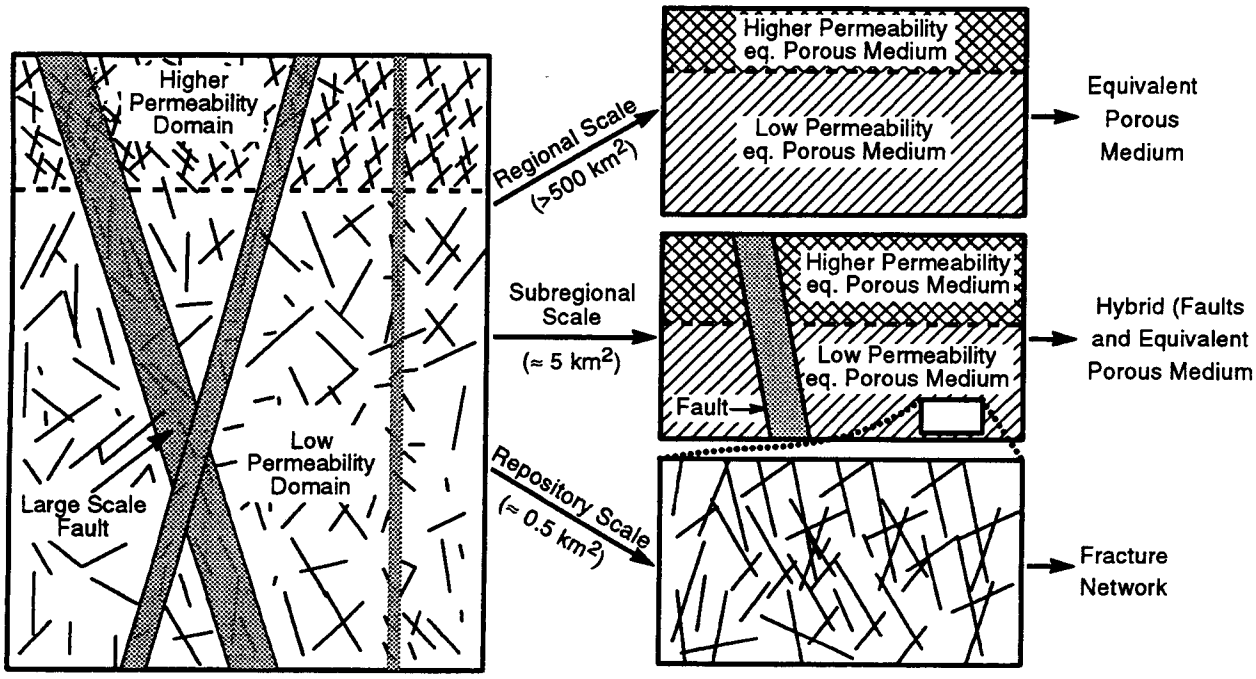

Figure 1-1. Different hydrogeological conceptual models for the representation of a stratified, highly fractured rock [adapted from Mazurek et al. (1993)]

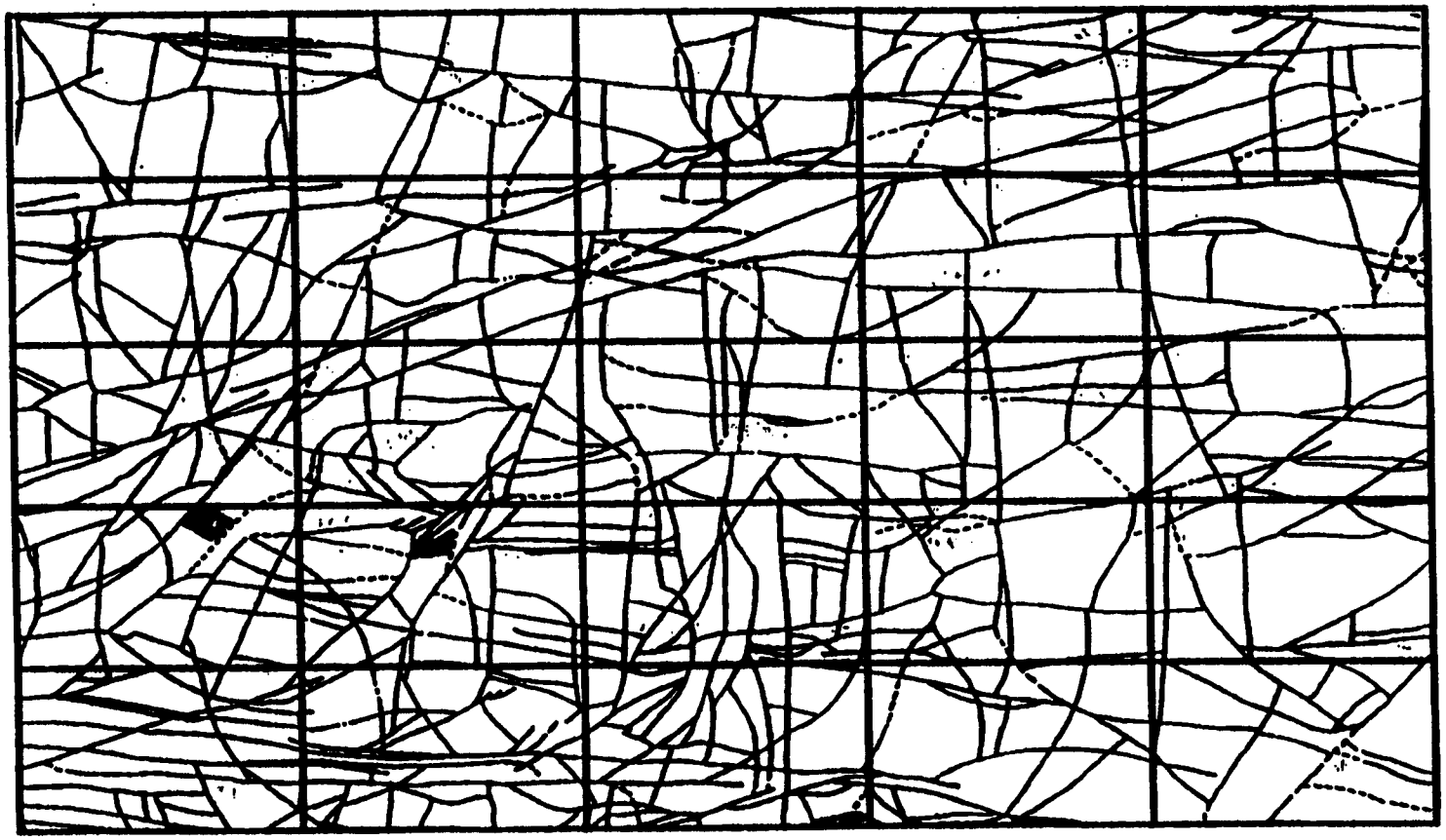

Figure 1-2. Schematic of a 2D fractured system to be used in flow simulations with a large-scale flow simulator

compressive forces, or forces associated with the movement of rock. Several terms associated with fracture-related terminology are often used synonymously and, therefore, are useful to define at this point.

- A fracture is a planar feature across which rock continuity has been broken (Gary et al., 1972) without the details of an offset being visible. According to Griggs and Handin (1960), "a fracture is defined as a surface along which a loss of cohesion has taken place." The two rock faces of a fracture may be: (i) completely separated, (ii) in complete contact, or (iii) healed by either rubblized material or mineralized/brecciated material. Figure 1-3 depicts three types of fractures: (i) fractures *s* and *d*, which follow the general orientation of the beds, are developed due to the upward movement of the rock mass; (ii) fractures *t* are developed by tensile forces due to the folding of the beds; and (iii) fractures *o* are developed due to shear stresses and are, generally, oblique to the trend of the fold. Even though these fractures are not necessarily developed due to shear stresses, the conjugate sets intersect each other at acute angles (approximately 60°).

- A joint is a fracture with the two opposing faces being offset by normal stresses. The opening between the two rock faces, called aperture, is distinguishable and typically is not associated with shear-related displacements. However, according to Bates and Jackson (1980), a joint is a fracture surface with no visible displacement parallel to the surface. Hancock (1985) classifies fractures *s* and *d* as extension fractures and *o* as conjugate shear fractures, enclosing an acute angle.

- A fault is a fracture feature that has not only been offset normally, but also has been under the influence of substantial shear stresses, thus exhibiting displacements parallel to the fracture. A collection of interlacing fractures is called a fault zone and is characterized by numerous fractures which vary in density with the distance from the fault offset. This can be seen in schematic form in Figure 1-4.

Howard and Nolen-Hoeksema (1990) define fractures to include the entire volume between two fracture walls. They distinguish this term from the notion of fracture pore space, which excludes fracture-filling cement or other mineral fillings. Therefore, according to Howard and Nolen-Hoeksema (1990), the total volume within a fracture is the sum of the fracture pore space plus the volume of the fracture filling. A detailed discussion on the subject of joints and shear fractures in rock can be found in the work of Engelder (1987).

Fractures are found over a wide range of length scales, from microfractures which extend over the submillimeter scale to intra-crustal-plate features which extend over thousands of kilometers in length. In stark contrast to porous media flow and transport theories, there are no widely acceptable theories for the study of fracture flow, especially under unsaturated conditions. Due to their extremely anisotropic geometric topology, fractures can strongly influence fluid flow in rock masses, either as a flow conduit or as a flow barrier. There are several physical parameters that affect fracture flow. According to Long (1983), characterization of a fracture system is considered complete only after each fracture is described in terms of the strike (azimuth), dip (inclination), aperture, extent, roughness, shape, density, spatial distribution (regionalization) of fracture-related parameters, connectivity, and the type of mineral fillings associated with each individual fracture. However, as it was pointed out in Section 1.1, this is rarely feasible in real-life applications.

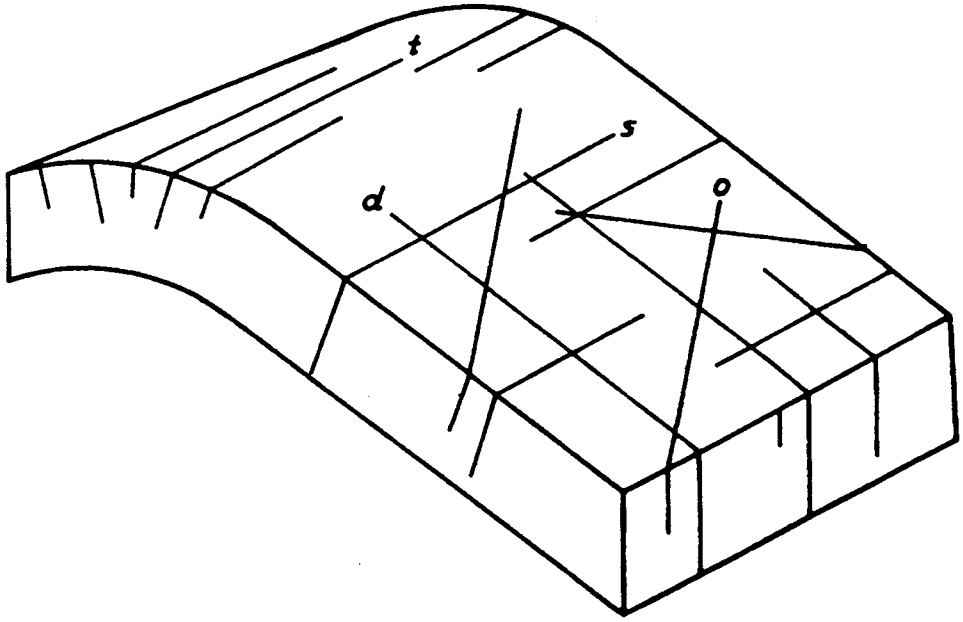

Figure 1-3. Distinction among fractures based on their mechanism of formation

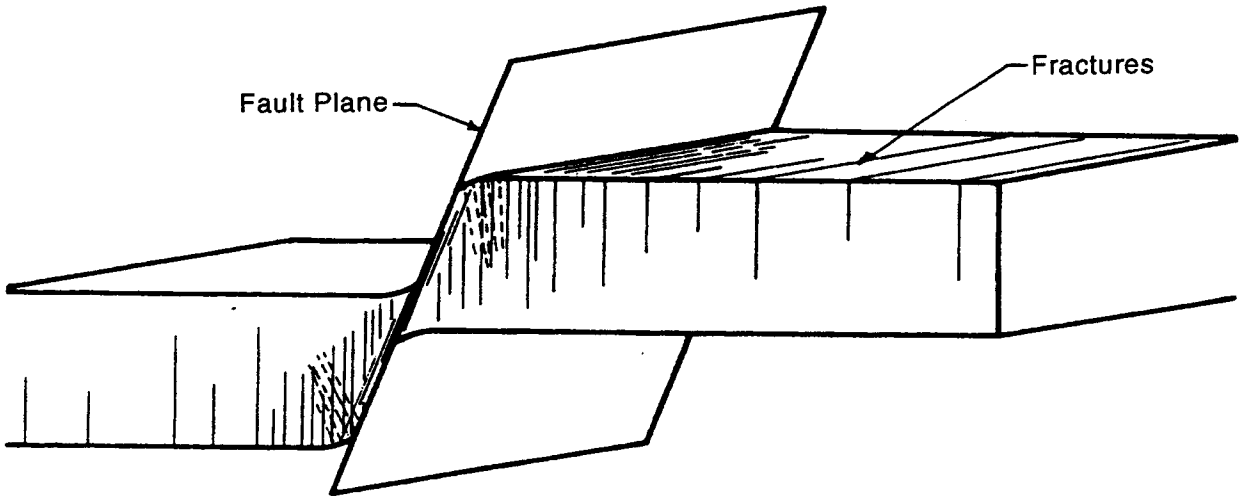

Figure 1-4. Schematic of a fault zone and variability in the fracture density around the fault offset

1.2.1 Fracture Orientation and Inclination

The strike (azimuth) and dip (inclination) of an individual fracture or fracture set are perhaps the most important characteristics of fractured rock for fluid flow patterns. They are typically closely related to the tectonic history of the rock and as such provide a very convenient platform to classify or group fracture sets and associated tectonic events. For example, at Yucca Mountain there exist two major sets of fractures and faults. One striking north-northwest and the other striking north-northeast. Even though both sets are steeply dipping to the west, the second set is believed to be more open and thus more conductive, indicating a differentiation in their development (Scott et al., 1983).

The strike and dip of a fracture plane can be represented readily by plotting the projection of the plane on a lower-hemisphere equal-area stereographic projection diagram. However, a more convenient way of representing a fracture plane is through the plane pole which is defined as the intersection of the reference sphere by the plane normal vector. Figure 1-5 depicts the stereographic and lower-hemisphere projection representation of a fracture plane and its corresponding pole. This type of diagram, also called a Schmidt diagram, has been extensively used for analyses of rock mass stability, highway engineering, etc. Their use, in conjunction with aerial photography and layer drilling of intersecting lineaments, has been successful in locating major water-bearing fracture zones [e.g., in the vicinity of Lake Tahoe, California (Gates, 1993)].

1.2.2 Fracture Aperture

One of the most common assumptions made in studying flow in fractures is that, for smooth-walled fractures, the volumetric flow rate is a function of the cube of the aperture. In reality, fractures have complex surfaces and highly variable apertures. Therefore, for rough-walled fractures, the volumetric flow rate may be expected to deviate from being a function of the cube of aperture. Montazer and Harrold (1985) have used roughness profiles for calculating hydraulic properties of rocks. Under unsaturated conditions, these assumptions are still to be verified. A further complication is that a large-scale negative trend of fracture aperture is often observed due to the closing of fractures under increased lithostatic stresses. For example, Rush et al. (1984) confirmed the lithostatic stress-based closure of fractures at Yucca Mountain. Similarly, Pollard and Aydin (1988) and Pollard and Segall (1987) studied displacements and stresses developing near fractures and rock joints and inferred the decrease of fracture intensity with distance away from the stress concentration points. Barton and Hsieh (1989) have fitted power-law functions to describe aperture frequency distributions from various layer-parallel pavements at Yucca Mountain.

1.2.3 Fracture Trace Length

Fracture trace lengths are measured from aerial photographs, outcrop maps, or direct outcrop observations. Associated with these measurements are two types of truncation errors: (i) low-end truncation because no fracture length less than a certain resolution length can be measured, and (ii) high-end truncation because there will always be fracture lengths that exceed the dimensions of the outcrop under study. Barton and Hsieh (1989) have attempted to fit various functions to describe trace-length frequency distributions for Yucca Mountain fractures. They concluded that the histograms were best fitted by power-law or exponential functions.

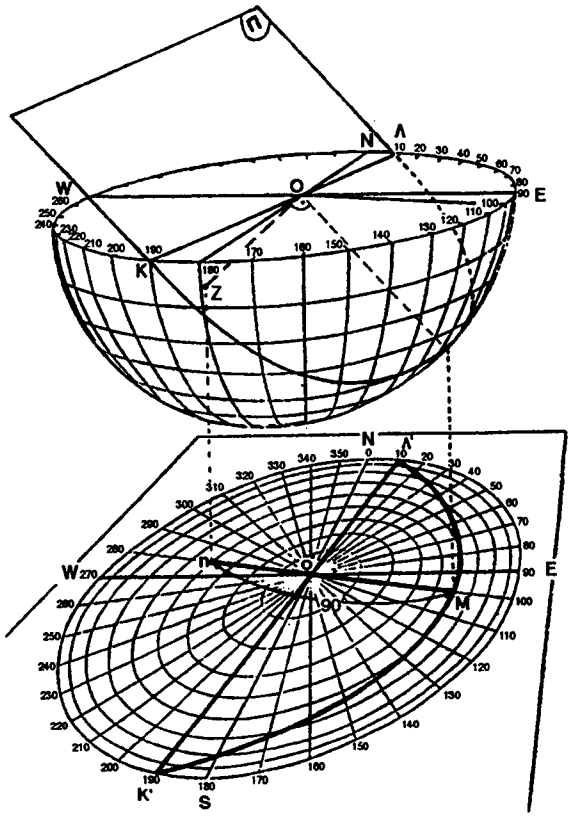

Figure 1-5. Determination of the pole of fracture plane II on a lower-hemisphere stereographic projection diagram

1.2.4 Fracture Mineralization and Alterations

The degree to which a fracture has been mineralized and/or altered affects its hydraulic characteristics. The nature of minerals deposited on the faces of fractures can provide information regarding the paleohydrology of a fracture network (Barton and Hsieh, 1989). Bates and Jackson (1980) discuss fracture mineralization and vein origin. For example, a filling material could be an external material, such as an intrusive igneous vein, or could be the result of *in situ* deformation. Groshong (1988) discusses several other types of mineral-filled veins, such as dilation veins filled with minerals precipitated from igneous solutions.

1.2.5 Fracture Conceptual Model

In modeling unsaturated flow in soil, the hydrologic properties are typically represented by characteristic curves (Ford, 1991). These characteristic curves describe the hydraulic conductivity and moisture content as functions of the suction head. Furthermore, the soil is assumed to behave as a continuum over which Darcy's law for unsaturated flow is applicable. A multitude of modeling approaches assume an analogous situation for flow within fractures. Standard laboratory methods capable of determining the characteristic curves of fractures are not yet available. As a necessary substitute, Wang and Narasimhan (1985) and Pruess and Tsang (1990) have developed theoretical models for the

description of flow in variably saturated fractures. These models generally assume that the fracture apertures vary within the fracture plane as a single heterogeneous continuum. Based on statistical theories, fracture hydraulic conductivity curves as a function of saturation have been generated for the densely welded tuff of the Topopah Spring Member of Yucca Mountain, Nevada. These theoretical studies concluded that, under such a conceptual model, fractures drain or fill over a range of matric potentials rather than a single value. Therefore, their flow and storage properties may be represented by functional relationships analogous to porous media. A recent study by Kwicklis and Healy (1993) has yielded some similar results. These investigators conducted a numerical study for the steady flow of liquid in a 5×5-m vertical section which contained a fracture network using the TOUGH numerical code. The fracture network contained either all 125 μm, or all 25 μm, or a combination of apertures. Figure 1-6 presents permeability as a function of suction head for a system consisting of two different aperture sizes and a mixture. A behavior characteristic of a porous medium is observed. The conceptual model for simulating flow in fractured rock, used in the work by Kwicklis and Healy (1993), assumes that the fracture can be represented by a continuum. In a similar effort, Zimmerman et al. (1990) studied the absorption of water in porous blocks and observed continuum behavior.

At this point, it is important to define the physical significance of a discrete fracture in the context of the analyses presented in this work. As shown in Figure 1-7, a fracture is represented by a continuum that possesses distinctly different hydraulic properties from the surrounding matrix. Any hydraulic conductivity or moisture retention model, in principle, can be applied within the context of this approach. It should be noted that this conceptual model is consistent with samples collected in the vicinity of Yucca Mountain, as evidenced by Figure 1-8.[1] The rock is a devitrified, densely welded ash-flow tuff from the Tiva Canyon Formation. Secondary vein filling mineralization (calcite) and angular clasts of host rock comprise an 11-mm thick vein. The vein consists of brecciated Tiva Canyon Tuff and carbonate mineralization. The resemblance of Figure 1-7 and Figure 1-8 should be noted. Our conceptual model is also consistent with some earlier works by Snow (1969) and Sagar and Runchal (1982). These researchers have assumed that fractures are filled with porous material and, consequently, the flow is described by Darcy's law. Sagar and Runchal (1982) claim that this is not a limiting assumption since, even for open fractures, a Darcian flow equation is usually employed in which a surrogate hydraulic conductivity is specified based on the cubic law and some average aperture.

1.3 MODELING APPROACHES FOR FLOW IN FRACTURED ROCK

According to Gureghian and Sagar (1991), there exist six candidate conceptual modeling approaches for predicting flow in fractured geologic media:

- The equivalent continuous porous medium model (ECPM); also known as single equivalent continuum model
- The double porosity model (DPM)
- The discrete fracture network model (DFNM)
- The discrete fracture equilibrium model (DFEM)

---

[1]This photograph depicts a rock sample collected by A.C. Bagtzoglou on November 18, 1993, at the general area of U.S. Department of Energy (DOE) well WT-7 at the south end of Boomerang Ridge, Nye County, Nevada. The sample was taken from the outcrop at the west edge of the drill pad.

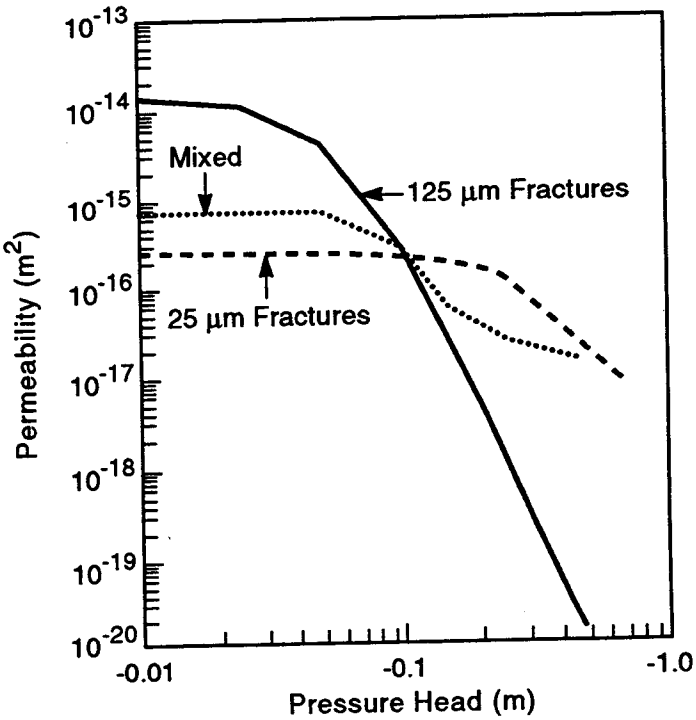

Figure 1-6. Permeability characteristic curve for three types of fractures [adapted from Kwicklis and Healy (1993)]

- The discrete fracture nonequilibrium model (DFNEM)
- The stochastic fracture continuum model

Combinations of these approaches are also conceivable. A brief description of these approaches is provided in Sections 1.3.1 to 1.3.6.

1.3.1 Single Continuum Models

The ECPM concept, related to saturated flow through fractured rock masses, was first introduced by Snow (1965). Later, Snow (1969) assumed an independence of flow at the intersection of the joints and derived the permeability tensor of a network of parallel fractures by adding the contribution from each one of these. Long (1983) conducted similar studies which revealed that the ECPM becomes applicable when "the fracture density is increased, apertures are constant rather than distributed, orientations rather constant, and larger sample sizes tested." Similarly, Long et al. (1985b) were able to determine whether a given fracture network could be modeled as an equivalent porous medium as a function of interconnectivity and heterogeneity.

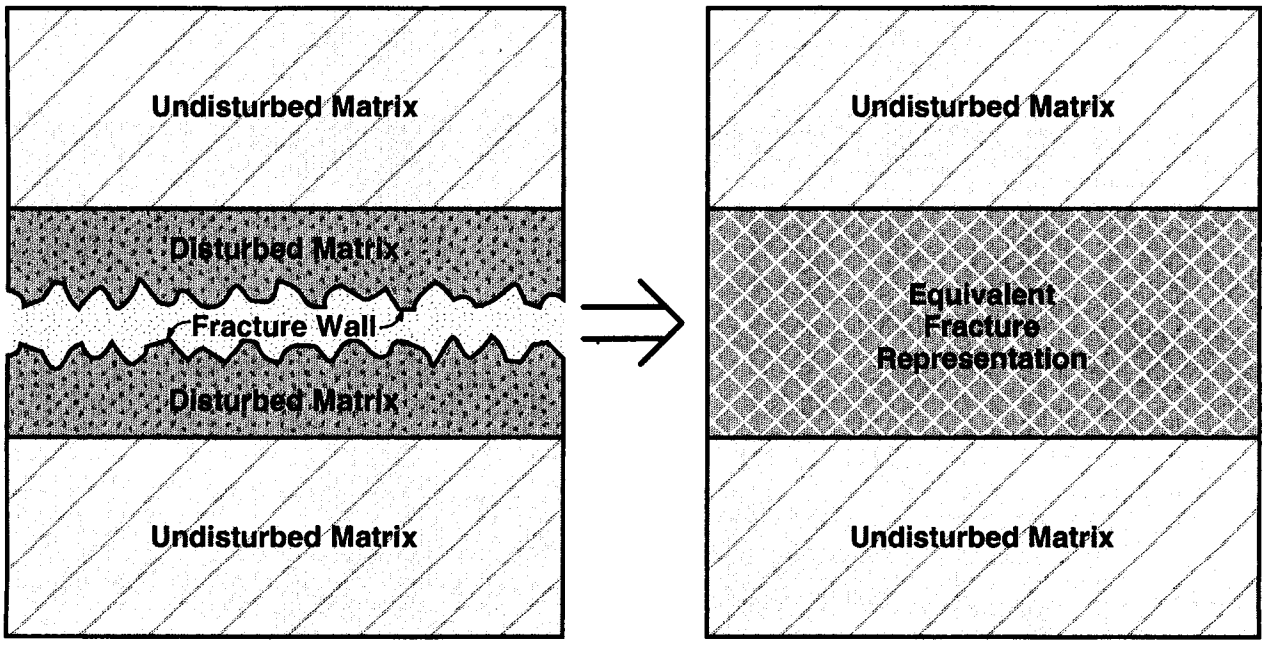

Figure 1-7. Schematic of fracture conceptual model and the corresponding continuum approximation

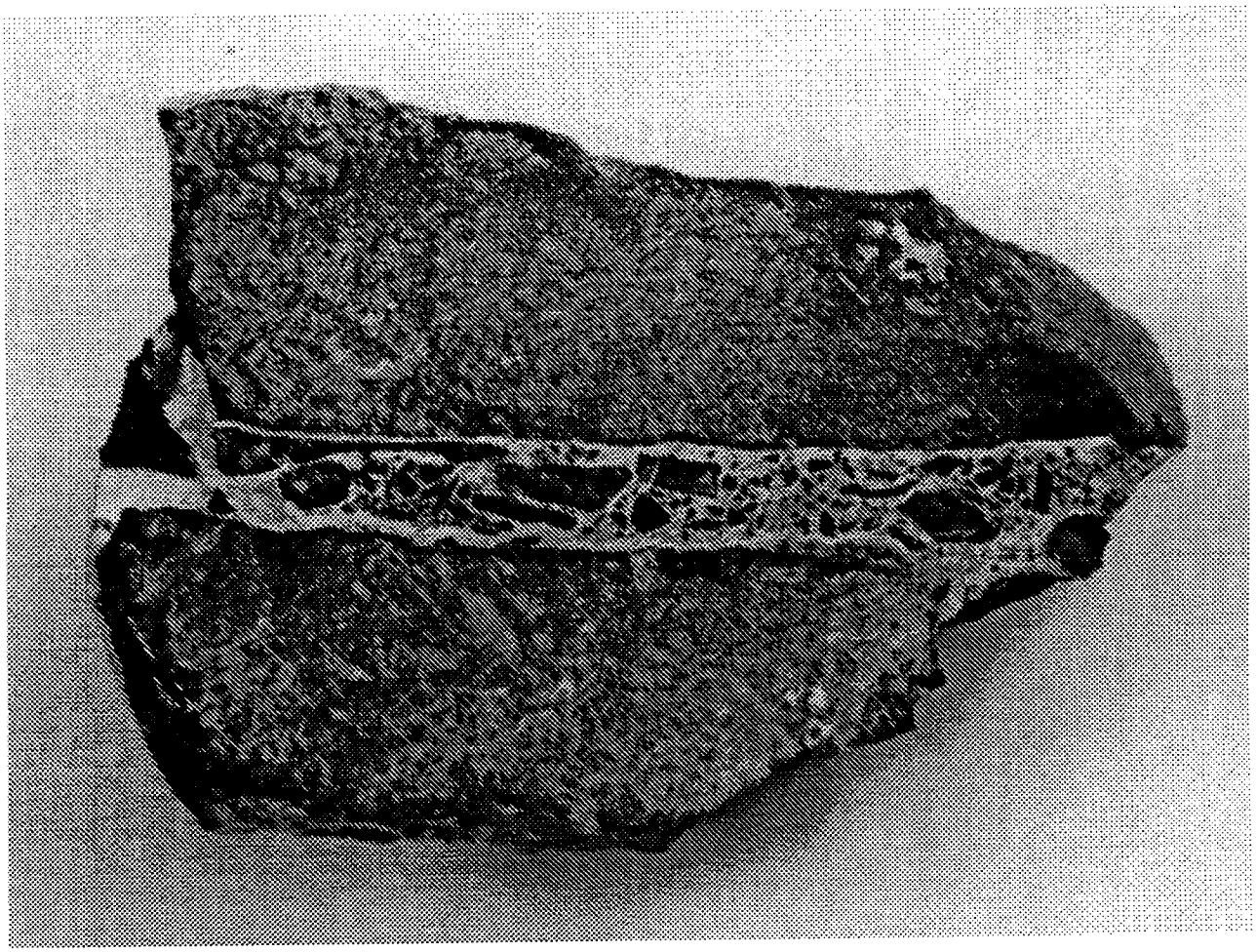

Figure 1-8. Photograph of rock sample showing vein filled with angular clasts of host rock and calcite mineralization

One notable semi-empirical model for representing the unsaturated fracture/matrix system as a single equivalent continuum was proposed and tested by Pruess et al. (1986). In this effective continuum approach, the unsaturated conductivity is approximated by the simple arithmetic sum:

$$K(h) = K_m(h) + K_f(h) \tag{1-1}$$

where K is the hydraulic conductivity, h is the pressure head, and subscripts m and f correspond to matrix and fracture properties, respectively. A similar isotropic conductivity for composite fracture/matrix media was also employed by Peters and Klavetter (1988). Pruess et al. (1986) recognized and demonstrated that this approximation is based on a hypothetical equilibrium between fracture and matrix pressures and breaks down in the presence of rapid pressure transients. More recently, Pruess et al. (1990a,b) tested their effective continuum approximation under various conditions involving near-field nonisothermal, two-phase flow in the vicinity of a hot waste package. They concluded again that the approximation breaks down for very tight rock matrix, large fracture spacings, and/or rapid transients. A well-recognized problem with using composite characteristic curves is that these may have a complex shape, which is difficult to represent mathematically. This problem may create numerical stability problems, especially when the composite characteristic curve contains a very sharp transition from predominantly matrix flow to predominantly fracture flow (Ford, 1991). A more detailed description of this model can be found in Chapter 3 of this report.

1.3.2 Dual Porosity Models

Comprehensive reviews of the dual continuum approximation can be found in the works of Shapiro (1987), Barenblatt et al. (1990), and Gureghian and Sagar (1991). The dual continuum approach was first introduced and applied by Barenblatt et al. (1960), Warren and Root (1963), and Streltsova (1976). The dual continuum approximation considers separate governing equations for the fluid in the fracture system (f) and the fluid in the porous matrix (m) with a coupling term to account for mass transfers between the two systems. In the case of transient saturated flow through a fractured porous rock, the dual continuum equations are of the form (Ababou, 1991):

$$\frac{\partial}{\partial t}(\rho\theta_m) = \rho C_m \frac{\partial h_m}{\partial t} = -\nabla(\rho q_m) - \rho\Gamma \tag{1-2}$$

$$\frac{\partial}{\partial t}(\rho\theta_f) = \rho C_f \frac{\partial h_f}{\partial t} = -\nabla(\rho q_f) + \rho\Gamma \tag{1-3}$$

where θ is the void volume fraction, C is the specific capacity, q is the specific discharge rate or flux (related to velocity by $q=\theta V$), and ρ is the fluid density. All quantities are defined for the matrix fluid and the fracture fluid, respectively, except for fluid density which is assumed to be constant (i.e., $\rho=\rho_m\approx\rho_f$). Finally, $\rho\Gamma$ is the rate of exchange of fluid mass between the two continua.

The main assumptions of the dual continuum model are: (i) the flux q in each continuum is governed by Darcy's law, and (ii) the exchange term Γ is proportional to the local pressure difference between the fluid in the matrix and the fracture. The individual Darcy's laws are given by:

$$q_m = -K_m \nabla(h_m + z) \tag{1-4}$$

$$q_f = -K_f \nabla(h_f + z) \tag{1-5}$$

where z is the elevation head. Furthermore, Barenblatt et al. (1960) assumed that the exchange term is proportional to $(h_m - h_f)$ times porous matrix conductivity divided by an areal scale $A_f\,(m^2)$:

$$\Gamma = \frac{K_m}{A_f}(h_m - h_f) \tag{1-6}$$

In the conventional implementation of dual porosity models, Γ is a scalar quantity.

One of the advantages of this approach is that the matrix-fracture transfer term can be used to simulate other physical phenomena such as flow through mineral fillings between fracture walls. Even though the dual porosity approach will have its time-stepping dictated by the magnitude of the transfer term, it generally has far fewer problems with code instabilities when compared to the single continuum models. Under this conceptual model, the two continua assume the existence of a Representative Elementary Volume (REV) which is common to both subsystems (Bear, 1993). If the scales of the pores and the fractures are approximately equivalent, the double porosity approach is applicable. However, if the fracture scale is much larger than the pore scale, then this approach is probably not valid (Updegraff and Lee, 1990). Similar to the single continuum approaches, the dual porosity model requires the fracture continuum to exhibit a characteristic curve. This is an issue that to date has not been verified experimentally. Furthermore, the matrix-fracture interaction term is a parameter that cannot be measured in the field (Ford, 1991). Ababou (1991) presented an extensive discussion on dual porosity models and identified several of their shortcomings.

1.3.3 Discrete Fracture Network Models

In the DFNM approach, the flow is simulated in all significant, conductive, individual fractures. Therefore, a detailed description of all fractures is necessary. Nevertheless, the discrete models play a significant role for studying the mechanism of flow in fractured media, for setting defensible criteria for equivalent porous-media approximations, and for deriving equivalent porous-media characteristics. In the stochastic approach for modeling flow in discrete fracture networks (Robinson, 1984; Schwartz et al., 1982; Long, 1983), the geometry of the fractures is described as a random process. Interconnected networks of discrete fractures are generated using appropriate probability distribution functions.

According to Gureghian and Sagar (1991), the disadvantage of this modeling concept is the vast amount of geometric details that it requires. The computational complexity of the DFNM seems to be far beyond the capacity of present-day computers. Furthermore, the availability of field data on fracture distributions, which for their physical interpretation rely strongly on statistics and probability, may not support the use of such a model.

1.3.4 Discrete Fracture Equilibrium Models

In the DFEM, in addition to considering the geometry of the fracture system explicitly, flow through the rock matrix is also accounted for. This modeling approach, first proposed by Gureghian (1975), has gained wide acceptance. The main assumption of this approach is that at some finite scale of discretization of the rock-fracture system, the fluid pressure in the fracture is the same as that in the adjoining rock. Thus, within an element of a numerical grid, pressure is a single value, in contrast to the two values in DPMs. However, its use becomes quite cumbersome when the fracture density exceeds a certain threshold. An example of this type of formulation in fractured media is found in the work of Runchal and Sagar (1993).

The advantage of the DFEM approach is that the geometry and the hydraulic properties of the fractures is directly used in the model and the interaction between the fractures and the rock matrix is considered at a scale larger than the scale of discretization. While the computational effort required in DFEM is less than that required in the double porosity formulation (because only one equation per node is solved rather than two), the amount of input data required is much greater. The main disadvantage of the DFEM approach is that the pressure distribution very close to the fracture is not accurately obtained, as the matrix-fracture interaction occurs only at scales larger than the scale of the calculational element.

1.3.5 Discrete Fracture Nonequilibrium Models

In the DFNEM approach, no assumption regarding matrix-fracture interactions is made. In this approach, fractures are treated as porous media embedded in the rock. In obtaining numerical solutions to flow problems in this approach, the fractures are treated as elements with distinct properties. Full geometry and hydraulic characteristics of the fractures are required as input. In such models, channeling of flow within individual fractures can also be treated. Because no assumption is made regarding flow interaction between the fractures and rock matrix, this formulation has the potential of producing the best results. It is limited, however, by large computational effort, numerical instabilities, and huge data input requirements. The great advantage is that almost any model designed to model flow through porous media can be adapted to this approach.

1.3.6 Stochastic Fracture Continuum Models

The stochastic methodology treats fractured rock at the field scale as either a network of discrete fractures whose characteristics are known in a statistical sense or as a heterogeneous porous medium whose variability is great, thus permitting flow to occur through highly channelized preferential pathways. Neuman (1987) has been a very strong proponent of the stochastic continuum approach as an alternative to both the REV and fracture network concepts. Neuman's rationale is based on the notion that if rock properties are measured over distances smaller than the REV (and fractured rock is usually characterized by large REVs), then these properties should be described in a geostatistical sense only. Neuman (1987) demonstrated the feasibility of such an approach by performing packer tests in several boreholes having different orientations. The effect of fracture set orientation on the hydraulic conductivity of the rock is assumed by Neuman to be inherent in the observed large-scale structural anisotropy.

1.4 REGIONALIZATION OF FRACTURE PARAMETERS

Even though the majority of fracture network generation models assume independent, or nearly independent fractures, it is common knowledge that geologic phenomena are partially structured and as such may require a geostatistical description. For example, LaPoint and Hudson (1981) have observed that in many cases, fractures occur in zones or bands of subparallel features, indicating that spatial correlation between fracture characteristics may exist. Lin and Logan (1991) conducted a microscopic study and showed that microfractures are highly concentrated in the area immediately adjacent to existing macrofractures. They also demonstrated that the majority of the grains away from the macrofractures remain unfractured. Long and Billaux (1987) pointed out that the presence of several fracture clusters which overlap may have a large effect on the interconnectivity and flow characteristics of the network. They also advocated the use of geostatistics to estimate the value of a given regionalized variable such as the average fracture trace length or fracture density.

De Marsily (1985) discussed various applications of geostatistics to study rock fracturing, and concluded that the density, length, and (possibly) orientations of fractures can be adequately described within a geostatistical context. This implies that rock fracturing may be defined as a regionalized phenomenon and, therefore, fracture characteristics display correlation structures. Neuman et al. (1985) applied such an approach at the Oracle site in Arizona, and found a strong correlation between the hydraulic conductivity tensor principal directions and the orientations of major fracture sets. Similarly, Gentier (1990) has applied geostatistical techniques to the study of fracture surface topography and fitted theoretical variogram models to the variogram of the heights along the profile of a fracture surface. Another very similar effort is the work of Nordqvist et al. (1992) who were able to characterize, and subsequently generate, spatially varying fracture aperture fields based on geostatistical methods.

Chiles (1976, 1989a) has presented numerous examples of fracture characteristics being treated successfully as regionalized variables. Both fracture spacing and trace density have been found to exhibit spatial structure. Variograms were successfully calculated and fitted to data from subvertical fracture sets in the Fanay granitic massif, in France. Finally, fracture cluster centers, used in the parent-daughter network models (see Chapter 3), have been found to exhibit spatial structure. Moreover, Chiles (1989b) reported that a cubic variogram appears to best represent the variogram of trace cluster center number count.

LaPoint (1980) severely criticized conventional methods for analysis of fractured rock and pointed to the locational independence as the major flaw of these methods. He then presented a generalization of the semivariogram for vectorial and tensorial quantities. The theoretical semivariogram, for a scalar quantity X, $\hat{\gamma}(\vec{h})$ is calculated empirically as:

$$\hat{\gamma}(\vec{h}) = \frac{1}{2n(\vec{h})} \sum_{i=1}^{n(\vec{h})} \left[X(\vec{z}_i) - X(\vec{z}_i + \vec{h}) \right]^2 \tag{1-7}$$

where $n(\vec{h})$ is the number of samples a distance $\vec{h}$ apart. Note that the squared quantity in the equation above is a scalar measure of the difference in the values at two points. Similarly, there exists a scalar measure of the difference between two vectors. Let the two vectors be:

$$\vec{X}(\vec{z_i}) = \left\{X_1(\vec{z_i}),\ X_2(\vec{z_i}),\ X_3(\vec{z_i})\right\} \tag{1-8}$$

and

$$\vec{X}\left(\vec{z_i} + \vec{h}\right) = \left\{X_1\left(\vec{z_i} + \vec{h}\right),\ X_2\left(\vec{z_i} + \vec{h}\right),\ X_3\left(\vec{z_i} + \vec{h}\right)\right\} \tag{1-9}$$

The scalar difference between these two vectors is given by the square of their difference, or:

$$\begin{gathered} \| \vec{X}(\vec{z_i}) - \vec{X}\left(\vec{z_i} + \vec{h}\right) \|^2 = \\ \left[X_1(\vec{z_i}) - X_1\left(\vec{z_i} + \vec{h}\right)\right]^2 + \left[X_2(\vec{z_i}) - X_2\left(\vec{z_i} + \vec{h}\right)\right]^2 + \left[X_3(\vec{z_i}) - X_3\left(\vec{z_i} + \vec{h}\right)\right]^2 \end{gathered} \tag{1-10}$$

Thus, for a vectorial quantity $\vec{X}$, that is a quantity which has orthogonal components, the semivariogram becomes:

$$\hat{\gamma}(\vec{h}) = \frac{1}{2n(\vec{h})} \sum_{i=1}^{n(\vec{h})} \| \vec{X}(\vec{z_i}) - \vec{X}\left(\vec{z_i} + \vec{h}\right) \|^2 \tag{1-11}$$

where $\hat{\gamma}(\vec{h})$ is the semivariogram of a vectorial quantity, $n(\vec{h})$ is the number of pairs of samples whose centers are a vectorial distance $\vec{h}$ apart, $\vec{X}(\vec{z_i})$ is the value of a vectorial property (such as the direction cosines of the normal to a joint plane) of a sample centered at $\vec{z_i}$ in the rock, and $\vec{X}\left(\vec{z_i} + \vec{h}\right)$ is the value determined for a sample located at a vectorial distance $\vec{h}$ from $\vec{z_i}$.

In a similar manner, tensors can be handled as a set of vectors. Thus, instead of a single semivariogram to represent the correlation characteristics of a property, tensors require as many semivariograms as there are independent quantities in the tensor. Rock properties at unknown points can be estimated from known sample values and their semivariograms through a process known as Kriging. For scalar and vector rock properties, the Kriging process follows the procedures used in mining applications, details of which can be found in standard geostatistics texts. For tensors, the process remains substantively the same except that each tensor component is estimated separately. This generalization by LaPoint (1980) is an important step for describing vectorial quantities, such as fracture orientations, as regionalized variables.

2 VISUALIZATION AND NUMERICAL GENERATION OF REALISTIC FRACTURE SETS

2.1 STATISTICAL STUDY OF FRACTURE SETS

In this section, a presentation of the common assumptions made when describing the geometry of fracture sets is given. This discussion covers the characteristics identified in Chapter 1, and extends to the presentation and mathematical description of the distributions used for the statistical analyses of these fracture characteristics.

2.1.1 Orientation of Fracture Sets

The orientation of fractures cannot be classified as either a purely random or regular process (Chiles and de Marsily, 1993). For example, fracture orientation can be extremely regular (e.g., Engelder, 1985; Dunne and North, 1990), or in some cases purely random or nearly random (e.g., implosion breccia; Sibson, 1986). Fractures with approximately the same orientation form or constitute a fracture set. The formation of fracture sets is due to the origin of the host material or tectonic history. Since fracture sets that are formed at a later time usually terminate at intersections with older sets, it is best to study each fracture set independently of the others. The orientation of a fracture plane is most conveniently described by its strike and dip, or by its pole, that is the unit vector normal to the fracture plane (Chiles, 1989a,b). This, as explained in Chapter 1, is typically visualized on an equal area lower hemisphere projection diagram called a stereographic projection or Schmidt diagram. The results of a fracture survey are best represented as a contoured stereographic projection diagram. This is accomplished by moving a relatively small circle (window) around the Schmidt diagram in a systematic way. The number of poles inside the moving circle is counted and then, expressed as a percentage of the total number of fractures, is plotted as contours on the projection diagram. An example of this process is illustrated in Figure 2-1.

Once a set of fracture observations is plotted in stereographic projection, outliers can be identified and eliminated (censored) from the set. The statistical analysis of directional data is facilitated by performing the analysis for points distributed on a sphere. Procedures have been developed for the statistical analysis of points in one cluster or a girdle. If the poles appear to define one or more clusters, the following steps can be followed in order to analyze the data (Koch and Link, 1980; Barnett and Lewis, 1984): (i) determine whether the poles are clustered or are randomly distributed on the sphere; (ii) estimate the mean strike and dip of the cluster, and the dispersion of poles within the cluster; (iii) determine whether one or more clusters share the same mean direction; and (iv) determine whether the two clusters are equally dispersed.

The azimuthal parameters (i.e., the strike and dip) of a fracture set are typically approximated by normal distributions, although it may sometimes be difficult to separate superimposed fracture sets and, therefore, deconvolve the observed bimodal distribution. There exist several other distributions for the statistical analysis of clustering of poles but the analysis is, usually, based on the Fisher or bivariate Gaussian frequency distribution in the plane tangent to the central orientation of the cluster. The Fisher distribution is symmetrical about the mean direction of a cluster, and its measure of tightness (or inverse dispersion) is a statistic called the estimate of precision. The mathematical description of this and other distributions used in the statistical analysis of fracture set orientations is presented in the following.

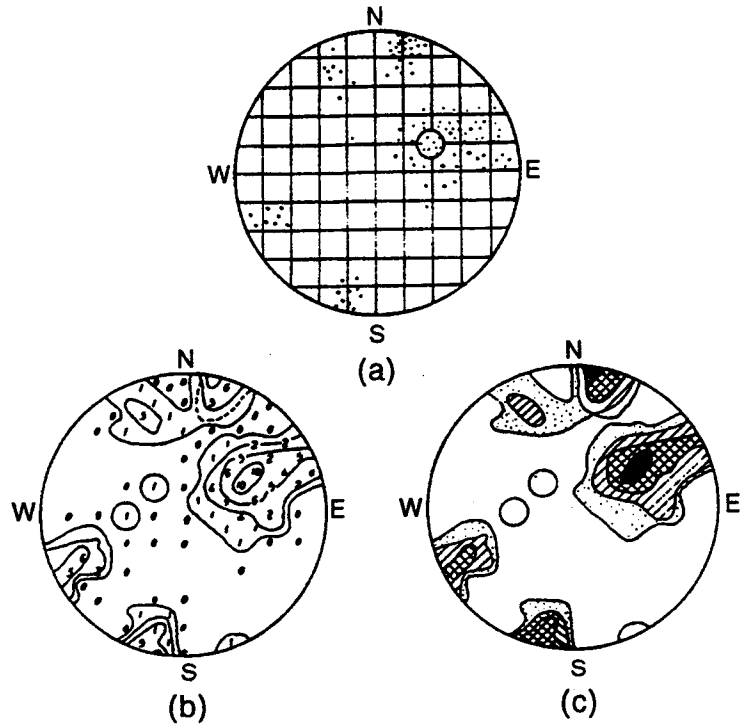

Figure 2-1. Pole analysis and contouring of the stereographic projection diagram. a) Counting number of poles within a moving window; b) and c) contouring and grey shading of results.

2.1.2 Probability Distributions for Directional Data

There exist five types of probability distributions for directional variables: the univariate and the bivariate Fisher, the bivariate normal, the bivariate Bingham, and the spherical Dirac delta (i.e., constant direction) distribution. The spherical Dirac delta distribution is trivial and is not discussed further. These distributions are stated in terms of their probability density functions, $f(\phi,\theta)$, for a variation (ϕ',θ') about the mean direction $(\bar{\phi},\bar{\theta})$. Parameters ϕ and θ denote the dip and strike-azimuth angles, respectively. The mathematical description of the distributions, used more often, follows.

2.1.2.1 Univariate Fisher Distribution

The univariate Fisher distribution is defined by the probability density function (Mardia, 1972):

$$f(\phi',\theta') = \frac{\kappa \sin \phi' \; e^{\kappa \cos \phi'}}{2\pi(e^{\kappa}-1)} \; , \; 0 \le \phi' \le \frac{\pi}{2} \tag{2-1}$$

where κ is the distribution parameter. This distribution is unimodal and symmetric about the ϕ' axis. Increasing κ produces a distribution more concentrated around the ϕ' axis.

The Fisher dispersion parameter κ is generally found from the equation:

$$\kappa \approx \frac{N_f}{N_f - |R|} \tag{2-2}$$

where $|R|$ is the magnitude of the vector sum of the unit vectors for orientation, and N_f is the number of fractures. Snow (1969) used the Fisher distribution (Fisher, 1953) to generate a variety of synthetic joint orientation distributions. These orientations are symmetric about a central or average orientation whereas natural distributions may not be.

2.1.2.2 Bivariate Fisher Distribution

The bivariate Fisher distribution is defined by the probability density function (Dershowitz, 1979):

$$f(\phi', \theta') = C^{-1} \sin \phi' \exp\left[\left(\kappa_1 \sin^2\theta' + \kappa_2 \cos^2\theta'\right) \cos \phi'\right] \tag{2-3}$$

$$0 \leq \phi' \leq \pi, \quad 0 \leq \theta' \leq 2\pi$$

where C is the normalizing constant:

$$C = \int_0^{2\pi} \int_0^{\pi/2} \sin \phi' \exp\left[\left(\kappa_1 \sin^2\theta' + \kappa_2 \cos^2\theta'\right)\cos \phi'\right] d\phi' d\theta' \tag{2-4}$$

and κ_1 and κ_2 are the distribution parameters. When $\kappa_1 = \kappa_2$, this distribution reduces to the univariate Fisher distribution. When $\kappa_1 \neq \kappa_2$, this distribution is unimodal with planes of symmetry normal to the axes $(\phi' = 90°, \theta = 0°)$ and $(\phi' = 90°, \theta = 90°)$. When $\kappa_1 > \kappa_2$, the distribution is more concentrated in the $\theta = 0°$ and $\theta = 180°$ directions, and more scattered in the $\theta = 90°$ and $\theta = 270°$ directions.

2.1.2.3 Bivariate Normal Distribution

The bivariate normal distribution for orientation is defined by the probability density function:

$$f(\phi,\theta) = \frac{1}{2\pi\phi_\sigma\theta_\sigma\sqrt{1-\rho^2}} \cdot$$

$$\exp\left\{-\frac{1}{2(1-\rho^2)}\left[\left[\frac{(\phi-\overline{\phi})}{\phi_\sigma}\right]^2 - 2\rho\frac{(\phi-\overline{\phi})(\theta-\overline{\theta})}{\theta_\sigma\phi_\sigma} + \left[\frac{\theta-\overline{\theta}}{\theta_\sigma}\right]^2\right]\right\} \tag{2-5}$$

where $(\phi_\sigma,\theta_\sigma)$ are the standard deviation of the dip and strike, and ρ is the correlation coefficient. Decreasing ϕ_σ and θ_σ produces a distribution more concentrated around the mean orientation.

2.1.2.4 Bivariate Bingham Distribution

The bivariate Bingham distribution is defined by the probability density function (Dershowitz, 1979):

$$f(\phi',\theta') = C^{-1}\sin\phi'\exp\left[\left(\kappa_1\cos^2\theta' + \kappa_2\sin^2\theta'\right)\sin^2\phi'\right] \tag{2-6}$$

$$0 \le \phi' \le \pi, \quad 0 \le \theta' \le 2\pi$$

where C is the normalizing constant:

$$C = \int_0^{2\pi}\int_0^{\pi}\sin\phi'\exp\left[\left(\kappa_1\cos^2\theta' + \kappa_2\sin^2\theta'\right)\sin^2\phi'\right]d\phi'\,d\theta' \tag{2-7}$$

and κ_1 and κ_2 are the distribution parameters. When $\kappa_1=\kappa_2$, this is a girdle distribution, with the region of highest concentration lying around the equator $\phi'=90°$. When $\kappa_1>\kappa_2$, this is a bimodal distribution with the regions of highest concentration lying at $(\phi'=90°,\ \theta'=0°)$ and $(\phi'=90°,\ \theta'=180°)$; when $\kappa_1<\kappa_2$, this is a bimodal distribution with the regions of highest concentration lying at $(\phi'=90°,\ \theta'=90°)$ and $(\phi'=90°,\ \theta'=270°)$. This distribution will produce a population of directions predominantly normal to the specified mean direction $(\overline{\phi},\ \overline{\theta})$. Chiles and de Marsily (1993) have presented similar formulae for the case of isotropic distributions.

2.1.3 Fracture Density and Spacing

A wide variety of measures is available for quantifying the intensity of geologic features. Thus, fracture intensity can be measured in terms of N_f, the total number of fractures in the region; P_{32}, the areal intensity; and P_{33}, the volume percent. P_{32} is defined as the total area of features per unit volume (Dershowitz, 1984) given by:

$$P_{32} = A_f / V_t \tag{2-8}$$

where A_f is the total area of features, and V_t is the total volume. The measure P_{32} is dimensional (in units of 1/m or 1/km), but is scale-independent (i.e., it does not depend upon the volume studied or the orientation of the measurements). Note that alternative measures such as the number of features per unit are scale-dependent. The volume percent, P_{33} is the percentage of a feature by volume given by:

$$P_{33} = V_f / V_t \tag{2-9}$$

where V_f is the total volume of features. All of these measures are interrelated through the distribution of fracture size (area or volume). They are also related to the more common measures of fracture intensity, the distribution of spacings between fractures as encountered in a borehole or along an outcrop transect.

Fracture spacing is measured as the separation between intersections of fractures within a borehole or a surveying traverse. It is a measure that applies to both fractures of finite and infinite extent. The fracture density is calculated, in an average sense, as the inverse of the mean fracture spacing. Fracture spacings are typically observed to obey an exponential distribution, supporting the premise of a Poisson random field. Baecher et al. (1977) found that the exponential distribution is honored irrespective of the orientation of the sampling line. It is possible, however, to observe anisotropic exponential distributions. Other assumptions regarding the fracture spacing distributions can be made, for example, that they are normal in the case of cooling joints in basalts or clustered distributions.

Since both areal- and line-based measures of fracture density (d_2, d_1) depend on the orientation of the plane or line considered, the most interesting parameter is the volumetric-based fracture density (d_3). In order to account for the bias introduced when sampling at planes or lines of a certain orientation, the parameter d_3 is weighted by the acute angle of intersection θ_i which corresponds to the ith of the n fractures intersecting the plane or borehole. Therefore, the volumetric fracture density measure is given by:

$$d_3 = \frac{1}{L} \sum_{i=1}^{n} \left[\frac{1}{\sin \theta_i} \right] \tag{2-10}$$

2.1.4 Fracture Trace Length

Under the assumption of circular fractures, Baecher et al. (1977) suggest that the fracture radii follow lognormal distributions. In similar efforts, Baecher (1983) concluded that trace lengths are lognormally distributed, although exponential distributions have also been used to describe fracture trace lengths. Through stereological transformations one can relate the observed outcrop trace lengths to their actual three-dimensional (3D) diameters.

The effect of distribution truncations due to the inability to observe: (i) trace lengths shorter than a low cutoff limit (truncation); (ii) trace lengths that extend beyond the outcrop, planar, or drift sampling area (censoring); and (iii) long traces in a very small sampling area (trace size biasing) is associated with the techniques used during sampling of fracture geometry. The orientation of the fractures, relative to the

outcrop plane or the boreholes, also introduces sampling bias since there will be a large number of fractures that may not be accounted for. For example, a horizontal outcrop will discriminate against subhorizontal fractures. Several methods have been proposed by Chiles (1989a) to correct these biases.

2.1.5 Aperture and Thickness

Several researchers have found apertures to be lognormally distributed with the means being a decreasing function of depth. However, Chiles (1989b) considers the aperture as a meaningless fracture parameter because: (i) it is not constant in space and therefore there will always exist void spaces and contact areas which cannot be accounted for, and (ii) the measured parameter is drastically different than the *in situ* parameter due to the stress release. However, in cases where the fracture has been calcified or filled with some other material, the term aperture can be replaced by the term thickness. The fracture thickness has been found to follow a lognormal distribution and to be highly correlated with the length of the fracture (Chiles, 1989b).

2.1.6 Probability Distributions for Scalar Data

The following probability distributions exist for scalar variables, such as the ones described in Sections 2.1.3 to 2.1.5: uniform, exponential, normal, lognormal, power law, gamma, and Dirac delta (i.e., constant) distributions. The Dirac delta distribution is trivial, the gamma distribution has limited applicability and are not discussed here. Exponential, normal, and lognormal distributions can be specified in either truncated or standard forms. The mathematical description of the distributions, used more often, follows.

2.1.6.1 Uniform Distribution

The uniform distribution is specified by the probability density function:

$$f(x) = 1/2a,\ \bar{x} - a \leq x \leq \bar{x} + a, \text{ and} \qquad (2\text{-}11)$$

$$f(x) = 0 \text{ otherwise}$$

where a is the maximal deviation and $\bar{x}$ is the mean value. This distribution is also known as the rectangular distribution.

2.1.6.2 Exponential Distribution

The exponential distribution is specified by the probability density function:

$$f(x) = \lambda \exp(-\lambda x) \qquad (2\text{-}12)$$

and has a mean value $\bar{x} = 1/\lambda$. Thus, the exponential distribution is completely specified by its mean value $\bar{x}$. The truncated exponential distribution has two additional parameters $(x_-,\ x_+)$, the minimum and maximum values. The mean and standard deviation values for the nontruncated distribution are related to the actual mean, $\overline{x^T}$ and standard deviation, x_σ, of the truncated exponential distribution by:

$$\overline{x^T} = \frac{x_+ e^{\left(-x + \sqrt{\bar{x}}\right)} - x_- e^{\left(-x - \sqrt{\bar{x}}\right)}}{e^{\left(-x + \sqrt{\bar{x}}\right)} - e^{\left(-x - \sqrt{\bar{x}}\right)}} + \bar{x} \tag{2-13}$$

$$x_\sigma = \left\{ \frac{\left(x_+^2 + 2\bar{x}x_+\right) e^{\left(-x+\sqrt{\bar{x}}\right)} - \left(x_-^2 + 2\bar{x}x_-\right) e^{\left(-x-\sqrt{\bar{x}}\right)}}{e^{\left(-x+\sqrt{\bar{x}}\right)} - e^{\left(-x-\sqrt{\bar{x}}\right)}} + 2\bar{x}^2 - \left(\overline{x^T}\right)^2 \right\}^{1/2} \tag{2-14}$$

2.1.6.3 Normal Distribution

The normal distribution is specified by the probability density function:

$$f(x) = \exp\left\{-(x - \bar{x})^2/2\sigma^2\right\}/\sqrt{(2\pi\sigma^2)} \tag{2-15}$$

where $\bar{x}$ is the mean value of x and σ is the standard deviation of x. The truncated normal distribution has two additional parameters (x_-, x_+), the minimum and maximum values. The mean and standard deviation values for the nontruncated distribution are related to the actual mean $\overline{x^T}$ of the truncated normal distribution by:

$$\overline{x^T} = \bar{x} + \sqrt{\frac{2}{\pi}}\, x_\sigma \frac{e^{-y_-^2} - e^{y_+^2}}{\operatorname{erf}(y_+) - \operatorname{erf}(y_-)} \tag{2-16}$$

where $y_- = \dfrac{x_- - \bar{x}}{\sqrt{2}\,x_\sigma}$, $y_+ = \dfrac{x_+ - \bar{x}}{\sqrt{2}\,x_\sigma}$, and erf is the error function.

2.1.6.4 Lognormal Distribution

The lognormal distribution is specified by the probability density function:

$$f(x) = \frac{1}{x y_\sigma \sqrt{2}\,\pi} \exp\left\{ -\frac{1}{2}\left[\frac{\ln x - \bar{y}}{y_\sigma}\right]^2 \right\} \tag{2-17}$$

where $\bar{y}$ and y_σ are the mean and standard deviation of the natural base logarithm.

The truncated lognormal distribution has two additional parameters (x_-, x_+), the minimum and maximum values. The mean and standard deviation values for the nontruncated distributions are related to the actual mean $\overline{x^T}$ of the truncated lognormal distribution by:

$$\overline{x^T} = \bar{y} + \sqrt{\frac{2}{\pi}}\, y_\sigma \frac{e^{-y_-^2} - e^{-y_+^2}}{\mathrm{erf}\,(y_+) - \mathrm{erf}\,(y_-)} \tag{2-18}$$

where

$$y_- = \frac{\log x - \bar{y}}{\sqrt{2}\, y_\sigma} \text{ and } y_+ = \frac{\log x_+ - \bar{y}}{\sqrt{2}\, y_\sigma} \tag{2-19}$$

2.1.6.5 Power-Law Distribution

The power-law distribution can be useful for describing the distribution of fracture size which can exhibit scale independent (fractal) behavior. The power-law distribution is described by two parameters, the minimum value $x_{\min}$ and the exponent b.

$$f_x(x) = \frac{b-1}{x_{\min}} \left[\frac{x_{\min}}{x}\right]^b, \text{ when } x \geq x_{\min},\ b > 1 \tag{2-20}$$

$$F_x(x) = 1 - \left[\frac{x_{\min}}{x}\right]^{b-1}, \text{ when } x \geq x_{\min},\ b > 1 \tag{2-21}$$

The mean $\bar{x}$ and standard deviation x_σ are related to $x_{\min}$ and b by:

$$\bar{x} = \left[\frac{b-1}{b-2}\right] x_{\min}, \text{ when } b > 2 \tag{2-22}$$

$$\bar{x} = \infty, \text{ when } 1 < b \leq 2 \tag{2-23}$$

$$x_\sigma = \left[\frac{b-1}{b-3}\right]^{1/2} \left[\frac{x_{\min}}{b-2}\right], \text{ when } b > 3 \tag{2-24}$$

$$x_\sigma = \infty, \text{ when } 1 < b \leq 3 \tag{2-25}$$

$$x_{\min} = \left[\frac{b-2}{b-1}\right] \bar{x}, \text{ when } b > 3 \tag{2-26}$$

$$b = 2 + \left[1 + \left(\frac{\bar{x}}{x_\sigma}\right)^2\right]^{1/2}, \text{ when } b > 3 \tag{2-27}$$

2.2 VISUALIZATION, STATISTICAL, AND CONNECTIVITY ANALYSES OF APACHE LEAP TUFF SITE FRACTURE SETS

2.2.1 Visualization and Statistical Analyses

In order to evaluate whether geologic disposal of HLW in unsaturated fractured rock can be carried out in accordance with applicable environmental and radiological health and safety regulations, a thorough understanding of the flow processes occurring is imperative. One way of accomplishing this objective is to define or adopt site-specific conceptual models. Moreover, model parameters have to be estimated through experimental and/or field techniques. In addition to the Yucca Mountain fracture data compiled in the Site Characterization Plan (U.S. Department of Energy, 1988) and those available from the Nevada Test Site G-Tunnel (Nuclear Energy Agency, 1993), two possible sources of data have been identified as applicable to the study of multidimensional geometry of rock fracture networks: (i) fracture traces and the 3D fracture network at the inclined borehole site of the Apache Leap Tuff Site (ALTS) (Rasmussen et al., 1990); and (ii) statistical data on 2D and 3D fracture orientations at the uranium mine drift site of Faney-Augères, France (Long and Billaux, 1987). The ALTS is one of the Nuclear Regulatory Commission (NRC) sponsored test sites located near Superior, Arizona. Data collection at the ALTS is conducted with the help of inclined boreholes that were drilled with the specific objective of obtaining: (i) core samples for laboratory analyses; and (ii) hydraulic, pneumatic, and transport parameters. Site and data description can be found in the report by Yeh et al. (1988).

The ALTS is located in central Arizona, approximately 160 km north of Tucson, near Superior, Arizona at an elevation of 1,200 m. It is a 20-million-year-old tuff formation similar, to some extent, to the tuffs found at Yucca Mountain, Nevada. This formation is slightly to moderately welded near the surface and densely welded near the base of the formation, which has an approximate thickness of 150 m (Rasmussen et al., 1993). The field site is located in the White Unit of the tuff formation, which has a matrix porosity of 17.5 percent and an average number of 0.77 fractures per meter. Nine inclined boreholes have been drilled at an approximate angle of 45° and spacings of 10 m, as shown in Figure 2-2(a). The boreholes are parallel to each other (horizontal plane), with the exception of the third set which is perpendicular to the other two (vertical plane), as shown in Figure 2-2(b). A substantial amount of information has been collected and documented during the ALTS characterization effort. Approximately 100 core samples were collected and over 200 fracture planes have been identified. Among the parameters that have the greatest effect on flow and transport through fractured rock are: (i) fracture orientations, areal extents, and shapes; (ii) number of fracture sets and center locations; (iii) fracture density, porosity, and aperture distributions; (iv) fracture connectivity; and (v) fracture hydraulic properties (unsaturated conductivity and moisture retention curve). At the ALTS, only the one-dimensional (1D) measure of fracture density is available from borehole core logs. The fracture density variation is high, with a range from no fractures per 3-m interval to a maximum of 4.3 fractures per meter. The distribution is very close to being exponential, consistent with a Poisson process for fracture locations. One can infer fracture spacing as the inverse of fracture density.

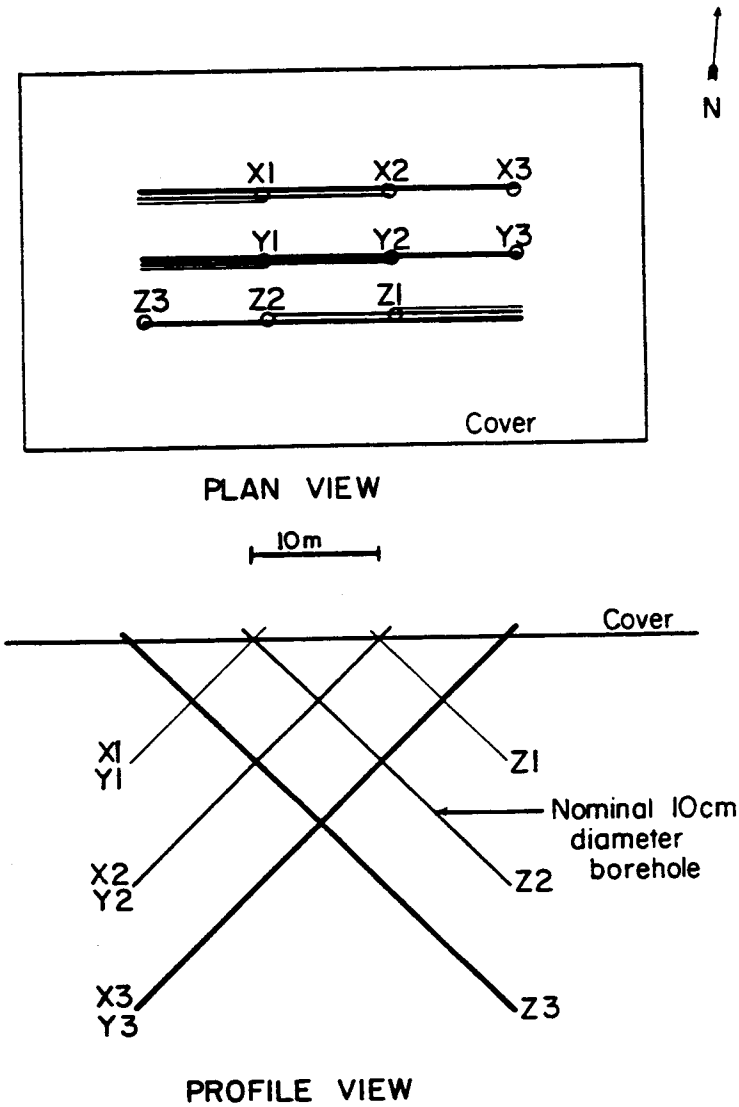

Figure 2-2. Borehole configuration at the ALTS: (a) plan view and (b) profile view (after Yeh et al., 1988)

In this section, emphasis is given mainly on the strike and dip (azimuth and inclination) statistics and connectivity of the fracture sets encountered at the ALTS. More importantly, the work reported herein presents the results obtained with numerical tools developed for efficient data manipulation and visualization. This is a step towards understanding of the site-specific important features and the incorporation of realistic hydrogeologic data in the large-scale flow and transport simulations to be conducted in the future.

Information on strike and dip angles can be incorporated in the visualization tool GLFRACT3D and its associated preprocessor by simply providing the lower-hemisphere stereonet projection data. The cartesian coordinates of the drill core extraction point serve as conditioning points upon which the fracture plane description is based. GLFRACT3D is an interactive graphics program for plotting 3D networks of planar fractures. It runs on a Silicon Graphics (SG) IRIS powervision VGX series workstation and makes use of the Graphics Library (GL) graphics language. It implements z-buffering to show hidden surfaces and the IRIS alpha-planes to provide translucency, if so desired. Coupled with its preprocessor, the package provides the user with the option to plot the stereonet projection, separate the dominant fracture sets based on ranges of strike and dip angles, and calculate triplets of x, y, and z coordinates which are needed to define a fracture plane. These coordinates can be conditioned upon the borehole extraction point cartesian coordinates, providing a much more realistic and meaningful representation of the data. Each fracture plane is subsequently coded a different color from a set of 64 with the colors re-used as necessary.

Figure 2-3 depicts the ALTS fracture plane data as a lower-hemisphere pole stereographic projection. Qualitatively, one can readily identify three dominant sets of fracture plane poles. The first, and most important one in terms of frequency of occurrence, is the set that spans the range of 30 to 120° and 210 to 300° in pole strike, and 60 to 90° in pole dip. The second set, much less frequently encountered, is complementary to the first in terms of strike. However, it spans the dip range almost at random. Finally, the third set consists of almost horizontal planes. The same data can be viewed in terms of the fracture plane distribution of strikes and dips, as shown in Figure 2-4. It is important to keep in mind the dominant set's northwest-to-north orientation and almost vertical dip. Moreover, it is also interesting to note that the second most frequently occurring set corresponds to the subhorizontal fractures. These observations are in close agreement with data presented by Barton and Hsieh (1989) for pavement 300 at Yucca Mountain, Nevada. It is also consistent with the calculation by Thornburg (1990) who analyzed data from the surface of the rock knoll at the ALTS. Figure 2-5 depicts a line interpretation of structural lineaments in the ALTS and exemplifies the complex structure of the fractures present at the ALTS. Nevertheless, Thornburg (1990) processed approximately 300 azimuthal measurements collected from a rock knoll 80 m in diameter near the shallow borehole site and was able to identify useful statistics. Sampling bias was minimized since measurements were taken on the slopes of the knoll and on a steep roadcut. The poles of identified fracture planes were plotted in lower-hemisphere, equal area projections. The densities of fracture poles were contoured according to the method by Kamb (1959) and the orthogonal principal axes were determined using the Bingham probability density function (Cheeney, 1983). This method provided eigenvector solutions of the Bingham distribution and identified the existence of subhorizontal and complementary subvertical fracture planes at the ALTS, even for cases when only horizontal outcrop data were analyzed.

A typical example of the statistical analyses performed by GLFRACT3D and its preprocessor is shown in Figure 2-6. The strike angle distribution is presented in histogram form for the dominant subvertical fracture set. Superimposed on the same figure is a normal distribution honoring the first two moment statistics of the sample. Even though no formal χ^2 test of normality was performed, such an

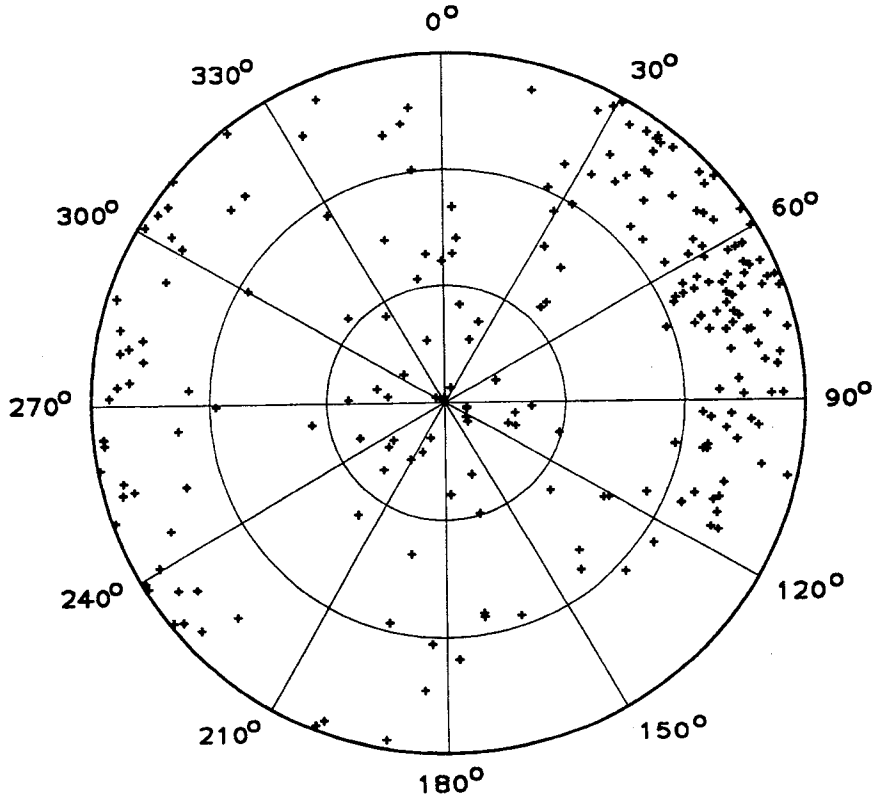

Figure 2-3. Lower-hemisphere stereonet projection of fracture pole orientations observed at the ALTS

assumption seems to be justified based on qualitative reasons and inspection of the histogram of Figure 2-6.

The importance of spatial conditioning is clearly seen in Figure 2-7, which presents a fully 3D representation of all identified fracture planes at the ALTS. The exact points where cores were removed serve as conditioning points and the fracture planes pass through them. The nine boreholes are also shown, together with a parallelepiped bounding the domain for reference. The dimensions of the parallelepiped are 50×20×50 m in the x, y, and z directions, respectively. Figure 2-8 shows the 3D spatial distribution of all 224 fracture planes in the ALTS, assuming that they extend infinitely. We recognize that this assumption, of infinite extent, is not a generic one and could, therefore, be questioned. However, according to Thornburg (1990), the surficial trace length distributions at the ALTS, which are found to be lognormal, have means of 270 and 100 m, depending on the scale of mapping and subsequent statistical analyses. Since the domain extends less than 50 m in any direction, the infinitely extensive fractures assumption appears to be a reasonable one. Andersson et al. (1984) assumed as a first approximation, fractures to be of infinite areal extent, or at least long enough to totally traverse the investigated (and modeled) region. With this assumption the fracture network is defined by the fracture plane orientations only. The assumption of arbitrary fracture positions implies that a single fracture has an equal probability to occur anywhere in the modeled region. This assumption is, at least to some extent, contrary to experimental evidence, since fractures are related to regional and local stress concentrations and the rock geology (Aguilera, 1980).

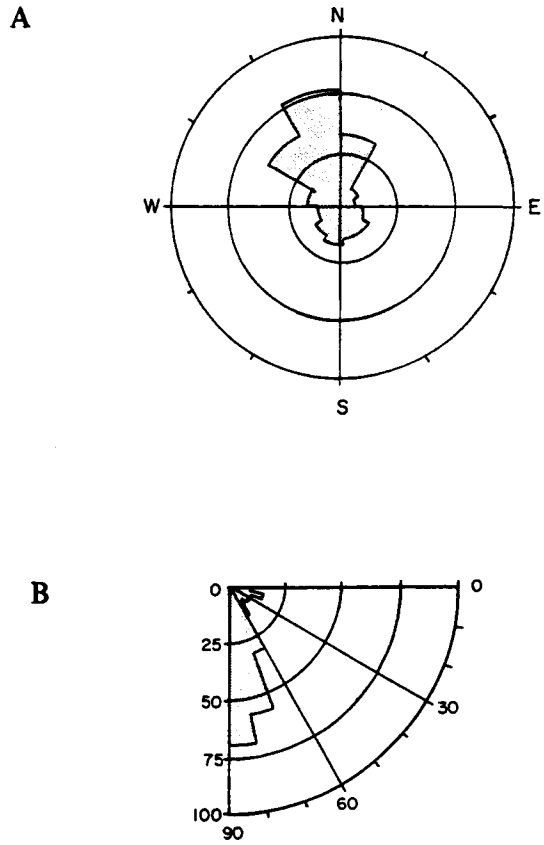

Figure 2-4. Fracture plane strike (A) and dip (B) distribution at the ALTS (after Yeh et al., 1988)

Finally, Figure 2-9 depicts the traces at the top of the domain (considered as an outcrop). This type of a figure could very well serve as a verification tool since it can be easily compared with trace mappings. These figures clearly exemplify the power of the GLFRACT3D package for visualization-based problem conceptualization.

2.2.2 Connectivity Analyses

Several authors have addressed the issue of connectivity for fractured rock. Billaux and Guérin (1993) define a connectivity index I^C for a fracture field as the mean number of intersections per fracture, weighted by fracture size (diameter). This simple geometrical characteristic does not vary with the scale considered, although it may be biased if computed on too small a region (under-representation of very large fractures). It is easily computed, given the statistical properties of a fracture network. The diameter weighting accounts for the fact that an intersection with a large fracture contributes more to the network connectivity than an intersection with a small one. This weighting is also consistent with numerical studies performed earlier (Charlaix, 1987) on percolation invariants. Odling (1992) studied a variety of fractured rock samples and concluded that, in three dimensions, fractures intersect to form a fracture network. The degree to which this network provides continuous pathways through the rock is termed connectivity (Stauffer, 1985) and is controlled by many factors including fracture density, length and orientation distributions, and spatial distribution. Traditional methods of describing fracture patterns within the

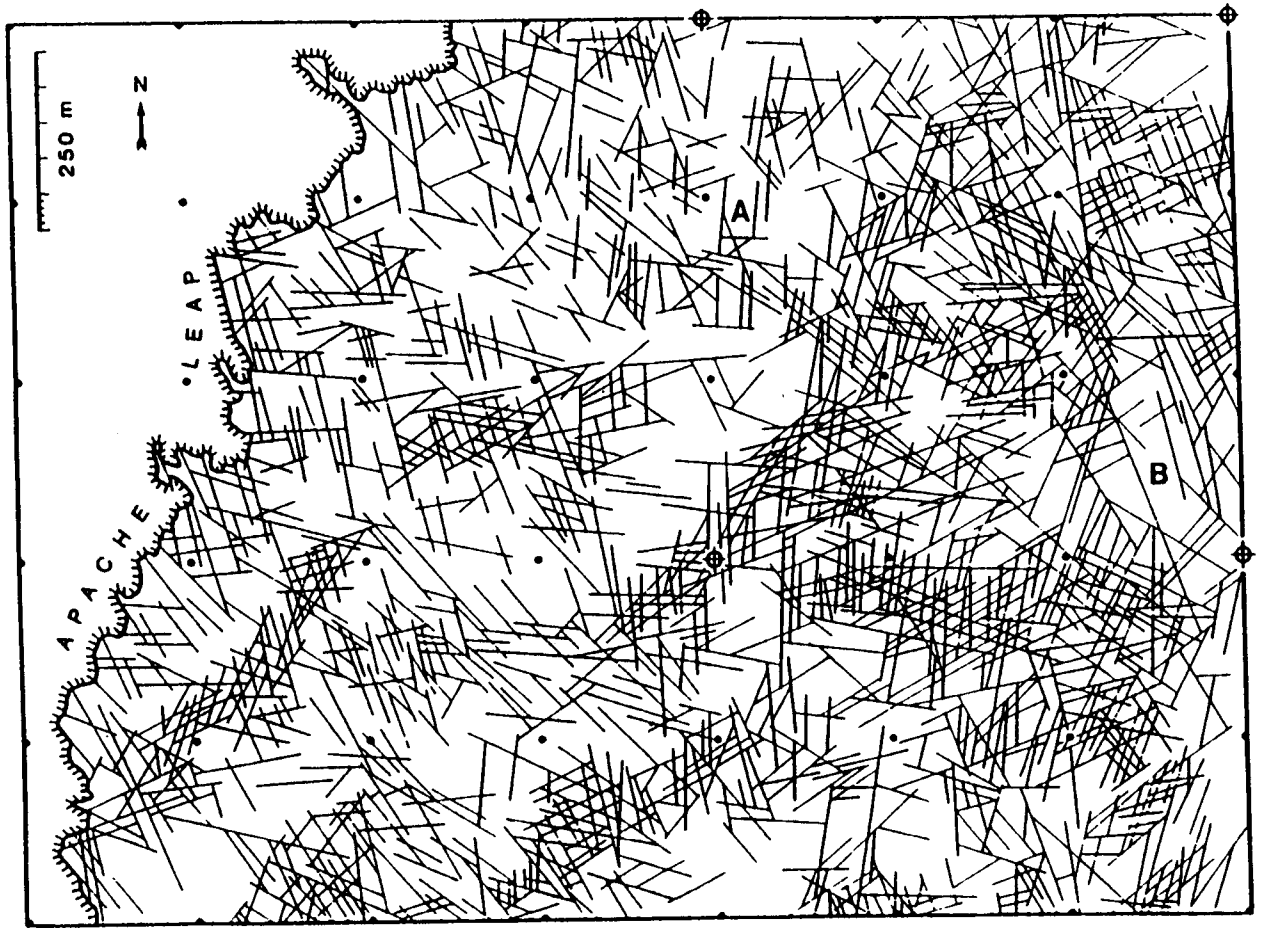

Figure 2-5. Line interpretation of structural lineaments in the ALTS. Fractures were traced from an aerial photo scaled at 1:7,180 (from Thornburg, 1990).

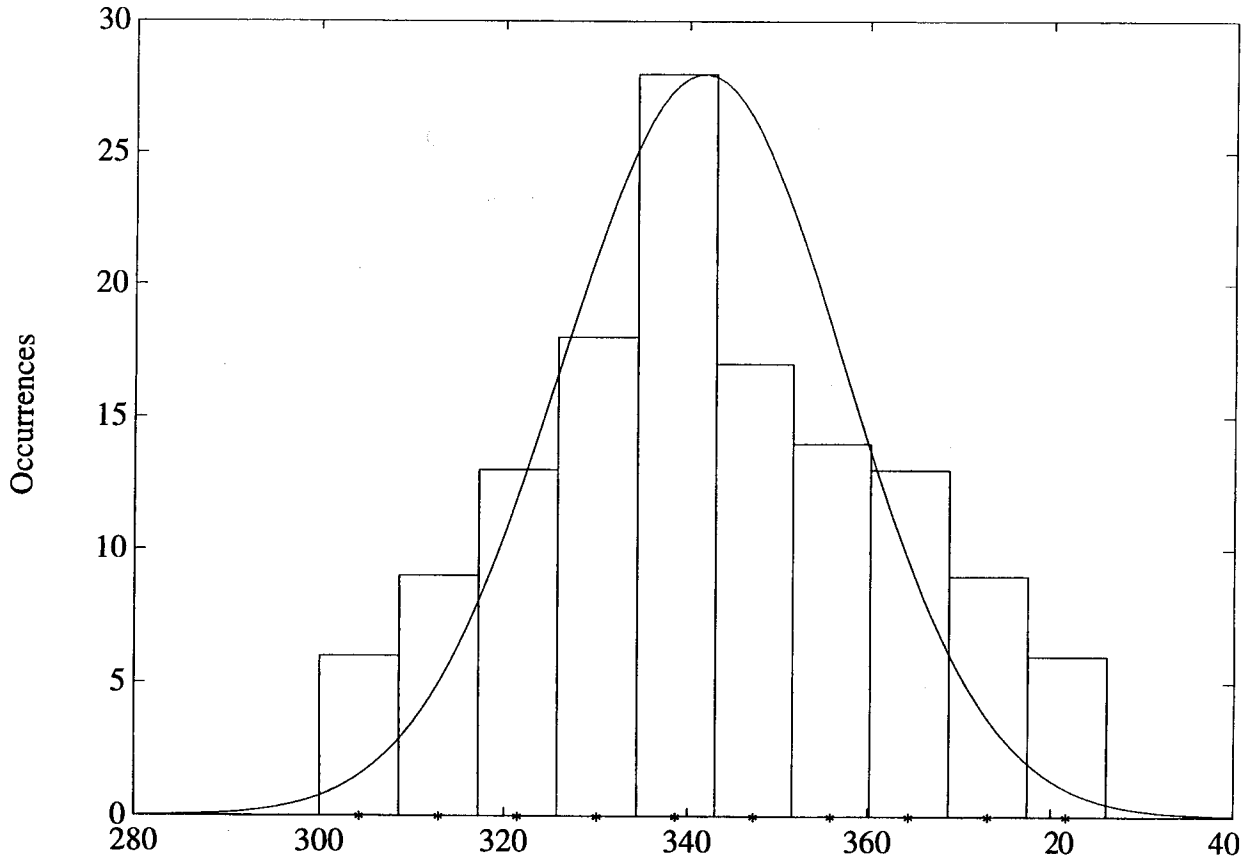

Figure 2-6. Histogram of strike azimuth for the dominant fracture set and normal distribution honoring the first two moments. Note that angles over 360° fall in the N to NE quadrant. The symbol * denotes the class representative value.

discipline of geology have consisted of the determination of orientation and length distributions with some semiquantitative information on fracture spacing. Robinson (1984), Charlaix (1985), and de Marsily (1985), among others, approached connectivity from the perspective of percolation theory. There is no consensus on exactly how to define or calculate the connectivity of a fracture network. Hestir et al. (1989), for example, proposed a measure of connectivity as a simple summary of the number of paths through which water flows from a starting to some ending point. Dershowitz et al. (1992) proposed two other measures of connectivity: (i) the number of fracture plane intersections per unit volume of rock, and (ii) the total fracture plane intersection length per unit volume of rock. Another heuristic approximation to the connectivity issue is the conjecture by Charlaix (1985), who suggested that, for randomly oriented fractures, the density of fractures and the mean size of fractures (assumed to be circular) are related by:

$$(\text{fracture density}) \times (\text{mean radius of fractures})^2 = 0.15 \text{ to } 0.30$$

Even though these three measures of connectivity provide some understanding on how well connected the fracture network is, there is nothing in these measures that demonstrates or accounts for the effect of interactions between the rock matrix and the fractures.

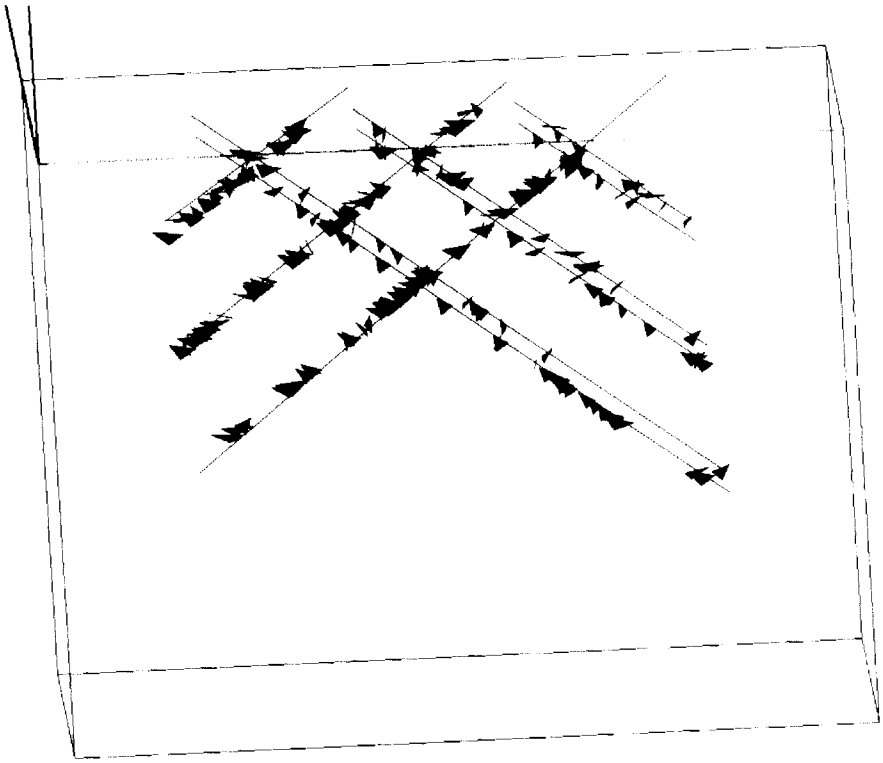

Figure 2-7. 3D representation of inventory of observed fracture traces obtained from oriented cores along the boreholes of ALTS. Dimensions of the parallelepiped are 50×20×50 m.

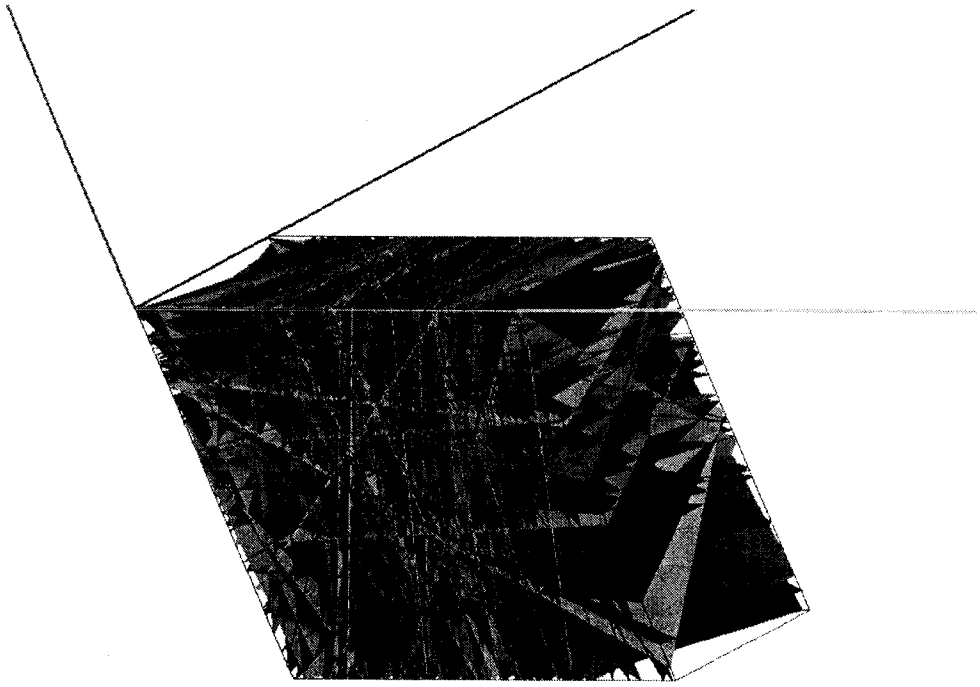

Figure 2-8. 3D representation of 224 fracture planes at the ALTS. The fractures are assumed to be of infinite extent. Dimensions of the parallelepiped are 50×20×50 m.

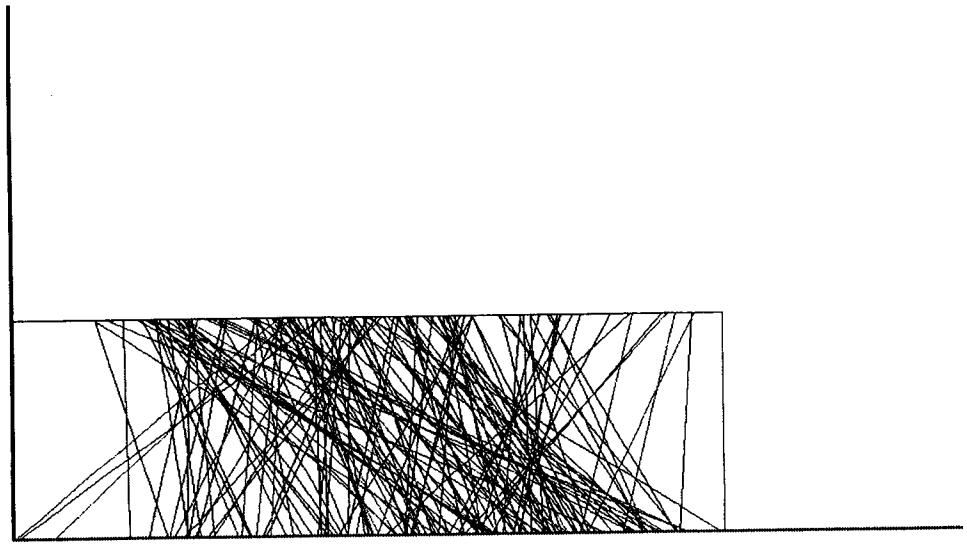

Figure 2-9. Outcropping traces for the fractures of Figure 2-8. Dimensions of the outcrop are 20×50 m.

The calculation of a new connectivity measure is proposed as follows: (i) for a given fracture set geometry identify all possible fracture plane intersections, (ii) calculate the shortest distance between all fracture plane intersections, (iii) identify all plane intersections with shortest distances smaller than a certain penetration depth (classify these intersections as connected and count the number of connections), and (iv) establish and plot in 3D space the cloud of connections. A schematic that provides some explanatory descriptions for three fracture planes is depicted in Figure 2-10. It is clear that the shortest distance is always less than or equal to the actual length that the water will traverse while flowing along the connecting plane. However, for a large number of fractures spanning a relatively wide range of strikes and dips, this is a valid measure of connectivity. Moreover, the procedure provides for the incorporation of hydraulic data into the calculation of connectivity. For example, the assumed penetration depth of step (iii) can be related to the fracture aperture and permeability. This could be based on theoretical or experimental analyses (e.g., Thoma et al., 1992). Rasmussen et al. (1985) have implemented a similar connection between the fracture plane lines of intersections. They calculate the trapezoidal area through which fluid flow occurs and apply it to the straight line segment connecting the midpoint of the lines of intersection.

If the shortest distance between two fracture plane intersections is greater than the penetration depth, the top and bottom fracture planes of Figure 2-10 will not be connected hydraulically. This approach assumes that: (i) such a penetration depth has been or could be calculated; (ii) this number is constant over the 3D domain of interest; and (iii) the supply of water is infinite, or the storage capacity

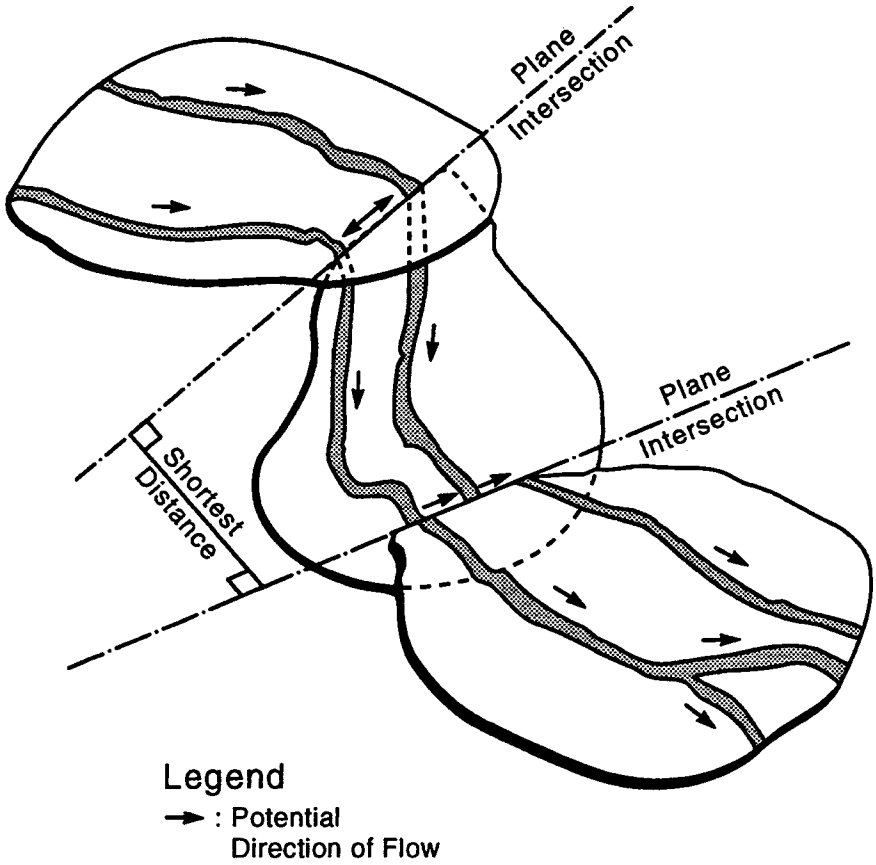

Figure 2-10. Schematic of three intersecting fracture planes and associated fracture plane intersections

of the fracture network is negligible. Nevertheless, it provides a very convenient way of understanding how well connected the fracture network is for a specific given value of the penetration depth.

Figure 2-11 shows the 845 fracture plane intersections identified at the ALTS. Note that for clarity this and all subsequent analyses were performed with a subset of only 56 (out of the 224) fracture planes. All numbers, therefore, are smaller than what would be the case if all 224 fracture planes were used in the analyses. Figure 2-12 depicts an x-z projection of all 6,309 identified connections between the fracture plane intersections of Figure 2-11, with the shortest distance smaller than 5 cm. Figure 2-13 presents the same results in an x-y projection. Several observations can be made based on these results: (i) the fractured rock at the ALTS appears to be much more connected near the surface (this implies that for depths up to 10 m, an equivalent porous assumption may be justified on connectivity grounds); and (ii) there exist four highly connected zones that extend downward. The first two are relatively shallow and appear to end at a depth less than 5 to 7 m. The other two extend much further, to a depth of 40 to 50 m.

Based on this analysis, it would seem appropriate to model flow phenomena at the ALTS using a hybrid approach whereby an equivalent or stochastic porous medium is enhanced by the presence of several well-connected zones of fractures. These zones could be modeled as persistent discontinuities.

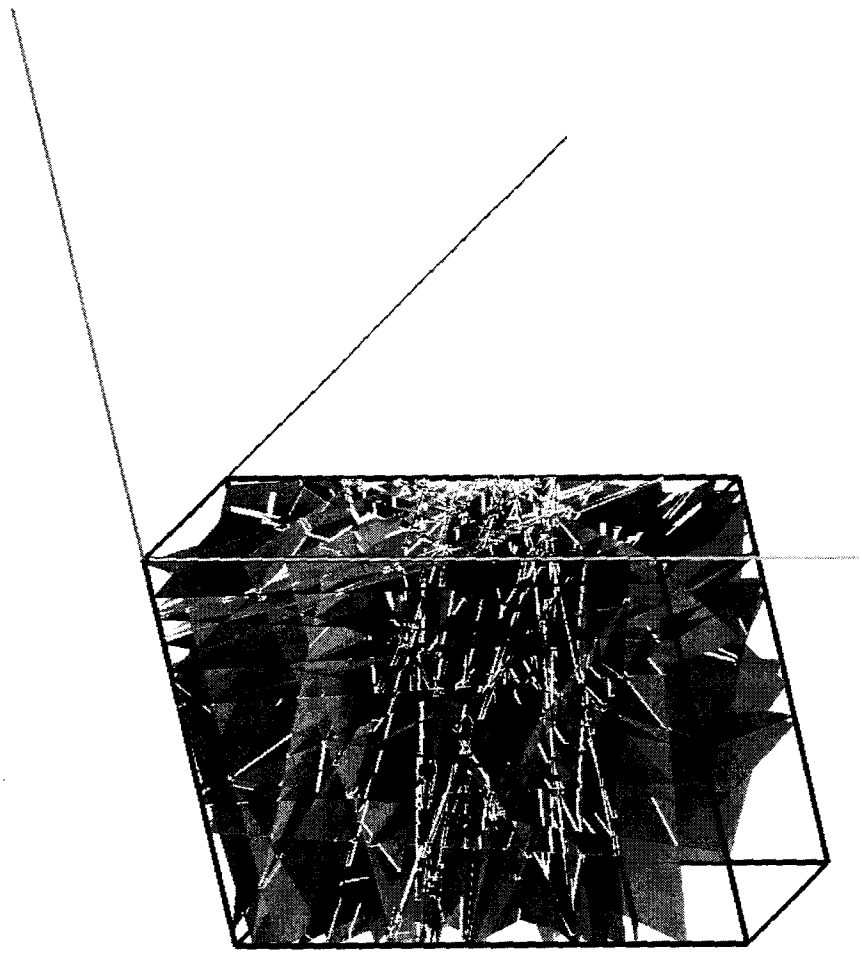

Figure 2-11. 3D representation of 56 fracture planes and their 845 fracture plane intersections. Dimensions of the parallelepiped are 50×20×50 m.

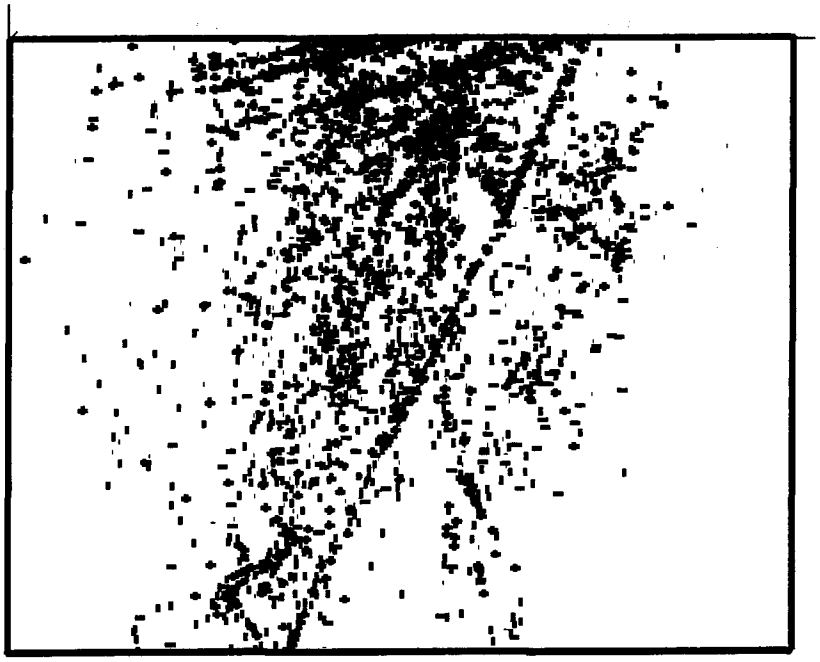

Figure 2-12. X-Z projection of 6,309 identified connections between fracture plane intersections. Dimensions of the rectangle are 50×50 m.

Figure 2-13. X-Y projection of 6,309 identified connections between fracture plane intersections. Dimensions of the rectangle are 20×50 m.

2.3 NUMERICAL GENERATION OF REALISTIC FRACTURE NETWORK SETS

The first models to be used for the generation of fracture sets were deterministic. Snow (1965) developed a model defined by orthogonal directions of equidistant planes. Since then, the application of stochastic fracture network generators has flourished. A presentation of some of the most widely used and accepted fracture generators follows.

An analysis of the confidence of flow solutions for stochastically generated rock formations was carried out by Braester and Thunvik (1987) with the aid of a simplified model. The rock formation was conceptualized and modeled as a 2D orthogonal fracture network with a known geometric structure intersecting an impervious mass of rock, while fracture permeability was considered a stochastic process. Andersson and Dverstorp (1987) modeled fractures as planar circular disks with radii, orientation (strike and dip), and transmissivity as stochastic parameters. Fracture centers were assumed to follow a constant intensity Poisson space process. This model was applied to model calibration and validation exercises in the Stripa research mine (Dverstorp and Andersson, 1989) and the results were compared to similar results by Rouleau (1984) who used a 2D DFNM. Fractures are commonly assumed to be planar features of circular or elliptical shape (Baecher et al., 1977). The centers of the fractures are further assumed to be randomly distributed in space, such that their volumetric concentration is approximated by a Poisson process. When more than one fracture set is present, superposition of independent Poisson processes will preserve the global Poisson distributional assumption. The Baecher model (Baecher et al., 1977) was one of the first well-characterized discrete fracture models. In this model, the fracture centers are located uniformly in space, using a Poisson process, and the fractures are generated as disks with a given radius and orientation. The enhanced Baecher model (Dershowitz et al., 1991) extends the Baecher model by providing for fracture terminations and more general fracture shapes.

One of the most widely used and simple models for fracture generation is the Poisson process. Its simplicity stems from the fact that it is very easy to fit parameters for this model. It is a close analog of cases where the fractures are long enough compared to the domain within which fractures are to be generated. As such, it is best suited for the generation of fractures of infinite extent which is, in many occasions, an unrealistic assumption. The assumption of uniform (Poisson process) locations for fracture centers implies that the number of fracture centers per unit areas follows a Poisson distribution (Benjamin and Cornell, 1970). Its mathematical representation is given by:

$$f_n(n_c) = \bar{n}_c \frac{e^{-\bar{n}_c}}{x!} \tag{2-28}$$

where n_c is the mean number of centers in a given sized region.

Long et al. (1985a) claim that the first step in developing a fracture flow model is to adopt a conceptual model for fracture networks which is compatible with the geometry observed in the field. Through the analysis of trace data and examination of fracture surfaces, several studies have reported that fractures are likely to be roughly elliptical or circular (Robertson, 1970; Pollard, 1976). The 3D model of Long et al. (1985a) assumes all fractures to be circular. The extension of the mathematics to elliptical fractures is possible but not trivial. For much of this work Long et al. (1985a) used a model which is essentially the same as that developed by Baecher and Lanney in which circular fractures have lognormally distributed radii and are randomly located in space. Baecher and Lanney have supported this

concept through analysis of trace data observed in outcrops, intersection data observed in boreholes, and the examination of fracture surfaces (Baecher and Lanney, 1978). A variety of fracture orientation distributions is possible and, in general, these distributions can be determined from field data. Arnold's hemispherical normal, Bingham's, Fisher's, and uniform distributions have all been used by various authors. Apertures can have lognormal distribution as was deduced by Snow (1969). Others (LaPoint and Hudson, 1981) have observed that in some cases fractures occur in zones or bands of subparallel features. In other words, fractures may be spatially correlated.

Long and Hestir (1990) have examined 2D Poisson systems where it was assumed that the fractures are 1D, finite line segments—in other words, 2D pipe networks. They concluded that this may be a reasonable model for 3D fracture network representation if most of the conductance is in the intersections between fractures or if the flow in the fractures is channelized. Studies of this type have been done by Long (1983), Robinson (1984), and Dershowitz (1984). An enhancement to the standard Poisson process was developed by Hestir et al. (1989) who implemented a stochastic parent-daughter model for representing fracture systems. A Poisson process places points in space independently of each other and is characterized by a constant rate. It will, therefore, not duplicate the clumping of fractures that is often observed in the field. Another enhancement of the Poisson model is the doubly stochastic Poisson process. This is a generalization of the standard Poisson process in the sense that the rate is allowed to vary in 3D space. However, the number of fracture centers is still an independent random variable. The parent-daughter model, introduced by Hestir et al. (1989), places points in 3D space according to a doubly stochastic Poisson process. These points are called parents, and around each one of them a number of daughter points is generated. This process yields the clumping behavior of fractures typically observed in the field. Another advantage of the parent-daughter point process, in comparison to the doubly stochastic Poisson process, is that the rate of parent point generation can be much smoother than the swarming rate of the daughter points. Hestir et al. (1989) calculated the variogram of trace density and were able to fit a variogram which was very close to a spherical model. A further enhancement of this model is the development of the regionalized parent-daughter process by Hestir et al. (1989). For this process there exists structure in the characteristics of the network and, therefore, a semivariogram can be defined. Snow (1968) found that small samples from an essentially infinite population (of fractures) should have a Poisson distribution of counts, provided that the fractures have no tendency to congregate.

Another fracture generation approach is the nearest neighbor model. It is a simple, non-stationary model in which fracture intensity P_{32} decreases exponentially with distance from identified major features. The intensity P_{32} at any point in space is defined by:

$$P_{32}(x) = C\ e^{-bd} \tag{2-29}$$

where C and b are constants, and d is the distance between location x and the nearest major feature.

This model is also called the random discs model, and is a particular case of a Boolean model. Each fracture is assumed to be a circular or elliptic disc. Each disk is defined by its center location, diameter, and orientation. The disks centers are assumed to be a 3D Poisson process, the diameter is random with some given distribution, the orientation is random, and all fractures are assumed to be independent of each other. Since in most cases fractures are studied at a scale that cannot justify considering them as infinitely extensive, a variety of fracture generation models, classified under the generic term of tessellation models, was developed in order to address this problem. The model by Veneziano (1978), for example, is based on a Poisson process to generate independent lines. Once the

lines are generated, their intersections are calculated and a network of polygons is formulated. Then, each of these polygons is randomly classified as part of fractured or intact rock.

Dershowitz et al. (1985) developed a fracture generator in which the intersections between fractures were defined in a relatively simple manner, yet it was a slight improvement to the Veneziano model. There are three steps in the application of the Dershowitz model: (i) define the fracture planes with an *a priori* assumed orientation distribution; (ii) use the line intersections between these planes to provide the definition of a line process, which can also be viewed as a set of convex polygons; and (iii) classify a certain percentage (also called persistence) of these polygons as fractures. Since fractures may be defined by several adjacent polygons, the model does not preclude the existence of intersections within the fracture rather than the boundary. The Dershowitz et al. (1985) model exhibits a much higher connectivity than the Baecher and Veneziano assumptions. This is because, for example, in 2D space, the network generated may consist of traces that terminate in intact rock, traces which penetrate plane intersections, and traces terminating at intersections with other fracture planes. Dershowitz et al. (1985) verified their generator by comparing its results to outcrop and trace mappings from tunnels in Cambridge, Massachusetts, and the Stripa project in Sweden.

One suite of tessellation models is based on the generation of Voronoi polyhedra. Under this type of model, each point in 3D space is considered a Poisson point process and viewed as the seed or grain. Each seed grows in every direction at a constant rate until two grains come into contact. The Voronoi model can be enhanced by the option of using a variable growth rate which results in polygons of variable side lengths. A similar type of model is the Delaunay model which is also based on a Poisson point process, with the difference that the Poisson seeds represent block vertices. In this model, all block faces are triangles. Models based on the tessellation of space by Voronoi polyhedra, and their derivatives, are very good analogues of metallic grains and cracks but are less suited for simulating rock fractures. An exception is the case of columnar jointing in basalt (Chiles and de Marsily, 1993).

Other notable efforts are the studies by Rasmussen et al. (1985) and Rasmussen and Evans (1989) who presented a 3D fracture network generation model capable of synthesizing up to 1,000 fracture intersections within a matrix block broken into a maximum of 200 fractures. This model is similar in some respects with the Baecher model and addresses variability in the following fracture parameters: (i) aperture; (ii) density; (iii) orientation; (iv) shape (circular, elliptical, square, or rectangular); and (v) length. Rasmussen et al. (1985) implemented the following distributions: uniform, normal, lognormal, and exponential. Similar assumptions regarding the shape of fractures have been supported by trace data analysis by Pollard (1976). Once the fracture network is generated, the Rasmussen model solves the flow problem by reducing the complexity of the 3D problem with a collapse in dimensionality. This renders the active flow domain a sequence of interconnected 1D line elements. Finally, Billaux and Fuller (1989) have presented an algorithm that treats the fractures as random assemblages of conductive elements in a non-conductive matrix. The most important contribution of their model, however, is the application of an algorithm to remove dead-end fracture clusters, thus simplifying the mesh and speeding up the flow computations.

Long and Billaux (1987) analyzed the distributions (mean and variance) of orientation angles and fracture lengths for data collected at the Fanay-Augeres drift site. In all, about 7,000 fractures were analyzed for either orientation, location, and permeability or aperture characteristics. Long and Billaux used a single random network model to generate a 2D synthetic fracture network comprising 65,740 fractures. This synthetic network is reproduced in Figure 2-14, adapted from Long and Billaux (1987). The generation procedure is conceptually relatively straightforward. Each of the five sets was generated

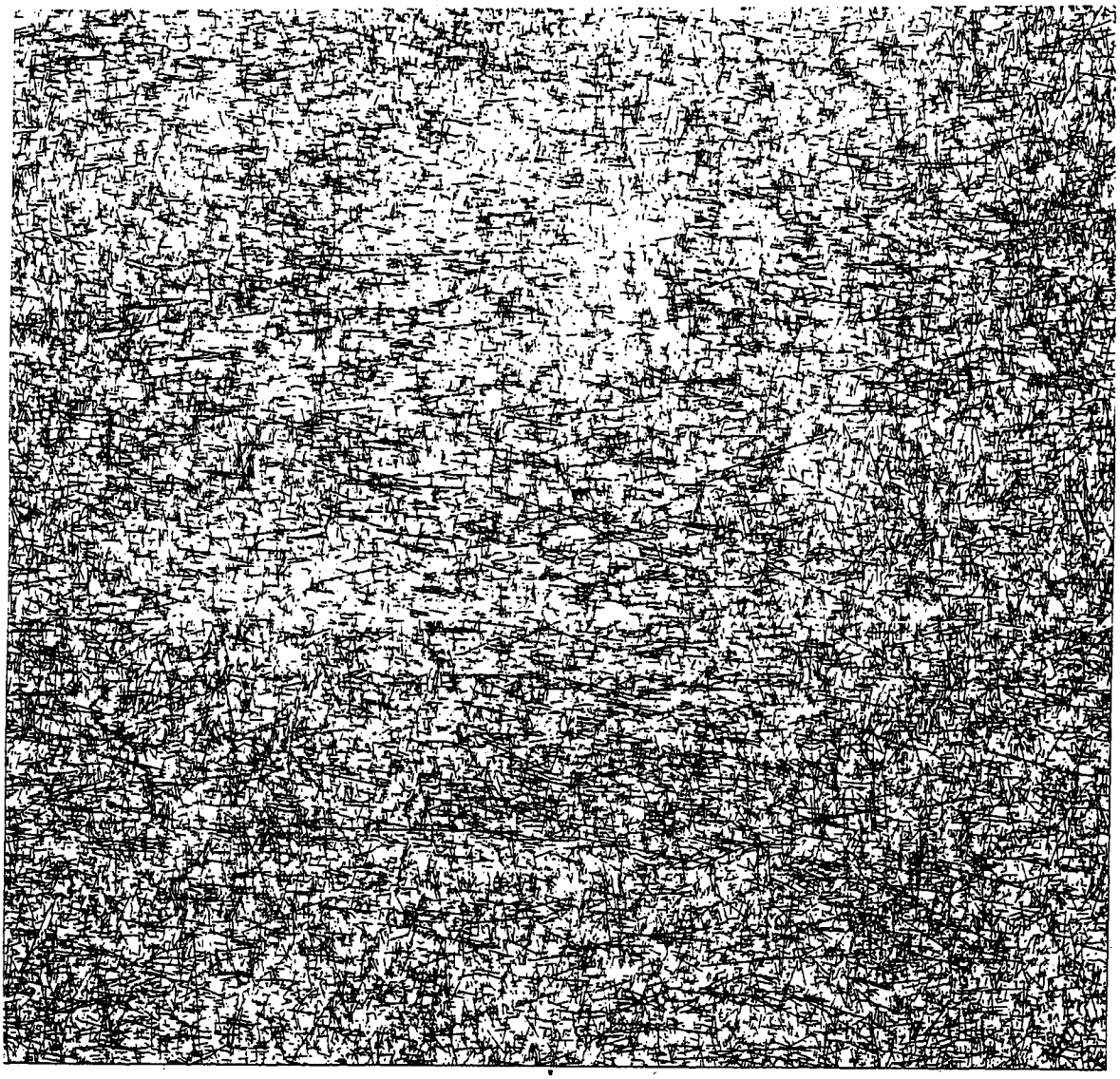

Figure 2-14. Synthetic 2D fracture network in a 100×100 m domain, where each 10×10 m subdomain was generated independently. The total number of fractures is 65,740 [from Ababou (1991), as adapted from Long and Billaux (1987)].

separately, and all five fracture sets were then superimposed in space. For each set, the generation procedure was as follows: (i) fracture centers were generated randomly based on measured fracture density, (ii) fracture orientations were randomly assigned to each center based on measured fracture orientation, (iii) fracture lengths were randomly assigned based on lognormal or exponential distribution, and (iv) fracture apertures were randomly assigned based on lognormal distribution. Each random parameter was generated independently, for example, without correlations between fracture aperture and orientation, etc. The procedure can be applied to subdomains, in order to allow for large-scale variations of fracture network statistics such as density, mean aperture, mean orientation, etc.

A relatively new type of fracture network generation model is based on concepts from the field of fractals. Fault zones, for example, have been found to obey fractal statistics (Levi, 1990). Rock mass discontinuities have been investigated for fractal behavior. Ghosh and Daemen (1993) applied the theory of fractal geometry to describe the rock fracture networks from all four faces of a copper mine in Arizona. Other investigators (Hestir et al., 1991) have observed scaling and self-similar behavior in fracture networks. In a tangential effort, Kumar and Bodvarsson (1990) postulated a deterministic representation of fracture roughness profiles based on the fractal dimension of geophysical surfaces. Based on these observations, Martel et al. (1991) have proposed and developed fracture pattern generators using self-similar Iterated Function system concepts.

Fractal patterns may be either self-similar (topologically identical at different scales), or self-affine (topologically similar but anisotropically distorted at different scales). Fractal fracture patterns can be generated in three ways:

- Utilize a recursive generation scheme which produces fracture patterns at one scale, then superimposes them at different scales (with self-affine distortion if appropriate) to directly produce a fractal pattern
- Generate fractures according to a process such as Levy-Flight which has been shown mathematically to produce fractal patterns
- Generate fractures using nonfractal processes, then test the resulting patterns to determine whether the resulting pattern is fractal

The Levy-Lee fractal fracture model utilizes the second of the above approaches, based upon the Levy-Flight (Mandelbrot, 1985). The Levy-Flight process is a type of random walk, for which the length L of each step is given by the probability function:

$$P_{L_S}[L > L_S] = L_S^{-D} \tag{2-30}$$

where D is the fractal mass dimension of the point field of fracture centers, and L_S is the distance from one fracture to the next for the previous step in the generation sequence. For $D=0$, the distribution of the step length is uniform, such that there is no clustering or heterogeneity. For large D, there is a very low probability of large steps, and therefore fractures are formed close to each other in concentrated clusters. The Levy-Flight is a 1D process for points on a line (Bartlett, 1975).

2.4 APPLICATION AND VERIFICATION OF A TWO-DIMENSIONAL FRACTURE NETWORK GENERATOR

A numerical code has been developed to generate 2D fracture networks consisting of horizontal and vertical fractures. This network topology is not as restricting as it may seem since it is very much consistent with fracture data observed at the ALTS and several pavements at Yucca Mountain, Nevada (Yeh et al., 1988; Barton and Hsieh, 1989; Thornburg, 1990; Bagtzoglou, 1993). Figure 2-15 depicts a conceptualization of how the fracture sets identified at the ALTS may look in 3D space, assuming that all subvertical and subhorizontal fracture planes have been lumped under the vertical and horizontal category, respectively. Therefore, if the fracture sets are to be observed and studied along vertical planes, as is the case in hand, the adopted fracture network topology is applicable. Furthermore, this assumption is supported by the findings of Wang and Narasimhan (1985) who studied fracture inclinations from densely welded Topopah Spring tuff and classified them as: (i) 56 percent nearly vertical (75 to 90° dip), and (ii) 44 percent nearly horizontal (0 to 25° dip). Wang and Narasimhan (1985) estimated that a fracture density anisotropy of 1.33 exists between the vertical and horizontal directions.

The approach used to place the fractures in space is similar to the methodology used by Sheridan (1992) for estimating the probability of occurrence of future volcanic dikes in the vicinity of Yucca Mountain. Sheridan's model is based on a geometric approach that assumes the centers of the volcanic dikes to be spatially distributed according to a bivariate Gaussian distribution. In a similar fashion, the generator presented here distributes the fracture center locations following either a spatially random or exponential distribution around a specified point within the domain. This point is called, in this formulation, the centroid of the cluster of fractures. The distribution of fracture centers becomes a Poisson process in the case of the exponential distribution. The clustering or development of spatial structure of fracture centers is controlled by defining the centroid of the cluster of fractures to be either fixed or randomly distributed in space. The number of fracture centers is determined based on a user-defined fracture density along the horizontal direction. The horizontal fracture density is specified as a fraction of the total number of pixels (or computational cells). Anisotropy in fracture density can be introduced by assigning the density of the vertical fractures as a fraction of the density of the horizontal fractures. Obviously, when the fracture density is isotropic, this ratio is equal to one, and for every fracture center, two orthogonal fractures exist creating a fracture feature with the shape of a cross. After the center of a fracture has been set, the fractures get placed by determining their half-length in each possible direction through sampling from an exponential distribution. This choice is corroborated by trace length data presented by Barton and Hsieh (1989) who fitted power-law functions of the form $f=aL^b$, where f is the frequency, L is the trace length, and a and b are some fitting parameters. A power-law distribution of this form is a strong indication of self-similarity and, therefore, analyses of such features by recursive scale transformations are expected to prove extremely compatible. Anisotropic behavior can be introduced also by choosing different means for the exponential distribution along the horizontal and vertical directions, or by choosing the half-length in the vertical direction to be a fraction of the horizontal fracture half-length. A schematic of the fracture generator flowchart is shown in Figure 2-16. The generator also provides for the fractures to have uniform lengths. If the length of a fracture is greater than the system length, it is assumed that the fracture is fully connecting the two opposite ends of the system.

The width of the fracture is assumed to be one pixel, and the length of the fracture is represented as a row or column of pixels, where the pixels are square. Obviously, the aperture assigned to the fracture is dependent on the resolution with which the domain has been discretized. What is important to keep in mind is that all subsequent analyses can be considered dimensionless since by changing the characteristic length of the domain (in this case the side of a square), all lengths and related

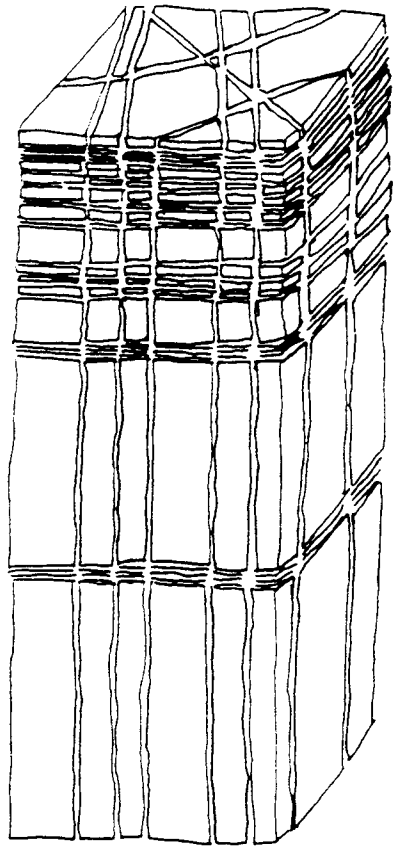

Figure 2-15. Conceptualization of fracture set appearance at the ALTS

properties are scaled appropriately. In order to mimic large system behavior (i.e., reduce the effects of finite domain size), the generator has been enhanced by a periodic boundary. This means that fractures loop around and appear at the opposite face of the computational domain when they are intercepted by a boundary. Provision has been made also for two parallel fractures to be separated from each other by at least one pixel. However, two parallel fractures can connect at their tips, thus giving rise to connectivity even when two fractures are not intersected. Thus, while sampling the center of fractures from a specified distribution, provision is made to reject candidate fractures that are not at least one pixel away from existing ones in every direction. This process of rejection of fractures was suspected of violating the distributional assumptions of centers and, therefore, a variogram analysis was conducted in a manner similar to the study by Hestir et al. (1989). No biasing of the generator was obvious from the semivariogram plots, indicating that the distributional assumptions were honored for the following tests.

First, the generator produced a series of parallel fractures in the vertical direction within a 256×256 domain (Figure 2-17). The choice of parameters was such that the fracture centers and associated half-lengths were sampled from an exponential distribution with a mean length of 50 length units. Figure 2-18 depicts the calculated variogram in the horizontal and vertical directions. Since the generated fracture pattern has no structure in the horizontal direction, the horizontal variogram is very close to a pure nugget variogram. In contrast to this behavior, the vertical variogram exhibits structure, and its range is approximately 100 length units, in close agreement with the prescribed mean length.

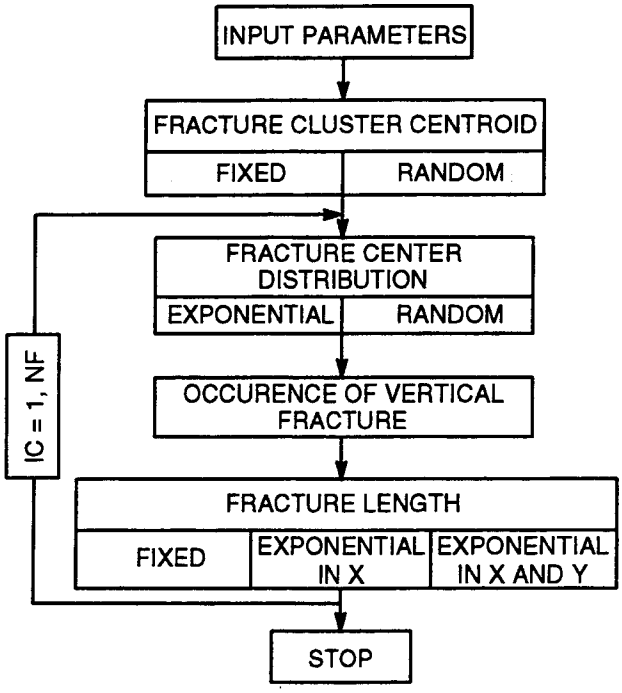

Figure 2-16. Fracture network generator flowchart

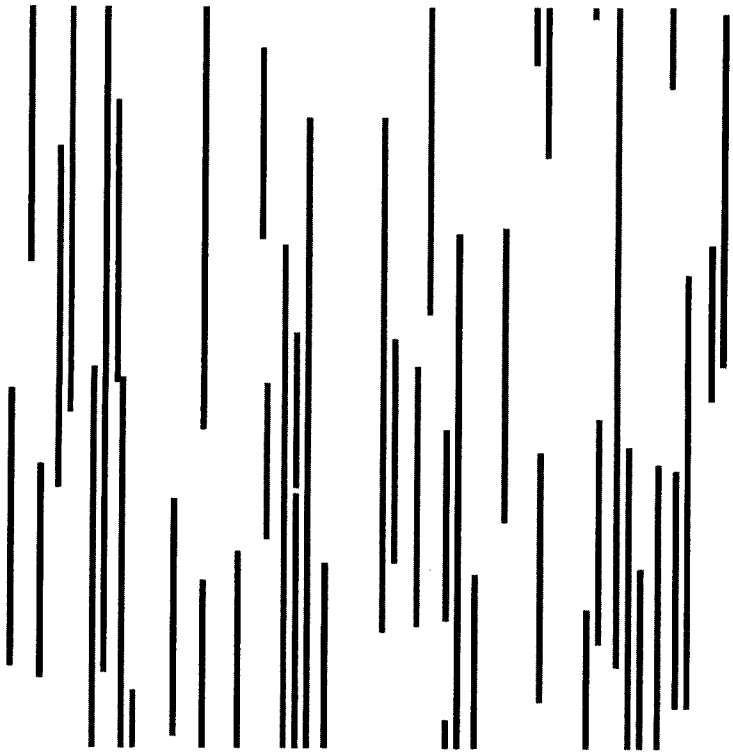

Figure 2-17. Set of vertical fractures used for network generator verification. Dimensions of the bounding box are 256×256 length units.

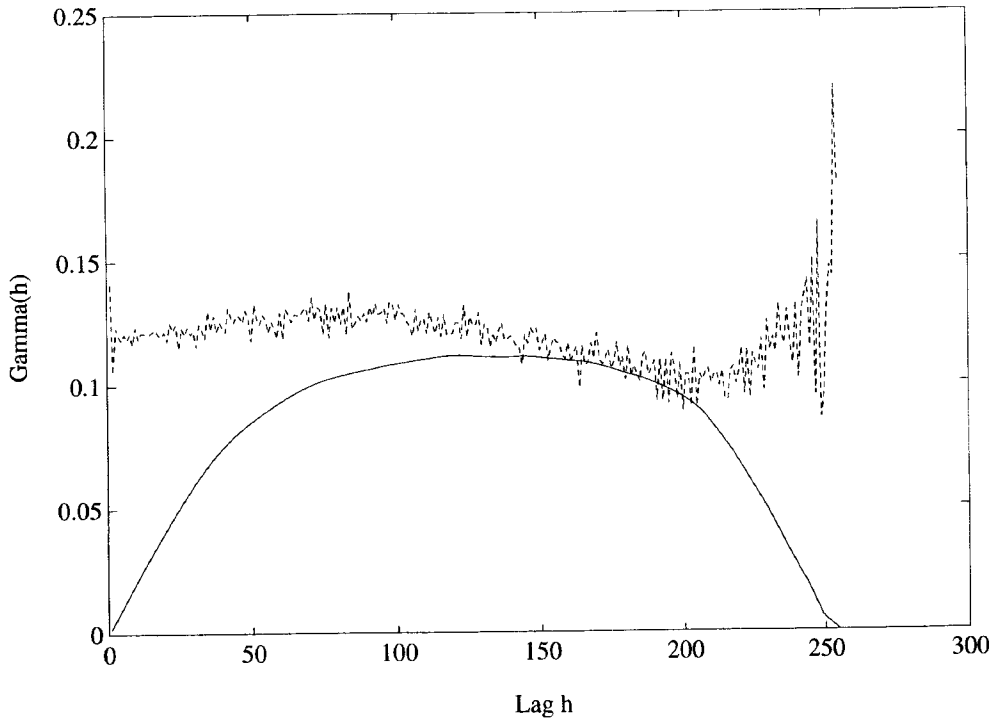

Figure 2-18. Horizontal (dashed) and vertical (solid) variograms for the fracture pattern of Figure 2-17

Furthermore, the sill of the vertical variogram approaches, at large separation distances, the pure nugget variance of the horizontal variogram, as it should. The results of Figure 2-18 are analyzed further by plotting only the vertical variogram in Figure 2-19. Two theoretical variograms, an exponential and a spherical, are fitted (by trial and error) to the variogram calculated numerically. It appears that the spherical variogram model better matches the variogram calculated from the fracture pattern. This is in agreement with the results by Hestir et al. (1989) for trace density and the results by Chiles (1989b) and Chiles and de Marsily (1993) who fitted a cubic variogram for trace center number count.

The second test involved the generation of a fracture network consisting of horizontal and vertical fractures, with centers sampled from an exponential distribution and half-lengths sampled from two independent exponential distributions with mean length of 50 length units in the vertical and horizontal directions. Figure 2-20 presents the trace length variogram for this fracture network, together with the best fitted exponential and spherical theoretical models. Again, the spherical model appears to be closer to the variogram calculated numerically. It should also be noted that the numerical variogram exhibits a nugget effect approximately equal to 0.12, which is in very close agreement with the sill of the variogram in Figure 2-18.

Finally, the fracture network generator is capable of superimposing the fracture sets on either a homogeneous or a heterogeneous matrix background. In this way, the user may choose to analyze a binary system or a fracture network superimposed on a stochastically generated matrix hydraulic property field. Typical examples of complex, highly fractured, heterogeneous structures generated by the numerical code discussed in this section are shown in Figures 2-21 and 2-22.

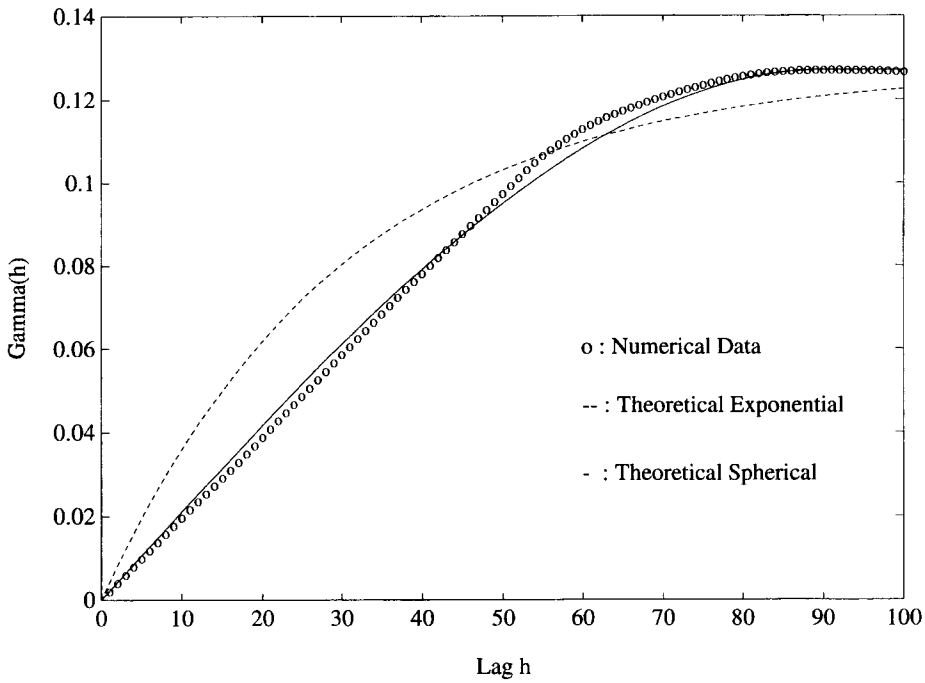

Figure 2-19. Vertical variogram for the fracture pattern of Figure 2-17 and fitted theoretical variogram models

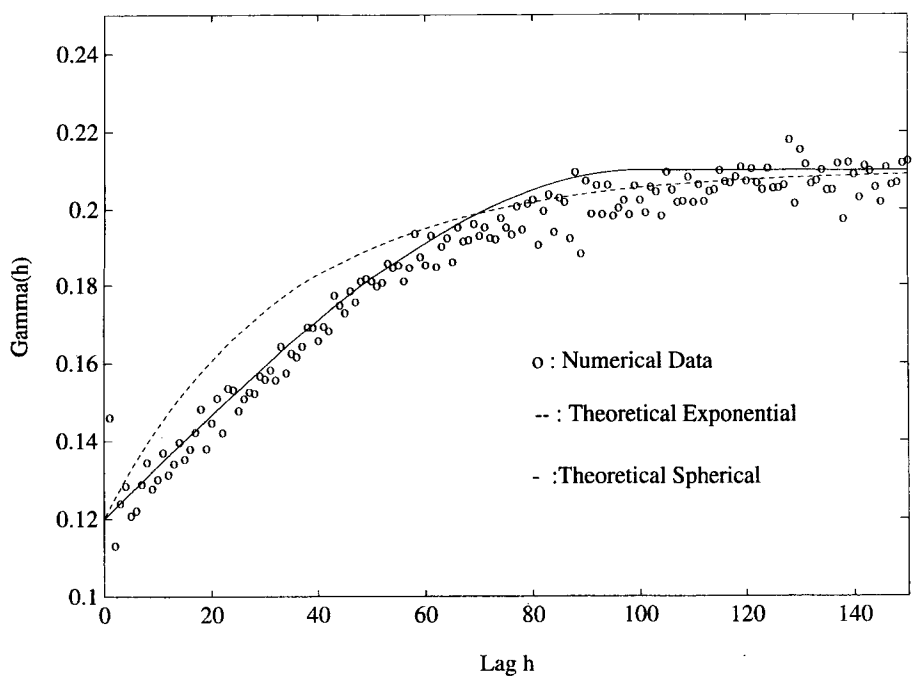

Figure 2-20. Trace length variogram and fitted theoretical variogram models

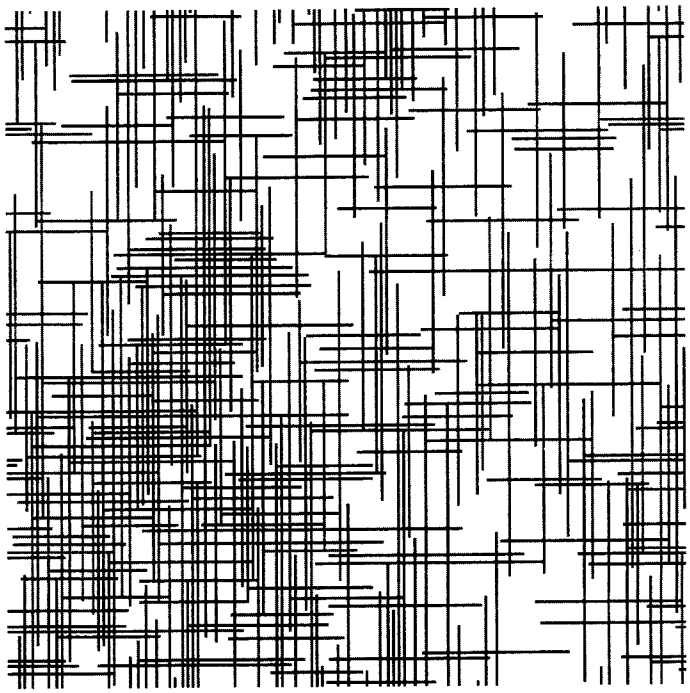

Figure 2-21. Highly fractured, heterogeneous structures for a binary matrix-fracture system. Dimensions of the bounding box are 512×512 length units.

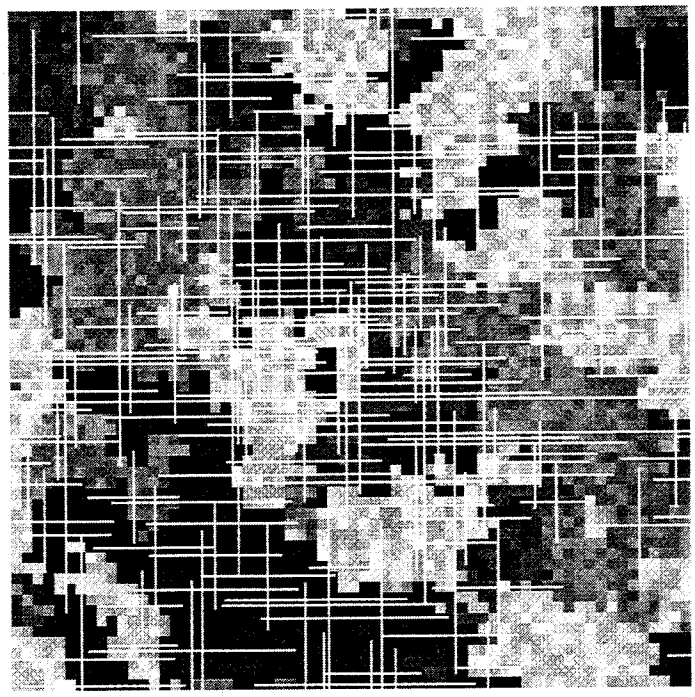

Figure 2-22. Highly fractured, heterogeneous structures for a stochastic matrix-fracture system. Dimensions of the bounding box are 256×256 length units.

3 METHODS FOR ESTIMATING EFFECTIVE UNSATURATED HYDRAULIC PROPERTIES

Fluid flow through fractured rock is a process that has importance for many areas of the geosciences, ranging from groundwater hydrology, to nuclear waste disposal, to petroleum engineering. Of key technical importance to these three fields is the detailed understanding of how fluids flow through individual fractures and sets of fractures in rock (Pyrak-Nolte and Cook, 1988). One of the challenges in modeling flow and transport in fractured rock is to account for the spatial variability in the physical and chemical properties of naturally occurring porous media. In realistic applications, there is always scarcity of data available for the precise description of a flow problem at any given scale. Given the fact that there is always going to be some heterogeneity of natural media for which we cannot account, the pertinent question is how to incorporate realism in models in the absence of adequate data and abundant computational resources. Dykaar and Kitanidis (1993) proposed a general approach to address this issue. Their approach employs spatial averaging of hydraulic parameters in some appropriate fashion, and moves information from the local scale (the scale of large heterogeneity and parameter uncertainty) to the global scale (the scale where the heterogeneity is smoothed out). This, and similar types of approaches, lumps small-scale details into a few representative macroscopic parameters with the aspiration of preserving the large-scale behavior of the system. As discussed in Chapter 1, effective property approaches provide great computational savings, and their spatial support is consistent with the small number of field measurements available. The effects of change in spatial support have been extensively studied by geostatisticians. These efforts have primarily focused on additive properties, such as shale fractions and (by extension) porosity. One disadvantage of the conventional geostatistical approach is that it leaves the mean of the property distributions unchanged (Rautman and Robey, 1993). These approaches have also been criticized for their failure to account for the anisotropic behavior of the relationship between saturation and effective permeability (Bear et al., 1987). As a result, while it may be possible to establish effective constitutive laws for background fracturing (Dershowitz, 1992) and lump the effects of numerous small fractures into submodels, the effective continuum approach must be enhanced through the explicit incorporation of discrete geological features. These discrete geological features can be fracture zones or faults and control the behavior of the flow system at scales larger than the fracturing.

The field of effective property calculations is not new and spans a great number of disciplines. Several approaches and methods have been proposed and applied in the past. A comprehensive review of some of these approaches can be found in the work of Durlofsky (1991). Notable examples are the works of Journel et al. (1986), Desbarats (1987), and Deutsch (1987) who calculated effective permeabilities based on the sand-shale ratio with the help of an empirical power-law. Other efforts include works on various other types of averaging, such as arithmetic, geometric, harmonic, and areally-based (Warren and Price, 1961; Begg and King, 1985; Kasap and Lake, 1989), direct numerical simulations, and homogenization approaches. One of the homogenization approaches discussed extensively in this work is the RSRG method. In the following sections, a thorough, but not exhaustive, presentation of some relevant literature is provided.

3.1 EFFECTIVE PROPERTY CALCULATIONS BASED ON ADDITIVE VOLUME FRACTIONS

Perhaps the most widely known, at least in the hydrologic community, equivalent continuum approach application is the work of Peters and Klavetter (1988). In their work, the fracture porosity, ϕ_f, can be defined as the ratio of the fracture volume to the total bulk rock volume. The matrix porosity, ϕ_m,

can be defined as the ratio of the volume of the voids in the matrix (excluding fracture void space) to the volume of the matrix. A bulk equivalent porosity, ϕ_b, is then defined after Nitao (1988) as:

$$\phi_b = \phi_f + (1 - \phi_f)\phi_m \tag{3-1}$$

The equivalent continuum approach is based on the assumption that the pressure head in the fractures and the matrix are identical in a plane perpendicular to flow. The major points of the conceptual model by Peters and Klavetter (1988) are summarized below:

- The saturated fracture conductivity is much larger than the adjacent matrix conductivity. Thus, flow across the fracture is controlled by the adjacent matrix conductivity. Consequently, the fracture conductivity for water movement across the fracture can be replaced by the matrix conductivity.

- In a flow system at or near steady-state, if the flux in the unsaturated rock is less than the value of the saturated conductivity of the matrix, then the water will flow only in the matrix. In cases when the flux is greater than the saturated conductivity of the matrix, the matrix will saturate, and the fractures (in addition to the matrix) will carry water.

- The more the fracture orientations become preferential, or consistent, the more this conceptual model will suffer due to the lack of anisotropic characteristics.

The steady-state version of the flow equation can be integrated to obtain the following form of Darcy's law:

$$-(K_{m,b} + K_{f,b}) \cdot \nabla(\psi + z) = q_m + q_f = q_{\text{tot}} \tag{3-2}$$

Then, it can be written in terms of a composite-porosity material:

$$-K_c \cdot \nabla(\psi + z) = q_c = q_{\text{tot}} \tag{3-3}$$

where the subscript c refers to the composite-porosity material, which is equivalent to the fractured, porous matrix system in terms of predicting the total fluxes and the pressure head field. The composite-porosity material parameters are given by (Peters and Klavetter, 1988):

$$K_c \equiv K_{m,b} + K_{f,b} \tag{3-4}$$

Given the saturation of the fracture, S_f, and matrix, S_m, the equivalent bulk saturation, S_b, can be defined as:

$$S_b = \frac{S_f\phi_f + S_m(1 - \phi_f)\phi_m}{\phi_f + (1 - \phi_f)\phi_m} \tag{3-5}$$

The weighting procedure of Klavetter and Peters (1986b) is used to obtain the equivalent bulk hydraulic conductivity:

$$K_c = K_m(1 - \phi_f) + K_f\phi_f \tag{3-6}$$

If the formation is highly fractured and the matrix blocks are small, the pressure and/or temperature within a matrix block will quickly equilibrate with the surrounding fractures (Wang and Narasimhan, 1985; Pruess et al., 1990a). If the local thermodynamic equilibrium conditions are satisfied, there is no need to separately calculate pressure/temperature values in the matrix and fractures. In this composite-porosity and effective continuum model (Peters and Klavetter, 1988; Pruess et al., 1990b), a fractured porous medium is represented by saturation and permeability functions which are arithmetic averages of the properties at the fracture and matrix system. The arithmetic averages of permeabilities are accurate for the special case of the flow in fractures being parallel to the flow in the matrix blocks. Rasmussen et al. (1989) studied the nonparallel flow effects by simulating a vertical square region and a cubic box region containing a fracture. The equivalent permeability was related to the fracture and matrix permeability by arithmetic, harmonic, or geometric means, depending on the fracture orientation.

Rulon et al. (1986) and Rockhold et al. (1992) conducted simulations using the equivalent continuum approach for a system analogous to Yucca Mountain, Nevada. The results by Rockhold et al. (1992) suggest that fracture flow, as approximated by the equivalent continuum model, is unlikely to occur at the level of the potential repository at recharge rates up to 4 mm/yr. Calculations, based on this approach, are valid under the assumption that there are enough fractures of varied orientation to ensure continuum behavior. A possible criticism is that, according to Pruess et al. (1990a), the continuum approach will break down for processes involving rapid transients and for conditions of a very tight rock matrix or large fracture spacing. Finally, the effective permeability or composite curves proposed by Wang and Narasimhan (1986), Klavetter and Peters (1986), Peters and Klavetter (1988), and Dudley et al. (1988) have never been validated since no comparison with data has been reported to date (Loeven, 1993).

Extensive literature on the subject of effective properties exists in the field of heat conduction and thermal materials. For example, a list of formulae useful in calculating thermal conductivity of a fibre composite has been given by Chawla (1987). Parang et al. (1987) have studied heat conduction normal to the axes of coolant tubes. Baker-Jarvis and Inguva (1985) have studied steady heat conduction in a region containing inclusions. Hatta and Taya (1985) have extended Eshelby's (1957) equivalent inclusion method in elasticity and determined the effective conductivity of a composite with highly conducting short fibres randomly oriented within it. More recently, Muralidhar (1990) has numerically investigated the thermal conductivity of a composite medium on a 2D square spatial domain. Two sides of the domain were insulated, while the other two were subject to fixed temperature boundary conditions. Effective conductivities were calculated for different patterns and numbers of inclusions in the form of circular voids. Void volume fractions ranged up to 20 percent. The numerical results of this study were compared to the rule of mixtures:

$$K_0 = VK_m + (1-V)K_f \tag{3-7}$$

and to the empirical transverse conductivity given by (Chawla, 1987):

$$K_0 = \left(1 - \sqrt{V}\right) K_m + \frac{K_m\sqrt{V}}{1 - \sqrt{V}\left[1 - \frac{K_m}{K_f}\right]} \tag{3-8}$$

where fraction V of the medium has conductivity K_m and fraction $1-V$ has conductivity K_f. Based on this analysis, Muralidhar concluded that the static equivalent conductivity of a composite region is primarily a function of the percentage of inhomogeneities. It depends weakly on the pattern of distribution and fineness of their size.

In similar efforts, Bergman (1982) showed that for a two-phase medium the effective conductivity of the medium is bounded by the volume-weighted arithmetic mean conductivity, K_A, from above, and from below by the corresponding harmonic mean, K_H:

$$K_A = 1 - V + V\alpha \tag{3-9}$$

and

$$K_H = \left[\frac{V}{\alpha} + 1 - V\right]^{-1} \tag{3-10}$$

where proportion V of the medium has conductivity α and proportion $1-V$ has a unit conductivity. This equation is the rule of mixtures result given by Chawla (1987). The proportion V is called the volume fraction and, alternatively, is associated with the symbol ϕ.

In order to predict the effective properties of a composite material from classical or statistical theories, we need to know not only the porosities and permeabilities of the various rock materials, but also the exact geometries of the phases in the composite. This requires a complete statistical characterization of the microstructure. Such a complete characterization, according to statistical theories, requires an infinite set of multipoint correlation functions due to the random nature of the phase geometries. The statistical correlation functions provide the microstructural information. The limited order of correlation functions obtainable cannot provide accurate predictions of effective permeability for a wide permeability contrast and arbitrary volume fraction of the phases. Nevertheless, given a limited amount of information on the microstructure, improved lower and upper bounds are obtainable (Torquato, 1987). The variational bounds tell us what rigorous statement can be made about the effective properties given that only certain statistical information about the distribution of the phase is available. The bounds are useful in the sense that they enable one to test the merits of both theory and experiment, and occasionally, one bound can provide a good estimate of effective properties for a large class of media. As successively more detailed microstructural information (statistical correlation functions of high orders) is incorporated, the separation between the bounds can be systematically decreased.

The first order bounds for effective conductivity of a composite, comprising two media of conductivities k_1 and k_2 due to Weiner (see Torquato, 1987) are:

$$K_L \leq K_e \leq K_U \tag{3-11}$$

where

$$K_L = \langle K^{-1} \rangle = \frac{k_1 k_2}{\phi k_1 + (1 - \phi) k_2} \tag{3-12}$$

$$K_U = \langle K \rangle = k_1 \phi + k_2 (1 - \phi) \tag{3-13}$$

The lower and upper bounds (K_L and K_U) grossly underestimate and overestimate the effective properties (K_e), respectively. The anisotropic parallel arrangement of the phases relative to the direction of fluid flow represents an upper limit for the permeability of the two-phase system. This is given by the porosity-weighted arithmetic mean of the two permeabilities. The anisotropic series arrangement of the phases represents the lower limit for the conductivity of any possible geometrical configuration of the two phases. This is given by the harmonic mean of the two permeabilities. An alternative is the weighted geometric mean for better prediction of the effective permeabilities:

$$K_e = k_1^{(1-\phi)} k_2^{\phi} \tag{3-14}$$

Hashin and Shtrikman (1962) studied effective magnetic permeabilities using a variational approach. For the case of a two-phase medium, they obtained improved bounds as compared with those in the equations above. Their upper (K_U) and lower (K_L) bounds are, respectively:

$$K_U = 1 + \frac{V}{\dfrac{1}{\alpha - 1} + \dfrac{1 - V}{2}} \tag{3-15}$$

and

$$K_L = \alpha + \frac{1 - V}{\dfrac{1}{1 - \alpha} + \dfrac{V}{2\alpha}} \tag{3-16}$$

where V and α were described previously.

Results obtained in the study of thermal conductivities are equally valid for the problem of groundwater flow through fractured rocks. This extension is possible by identifying temperature with pressure, conductivity with permeability, and thermal capacity with storage capacity. Dagan (1979) applied a self-consistent approach in a groundwater flow application and derived bounds on the effective permeability of isotropic systems. The determination of the effective hydraulic conductivity of the flow domain is derived from knowledge of the probability density function of the (assumed random) hydraulic conductivity. The following result from Dagan's work is relevant here:

$$K^* = \frac{1}{2}\left[\int \frac{f(k)\,dk}{k + K^*}\right]^{-1} \tag{3-17}$$

where K^* is the effective conductivity of the medium, f is the probability density function, and the range of integration is over the domain of f. This equation is based on the assumption of an unbounded, 2D spatial domain over which k can vary randomly. Dagan's results provided narrower bounds than those previously available. Kirkpatrick (1973) provides an alternative derivation of this equation. Kirkpatrick advocated a power averaging for random geometric mixtures of materials which falls between the arithmetic and harmonic averaging for materials with constant conductivities. Kirkpatrick presented the following transcendental equation for approximating the effective conductivity of a random mesh of resistors:

$$\int_0^{+\infty} \frac{(K_e - K)\, f(K)}{(c/2 - 1)K_e + K}\, dK = 0 \tag{3-18}$$

where K_e is the effective conductivity, $f(K)$ is the probability density function for the conductivity, and c is the connectivity of the resistor mesh. For a continuous region, the connectivity is twice the number of dimensions. This allows use of this averaging equation for 1, 2, and 3D continuum problems. In deriving the above equation, the assumption that the medium is of infinite extent and has the various conductivity levels distributed randomly was made. When these conditions are met, the equation has been demonstrated to be reasonably accurate (Kirkpatrick, 1973; Burganos and Sotirchos, 1987).

In summary, and regardless of the exact method with which the effective conductivity is calculated, K^* or K_e gives the effective conductivity of the two-phase medium with the bounds:

$$K_H \le K_L \le K^* \le K_U \le K_A \tag{3-19}$$

where K_L and K_U are the improved bounds by Hashin and Shtrikman (1962). Finally, the conclusion reached by Muralidhar (1990) that the static effective conductivity can be used for unsteady problems corresponds with a similar conclusion for unbounded groundwater flow domains reached by Dagan (1979).

A similar effort by Zimmerman (1992) studied the effective hydraulic conductivity of a 2D porous medium that contains elliptical inhomogeneities. The background medium has permeability k_o, whereas the inhomogeneities have permeability k_i. The shape of the inhomogeneities is quantified by their aspect ratio which can take on values between 0 and 1. The elliptical inhomogeneities are assumed to be randomly oriented, so that the effective conductivity is isotropic. Zimmerman used Maxwell's effective medium theory to find the overall conductivity. Results are obtained as a function of the area fraction of the inhomogeneities, c, for arbitrary inhomogeneity ratios k_i/k_o, and all aspect ratios. The effective conductivity is predicted to vary from k_o to k_i as the area fraction of the elliptical inhomogeneities varies from 0 to 1. In the limiting cases where k_i=0 or $k_i=\infty$, the theory predicts percolation-like behavior, in the sense that the effective conductivity reaches k_i at some value $c^*<1$. The critical area fraction c^* is found to depend on the aspect ratio, but the percolation exponent does not. Except in the region near

the percolation limit, the predictions are in agreement with experimental results which measured the electrical conductivity of a metallic sheet perforated with thin elliptical slits.

In other notable efforts, Warren and Price (1961) considered 3D systems with random permeabilities without any spatial structure, and showed that the geometric mean is a reasonable average property for such systems. Begg and King (1985) conducted a similar study for flow regions with discontinuous flow barriers and expressed the effective permeabilities as a function of shale size and shale volume fractions. Desbarats (1987) studied sand-shale sequences with both correlated and uncorrelated permeability fields. Using a distribution of permeability values, Johnson and Greenkorn (1962) found that when their data were approximately normally distributed arithmetic averaging gave the closest estimate (within 3.5 percent) to the well test permeability.

One other frequently used method to estimate the effective properties is geometric averaging. Although it has been widely used to predict effective permeability, there are some problems associated with it, and whether the geometric mean is the appropriate quantity to be estimated has been questioned in the past, since for any of the permeability values approaching zero it will lead to erroneous results. Moreover, the geometric mean does not exist for discontinuous distributions for which there is a non-zero probability of zero values occurring. This, of course, is seldom the situation for permeability of geologic materials. Although, theoretically, given a sufficiently large head or area of flow, most geologic material would permit some fluid flow, from the numerical point of view values close to zero entail some sort of bias in the average property. Percolation theory and numerical simulation have suggested that even if there are regions of zero permeabilities, the overall permeability can still be non-zero. On the other hand, results from the works of Matheron (1967), Bakr et al. (1978), and Dagan (1979; 1981) indicate that the geometric mean applies when permeabilities are lognormally distributed with small variances and the flow domain is 2D. Approximate corrections to the geometric averaging are also available for its application in 1D and 3D (Gutjahr et al., 1978).

3.2 EFFECTIVE PROPERTY CALCULATIONS BASED ON DIRECT NUMERICAL SIMULATIONS

The general formulation for numerical procedures used for the determination of effective properties for heterogeneous reservoirs involves a continuity equation for a single-phase, incompressible flow through porous media. This equation, given in dimensionless form, can be represented as:

$$\nabla \cdot (K \cdot \nabla p) = 0 \tag{3-20}$$

where p is pressure potential and K is the permeability tensor embodying the variation at many length scales. In this equation, the gravity terms are neglected for clarity reasons. Our intent here is to replace the above equation with an equation of identical form but with K being replaced with an effective permeability tensor, designated by K^*, where K^* now varies on a coarser (simulation grid block) scale. From the numerical simulation point of view, one would wish to decrease the number of grid blocks to save computation time. The intent, therefore, is to replace the above equation with an equation of identical form in which K is replaced with an effective permeability tensor, designated K^*, that is,

$$\nabla \cdot (K^* \cdot \nabla p) = 0 \tag{3-21}$$

where K^* now varies on a coarse (simulation grid block scale). Each grid block is assumed to be homogeneous and perfectly defined by its characteristics. The properties input to the model must therefore account for the heterogeneities, as well as the fluid distribution at any scale smaller than the grid block

size. These properties are generally called pseudo functions. They can be used to reduce the dimension of the problem or to reduce the number of grid blocks in a numerical model (Ahmadi et al., 1990).

In the direct numerical simulation approach, as the flow equation is (typically) solved using a block-centered finite difference scheme, the interface permeability rather than the block permeability will be sought. The effective permeability is determined by equating the integrated flux from the fine scale solution with those which would be obtained from the global pressure gradient and the effective permeability tensor. Each bond or each site is assigned a permeability value. One can also find the global permeability directly through a transfer matrix calculation. A notable example of this approach is the work of Gomez-Hernandez (1990) and Gomez-Hernandez and Journel (1990). In their numerical solution, the flow equation was solved at the grid block and subgrid block scales under the following two imposed conditions: (i) that the pressure from the grid block scale simulation should be equal to the storativity-weighted sum of subgrid block scale pressures within the grid block scale block, and (ii) that the flux at the interface between two nodes at the grid block scale is equal to the sum of the fluxes from the subgrid blocks. These investigators used a least square approach based on the solution of flow for different boundary conditions and claim that this block permeability reproduced better total fluxes, especially in the direction orthogonal to the elongation of the heterogeneities. In similar efforts, Huppler (1970) and Saez et al. (1989) employed direct numerical simulations to study the effective homogeneous behavior of heterogeneous porous media.

Several methods are used to calculate equivalent conductivities for a numerical simulation (Durlofsky, 1991). The essential difference between these methods is the nature of the boundary conditions specified on the subdomains, which is of particular interest when calculating off diagonal terms of the conductivity tensor. However, as the primitive fields are isotropic, the off-diagonal terms are expected to be insignificant. Beckie et al. (1994) showed that the x and y components of K exhibit only very weak and spatially random anisotropy. A comparison of their numerically determined coarse grid block equivalent conductivities to those found using the renormalization strategy of King (1989) yielded almost indistinguishable results.

Furmański (1992) studied the macroscopic thermal behavior of heterogeneous materials using the ensemble averaging technique. The nonlocal constitutive relations for heat conduction were derived and found to relate the ensemble averaged heat flux and energy density to the ensemble averaged temperature of the medium. All the effective properties appearing in the relations were defined with the help of microstructure functions. Furmański's results showed that an effective parameter approach is a valid resolved-scale model when there exists a separation between the grid and subgrid scales. The existence of a local resolved-scale equation is guaranteed if the subgrid scale fluctuations are much smaller than the resolved-scale variation (Auriault, 1991; Beckie et al., 1994). Eaton et al. (1991) studied flow through nonhomogeneous porous media and, although the material properties and boundary conditions used in this study resulted in nonlinear solutions, they compared these results with averaging methods for the linear case.

Rautman and Robey (1993) discuss various issues of numerical computation of the effective permeability of a limited number of block scale cells positioned within a large microscale simulation conditioned to existing well data. The effective permeabilities of a number of such block scale cells are computed, and the variograms and cross variograms for the (exhaustive) point values and (sparser) block values can be computed. Once the point-to-block correlation structure has been approximated, it is a relatively simple matter to directly simulate a large field of block values conditioned to data measured on the smaller scale. Upscaling flow properties has serious difficulty when applied to Yucca Mountain

since it appears unlikely that the effective permeability of tuff is related to the proportion of welded and nonwelded material. The direct simulation of block scale effective permeabilities could be used at Yucca Mountain in certain limited instances. However, serious difficulties exist in performing such a task since the Yucca Mountain problem is 3D and multilayered (Rautman and Flint, 1992). In addition, a major focus within the Yucca Mountain project is on assessing uncertainty, which implies that numerous realizations must be produced, scaled up, and evaluated.

Rautman and Robey introduced an adaptive grid algorithm based on concepts originally described by Garcia et al. (1990). They construct a mesh covering the area (or volume) of interest, for which the sides of each cell are conceptually and mathematically represented as springs with an appropriate coefficient of elasticity. By adjusting the coefficients of elasticity in a manner proportional to some measure of heterogeneity of the discretized cells, it is possible to have the spring sides of the cells expand or contract to minimize some aspect of that heterogeneity. The effect of this algorithm is that the final grid adapts to follow geological features reflected in the underlying geostatistical simulation of a material property, and the individual cells are as homogeneous as possible. Finally, Kasap and Lake (1989) proposed and applied an analytical technique that essentially provides the ability to calculate the arithmetic and harmonic means for layered systems comprising full tensorial permeabilities. Their method is based on a parallel and series combination at a local scale which is subsequently rotated to arrive at tensorial permeabilities from the orientations of these layers. They validated their method using a finite element numerical simulator which models permeability discontinuities explicitly.

3.3 EFFECTIVE PROPERTY CALCULATIONS BASED ON HOMOGENIZATION AND RENORMALIZATION METHODS

Phenomenological scaling laws are usually considered adequate to provide quantitative means for organizing data, and thereby allow some sense of order or coherence to be brought to a complex natural system. The response of any such complex system to a change in scale typically reflects some deep underlying features that are often independent of its detailed dynamics. Generally speaking, scaling up from the small to the large is usually accompanied by a change from simplicity to complexity. This occurs while maintaining certain fundamental elements of the system invariants or conservation laws.

For example, when considering double-conductivity media, the phenomenological reasoning is characterized by the introduction of one temperature field for each constituent (Rubinstein, 1948). These temperatures are defined at a macroscopic scale, directly, and the description is assumed to be continuous. Because of the two different temperatures, a heat flux between the two constituents appears and is given by Auriault and Royer (1992) as:

$$\psi_1 = \alpha(T_1 - T_2) \tag{3-22}$$

where α is a negative constant and denotes the transfer coefficient expressed in $Wm^{-3}\ K^{-1}$, and T_1 and T_2 are temperatures. Consequently, ψ_2 characterizes the heat transfer from medium 1 to medium 2 and is written:

$$\psi_2 = -\psi_1 \tag{3-23}$$

In contrast to the phenomenological approaches, homogenization methods are based on the passage from the microscopic description to the macroscopic one. The main idea of these methods is to

define, if possible, a fictitious homogeneous medium that will be referred to as the homogeneous medium or the equivalent macroscopic medium. It will behave as the composite medium when submitted to the same external constraints. The description of this medium must be intrinsic to the material and the phenomenon considered. In particular, it should not depend on the macroscopic boundary conditions. An effective macroscopic description for transient heat conduction in periodic composites has already been derived by Auriault (1983).

Auriault and Royer (1992) have investigated the heat transfer process in double-conductivity media by both phenomenological and homogenization approaches. They were critical of the former because it leads to a description governed by the temperature of the most conductive constituent. Moreover, the conductivity of the less conductive constituent is neglected and is not taken into account in the macroscopic model, and the corresponding temperature field has no real physical interpretation. They implemented a homogenization process, first proposed by Auriault (1991), and compared the two approaches.

Other methods of calculation of effective properties for periodic or random structures, also called homogenization techniques, are well documented. In the case of probabilistic models, only linear constitutive behavior (like Darcy's law) is fully studied. A possible paradigmatic structure for discussing some of these methods and associated scaling questions within a general framework is one that has arisen in the context of understanding scaling phenomena in quantum field theory and statistical physics. One specific analytic technique developed there is called the Renormalization Group (RG). It is a rather powerful and general one, and it has potentially important applications in areas of science other than that where it was first applied. It has a precise formulation and, consequently, precise quantitative statements concerning scaling in both elementary particle physics and phase transition phenomena in statistical mechanics. For example, anomalous dimensions and the consequent power-law behavior that appear in this context are quite analogous to fractal dimensions that occur, for example, in classical complex systems. In a practical application of the RG approach, Abu-Elbashar et al. (1990) assigned permeability values at each node proportional to the net-to-gross thickness of the layer as observed from well data. By using the RG formalism, as introduced by King (1989), they claim to have obtained good results. However, their effort seems limiting due to the alignment of the anisotropy in the flow direction only and the use of a rather high to medium conductivity permeability range. In statistical physics, one typically assumes no spatial correlations among the local permeabilities (i.e., fully random systems). The issue of spatial anisotropy also has not been addressed in detail by these authors. In addition, these studies have obtained effective permeabilities by averaging over an ensemble of systems in the limit of infinite size.

One of the advantages of the RG-based approaches is that they compare very favorably to direct numerical simulations in terms of computational requirements. The time for direct calculation scales with the size of the domain to a power normally between 2 and 3. Contrary to that, the RG algorithm scales linearly with the size of the domain. Aharony et al. (1991) obtained results in 2D and 3D domains with accuracy in the range of 5 percent or better, irrespective of anisotropy or correlation. Further details on the RG algorithm, its implementation, and computational savings can be found in Chapter 4 of this report.

3.4 EFFECTIVE PROPERTY CALCULATIONS BASED ON POWER AVERAGING

Many equations have been proposed to find average conductivities that fall between the limiting cases of arithmetic and harmonic averaging (Journel et al., 1986). Some empirical approaches derive

estimates of the effective properties by averaging the point values of the coefficient after an appropriate transformation (such as a power law); this kind of averaging has no theoretical foundation, except in the case of log-symmetrical 2D media where the geometric consideration is exact (Matheron, 1967). The main limitation of these methods is that the above developments diverge for a zero or infinite hydraulic conductivity. In these conditions, other techniques are available like the self-consistent method.

Gomez-Hernandez and Journel (1990) have proposed a numerical averaging technique from point-to-block permeabilities accounting for the tensorial character of permeability. In the power averaging method, the vertical and horizontal block permeabilities are identified in an elaborate way to two different power averages (or p-norms) of the core values (Deutsch, 1989). Although the numerical simulation method is considered to be accurate in obtaining effective properties, there are questions raised about its validity. Begg et al. (1989) point out that such a technique would fail in the case of large heterogeneities of the order of magnitude of the block size. The block permeabilities thus obtained are dependent on the boundary conditions needed to solve from within each block. Gomez-Hernandez (1990) points out that this is the case because the block permeabilities are not intrinsic to the internal distribution of core values (i.e., known permeabilities assigned to the smallest grid block) even when these core values are exhaustively known. It is impossible to assign block permeability that will be valid for any boundary condition. However, from the analytical solution of simple 2D cases by Kitanidis (1990), it can be inferred that if the range of the fine-scale permeability distribution covariance is finite, then there will be a minimum block size beyond which the block permeability will become independent of the boundary conditions needed to obtain it.

A statistical continuum approach was used by Ababou and Yeh (1992) to investigate effective flow behavior in heterogeneous, unsaturated porous media. At small scales, the constitutive relation between hydraulic conductivity and suction head is represented by a nonlinear function with two cross-correlated (with correlation coefficient given by ρ) random field parameters, namely the saturated log-conductivity and the logarithm of the moisture dispersivity length scale or inverse slope of unsaturated conductivity. A probabilistic analysis of the random set of conductivity curves reveals the existence of a fuzzy cluster of crossing points centered around suction $\psi=\psi_0$. An upper bound conductivity curve is also identified, which decreases more smoothly with suction than any local curve. The analytical results are compared to perturbation solutions of the random flow equations, and checked against direct numerical simulations for periodic or random layers with uncorrelated or cross-correlated parameters. It turns out that the envelope curve $K_{sup}(\psi)$ behaves like a power law rather than an exponential function, that is it decreases less steeply as suction increases. Note that K_{sup} is a scalar quantity which does not distinguish vertical and horizontal flow. It could be used, however, as an alternative to directional effective conductivities for predictions of contaminant transport. In the special case $\rho=1$, there exists an exact deterministic upper bound to the random set of conductivity curves. The highest density point on the upper-bound conductivity curve occurs at the same critical suction that maximizes the density of crossing points.

Finally, in the more general case of imperfect correlation, $0 \leq \rho \leq 1$, there is no longer an exact upper-bound conductivity curve, except asymptotically as $\rho \rightarrow 1$. Nonetheless, if the correlation is significant, an approximate or fuzzy upper bound exists in some statistical sense. The general expression of the fuzzy upper-bound conductivity curve, or upper-envelope curve, is given by:

$$K_{\sup}(\psi) \approx K_G \exp\left\{-\frac{\sigma_F}{\rho\sigma_A}\right\} \left\{\frac{1}{\psi} \cdot \frac{\sigma_F}{\rho\sigma_A}\right\}^{\frac{\sigma_F}{\rho\sigma_A}} \tag{3-24}$$

where K_G is the geometric mean of conductivity. This expression reduces to the crisp curve in the case of perfect cross-correlation, as it should. Note again that the upper-envelope conductivity-suction curve is a power law, in contrast with the postulated exponential form of the local conductivity-suction curves. The crispness of the upper envelope degrades as the coefficient of correlation decreases from $\rho=+1$ to $\rho=0$.

An analytical model proposed by Ababou (1990, 1993) gives the components of a macro-scale conductivity tensor in terms of the micro-scale conductivity field $K(x_1, x_2, x_3)$, under certain conditions of randomness, statistical homogeneity, and statistical anisotropy. The proposed relation is empirical, although specialized forms of it are confirmed by other, more fundamental results, including: (i) exact bounds, (ii) exact solutions in special cases involving lower dimensionality, statistical isotropy, symmetric distributions, and binary distributions, and (iii) approximate analytical solutions based on linearization and/or perturbation of the governing equations.

Underlying this model is the assumption that spatial variability can be represented by a random function of space. Imperfectly stratified and anisotropic structures are described by means of directional fluctuation scales or correlation scales, while other features such as degree of variability, bimodality, etc., are conveyed by a probability distribution. The dimensionality of the flow system is also an important factor; therefore, the general case of a D-dimensional flow system will be considered ($D=1$, 2, or 3). The proposed model, then, postulates that effective conductivity is a second rank symmetric tensor and expresses the principal components of this tensor by means of a power-average operator:

$$\hat{K}_{ii} = \langle K^{p_i} \rangle^{1/p_i} \quad (i = 1, \ldots, D) \tag{3-25}$$

where the angular brackets $\langle\,\rangle$ designate the operation of averaging. In this equation, the p_i values are directional averaging exponents. They are expressed in terms of the directional correlation lengths l_i, as follows:

$$p_i = 1 - \frac{2}{D}\frac{l_H}{l_i} \quad (i = 1, \ldots, D) \tag{3-26}$$

where l_H is the D-dimensional harmonic mean fluctuation scale:

$$l_{\mathrm{H}} = \left[\frac{1}{D}\sum_{i=1}^{i=D} l_i^{-1}\right]^{-1} \tag{3-27}$$

Note that the averaging exponents are constrained to lie within the interval $[-1, +1]$, and that they sum to D-2. The above equations give an analytical relation for the D-dimensional effective conductivity tensor in terms of the single-point probability distribution, the principal directions, and the directional fluctuation scales of the micro-scale log-conductivity field. Note that the micro-scale data required for this implementation are all of a statistical nature. For technical reasons, the statistics of log-conductivity rather than conductivity are preferred.

The power-average effective conductivity tensor can be expressed in closed form for several common types of log-conductivity distributions, such as Gaussian and binary. In the case of a Gaussian medium with normally distributed ln K, applying the equations given above leads to:

$$\hat{K}_{ii} = K_G \exp\left\{\frac{\sigma_Y^2}{2}\left[1 - \frac{2}{D}\frac{l_H}{l_i}\right]\right\} \quad (i = 1, \ldots, D) \tag{3-28}$$

where σ_Y^2 is the ln K variance, and K_G is the geometric mean conductivity. This relation was initially developed by Ababou (1988) in the equivalent form:

$$\hat{K}_{ii} = (K_A)^{\alpha_i}(K_H)^{1-\alpha_i} \quad (i = 1, \ldots, D) \tag{3-29}$$

where $\alpha_i = (D - l_H/l_i)/D$, and K_A and K_H represent the arithmetic and harmonic mean conductivities, respectively.

Another case of interest is that of a binary medium comprising conductive phases α and β, present in the proportions (V) and ($1-V$), respectively. For instance, phase α could be a sandstone matrix, and phase β might be a set of shale lenses or shale clast inclusions (Desbarats, 1987; Bachu and Cuthiell, 1990). The conductivity distribution of such a composite medium is of the form:

$$\begin{aligned} \text{Prob}\left\{K(x_1, x_2, x_3) = K_\alpha\right\} &= V \\ \text{Prob}\left\{K(x_1, x_2, x_3) = K_\beta\right\} &= 1 - V \end{aligned} \tag{3-30}$$

As before, it is assumed, as a first approximation, that the spatial anisotropy of the random structure can be defined with three fluctuation scales l_1, l_2, l_3. Then the equation for the binary distribution becomes:

$$\hat{K}_{ii} = \left\{VK_\alpha^{p_i} + (1 - V)K_\beta^{p_i}\right\}^{1/p_i} \quad (i = 1, \ldots, D) \tag{3-31}$$

with averaging powers (p_i) given previously. In the case of a 3D isotropic binary medium, let $D=3$, and $l_1 = l_2 = l_3$. This yields $p_i = 1/3 (i=1,2,3,)$. In the case of a 2D isotropic binary medium, let $l_1 = l_2$ for horizontal isotropy, and $D=2$ for restriction to 2D space, or equivalently $D=3$ with $l_3 \to +\infty$ for 2D horizontal flow through a vertically homogeneous medium. Either case yields $p_i \to 0$ for $i=1$ and 2. Inserting the equation above and using Taylor series expansions leads to:

$$\hat{K}_{ii} = (K_\alpha)^V (K_\beta)^{1-V} \quad (i = 1, 2) \tag{3-32}$$

where ρ represents the concentration of phase α and $1-\rho$ is the concentration of phase β. In another effort, Berkowitz and Clemo (1992) showed that effective parameter laws concerning medium connectivity, especially with regard to fractured formations, can be applied and, therefore, power-law relationships can characterize properties of disordered media.

Perturbation techniques were applied by Gelhar and Axness (1983) to determine the effective permeability in porous media with statistically anisotropic permeability fields and small permeability variances. Similar yet more sophisticated efforts are the effective unsaturated conductivity models proposed by Yeh et al. (1985 a,b,c), Mantoglou and Gelhar (1987), and Ababou and Yeh (1992). They all share the following features:

- They are based on a statistical continuum representation of the heterogeneous porous medium (without explicit fracturing so far)
- They can be expressed in closed form in some cases, and the most tractable results are obtained when the local conductivity is an exponential function of pressure (Gardner model)
- They can incorporate cross-correlations that are known to occur among material properties, particularly between saturated conductivity and other parameters indicative of pore size distribution, such as capillary length scale and moisture dispersivity, the latter being a length scale equal to the inverse slope of the log-conductivity curve
- They can incorporate the anisotropic structure of the medium in such a way that the resulting conductivity has an anisotropy ratio that is pressure-dependent

The Mantoglou-Gelhar and Yeh (MGY) work reduces to specializations of essentially one unique effective model. This model is based on solutions of linearized and perturbed unsaturated flow equations and on ensemble averaging for defining the effective conductivity. Ababou and Yeh (1992) has proposed a model based directly on a more general kind of ensemble averaging, namely power averaging of the local conductivity curves. It yields closed-form results analogous, but not identical, to the MGY model. The behavior of the conductivity anisotropy ratios given by the MGY and the proposed models are identical in certain cases. While this model is not restricted to exponential (Gardner) curves for local conductivity $K(h,x)$, the results are simpler with this assumption. A method for extending the results from the Gardner curves to any other type of $K(h,x)$ curve will be given later where $\psi=-h$ equals suction head. Briefly, the model can be expressed as follows in the case of unimodal (lognormal) statistical parameters:

$$K_{p_i}(\Psi) = K_G \exp\left[\frac{1}{2}\left(A_i\Psi^2 + B_i\Psi + C_i\right)\right] \tag{3-33}$$

$$\Psi = \alpha_G\psi$$

The values for A_i, B_i, and C_i are given by:

$$A_i = p_i \alpha_G^2 \sigma_a^2$$

$$B_i = -2\alpha_G(1 + p_i \rho \sigma_a \sigma_f) \tag{3-34}$$

$$C_i = p_i \sigma_f^2$$

Here, p_i is the power of averaging for direction X_i; Ψ is a dimensionless suction head; α_G is the geometric mean of $\alpha(x)$, the slope of log-conductivity $\left[\partial \ln K(h,x)/\partial h\right]$; σ_a is the standard deviation of $a(x) = \ln\alpha(x)$; σ_f is the standard deviation of $f(x) = \ln K_s(x)$, the logarithm of saturated conductivity; and ρ is the correlation coefficient between random fields $a(x)$ and $f(x)$.

The MGY model is of the same form as Eq. (3-33), but with different expressions for the coefficients A_i, B_i, and C_i. The expressions for the $\hat{K}_{xx}(\Psi)$ and $\hat{K}_{zz}(\Psi)$ can be given by:

$$\hat{K}_{xx}(\Psi) = K_G \exp\left[\frac{1}{2}\left(A_x \Psi^2 + B_x \Psi + C_x\right)\right]$$

$$\hat{K}_{zz}(\Psi) = K_G \exp\left[\frac{1}{2}\left(A_z \Psi^2 + B_z \Psi + C_z\right)\right] \tag{3-35}$$

where $A_x = \dfrac{\alpha_G^2 \sigma_\alpha^2}{1+\alpha_G\lambda}$, $B_x = -2\alpha_G\left[1 + \dfrac{\rho\sigma_a\sigma_f}{1+\alpha_G\lambda} + \sigma_a^2 \dfrac{\alpha_G\lambda}{1+\alpha_G\lambda}\right]$, $C_x = \dfrac{\sigma_f^2 + 2\rho\sigma_a\sigma_f\alpha_G\lambda}{1+\alpha_G\lambda}$, $A_z = -A_x$, $B_z = -(B_x + 4\alpha_G)$, and $C_z = -C_x$.

Equating K_p and $\hat{K}_{xx}$ or K_p and $\hat{K}_{zz}$ term by term gives, respectively, the values of p that would make the coefficients of the two approaches coincide. As will be seen, it is not always possible to make all the coefficients coincide (quadratic plus linear plus constant terms). Cases for which the stochastic perturbation approach yields power-averages for $\hat{K}_{xx}$ and $\hat{K}_{zz}$ are identified in Table 3-1. For $\rho = 0$, the identification of the two approaches leads to the equivalences presented in Table 3-2.

Comparisons of predicted effective conductivities with direct numerical simulations do not clearly give the advantage to one or the other model; this provisional conclusion is based on work done in Ababou and Yeh (1992). However, their model appears more flexible in two respects:

- It admits free parameters that can be adjusted empirically
- It may be extended to handle explicitly fractured media

The free parameters of this model correspond to the exponent, or averaging power p_i, which can be different horizontally and vertically. For a horizontally stratified medium, assuming $p_x = +1$ horizontally and $p_z = -1$ vertically, the model yields arithmetic and harmonic means of nonlinear $K(h,x)$ curves.

Table 3-1. Equivalence between the stochastic perturbation and power average approaches ($\rho \neq 0$)

$\rho \neq 0$	$\hat{K}_{xx}$	$\hat{K}_{zz}$
A	$p_x = \dfrac{1}{1+\alpha_G\lambda}$	$p_z = -p_x$
B	$p_x = \dfrac{1}{1+\alpha_G\lambda}\left[1+\dfrac{\sigma_a}{\rho\sigma_f}\alpha_G\lambda\right]$	$p_z = -p_x$
C	$p_x = \dfrac{1}{1+\alpha_G\lambda}\left[1+2\dfrac{\rho\sigma_a}{\sigma_f}\alpha_G\lambda\right]$	$p_z = -p_x$

Table 3-2. Equivalence between the stochastic perturbation and power average approaches ($\rho = 0$)

$\rho = 0$	$\hat{K}_{xx}$	$\hat{K}_{zz}$
A	$p_x = \dfrac{1}{1+\alpha_G\lambda}$	$p_z = -p_x$
B	$p_x \to +\infty$ or $\sigma_a^2 \dfrac{\alpha_G\lambda}{1+\alpha_G\lambda} \to 0$ and $\lvert p_x \rvert < \infty$ arbitrary	$p_z \to -\infty$ or $\sigma_a^2 \dfrac{\alpha_G\lambda}{1+\alpha_G\lambda} \to 0$ and $\lvert p_z \rvert < \infty$ arbitrary
C	$p_x = \dfrac{1}{1+\alpha_G\lambda}$	$p_z = -p_x$

The model by Ababou and Yeh (1992) may be extended to also treat, more explicitly, the case of fractured media. This extension is possible because it is semi-empirical and, unlike the MGY model, does not require analytical treatment of complicated flow equations. In that respect, the Ababou model can be made to resemble the familiar effective continuum approximation of Pruess et al. (1990a,b). The model by Pruess et al. is totally empirical and gives an isotropic double-humped conductivity curve for a matrix-fracture composite. This model has been criticized for its inability to represent anisotropic behavior, particularly pressure-dependent anisotropy. Indeed, the anisotropic behavior of flow may be

highly pressure-dependent and therefore moisture-dependent, as unsaturated flow can potentially switch from horizontal paths (matrix strata) to vertical paths (fractures) (Ababou, 1991).

One way to explicitly account for the influence of fractures in this model may be to introduce a bimodal (binary) distribution rather than lognormal distributions and to develop the consequences in terms of effective conductivity. The result should account for fracture-induced anisotropy, as well as porous matrix anisotropy. A rather simplified way of picturing the expected result is as follows: provided the fractures and strata are both more or less aligned with the same coordinate system X_i, there should be two different double-humped directional conductivity curves, one for X_1 (horizontal) and the other for X_2 (vertical). This model would, therefore, share some features in common with the less realistic Pruess et al. (1990a,b) model.

Finally, the following extension is proposed here for the case where local conductivity curves $K(h,x)$ do not follow the exponential Gardner model. For any fixed point in space, assume that the conductivity curve is given by an arbitrary function denoted $K(\psi)$. Let:

$$\alpha(\psi) = -\frac{\partial \ln K(\psi)}{\partial \psi}$$

$$K_0(\psi) = K_s \exp\left\{ -\int_0^{\psi} \left[\alpha(\phi) - \alpha(\psi)\right] d\phi \right\} \tag{3-36}$$

Thus, any function $K(\psi)$ can be expressed as:

$$K(\psi) = K_0(\psi)\exp\left[-\alpha(\psi)\psi\right] \tag{3-37}$$

If $K_0(\psi)$ and $\alpha(\psi)$ are smooth and slowly varying functions of ψ, relations obtained using the Gardner conductivity function can be extrapolated to the desired $K(\psi)$ function by holding constant the suction-dependent K_0 and α when computing statistical quantities. Thus, in the present and MGY models, let K_G become $K_G(\psi)$, α_G become $\alpha_G(\psi)$, etc. Possible candidates to implement this idea are the Brooks-Corey conductivity curve and the Mualem-van Genuchten conductivity curve, among others.

4 SEMI-ANALYTICAL PREDICTION OF EFFECTIVE HYDRAULIC PROPERTIES WITH THE REAL SPACE RENORMALIZATION GROUP METHOD

Scaling effects arise when the scale of measurements differs from the scale of application. Scale effects arise as the relative importance of different flow and transport processes shifts where the scale of analysis changes. As Tidwell et al. (1993) pointed out, scaling models are designed to provide a means of transforming heterogeneous small-scale data to a larger scale in terms of effective properties, while preserving the signature of small-scale flow and transport processes and media heterogeneity. An effective hydraulic conductivity is a conductivity that preserves the fluid flux-potential gradient quotient between a heterogeneous block and an equivalent (same geometry and fluid viscosity) homogeneous block (Kasap and Lake, 1990). The scaling (averaging) process for moving from a smaller scale to a larger scale is particularly complicated for properties such as saturated and unsaturated conductivities that are nonadditive. A discussion of various techniques for the calculation of effective properties was presented in Chapter 3.

David et al. (1990) and Wang (1991) pointed out that systems with nearly narrow distributions can be treated with the effective medium approximation, whereas systems with broad distributions must be treated with different types of analysis. In this chapter we present, in more detail, a semi-analytical method for the calculation of effective properties, namely the RSRG method. The RSRG method works equally well for any fraction of the dispersed phase (e.g., fractures), especially near the percolation threshold, defined as the minimum volume fraction of the conducting component at which a conductor/nonconductor binary mixture allows conduction. Owing to the sharp contrast in the fracture and matrix hydraulic conductivity, percolation-type behavior is expected in an unsaturated fracture/matrix system.

Various aspects of the percolation theory have been extensively reviewed by Kirkpatrick (1973) and Ferrand et al. (1990). In the percolation problem, a binary conductor-nonconductor system is considered, usually on a lattice in which either bonds (or sites) are occupied (conductors) or are vacant (insulators). The objective of a percolation problem is to study the size distribution of clusters of connected bonds or sites (cluster size distribution), and the probability that the flow injected at one arbitrary site finds an infinite conducting pathway (percolation probability). Three kinds of percolation problems have been studied: site percolation, bond percolation, and site-bond percolation. In the pure site percolation problem, the conductors are randomly distributed on sites of a lattice. In the bond percolation problem, the vertices are all occupied by the particles and the bonds may be present or absent. In the site-bond percolation problem, the vertices may or may not be occupied and also the bonds may or may not be present.

In a percolation problem, the local permeability has one of two values: 1 with probability p and 0 with probability $(1-p)$ or vice versa (Chandler et al., 1982). The average macroscopic permeability varies as p decreases from 1 to 0. The permeability of the macroscopic system vanishes well before p reaches 0 if the microscopic permeability distribution is isotropic. The percolation-conduction problem is of interest because the majority of the methods discussed here were first implemented for such problems before being extended to determine effective properties for a distribution of conductances. Moreover, the behavior of the field near the percolation threshold proves to be an extreme test for any new method. Percolation-theory-based approaches are well explored either for fully random systems or for systems with very small correlation lengths.

For the fluid flow problem, the porous medium can be discretized into smaller units to adequately describe the microscopic structural details. Various rock conductivities can be represented as components in the resistor network according to their locations and conductances, where all resistors conduct to a lesser or greater degree. In a typical arrangement, the centers of various units can be put at the nodes and the communication between different units can be represented by resistors or conductors. Jerauld and Salter (1990) have pointed out that as long as the average coordination number of the disordered network is the same as the average coordination number of the continuum under consideration, for all practical purposes the two systems are indistinguishable from each other. The following is a brief description of the background of the RSRG method and its implementation in its simplest form.

4.1 REAL SPACE RENORMALIZATION GROUP METHOD

The RG method (Wilson and Kogut, 1974) is a statistical mechanics approach originally developed to study the phase transition behavior of fluids near a critical point. This method involves a recursive scale transformation process in which, while going from the smallest to the largest length scale, the small-scale fluctuations are integrated and only the important features that contribute to the macroscopic behavior are preserved. This method is suitable for dealing with any problem in which complex microscopic effects underlie macroscopic properties (i.e., a problem that involves many length scales). The method has largely been applied in the past to study the Ising problems in magnetic systems (Wilson and Kogut, 1974).

The transformation of conductance distributions on a lattice was proposed by Stinchcombe and Watson (1974) to determine the conductivity exponent for a percolation conduction problem. This transformation uses a method of decimation to map a given lattice to another. To carry out a length rescaling, the lattice can be partitioned into cells with conducting and nonconducting blocks. The size of the cell b is called the spatial rescaling factor and is measured in the units of a lattice characteristic length. The lattice consists of conductors with conductivity k chosen from a distribution $\tilde{P}_n(k)$, and the renormalization transformation W maps this distribution to another lattice on which the conductors are distributed in accordance with a new conductance distribution $\tilde{P}_{n+1}(k)$ given by:

$$\tilde{P}_{n+1}(k) = W\{\tilde{P}_n(k)\} \tag{4-1}$$

where

$$\begin{aligned} W\{\tilde{P}_n(k)\} = \int & \tilde{P}_n(k_1)\tilde{P}_n(k_2)\tilde{P}_n(k_3) \ldots \tilde{P}_n(k_N) \\ \times\ & \delta\left[k - g(k_1, k_2, k_3, \ldots k_N)\right] dk_1 dk_2 dk_3 \ldots dk_N \end{aligned} \tag{4-2}$$

where δ is the Dirac function. By $g(k_1,\ldots.k_N)$ we denote the normalized equivalent conductivity of a cell constructed on the lattice with N conductors and nonconductors, n is the recursion step, and $k_1, k_2, \ldots, k_N$ are individual conductivities of the bonds/sites in the lattice. The distribution $\tilde{P}_{n+1}(k)$ is a narrower distribution since the fluctuations in conductivity values that occur at length scales smaller

than the lattice spacing are integrated out. At each step, the number of blocks is reduced by b^D in a D-dimensional lattice. In the spirit of the RG theory, if this process of scale transformation is continued recursively, we converge to the effective conductivity of the lattice, given by:

$$\tilde{P}_{\infty}(k) = \delta(k - \hat{k}) \tag{4-3}$$

A transformation of a distribution of conductances on a 2D lattice of spacing l results in a distribution of conductances of spacing $2l$. The simplest possible transformation corresponds to the case of infinite boundaries in one direction and impermeable boundaries in the other, and combines the four conductances (k_1, k_2, k_3, k_4) in a 2×2 renormalization cell into an effective conductivity in the renormalized lattice by connecting nearest neighbors in the direction of the infinite boundaries. Such a renormalization is of interest when the effective conductivity is for the direction of the infinite boundaries, and is represented by:

$$\begin{aligned}\tilde{P}_{n+1}(k) &= \int \tilde{P}_n(k_1)\tilde{P}_n(k_2)\tilde{P}_n(k_3)\tilde{P}_n(k_4) \\ &\times \delta\left[k - \left[\frac{k_1 k_2}{k_1 + k_2} + \frac{k_3 k_4}{k_3 + k_4}\right]\right] dk_1\, dk_2\, dk_3\, dk_4\end{aligned} \tag{4-4}$$

For the percolation conduction problem, the transformation of the previous equation can be represented by:

$$\tilde{P}_{n+1}(k) = (1 - p_{n+1})\delta(k - 0) + p_{n+1}\delta(k - k^{n+1}) \tag{4-5}$$

When both components of the random binary system are conducting, the above equation is written as:

$$\tilde{P}_{n+1}(k) = (1 - p_{n+1})\delta\left(k - k_1^{n+1}\right) + p_{n+1}\delta\left(k - k_2^{n+1}\right) \tag{4-6}$$

To obtain the terms p_{n+1} in the above equation, the closed form solution (Bernasconi, 1978) for random, uncorrelated lattices is applied. This solution is obtained from the probabilities for the cell configuration and their degeneracy, and is given by:

$$p_{n+1} = \sum_{i=1}^{M} f_i q_i(p_n) \tag{4-7}$$

For a 2D random uncorrelated system, p_{n+1} is obtained by summing up the product of the probability of occurrence of conducting configurations (p_i) with their degeneracy, according to:

$$p_{n+1} = \sum_{i=1}^{M} f_i\, q_i(p_n) = p_n^4 + 4p_n^3(1 - p_n) + 2p_n^2(1 - p_n)^2 \tag{4-8}$$

where f_i is assigned a value of 0 for nonconducting configurations and a value of 1 for conducting configurations. The right-hand side of the equation above is the sum of all possible cell configurations for b=2 that allow conduction. For example, p^4 is the probability that all four sites are occupied by

conductors, whereas $p^3(1-p)$ is the probability of occurrence for a configuration consisting of three conductors. For two conductors and two nonconductors, there are six possible configurations, of which two conduct and four (where conductors are located diagonally or vertically) do not conduct. Table 4-1 shows all possible configurations and their effective conductivities. The table assumes that the infinite boundaries are to the left and right of the grid blocks. For correlated systems, whether isotropic or anisotropic, the method assures statistical homogeneity for a given correlation length. A detailed description of the theoretical background and a multitude of application results can be found in the work by Mohanty (1993).

Table 4-1. Possible configurations of conductivity for a binary system and associated effective conductivity

Possible Configuration	Probability	Combinations	Effective Conductivity
$\begin{array}{\|c\|c\|}\hline k_1 & k_1 \\ \hline k_1 & k_1 \\ \hline\end{array}$	$(1-p_n)^4$	1	k_1
$\begin{array}{\|c\|c\|}\hline k_2 & k_1 \\ \hline k_1 & k_1 \\ \hline\end{array}$	$p_n(1-p_n)^3$	4	$\frac{k_1 k_2}{k_1+k_2} + \frac{k_1}{2}$
$\begin{array}{\|c\|c\|}\hline k_2 & k_1 \\ \hline k_1 & k_2 \\ \hline\end{array}$	$p_n^2(1-p_n)^2$	4	$\frac{2k_1\ k_2}{k_1+k_2}$
$\begin{array}{\|c\|c\|}\hline k_2 & k_2 \\ \hline k_1 & k_1 \\ \hline\end{array}$	$p_n^2(1-p_n)^2$	2	$\frac{k_1+k_2}{2}$
$\begin{array}{\|c\|c\|}\hline k_2 & k_2 \\ \hline k_2 & k_1 \\ \hline\end{array}$	$p_n^3(1-p_n)$	4	$\frac{k_1 k_2}{k_1+k_2} + \frac{k_2}{2}$
$\begin{array}{\|c\|c\|}\hline k_2 & k_2 \\ \hline k_2 & k_2 \\ \hline\end{array}$	p_n^4	1	k_2

The RG theory has been formulated in Fourier space and in real space. In the Fourier space method, the Fourier transform of the partition function or the probability distribution function is manipulated. Its implementation in real space is referred to as the RSRG method. RSRG methods are of

greater practical importance, and the method is intuitively appealing because of its geometric description on a lattice, which provides a direct analogy to a network model of conduction. The first application of the RSRG formalism to percolation problems was given by Young and Stinchcombe (1975). In a binary site percolation problem, the sites/nodes are considered to be occupied by a conductor/nonconductor binary mixture. The correlation length of the dispersed phase (i.e., fractures) is the first moment of the cluster size distribution. As the system approaches the percolation threshold, the correlation length tends to infinity. This implies that infinite or sample-spanning clusters are formed. The renormalization transformation is directly applied to the probability distribution of sites (nodes) or bonds (conductive links between the nodes). Application of the method to a system in which both phases are conducting is a logical extension of the conductor-insulator problem. The percolative behavior can still be observed, primarily because of the sharp contrast in the hydraulic conductivity of fracture and matrix cells. There is nothing in the method itself that prevents it from being applied to a system in which two or more phases are conducting. Mohanty and Sharma (1990) extended this approach to calculate effective properties of as many as four components. Amaziane et al. (1990) conducted similar studies for diphasic flow in heterogeneous media. Bernasconi (1978) implemented the RSRG approach using a bond disordered conductance distribution on a square lattice, and a simple cubic lattice with a binary distribution of conductances. He applied the theory only to conductor-insulator systems. As evident from the previous discussion, the RG has primarily been applied to fully random systems or to site percolation problems posed as a correlated bond percolation problem. Several applications have also been reported on anisotropic bond percolation problems.

Mohanty and Sharma (1991) developed a cluster-counting method for correlated isotropic and anisotropic systems that honors the true spirit of the RG formalism in keeping the nature of the conductance distribution invariant through the recursion steps. They used the explicit cluster-counting method to calculate degeneracy, which is necessary for implementing the recursion relation. Although their implementation minimized the finite lattice size effects, the method was more suitable for an ensemble of realizations rather than determining the conductivity of a given field. A much simpler and quicker alternative to the above method is to simply ignore the effects due to finite lattice size and to recursively calculate the average property. An average property is calculated for each cell. The process is repeated until only a single site/bond is obtained. This method is referred to as Simple Recursive Spatial Averaging (SRSA). No renormalization transform is required, no new lattice needs to be generated, and the number of cells is reduced by a factor of b^D at each step in the recursion until only one conductance remains. The SRSA method can provide incorrect answers because it attempts to apply a statistical method (such as RSRG) in an absolute sense to lattices with fixed geometry. For large enough lattices, this problem will be minimized because of some degree of statistical variation provided in the lattice itself. This, however, suggests that the results of the SRSA method will depend on the lattice size. How large the lattice needs to be depends on the correlation length.

In the proposed method, the SRSA recursion is continued until the probability of occurrence of conductors approaches one of the fixed points. That it takes so many recursion steps to converge is not apparent from the SRSA procedure, and this method has been used in the past by various investigators (King, 1989; Aharony et al., 1991; Ahmed et al., 1991) without any reference to its accuracy near the percolation threshold. The SRSA approach was first used by Lobb et al. (1981) for anisotropic conduction problems. Instead of performing an averaging of the cell conductivities with the purpose of regaining the original nature of the distribution function, they left the renormalized cells as such. This in fact allowed the use of any conductance distribution. Aharony et al. (1991) have pointed out that in the SRSA method, the finite size dependence, broad distributions, large anisotropies and strong correlations, as well as the

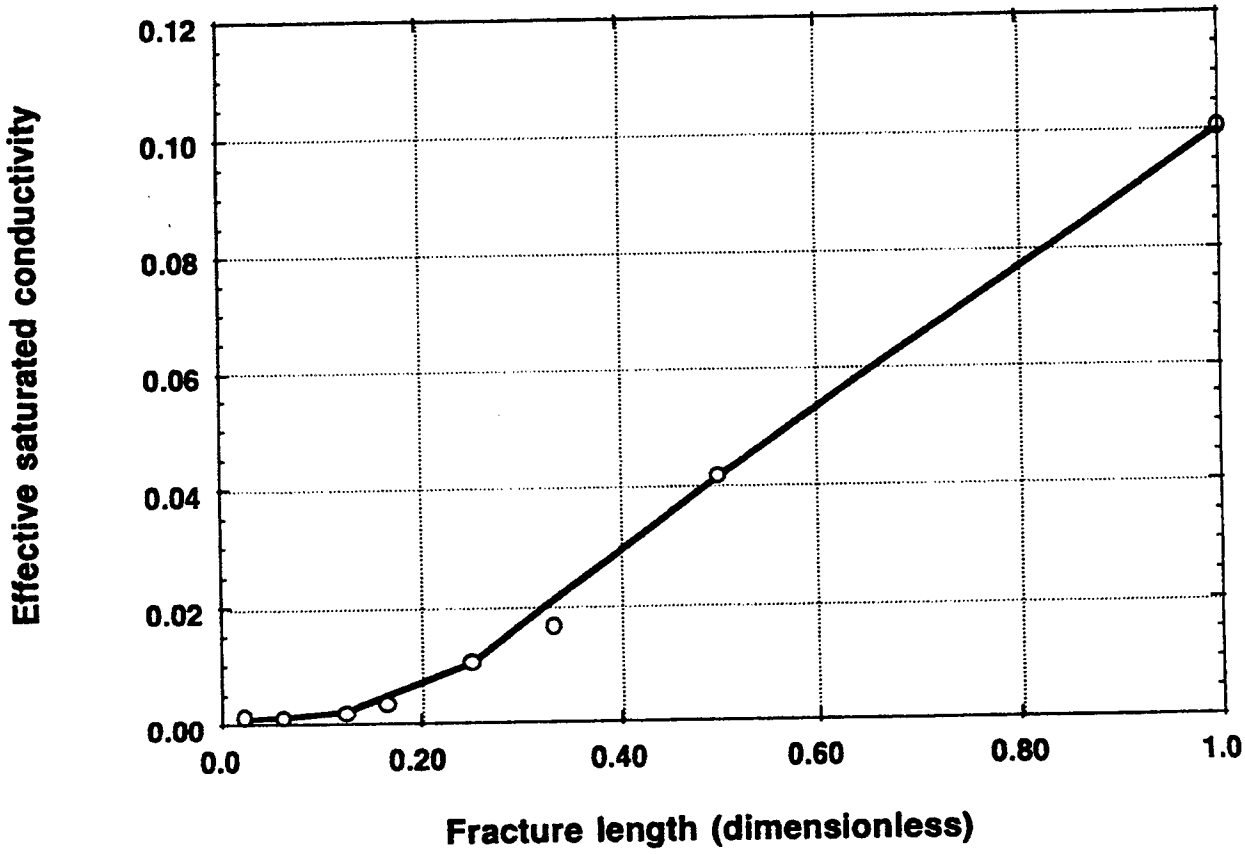

Figure 4-1. Effect of fracture length on the effective saturated conductivity of a 2D fracture network

question of self-averaging in such a system, should be addressed. Figure 4-1 demonstrates the percolation-like behavior of a fracture network system similar to the one shown in Figure 2-21. In Figure 4-1, the effective saturated conductivity is presented as a function of the fracture length for a saturated conductivity contrast of 1,000. It can be seen that as the fracture lengths increase, their connectivity increases and, therefore, beyond a certain value of fracture length a linear behavior is observed.

The limitation of this method lies in the fact that, in some cases, an artificially created connectivity between disconnected conductors will lead to an overestimation of the conductivity. Independent of exactly how the RSRG method is implemented, the following assumptions must hold: (i) the field is of infinite extent, (ii) steady-state conditions have been established, and (iii) the transformation keeps the random conductance field invariant. Comparison between the above two methods using isotropically and anisotropically correlated fields can be found in Mohanty (1993). The two methods give similar results away from the percolation threshold. The above methods are expected to give poor results when the fractures are oriented at an angle to the global flow and also when many of the conductivities in one direction are set equal to zero, which is reflected through large relative errors when the effective conductivity in that direction is small.

4.2 DETERMINING EFFECTIVE HYDRAULIC CONDUCTIVITY WITH THE REAL SPACE RENORMALIZATION GROUP METHOD

To obtain effective unsaturated conductivities, a numerical flow experiment is conducted in a heterogeneous medium and the flow rate and the pressure gradients at any cross-section are averaged to obtain the effective relative conductivity for each phase. The primary issue in the steady-state analysis of heterogeneous media is the determination of the saturation distribution. For relatively small capillary number flows, that is viscous forces $\ll$ capillary forces, capillary pressure will dictate the distribution of the fluids involved. The capillary number is defined as the ratio between viscous and capillary forces. Indeed, if no flow occurs, the pressure in the wetting component and the nonwetting component will be constant everywhere, and the difference will be controlled entirely by the capillarity. For such a case, the effective unsaturated conductivity will be a strong function of the structure of the permeability distribution.

The fractured porous medium, whether it is considered as a composite porosity or effective continuum (Peters and Klavetter, 1988; Pruess et al., 1990b), is characterized by saturation and permeability functions. The properties of the composites are represented by an arithmetic average of the fracture property and matrix property. This sort of averaging mimics a physical condition as if the flow in the fracture is parallel to the flow in the matrix. The study of Rasmussen et al. (1989) indicated that harmonic and geometric means would also be appropriate averaging methods, depending on the fracture orientation. Clearly, there is a need for a method that is robust enough for representing the composite properties for a broad range of fracture properties (such as distribution and orientation), yet at the same time maintaining some vital efficiency characteristics, such as high computational speed and low computer memory requirements. A particularly simple implementation of the RSRG concept has been to recursively calculate the average property (Mohanty and Sharma, 1991; Lobb et al., 1981; King, 1989). In this approach, a lattice, preferably a square lattice in 2D or a cubic lattice in 3D, is overlain on the given heterogeneous field. Each node on the lattice of a binary system represents either a matrix pixel or a fracture pixel. In reality, as the pixel size may be larger than the fracture width, an equivalent property is assigned to the fracture pixel, which is calculated by assuming that the fracture is surrounded by some matrix material that coexists in the same pixel as a portion of the fracture, according to the fracture conceptual model described in Section 1.2.5. Pruess and Tsang (1990) have made a similar assumption while studying the fracture pore space in terms of an aperture distribution. The crucial concept in their method is that all fracture properties can be approximated locally by a parallel-plate model (which invokes a form of an effective aperture approximation). Then, the whole lattice is subdivided into cells that contain a few matrix and/or fracture pixels. The average conductance of each cell is calculated by imposing a no-flow boundary condition in the transverse direction and a unit pressure gradient in the flow direction. If the heterogeneous field is anisotropic, one can interchange the boundary conditions and the flow direction to obtain the average conductivity in the transverse direction. This process of subdividing the lattice into cells and averaging the heterogeneities inside the cell is continued until only a single conductance block is obtained. The number of cells is reduced by a factor of 2^D (D is the dimensionality of the problem) at each step. This transformation process is depicted in schematic form in Figure 4-2. In this example, a cluster of cells transforms to a cell, a cell transforms to a conductance block, etc.

4.2.1 Assumptions

The following are the assumptions under which the proposed method is applicable: (i) a capillary-dominated flow regime exists; and (ii) for every change in the pressure, equilibrium is reached

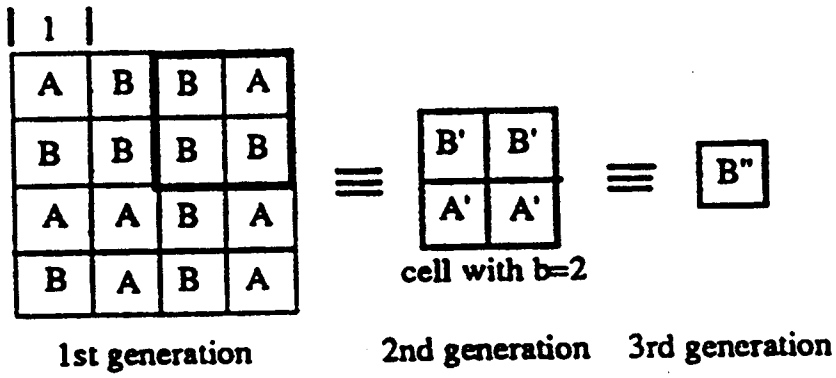

Figure 4-2. Schematic of RSRG transformation

instantaneously. Indeed, the first assumption is justified by the findings of Zimmerman and Bodvarsson (1992). Based on the sorptive length concept, these researchers showed that, for hydrological parameters believed to be similar to the Topopah Spring welded unit, one can assume that imbibition into the matrix is controlled by capillary forces. Wang and Narasimhan (1985) and Pruess et al. (1990a) have pointed out that when the matrix blocks are small, that is the formation is highly fractured, the pressure and temperature within the matrix block will quickly equilibrate with the surrounding fractures. The quick attainment of thermodynamic equilibrium eliminates the need to determine pressure separately in the matrix and in the fracture.

To implement the RSRG method, the following relationships can be used. The first is the saturation versus pressure head, represented by van Genuchten's moisture retention relation given by (van Genuchten, 1980):

$$\theta(h,x) = \theta_r(x) + \frac{\theta_s(x) - \theta_r(x)}{\left\{1 + \left[-\beta(x)\, h\right]^{n(x)}\right\}^{1-\frac{1}{n(x)}}} \qquad \text{if } h \le 0 \tag{4-9}$$

$$\theta(h,x) = \theta_s(x) \qquad \text{if } h \ge 0$$

where n is a dimensionless shape factor (a real number, not an integer), β is an inverse pressure head scale factor (L^{-1}), θ_s is the saturated water content, or effective porosity of the medium, and θ_r is the residual water content at very high or infinite negative pressure. Parameter θ_r is an empirical adjustment which should be taken equal to zero unless a better fit to experimental curves is obtained by using some nonzero value. The second is Gardner's unsaturated conductivity-pressure relation which is defined as:

$$K(h) = K_s \exp\left[\alpha(h - h_b)\right] \tag{4-10}$$

where $K(h)$ is the hydraulic conductivity at pressure head (h), K_s is the saturated conductivity, h_b is the air entry pressure head (bubbling pressure), and α is a scaling parameter.

4.2.2 Algorithm

The algorithm developed for determining effective unsaturated conductivity for a binary system is summarized as:

- Choose a water saturation value for the matrix
- Calculate the corresponding suction head in the matrix region, assume that suction heads in the matrix and fracture are at equilibrium, and calculate the fracture saturation corresponding to this suction
- Determine the corresponding unsaturated hydraulic conductivities with an appropriate model (e.g., Gardner or van Genuchten-Mualem)
- Apply the RSRG method to average the values for the binary system
- Assign weighted average saturation to the homogenized region.

Before implementing this algorithm, an equivalent saturated hydraulic conductivity must be assigned to the pixels representing the fractures. Here, several pixels may represent a single fracture. The equivalent saturated conductivity must be representative of the fracture roughness, disturbed matrix texture, and a portion of the surrounding undisturbed zone texture. Thus, the pixel need not be as small as the width of the aperture. The variation in aperture along the length of the fracture can be represented easily as a variable number of pixels corresponding to each fracture. However, in this work this was not attempted. The algorithm presented above is shown in diagrammatic form in Figure 4-3. More details can be found in the work of Mohanty and Bagtzoglou (1994). This algorithm has been enhanced with several scaling features that make it applicable to situations where the matrix is heterogeneous. This will be discussed in Chapter 6 of this report.

This approach is very similar to the one used in the work of Ferrand and Celia (1992) and Kueper and McWhorter (1992). For example, Ferrand and Celia simulated the drainage part of the pressure-saturation relation for a pore-scale network by starting at the saturation point and then incrementally increasing the capillary pressure. They concluded that the definition of an effective relationship between pressure and saturation in heterogeneous media is very much dependent on the structure of the material and drastically different than those which, for example, linear averaging would predict. Similarly, Kueper and McWhorter (1992) conducted analogous numerical experiments and increased the macroscopic capillary pressure in 100-KPa increments up to a maximum of 10,000 KPa.

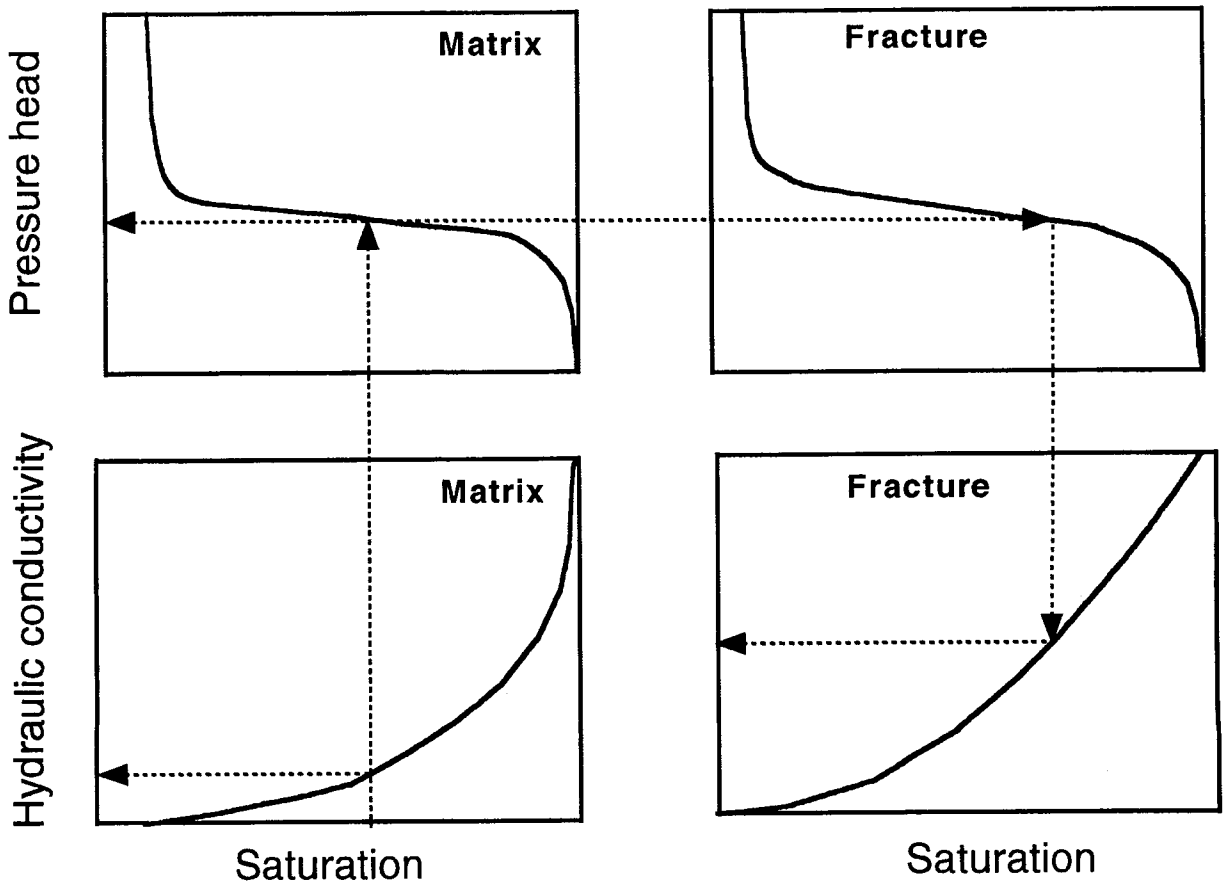

Figure 4-3. Schematic of algorithm for the determination of effective unsaturated conductivity

Their work is different in that they reversed the process, thereby obtaining the wetting curve behavior.

When a fracture-matrix binary system is used, for every matrix saturation a unique value of saturation can be determined for the fracture, as for every matrix saturation value there exists one and only one fracture saturation. However, for a distribution of matrix conductivities, this cannot be done as there is no unique value of pressure or saturation that characterizes the matrix. Therefore, two methods have been implemented. The first is method A, for which the saturation in each matrix block is evaluated at the specified pressure head in the fracture. The average of all the saturations in the matrix blocks is used to determine the matrix unsaturated conductivity. Then, the RSRG method is applied to obtain the effective hydraulic unsaturated conductivity of the matrix-fracture composite. The second is method B, for which the pressure head distribution is calculated for a specified saturation. Then, the average value of the pressure heads in the matrix is used to determine the unsaturated conductivity in the fracture before the RSRG is applied to determine the effective unsaturated conductivity of the matrix-fracture composite.

4.3 VERIFICATION RESULTS AND DISCUSSION

In the first part of this study, the effective saturated and unsaturated conductivities were obtained by using fully connected fracture networks. Figure 4-4 depicts a schematic representation of such a

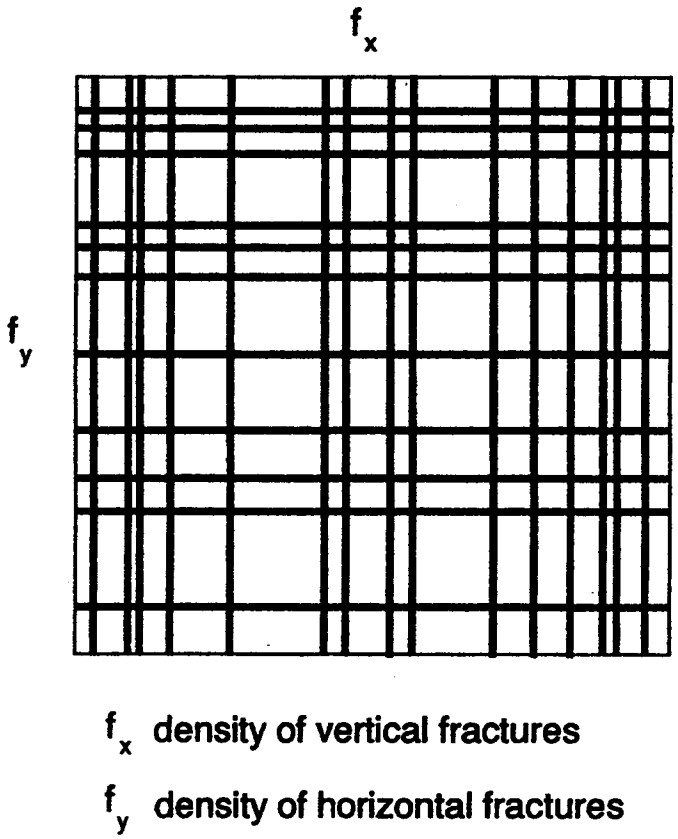

Figure 4-4. Schematic of a fully connected fracture network with anisotropic fracture density

network. The computational burden is not found to be significantly different for stochastically generated fracture networks. The execution times for saturated and unsaturated conductivities are presented in Tables 4-2 and 4-3, for direct numerical simulations and the RSRG method, respectively. Clearly, as the system size grows, the RSRG method becomes much faster than the numerical method.

The accuracy of the RSRG method was compared against the numerical solution by using a fully connected fracture network on a 64×64 grid with a fracture conductivity 1,000 times that of the matrix conductivity. Figure 4-5 depicts the dependence of the effective saturated conductivity on the horizontal or vertical fracture density for a network of fully connecting fractures. It also presents a comparison between the RSRG and direct numerical simulation results for a 2D system with a conductivity ratio between fracture and matrix equal to 1,000.The RSRG results are in excellent agreement (maximum error of 2 percent) with direct numerical simulation results in the case of saturated flow conditions and fully connecting fractures.

A slightly different verification of the RSRG approach is presented in Figure 4-6, where the semivariogram of saturated conductivity is calculated at four different steps through the recursive process. Note that the system possesses no spatial structure and, therefore, the variogram corresponds to a nugget effect. As the RSRG procedure advances from a 64×64, to a 16×16, to an 8×8 homogenized system, the variance (as this is inferred by the sill of the variogram) decreases rapidly, while the nature of the variogram does not change.

Table 4-2. Execution time comparison between numerical simulation and RSRG method for the determination of effective saturated conductivity. The calculation of the time ratio assumes that the Cray X-MP is about seven times faster than a SUN Sparc workstation.

Grid Size	Numerical (Cray X-MP)	RSRG (SUN Sparc)	Approximate Ratio
128×128	100 s	24 s	30
512×512	500 s	30 s	115

Table 4-3. Execution time comparison between numerical simulation and RSRG method for the determination of effective unsaturated conductivity. The calculation of the time ratio assumes that the Cray X-MP is about seven times faster than a SUN Sparc workstation.

Grid Size	Numerical (Cray X-MP)	RSRG (SUN Sparc)	Approximate Ratio
64×64	1,200 s	24 s	350
1,024×1,024	N/A	100 sec	N/A

Figure 4-7 shows comparisons between the RSRG results against direct numerical simulations with the BIGFLOW code (Ababou and Bagtzoglou, 1993) in the case of unsaturated flow conditions. In this figure two types of systems are analyzed: (i) a fracture system with a density anisotropy of two; and (ii) the same system but with the fracture and matrix pixels being fully randomized, that is no spatial correlation being present. In both cases the fractures are assumed to be homogeneous. The saturated hydraulic conductivity ratio between fracture and matrix is 1,000. The slope of the logarithm of unsaturated conductivity versus suction curve for the fractures is four times that of the matrix. A good match is obtained between the numerical and semianalytical results both at low and high suctions. One should also note that, for a relatively large range of the suction head (-110 to -77 cm), the effective unsaturated conductivity of a well-structured fractured system is identical to that of a fully random system. This observation suggests that under certain conditions (fracture volume fraction and suction head), a stochastic continuum approach may be appropriate for the study of flow in unsaturated fractured rock. Kwicklis and Healy (1993) have investigated two identical fracture networks which contained randomized apertures. The average fracture apertures were either all 125 μm, or all 25 μm, or a combination. They reached a similar conclusion in that they found that "representation of variably saturated fracture networks as an equivalent continuum may be more valid for some ranges in pressure head than others."

Figure 4-8 presents results very similar to Figure 4-7, with the exception that the ratio in saturated hydraulic conductivities is now 25. It can be seen that the match is not as great as in the case of a very sharp contrast in hydraulic properties. However, even in this case a relatively good match between the two methods is obtained at low suctions. It should also be noted that the direct simulation results, depicted in Figure 4-8, are suspected to not have been exactly at steady-state conditions, as was

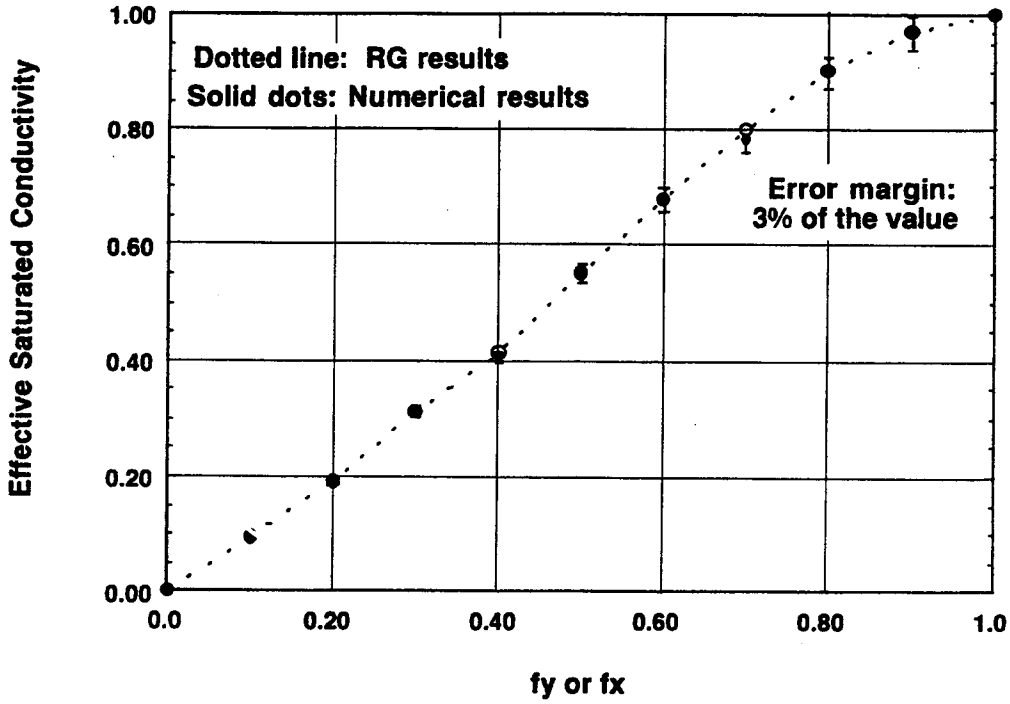

Figure 4-5. Comparison between RSRG and direct numerical simulation results for saturated flow in a network of fully connecting fractures

the case in Figure 4-7. Therefore, the deviations between the numerical and semianalytical results, especially at high suctions, may be explained.

Finally, Figure 4-9 depicts a comparison between RSRG results and BIGFLOW for a fracture network with orthogonal fractures of isotropic density and finite length. The fracture volume fraction for this network is 69 percent and, therefore, this exercise tests the RSRG capabilities for very high levels, most likely unrealistic, of fracturing. As can be seen in Figure 4-9, the match obtained is excellent. It should be noted that all the verification results presented in this chapter correspond to binary matrix-fracture systems, that is the matrix field is homogeneous. Results for the case of heterogeneous matrix fields will be presented in Chapter 6 of this report.

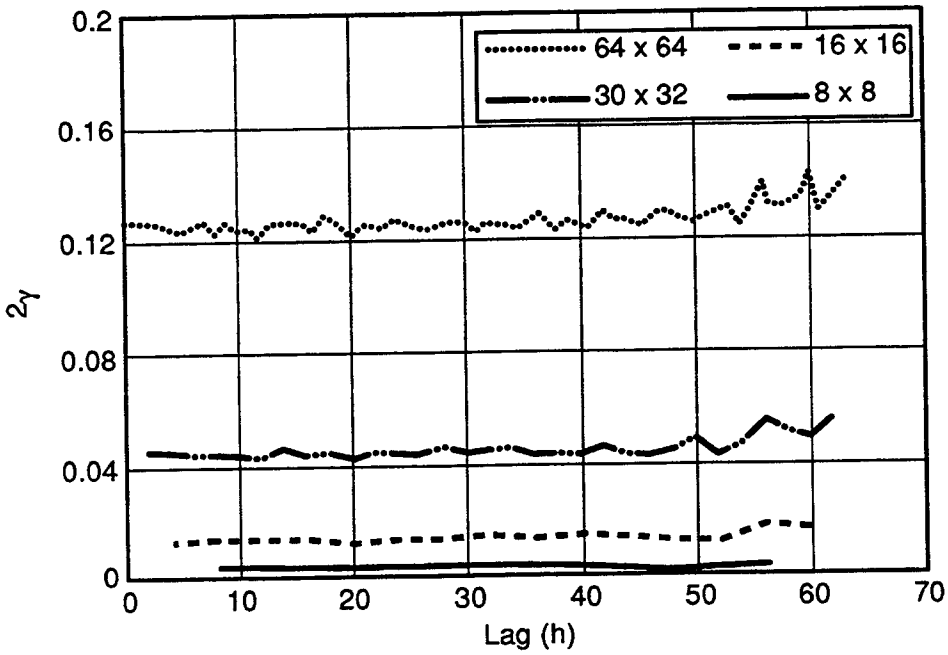

Figure 4-6. Semi-variogram of uncorrelated saturated conductivity at successive steps of the real space renormalization group process

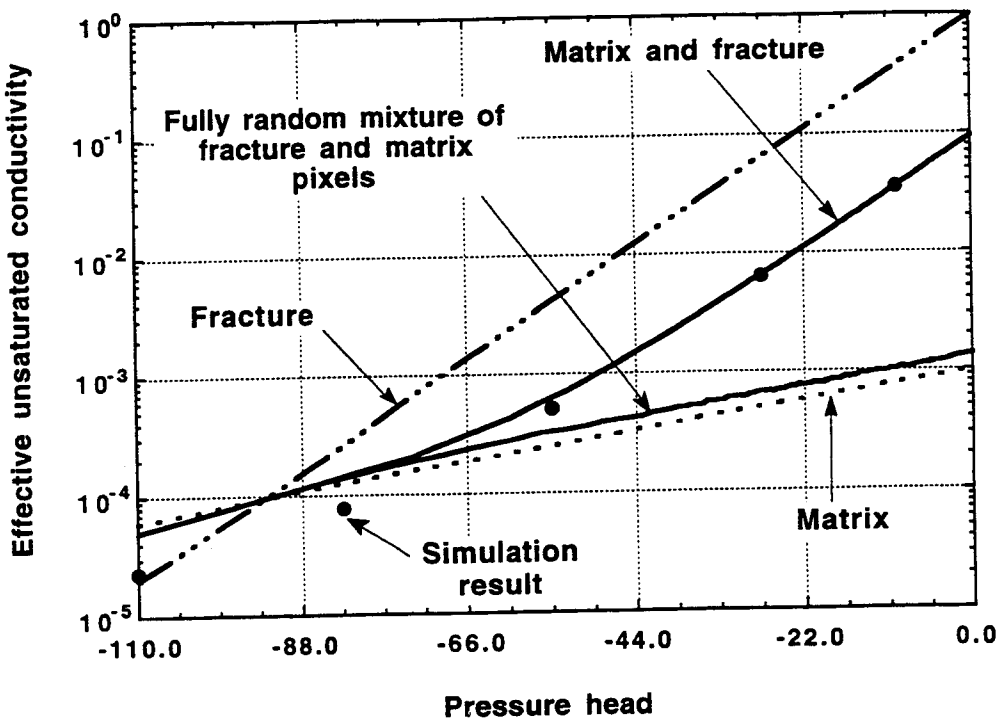

Figure 4-7. Comparison of effective unsaturated hydraulic conductivity between a fracture system with fully connecting fractures and a system with a random binary distribution of fracture and matrix pixels. The fracture density anisotropy is 2 and the ratio of saturated hydraulic conductivities between fracture and matrix is 1,000.

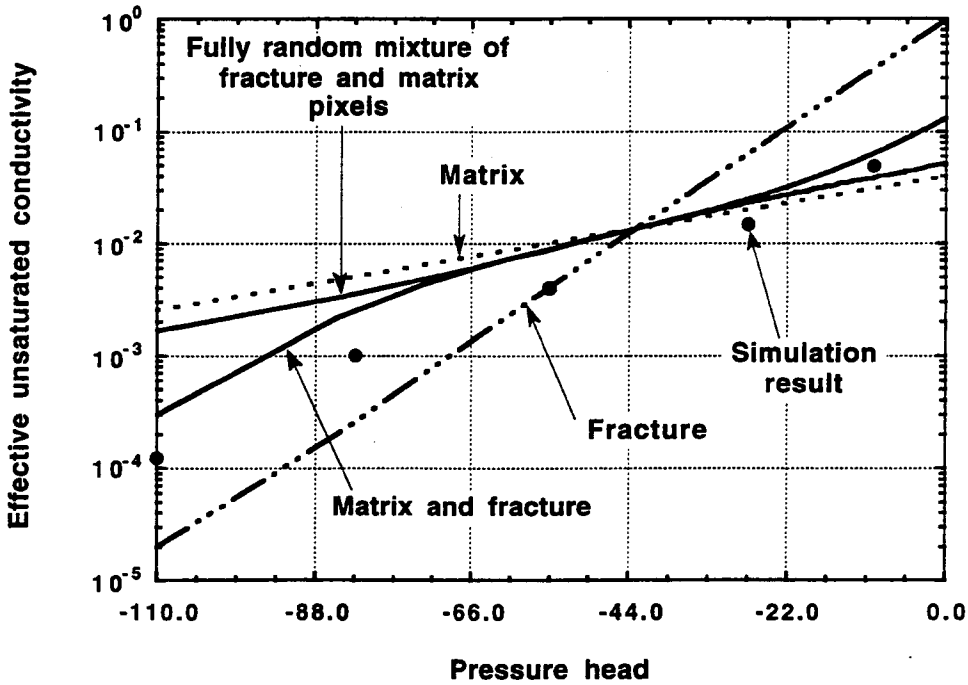

Figure 4-8. Comparison of effective unsaturated hydraulic conductivity between a fracture system with fully connecting fractures and a system with a random binary distribution of fracture and matrix pixels. The fracture density anisotropy is 2 and the ratio of saturated hydraulic conductivities between fracture and matrix is 25.

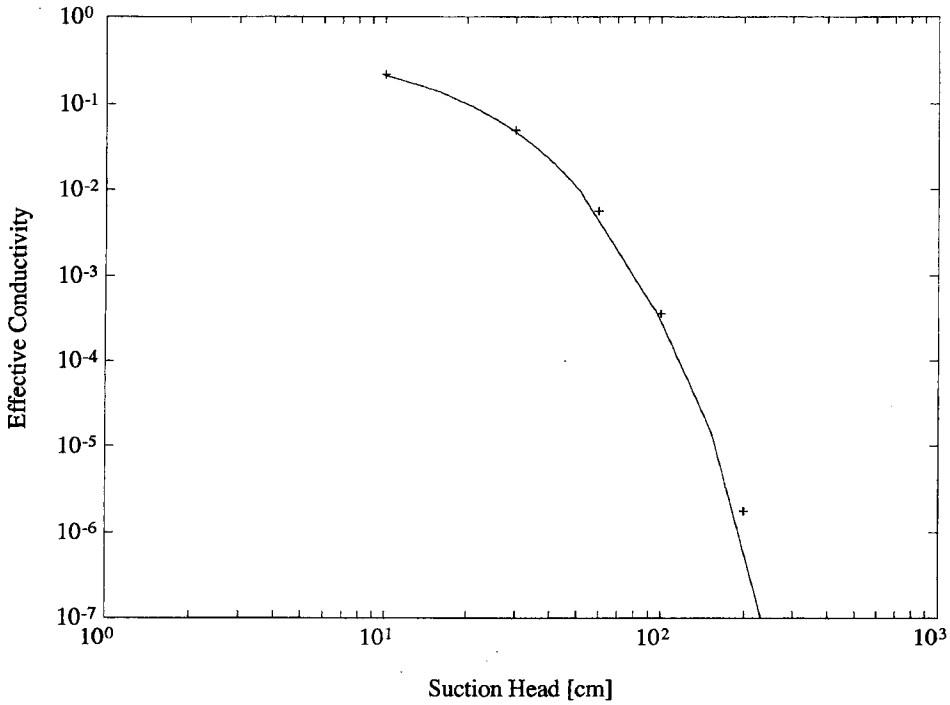

Figure 4-9. Comparison of effective unsaturated hydraulic conductivity for real space renormalization group and direct numerical simulation results for a system with fractures of finite length

5 CALCULATION OF EFFECTIVE HYDRAULIC PROPERTIES WITH DIRECT NUMERICAL SIMULATIONS

5.1 APPROACH

A number of numerical simulations of flow through different fracture/matrix arrangements in a fractured rock mass were conducted using either an exact analytical solution for infiltration into layered soils (Yeh, 1989) or two numerical codes for the simulation of flow in variably saturated media. These codes are: (i) a finite element model for variably saturated flow and transport, under the name Modified Method of Characteristics 2 (MMOC2) (Yeh et al., 1993); and (ii) the BIGFLOW finite difference model for variably saturated flow in heterogeneous media (Ababou and Bagtzoglou, 1993). The objective of this study was to determine the effective conductivity of the rock mass under steady-state unsaturated flow conditions. Four different cases were simulated: Case 1—Flow Perpendicular and Parallel to Unidirectional Fully Connecting Fractures; Case 2—Flow Through Orthogonal Fracture Sets Embedded in Homogeneous Rock Matrix; and finally, Cases 3 and 4, Flow Through a Random Network of Fractures Embedded in Homogeneous and Heterogeneous Rock Matrices, respectively. Within each case, several different scenarios were also investigated. Finally, the tensorial nature of the effective hydraulic conductivity was studied for the case of parallel inclined fractures of infinite extent.

In all the cases examined, fracture and matrix hydraulic conductivity as a function of pressure head (h) was assumed to be represented by the Gardner exponential model, given in Eq. (4-10). The water retention curves were assumed to be described by either an exponential model (Yeh et al., 1993) or the van Genuchten-Mualem model given in Eq. (4-9). The former model was used in conjunction with the MMOC2 analyses, whereas the latter model was used in conjunction with the BIGFLOW analyses. However, all the simulations considered steady-state flow conditions and the pressure head distribution was of primary interest. Thus, the water retention characteristics of the media were not relevant to the simulations and are not discussed in this report. In all subsequent discussions, subscripts m and f are associated with the matrix and fracture properties, respectively.

5.2 ANALYSIS AND RESULTS

5.2.1 Case 1—Flow Perpendicular and Parallel to Unidirectional Fully Connecting Fractures

In this case, each member of a set of parallel linear fractures completely crosses an otherwise uniform porous medium. Parameter values for the unsaturated hydraulic conductivity of the fracture were assumed $K_s^f = 1.0$ cm/s and $\alpha_f = 0.1$ cm^{-1}. However, two different sets of hydraulic properties were employed to represent two rock matrices to investigate the effect of the contrast in the saturated hydraulic conductivity between the fracture and rock matrix. The conductivities of the two rock matrices are $K_s^m = 0.001$ cm/s and $\alpha_m = 0.025$ cm^{-1} for Case 1a; and $K_s^m = 0.04$ cm/s and $\alpha_m = 0.025$ cm^{-1} for Case 1b.

Using the above hydraulic properties, two flow regimes were considered: (i) flow perpendicular to fractures, and (ii) flow parallel to fractures.

5.2.1.1 Flow Perpendicular to Fractures

For flow perpendicular to fractures, the dimension of the simulation domain was 390.48 cm in the vertical and 390.0 cm in the horizontal. The fracture aperture was considered constant and assumed at 0.04 cm with a separation between fractures of 30 cm, resulting in 12 horizontal line fractures in the domain. Boundary conditions were set as no-flow across the edges of the domain parallel to the flow, and constant flux at the upper boundary and constant head at the bottom boundary of the domain. An exact analytical solution developed by Yeh (1989) was employed to derive the pressure head distribution along the vertical. The imposed value of the flux combined with the mean suction along the hydraulic head unit mean gradient portion were used to define the effective conductivity (Yeh, 1989). For example, for Case 1a, when a flux equal to 1×10^{-5} cm/s was imposed, the resulting suction along the unit gradient portion varies from 165.1 to 174.1 cm with a mean of 169.6 cm.

Figure 5-1 shows the effective hydraulic conductivities for Cases 1a (circles) and 1b (triangles). Also shown are the hydraulic conductivity of the fracture and matrix along with the average conductivity resulting from a direct average approach (Yeh et al., 1985c). For flow perpendicular to fractures, the direct approach employs the weighted harmonic mean. That is, the average was computed taking into consideration the thicknesses of the fracture and the matrix according to:

$$K_H(\psi) = \sum_{i=1}^{n} \frac{L_i}{\sum_{i=1}^{n} \frac{L_i}{K_i(\psi)}} \tag{5-1}$$

where L_i is the thickness perpendicular to the flow of either the matrix or the fracture, and $K_i(\psi)$ is the hydraulic conductivity of either fracture or matrix at the given suction, ψ. The effective conductivity formula developed by Yeh et al. (1985b) and Yeh (1989) can be used to estimate the effective conductivity for this case. Since the fracture aperture is small, the effective conductivity based on Yeh's model is identical to the weighted harmonic average of the fracture and matrix conductivity for the given suction and for all the range considered. This applies to both Cases 1a and 1b, regardless of the contrast in hydraulic conductivity between the fracture and matrix. These results are different from those for layered porous media with much larger vertical correlation scales (e.g., layer thicknesses) (Yeh, 1989; Yeh and Harvey 1990).

Similar results were obtained for the cases where the spacing between fractures was randomly generated. However, the range of suction along the unit gradient portion was slightly larger than that observed for the case with uniformly spaced fractures. For instance, for flux equal to 1×10^{-5} cm/s the resulting suction along the unit gradient portion varies from 165.9 to 176.8 cm with a mean of 170.4 cm.

5.2.1.2 Flow Parallel to Fractures

To avoid increasing the computational burden, the flow domain for the simulation of this particular case was simplified because of flow symmetry with respect to the centerline of a fracture. Thus, only one half of a matrix block and a single fracture (i.e., 15.02 cm for the domain width) were considered. Boundary conditions were set as no-flow along the symmetry lines and constant head at top and bottom boundaries. The same value of suction head was used for both boundaries to force an overall

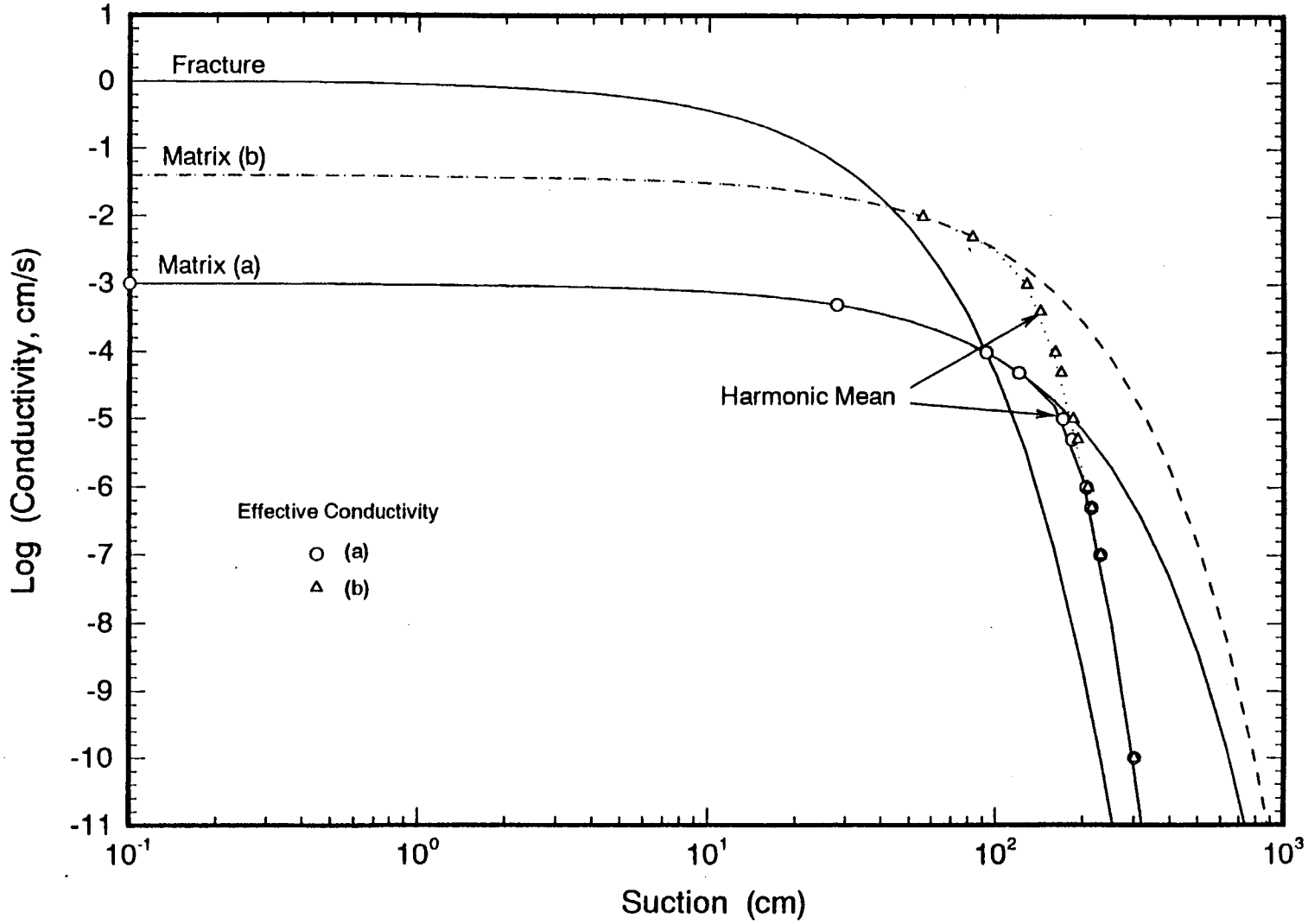

Figure 5-1. Comparison of effective hydraulic conductivity from numerical simulations and the weighted harmonic mean for flow perpendicular to a set of fully connecting fractures in homogeneous matrix

unit gradient across the domain. In this case, MMOC2 was used to simulate the suction head profile and calculate the infiltration and outflow fluxes at the upper and lower boundaries.

The effective conductivity for this case was set to be the average flux in the fracture and matrix over the top or bottom boundaries, and the corresponding mean suction value for the conductivity was the imposed constant suction value at the top and bottom boundaries. This approach takes advantage of the fact that the pressure head throughout the domain is uniform and equal to the value imposed at the boundaries. In fact, it is identical to the classical effective hydraulic conductivity approach for steady flow parallel to stratification and it yields an effective hydraulic conductivity that reproduces the observed volumetric flow corresponding to the imposed head. Analogous to steady-state saturated flow parallel to stratification, there is no pressure head difference across the fracture and matrix and the mean pressure within the domain equals the boundary pressure value. However, gravity is the driving force. Thus, the effective hydraulic conductivity must be closely approximated by the weighted arithmetic mean of the fracture and matrix according to the aperture of the fracture and the width of the matrix. Figure 5-2 depicts the hydraulic conductivity curves for the matrix and fracture, the arithmetic average weighted by the matrix and fracture area perpendicular to flow, and the simulated effective conductivities (circles). As expected, the weighted arithmetic mean provides an accurate representation of the effective conductivity over the complete suction range. Note the inflection point in the effective conductivity versus suction curve which exists around a suction value of 100 cm. This is in agreement with the composite, double-hump behavior of the Peters and Klavetter (1988) model. Note also that this suction value corresponds to the crossover point of the matrix and fracture hydraulic conductivity curves.

5.2.2 Case 2—Flow Through Orthogonal Fracture Sets Embedded in Homogeneous Rock Matrix

In this case, the effective hydraulic conductivity is determined for two fractured rock masses. The first rock mass contains an orthogonal fracture set with equal density in horizontal and vertical directions, while in the other, the fracture density in the horizontal direction is different from that in the vertical. The fractures were assumed to fully penetrate the rock mass, and hydraulic properties of the fracture and matrix for the two rock masses were assumed identical to those for Case 1a.

5.2.2.1 Fracture Sets with Equal Density in Horizontal and Vertical Directions

The first case considered an orthogonal fracture set which consisted of six horizontal fractures and six vertical fractures uniformly spaced (every 30 cm). Because of this arrangement of fractures, the flow regime must be symmetrical about the centerline of any vertical fracture. To save CPU time and storage space, flow was simulated only along a column 216.0 cm tall and 15.5 cm wide. This column consists of seven matrix blocks and six horizontal fractures in the vertical, and half of a single vertical fracture and half of a matrix block in the horizontal. Due to lack of convergence of the numerical solutions, the fracture thickness was later increased to 1.0 cm.

The boundary conditions in this case were assigned as constant pressure head values with equal magnitude at top and bottom boundaries. The effective conductivity was computed, as before, using the average flux through these boundaries. The hydraulic conductivity for the matrix and fracture, as well as the weighted average as a function of suction, are presented in Figure 5-3. The weighted average was computed based on the equation:

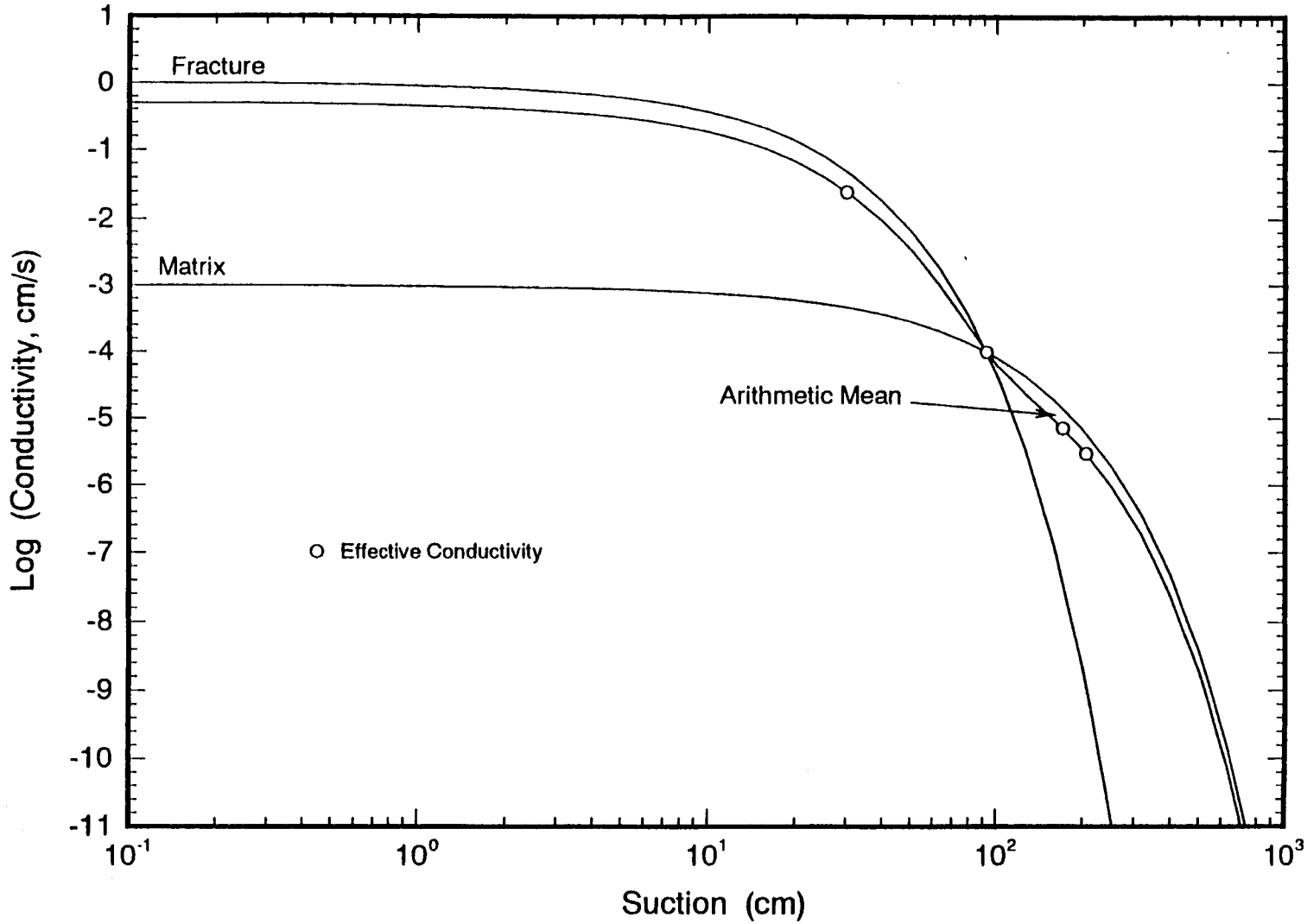

Figure 5-2. Comparison of effective hydraulic conductivity from numerical simulations and the weighted arithmetic mean for flow parallel to a set of fully connecting fractures in homogeneous matrix

$$K_e(\psi) = \frac{K_H(\psi)\ b_m + K_f(\psi)\ b_f}{b_m + b_f} \tag{5-2}$$

where $K_H(\psi)$ is the harmonic mean of the fracture and matrix conductivities at a given suction, ψ, and b_f and b_m are the areas perpendicular to the flow. The open circles in Figure 5-3 represent the effective conductivity obtained from the numerical simulations. As illustrated in Figure 5-3, the effective conductivity given by Eq. (5-2) seems to be a good approximation of the effective conductivity over most of the suction ranges, except for very dry conditions.

A second case with the same number of fractures but with random spacing was simulated and, since the results are identical to those for the uniformly spaced fractures, it is not reported here.

5.2.2.2 Fracture Sets with Different Density in Horizontal and Vertical Directions

The simulation domain, boundary conditions, and number of fractures in the horizontal direction for this case were identical to those in the previous case. However, the fracture locations were randomly selected and the number of fractures in the vertical direction was reduced to three corresponding to a fracture density anisotropy ratio of two. The horizontal fractures were located at 30.0, 55.0, 88.0, 122.0, 151.0, and 177.0 cm from the bottom boundary and the vertical fractures at 100.0, 151.0, and 192.0 cm from the left boundary. Figure 5-4 shows the numerical results and those computed using Eq. (5-2). Again, the analytically estimated effective conductivity, obtained by the weighted average, compares favorably to the results of numerical simulations.

5.2.3 Case 3—Flow Through a Random Network of Fractures Embedded in Homogeneous Rock Matrix

In this case, orthogonal fracture sets were randomly distributed in a homogeneous rock matrix in contrast to Case 2. In addition, the fracture trace was considered to be random in both horizontal and vertical directions. The fracture lengths were sampled from an exponential distribution, and the 2D fracture network was generated by the numerical code described in Chapter 2. Two hypothetical fractured rock masses were examined: (i) one with fracture sets which have a short average trace (short fractures), and (ii) another with long average fracture trace (long fractures). For each rock mass, two sets of simulations were conducted, one with the MMOC2 numerical code and one with the BIGFLOW numerical code. For the MMOC2 simulations, the boundary conditions imposed on the domain were identical constant pressure head on the top and bottom boundaries and no-flow across the vertical boundaries thus simulating gravity drainage. The constant head boundary conditions were varied to obtain the effective hydraulic conductivities at different mean suction values. However, the BIGFLOW simulations were conducted such that the flow was through the horizontal plane, driven by capillary forces. This was invoked by starting the simulation at an initial condition ψ_o and imposing constant suction head boundaries at left and right, differing by a very small suction differential, $\delta\psi$. Again, the value ψ_o varied in order to obtain the effective hydraulic conductivities at different mean suctions. A schematic of both approaches is depicted in Figure 5-5. There were three reasons for this approach. First, it was of interest to test the isotropy hypothesis within the fracture network generator; that is to determine whether the flow along the other direction yields a totally different effective conductivity for a presumably isotropic fracture network. Second, it was of interest to test whether different boundary conditions yield

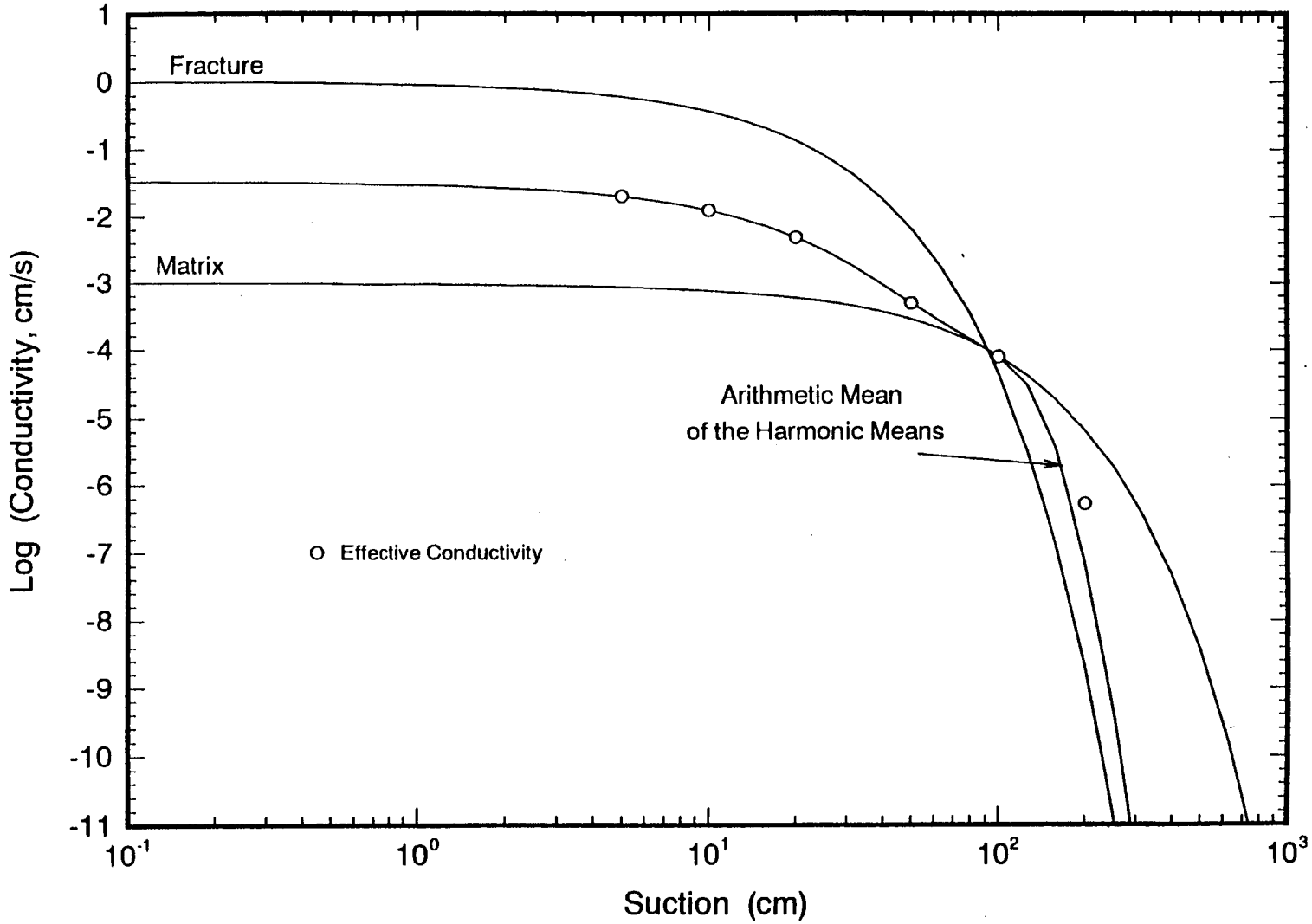

Figure 5-3. Comparison of effective hydraulic conductivity from numerical simulations and the weighted mean of Eq. (5-2) for flow in two orthogonal sets of fractures with isotropic densities and uniform spacing in homogeneous matrix

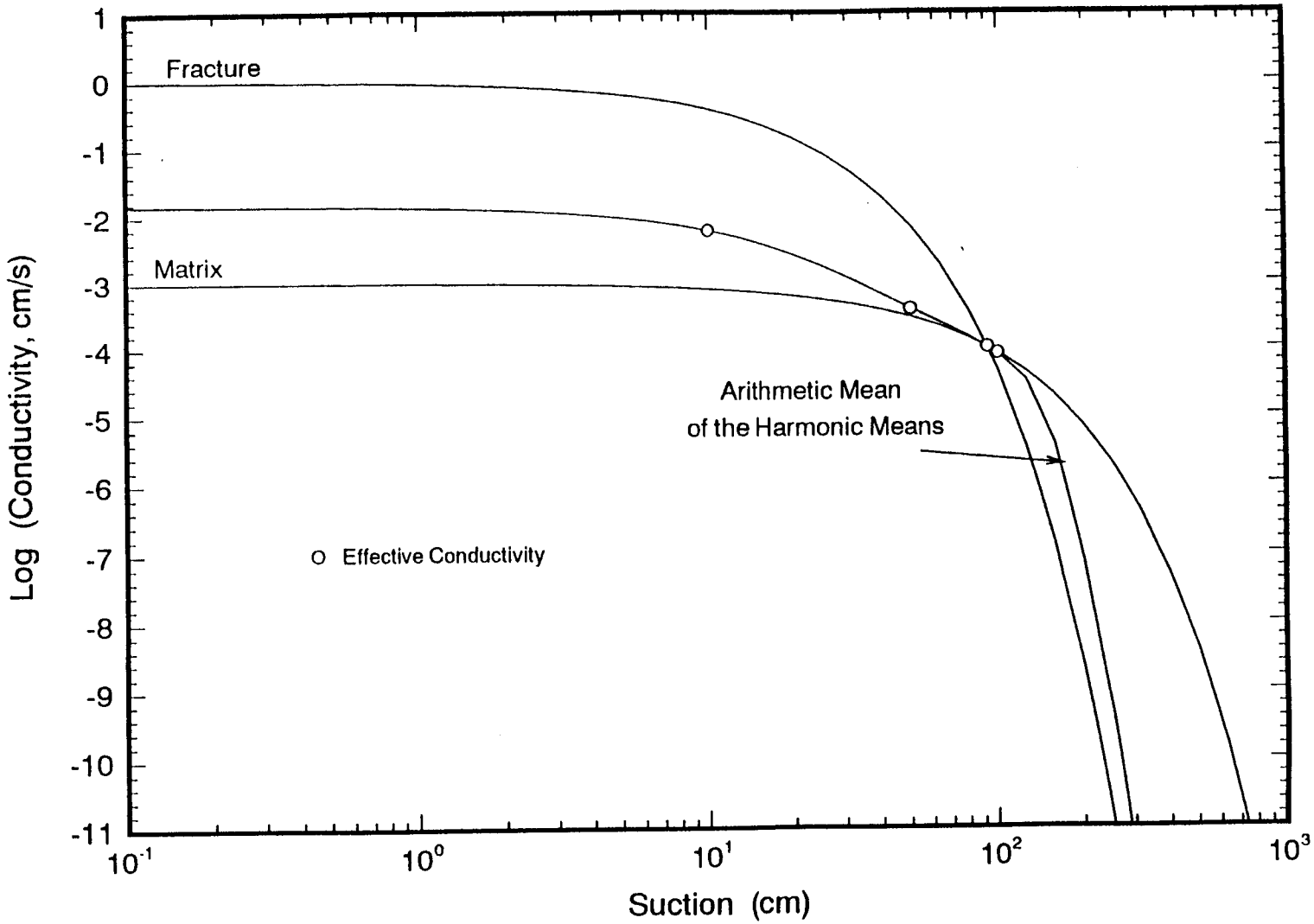

Figure 5-4. Comparison of effective hydraulic conductivity from numerical simulations and the weighted mean of Eq. (5-2) for flow in two orthogonal sets of fractures with anisotropic densities and random spacing in homogeneous matrix

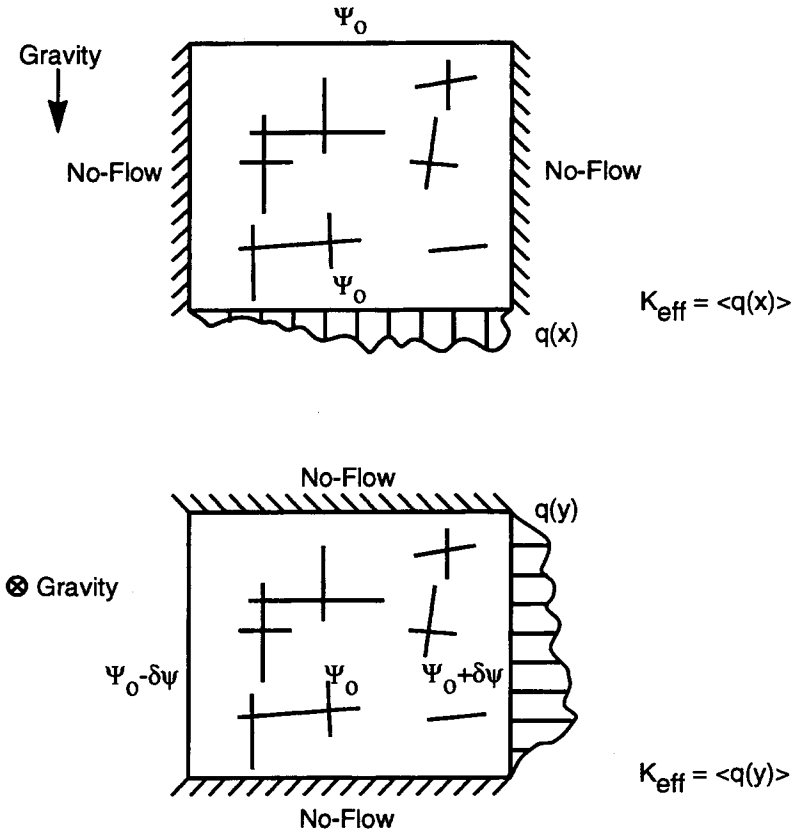

Figure 5-5. Schematic illustrating the two types of numerical simulations conducted for the calculation of effective hydraulic conductivities. a) MMOC2 simulations and b) BIGFLOW simulations.

different values for the effective conductivity; that is whether the results of this study corroborate the findings of Beckie et al. (1994) who found that under conditions of isotropy two different types of boundary conditions yielded similar results. Third, BIGFLOW simulation results were to be used at a later stage to test the RSRG results; therefore, a numerical analog of a pressure plate extractor experiment had to be tested.

5.2.3.1 Flow Through Short Fractures

Figure 5-6 shows the location of fractures and the finite element discretization used for the MMOC2 numerical simulation of this case. The size of the domain is 64.0 cm in both the vertical and horizontal directions. The fractures and the matrix were discretized using rectangular elements of dimension 1×1 cm and the matrix was further discretized into four triangular elements. Again, the exponential model was used to represent the unsaturated hydraulic conductivities of the fracture and matrix, with $K_s^f = 1.0$ cm/s and $\alpha_f = 0.075$ cm^{-1} for the fracture and $K_s^m = 0.000066$ cm/s and $\alpha_m = 0.00533$ cm^{-1} for the matrix.

The pressure head distributions simulated by the numerical code MMOC2 for two different imposed pressure head boundary values (-60 and -200 cm) are presented in Figures 5-7 and 5-8,

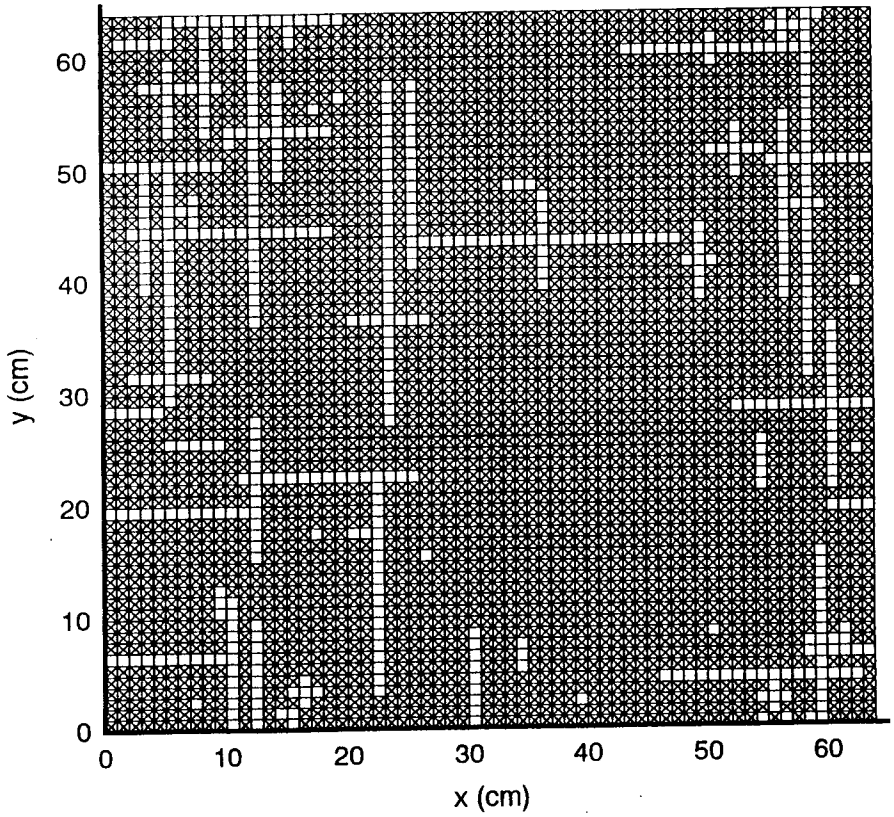

Figure 5-6. Schematic showing the location of fractures (denoted as open pixels) and the finite element discretization used for the MMOC2 numerical simulations of flow through a randomly generated set of short fractures

respectively. These figures show the contrast in pressure head distribution between the cases when the matrix is less conductive or more conductive than the fracture under different unsaturated conditions. The effective conductivity obtained from the numerical simulations using the average flux through the top and bottom boundaries at the given boundary head value is shown in Figure 5-9. In addition, Figure 5-9 shows the fracture and matrix conductivities, and the arithmetic, geometric and harmonic means. The effective conductivity lies between the arithmetic and the geometric means; however, it is closer to the geometric mean over a wide range of suction values. Again, it is worthwhile noticing the perceptible break in the effective conductivity curve around a suction value of 100 cm. Also depicted in Figure 5-9 are the BIGFLOW simulation results. The agreement between the two groups of numerical solutions is considered excellent. The pressure head distributions obtained by the BIGFLOW numerical simulations, for two imposed average pressure head boundary values (−10 and −200 cm), are presented in Figures 5-10 and 5-11, respectively. These figures show the extreme contrasts in suction head developing in the case when the matrix is less or more conductive than the fractures. Streamlines corresponding to the suction fields of Figures 5-10 and 5-11 are shown in Figures 5-12 and 5-13. As expected, the dramatically persistent nature of the fracture-dominated flow field is obvious in Figure 5-12, as a result of the fact that near saturation the fractures are much more conductive pathways than the matrix. At much higher suctions, the flow velocities decrease drastically and their distribution becomes much more uniform. Here, the fractures act as diverting barriers around which flow occurs. An example of this behavior is Figure 5-14, where typical equipotentials and flow lines are shown. These results were

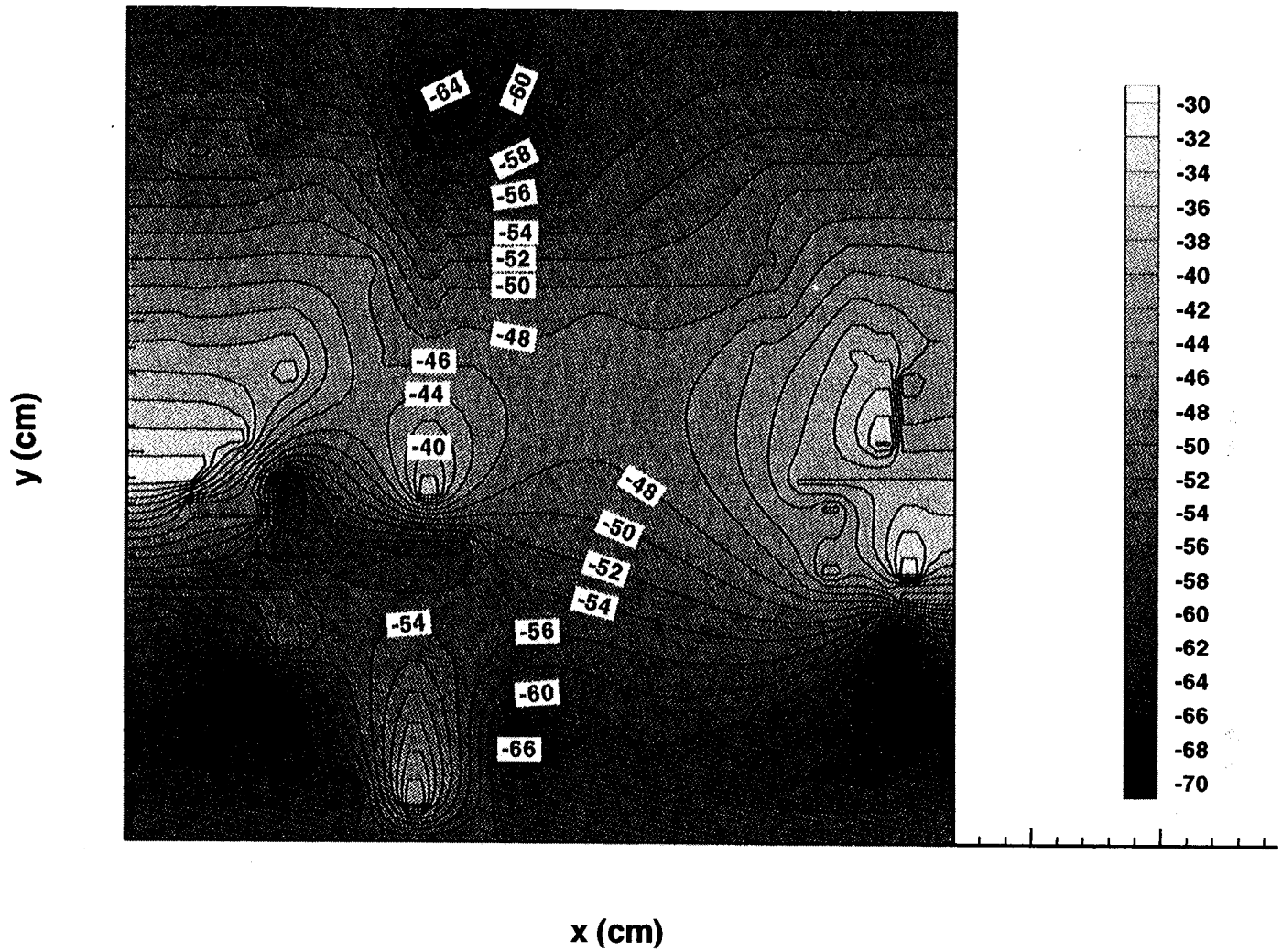

Figure 5-7. Pressure head distribution for flow through a randomly generated set of short fractures in homogeneous matrix. The average suction in the domain is $\Psi = 60$ cm.

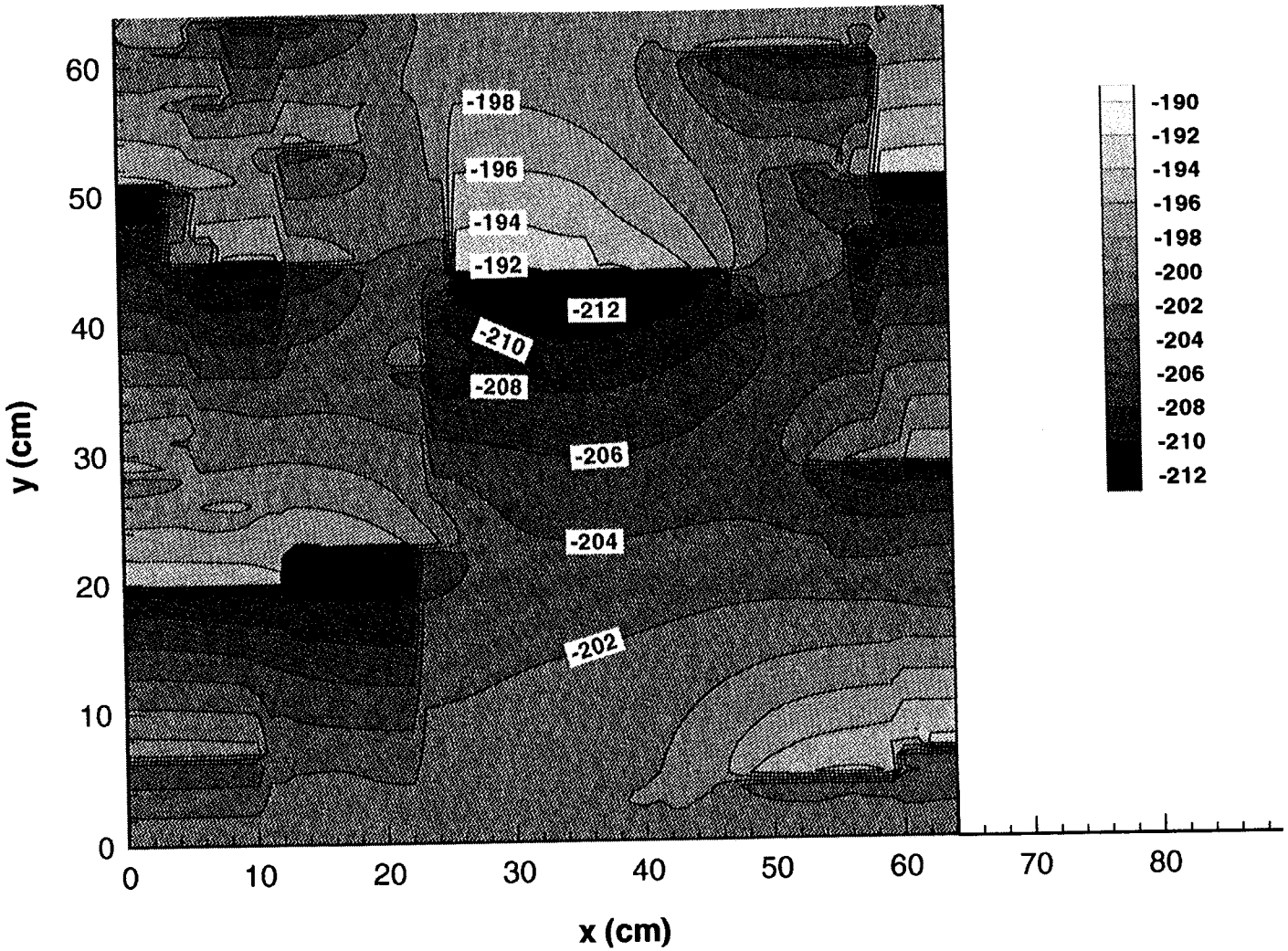

Figure 5-8. Pressure head distribution for flow through a randomly generated set of short fractures in homogeneous matrix. The average suction in the domain is $\Psi = 200$ cm.

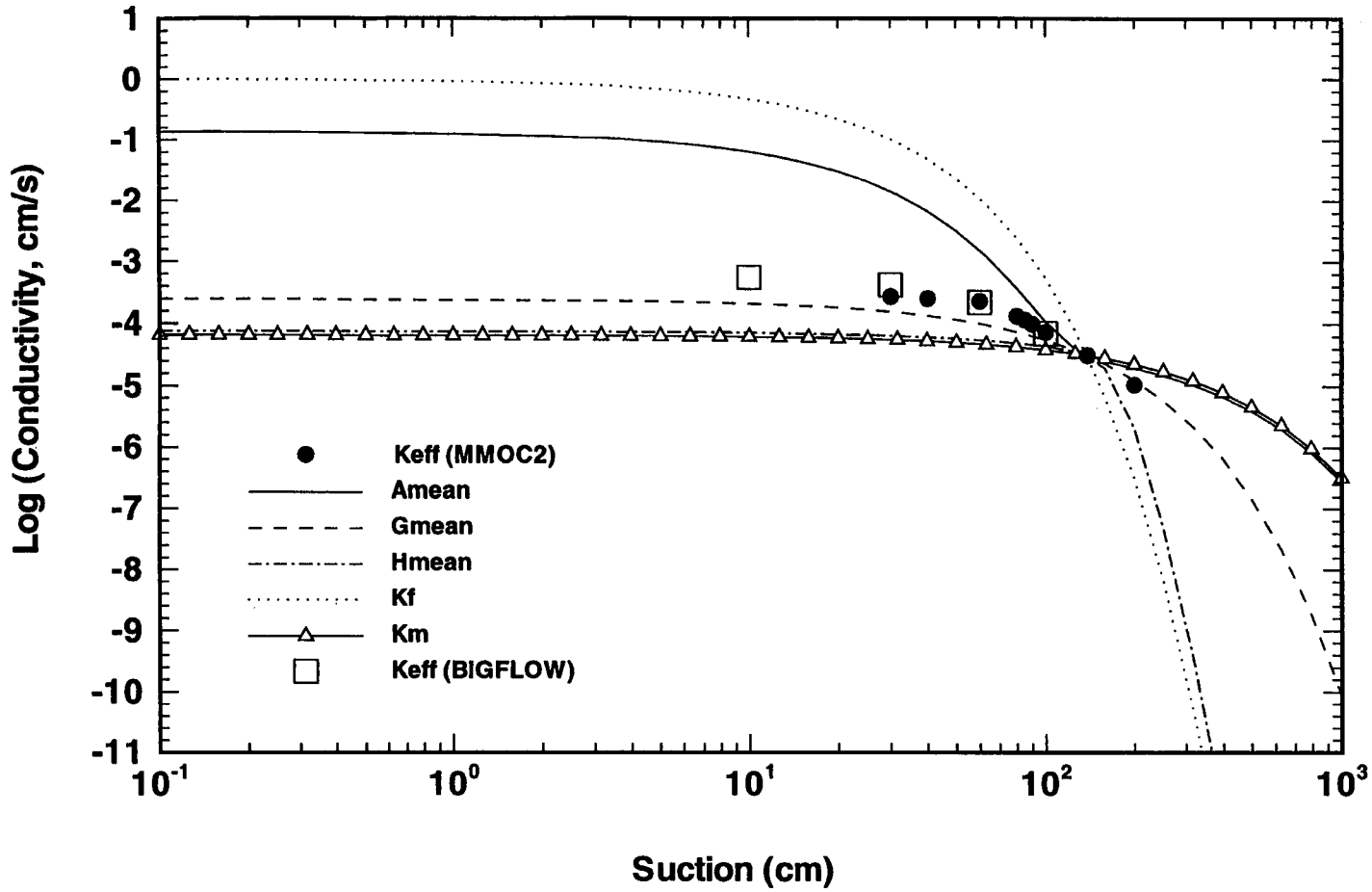

Figure 5-9. Comparison of effective hydraulic conductivity from numerical simulations and the arithmetic, geometric, and harmonic means for flow through a randomly generated set of short fractures in homogeneous matrix

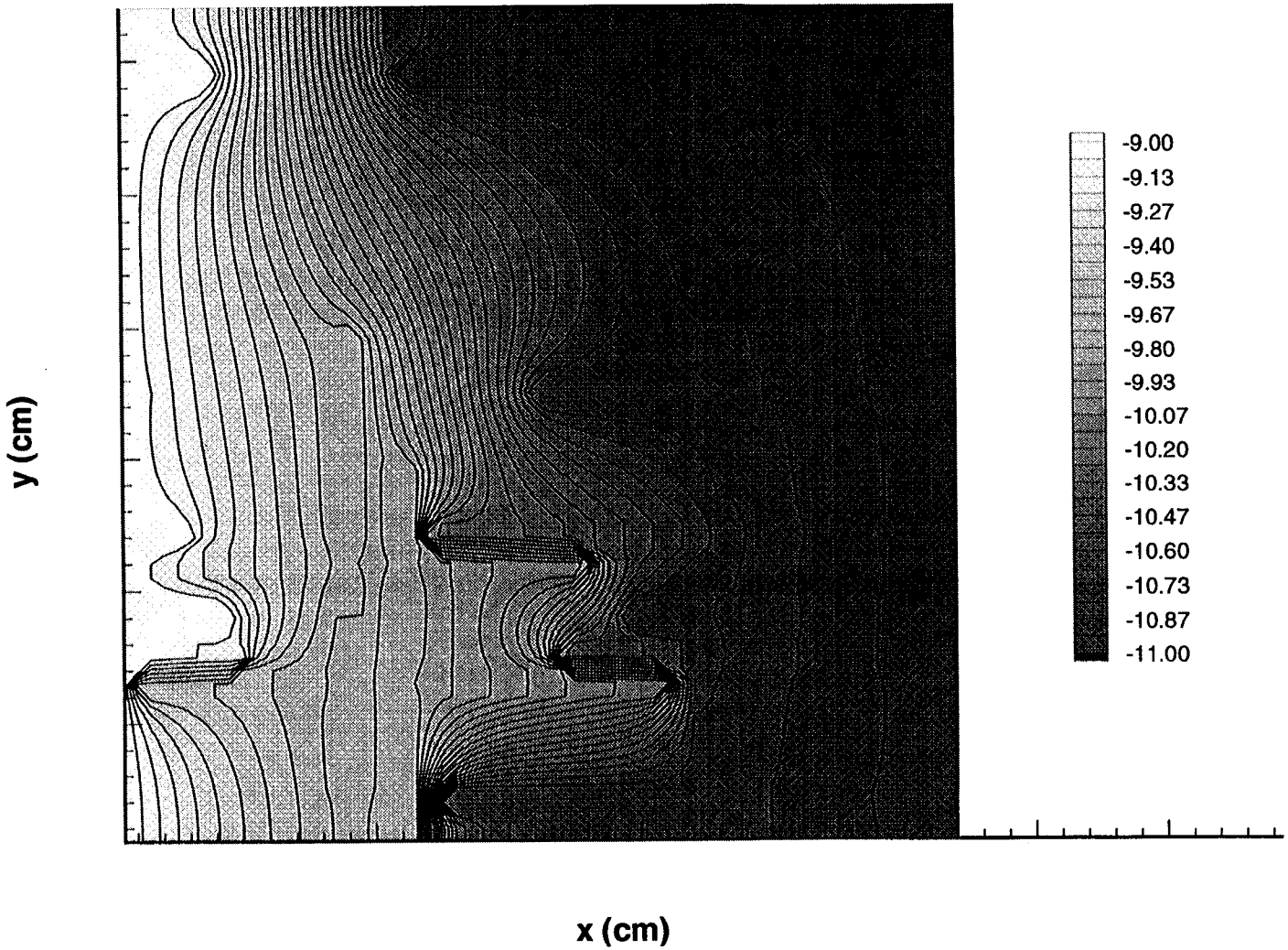

Figure 5-10. Pressure head distribution for flow through a randomly generated set of short fractures in homogeneous matrix. The average suction in the domain is $\Psi = 10$ cm.

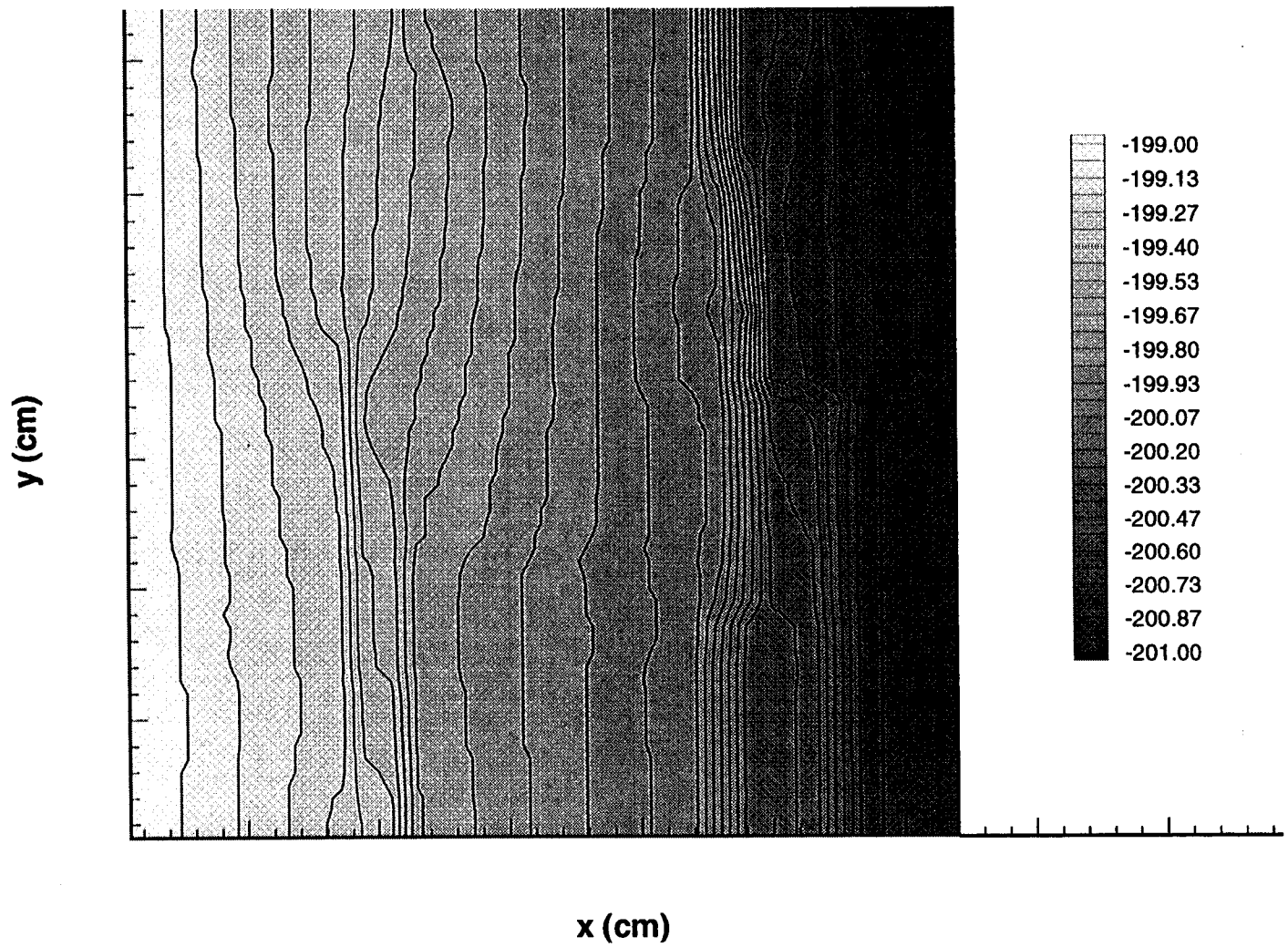

Figure 5-11. Pressure head distribution for flow through a randomly generated set of short fractures in homogeneous matrix. The average suction in the domain is $\Psi = 200$ cm.

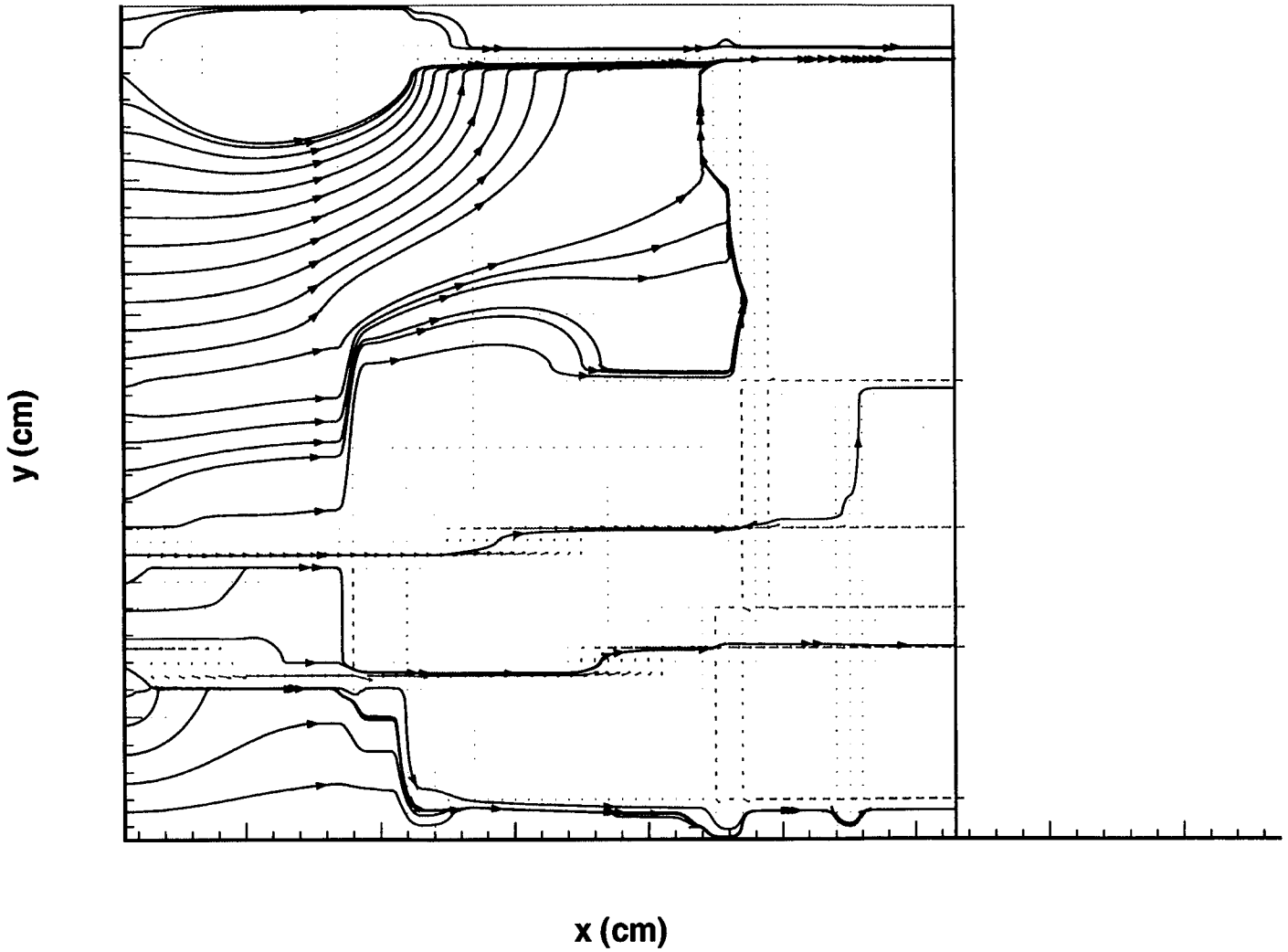

Figure 5-12. Streamlines corresponding to the pressure head field of Figure 5-10

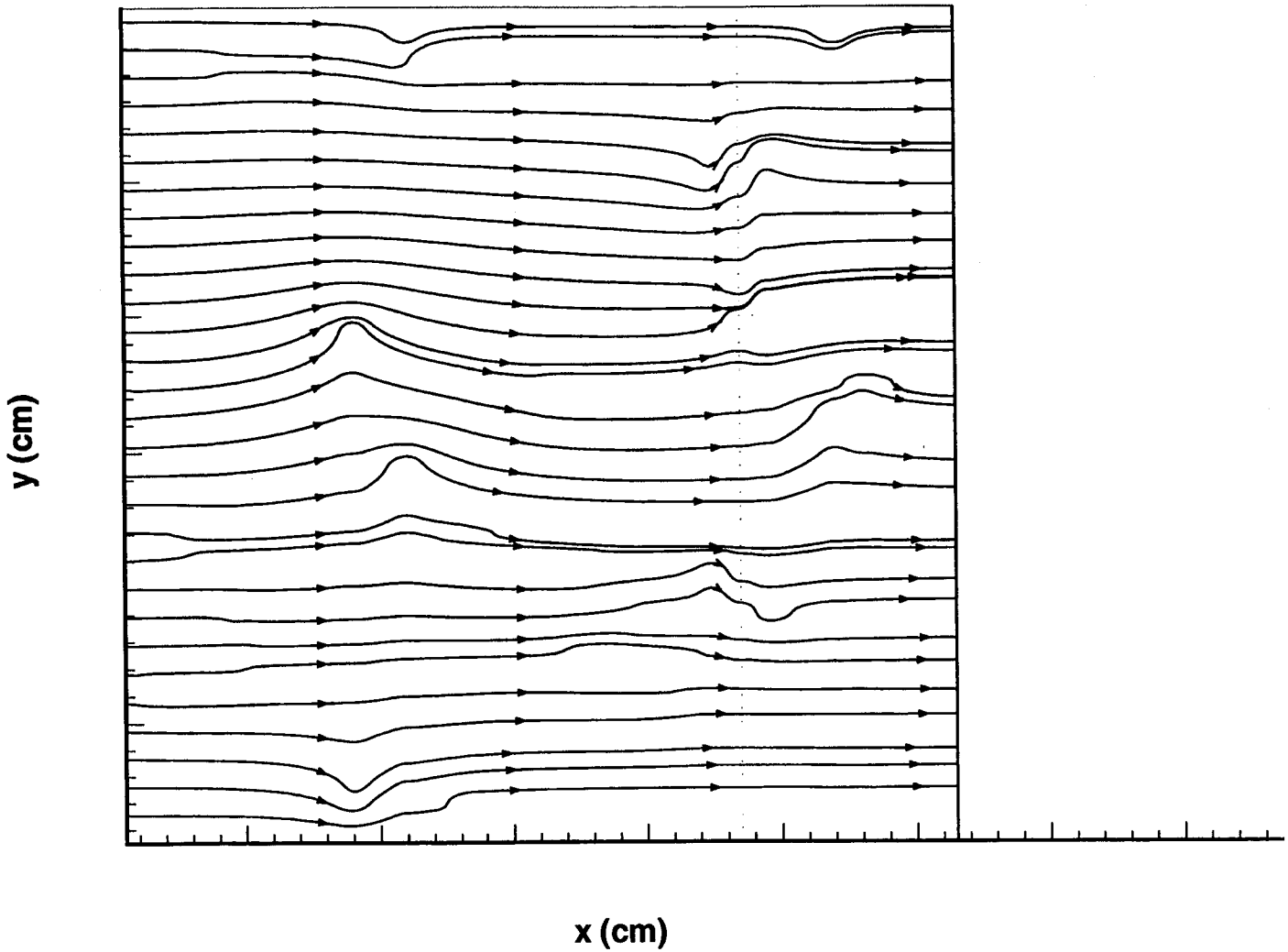

Figure 5-13. Streamlines corresponding to the pressure head field of Figure 5-11

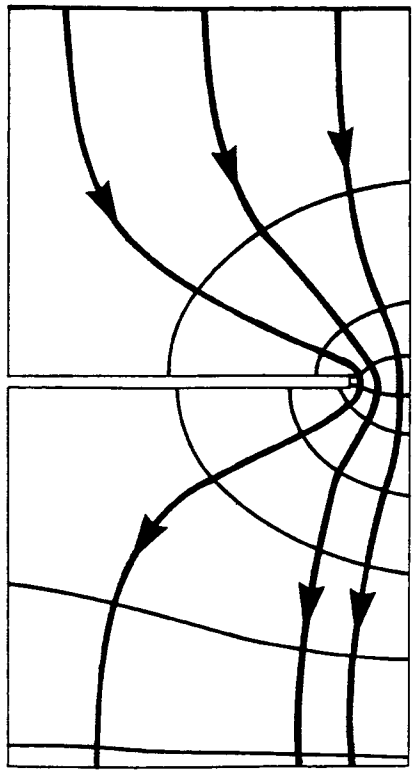

Figure 5-14. Typical equipotential lines and streamlines for flow around a intruding fracture [adapted from Tabatabai-Irani (1989)]

obtained from a numerical simulation of vertical infiltration around a fracture (Tabatabai-Irani, 1989). Martinez et al. (1992) have presented similar results based on numerical and approximate analytical solutions.

Additional effective conductivity values were not obtained with the MMOC2 numerical simulator for suction values smaller than 30 or larger than 200 cm. In fact, convergence problems were encountered by the MMOC2 code even for suction values in the range between 30 and 200 cm. To circumvent this problem, a number of strategies were applied, for example, transient time marching and pseudo-transient approaches (Fletcher, 1988), grid refinement, nonuniform discretization, and the use of good initial solution estimates based on solutions of stepwise increase in the conductivity contrast in steady-state simulations. However, none of these approaches seemed to completely alleviate the convergence problems. Finally, failure of these approaches forced a decrease in the hydraulic conductivity contrast between the matrix and the fracture. The saturated conductivity of the fracture was kept at 1 cm/s but that of the rock matrix was increased to 6.6×10^{-3} cm/s. The results of the simulation and analysis are shown in Figure 5-15. Under this reduced contrast, the interval of convergence was expanded, but to only between 10 and 200 cm. Numerical solution outside this range was not obtainable with the MMOC2 numerical code. The BIGFLOW solutions were obtained by time-marching to the steady-state conditions and no numerical problems were experienced.

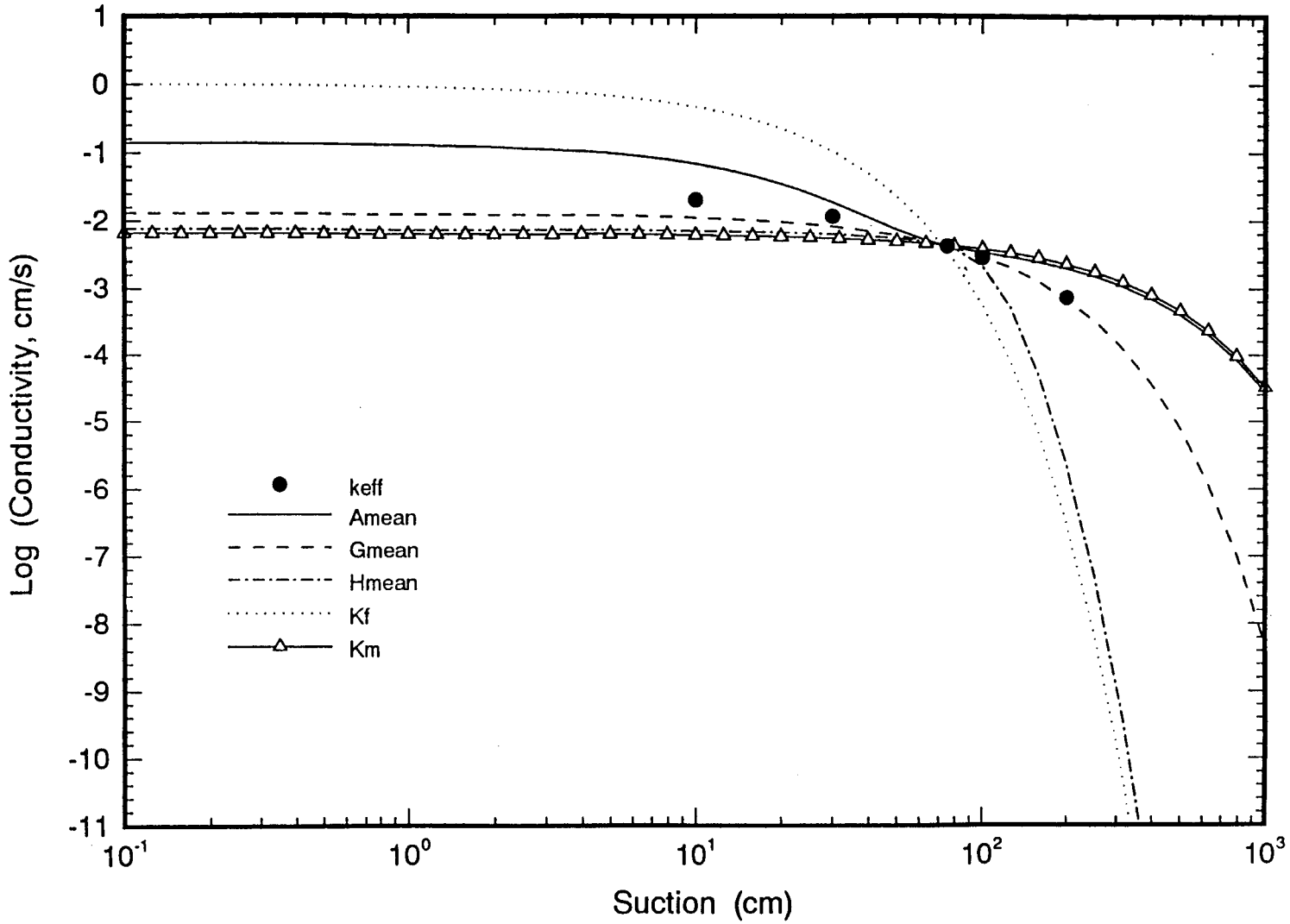

Figure 5-15. Comparison of effective hydraulic conductivity from numerical simulations and the arithmetic, geometric, and harmonic means for flow through a randomly generated set of short fractures in homogeneous matrix. Contrast between fracture and matrix saturated hydraulic conductivity was reduced by a factor of 100.

5.2.3.2 Flow Through Long Fractures

In this case, the material properties, domain size and discretization, and the boundary conditions are the same as in Section 5.2.3.1 (Figure 5-6), but the length of fractures is increased as shown in Figure 5-16. Numerical estimates of the effective hydraulic conductivity, the direct averages, and matrix and fracture conductivity as a function of suction are presented in Figure 5-17. The results indicate that the effective conductivity is close to the arithmetic average for suction values smaller than the crossover point of the fracture and matrix unsaturated conductivity curves and close to the harmonic average for suction values larger than this crossover point. This significantly different behavior (when compared to the results of Section 5.2.3.1; see Figure 5-9) is attributed to enhanced interconnectivity of the fracture network due to the longer fractures involved. BIGFLOW exhibited no numerical problems in this case, even under the presence of sharp contrast in properties. Therefore, the BIGFLOW results are not presented since they are not directly comparable with the MMOC2 results of Figure 5-17.

5.2.4 Case 4—Flow Through a Random Network of Fractures Embedded in Heterogeneous Rock Matrix

The scenarios considered in Case 4 are similar to those of Case 3 with the exception that hydraulic conductivity parameters of the matrix were considered as spatial random fields.

5.2.4.1 Flow Through Short Fractures

Fracture location, domain size, and the finite element discretization used for the numerical simulation of this case are identical to those of the homogeneous case (Figure 5-6). The parameter values for unsaturated hydraulic conductivity of the fractures were $K_s^f = 1.0$ cm/s and $\alpha_f = 0.075$ cm^{-1}. However, the hydraulic properties of matrix were assigned to each 1×1-cm element randomly, generated by the Turning Bands code (Tompson et al., 1987).

The boundary conditions are similar to those for Case 3. The effective conductivity obtained from the numerical simulations using the mean flux through the top and bottom boundaries is shown in Figure 5-18 along with the fracture and matrix conductivities, and their arithmetic, geometric, and harmonic means. Here again, the effective conductivity is closer to the geometric mean for a large range of suctions, and lies between the harmonic and arithmetic means for suctions near saturation. Results from the BIGFLOW simulations are also depicted in this figure. An excellent match between the two numerical codes is observed.

5.2.4.2 Flow Through Long Fractures

In this case, the material properties, domain size and discretization, and the boundary conditions are the same as in Case 3b (homogeneous matrix with long fractures), but the matrix hydraulic conductivity is heterogeneous and varies for each 1×1-cm element. Numerical estimates of the effective hydraulic conductivity, arithmetic, geometric, harmonic averages, and matrix and fracture permeability as functions of suction are presented in Figure 5-19. In this case, the effective conductivity is closer to the arithmetic and harmonic means for suction values smaller or larger than the crossover point, respectively. Again, a very good match is obtained between the MMOC2 and BIGFLOW simulation results.

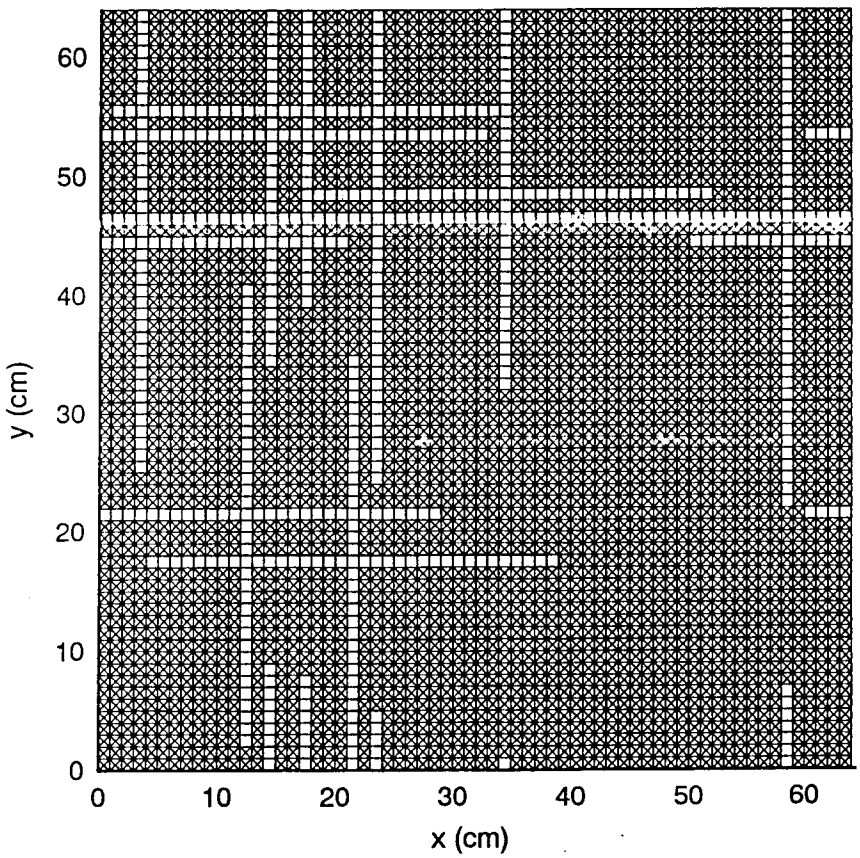

Figure 5-16. Schematic showing the location of fractures and the finite element discretization used for the MMOC2 numerical simulations of flow through a randomly generated set of long fractures

5.3 ANISOTROPIC EFFECTIVE HYDRAULIC CONDUCTIVITY FOR ROCKS WITH PARALLEL, INCLINED FRACTURES

A semi-analytical solution was derived to evaluate the anisotropic behavior of the effective hydraulic conductivity of a 2D fractured rock mass which consists of parallel fractures inclined at an angle θ with the horizontal axis. The rock matrix is assumed homogeneous and the fracture aperture uniform; the rock mass is also assumed unbounded in both the vertical and horizontal directions under steady uniform infiltration. Under these assumptions, the pressure head distribution along any vertical line can be described by a 1D steady-state infiltration equation for layered media (Zaslavsky and Sinai, 1981). Therefore, an analytical solution for the off-diagonal component of the effective hydraulic conductivity, $\langle K_{xz} \rangle$ (where z is the vertical coordinate and x is the horizontal), can be obtained.

Consider a fractured rock with properties changing in a direction n normal to the fracture. The direction parallel to the fracture is s; n and s form an angle θ with the vertical z and horizontal coordinate x (Figure 5-20). The specific discharges in x and z can be derived as:

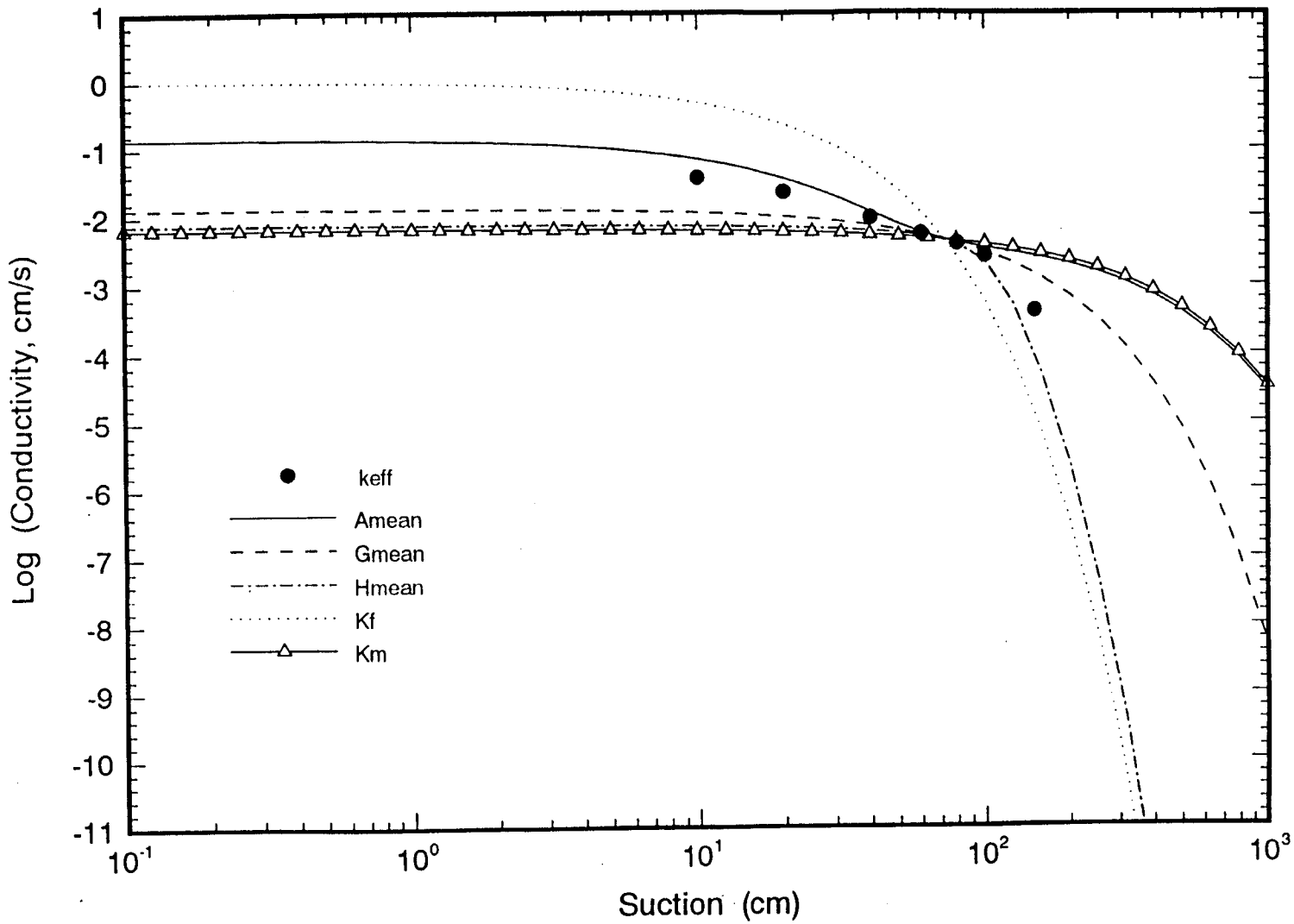

Figure 5-17. Comparison of effective hydraulic conductivity from numerical simulations and the arithmetic, geometric, and harmonic means for flow through a randomly generated set of long fractures in homogeneous matrix. Contrast between fracture and matrix saturated hydraulic conductivity was reduced by a factor of 100.

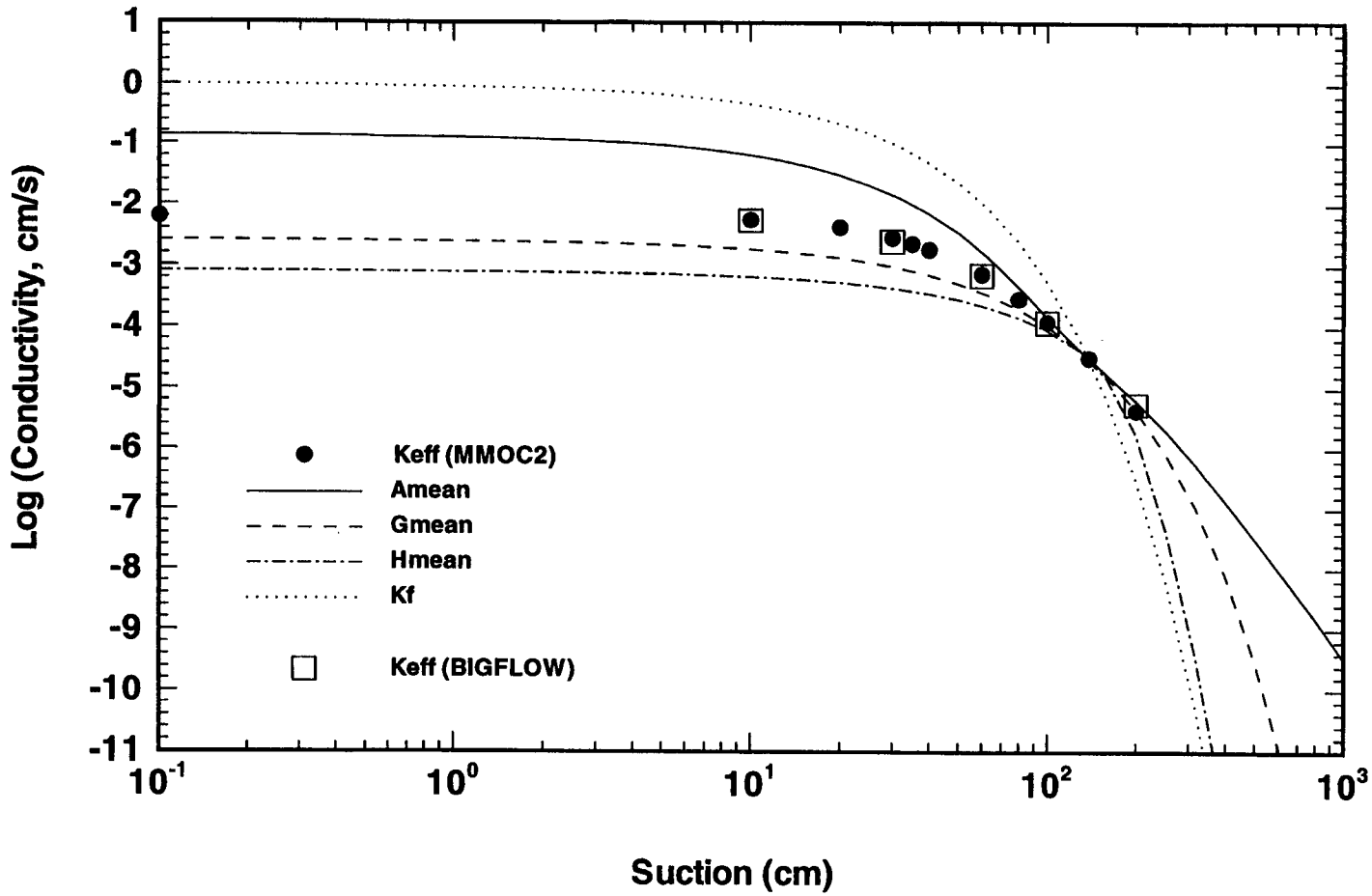

Figure 5-18. Comparison of effective hydraulic conductivity from numerical simulations and the arithmetic, geometric, and harmonic means for flow through a randomly generated set of short fractures in heterogeneous matrix

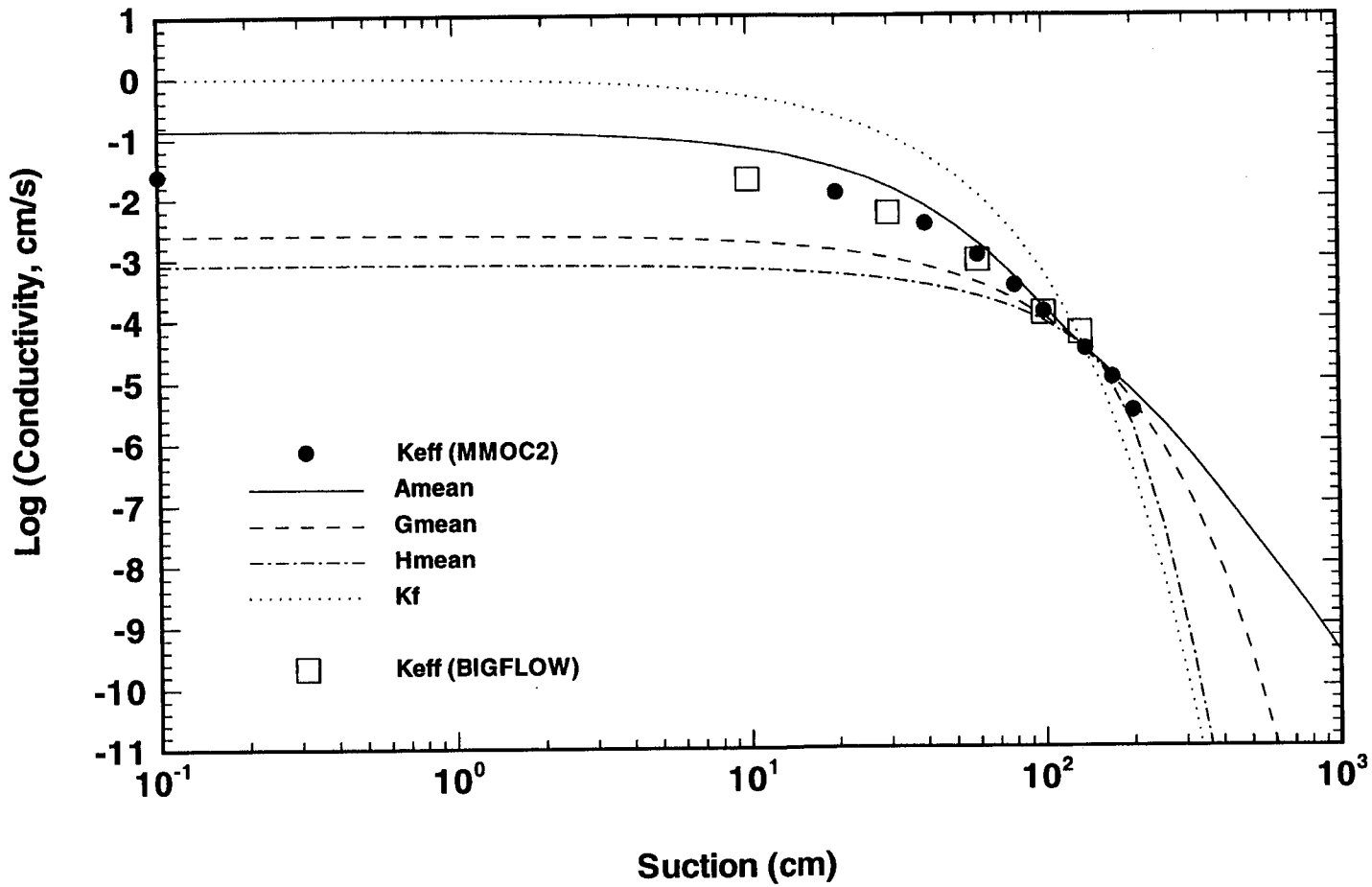

Figure 5-19. Comparison of effective hydraulic conductivity from numerical simulations and the arithmetic, geometric, and harmonic means for flow through a randomly generated set of long fractures in heterogeneous matrix

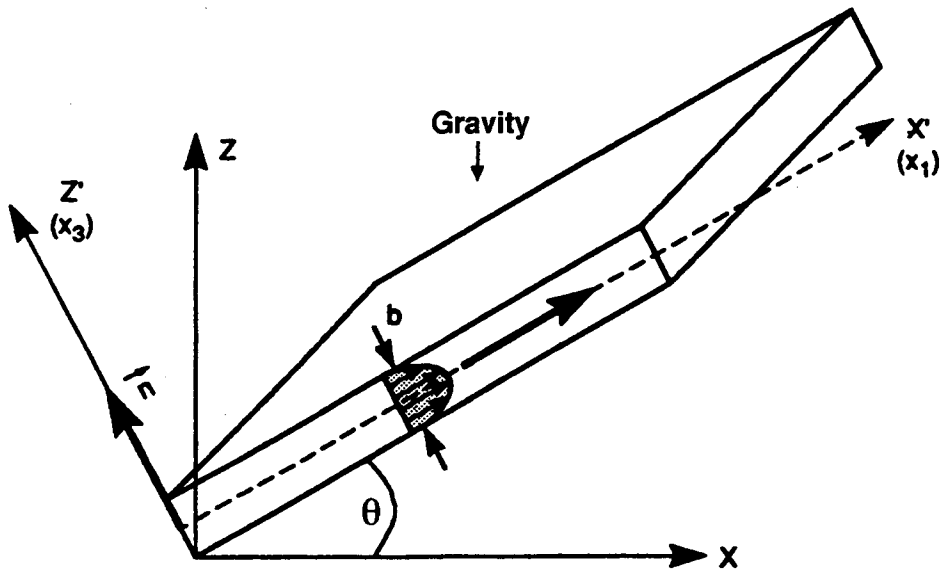

Figure 5-20. Schematic showing one of a set of infinite, parallel, inclined fractures

$$q_z = -K(\psi)\left[\frac{\partial\psi}{\partial z} + 1\right] \tag{5-3}$$

$$q_x = -K(\psi)\frac{\partial\psi}{\partial x} \tag{5-4}$$

for any point in the flow domain since the medium is assumed to have point isotropy. Note that $K(\psi)$ is the point unsaturated hydraulic conductivity which is a function of the point matric potential (or suction), ψ. Furthermore, using simple geometrical relations, we can obtain:

$$q_x = -K(\psi)\frac{\partial\psi}{\partial n}\sin\theta$$

$$= -K(\psi)\frac{\partial\psi}{\partial z\left[\frac{dn}{dz}\right]}\sin\theta \tag{5-5}$$

$$= -K(\psi)\frac{\partial\psi}{\partial z}\tan\theta$$

Now, integration of q_x over the z direction gives the total horizontal discharge as:

$$Q_x = -\tan\theta\int K(\psi)\frac{\partial\psi}{\partial z}\,dz = -\tan\theta\int K(\psi)\,d\psi \tag{5-6}$$

Then, the average specific discharge is given by:

$$q_x = -\frac{1}{D}\tan\theta\int K(\psi)\,d\psi \tag{5-7}$$

where D is the vertical distance where the integration takes place. Ross (1990) has applied this approach in determining the diversion capacity of capillary barriers.

If we assume the fracture rock is homogeneous even though the rock mass includes parallel fractures, the effective hydraulic conductivity will exhibit anisotropic behavior. Therefore, the specific discharge can be rewritten in terms of mean gradients, J_x and J_z, and the effective hydraulic conductivity, $\langle K_{xx}\rangle$, $\langle K_{xz}\rangle$, $\langle K_{zx}\rangle$, and $\langle K_{zz}\rangle$, according to:

$$\begin{aligned} q_x &= -\langle K_{xx}(\Psi)\rangle J_x - \langle K_{xz}(\Psi)\rangle J_z \\ q_z &= -\langle K_{zx}(\Psi)\rangle J_x - \langle K_{zz}(\Psi)\rangle J_z \end{aligned} \tag{5-8}$$

Note that Ψ represents the mean matric potential, given in the works by Yeh (1985 a,b,c), and is different from the point matric potential, ψ, at any point in the domain. If we further assume that the mean gradient is in the z direction only, and J_x=0, the effective conductivity tensor component, $\langle K_{xz}(\psi)\rangle$, can be obtained by:

$$\langle K_{xz}(\Psi)\rangle = \frac{q_x}{J_z} \tag{5-9}$$

Now, we assume that the point hydraulic conductivity of the rock matrix and the fracture are described locally by an exponential function of the form:

$$K(\psi) = K_s \exp(\alpha\psi) \tag{5-10}$$

where K_s is the saturated hydraulic conductivity and α is the capillary length-scale parameter. In this analysis the following parameters were used: K_s^f = 1.0 cm/s and α_f = 0.075 cm^{-1} for the fractures, and K_s^m = 0.001 cm/s and α_m=0.00533 cm^{-1} for the matrix. Then, the average specific discharge in Eq. (5-7) can be obtained by carrying out the integration for each medium over the point matric potential ranges in the medium. For a given infiltration rate, q_z, the point matric potential distribution for the fractured rock can be obtained analytically (Yeh, 1989; Warrick and Yeh, 1990). However, the average specific flux was evaluated numerically in this investigation. In this analysis, the distance between fractures is 30 cm and the fracture thickness was assumed to be 1.0 cm.

Once the average specific flux in the x direction was determined, a unit mean gradient was assumed for the entire fractured rock (i.e., J_z=1 and J_x=0). Therefore, the $\langle K_{xz}\rangle$ was obtained by Eq. (5-9). To verify this result, the analytical values for the effective conductivity tensor were derived using standard tensor algebra for a layered system at a 45° angle as:

$$\langle K_{xx}\rangle = \langle K_{zz}\rangle = \frac{\langle K_{11}\rangle + \langle K_{22}\rangle}{2} \qquad \langle K_{xz}\rangle = \frac{\langle K_{11}\rangle - \langle K_{22}\rangle}{2} \tag{5-11}$$

where $\langle K_{11}\rangle$ and $\langle K_{22}\rangle$ are the effective conductivities in the principal directions. For the fracture system under consideration, these directions are parallel and normal to the fractures with principal conductivities equal to weighted arithmetic and harmonic means. These values from Eq. (5-11) (analytical solution) were then compared with those obtained previously (semi-analytical solution) by evaluating numerically the integral in Eq. (5-7), with the matric potential ψ expressions derived by Yeh (1989) and Warrick and Yeh (1990).

Figure 5-21 compares the results from the semi-analytical solution with those from Eq. (5-9) which show excellent agreement over the entire range of suctions analyzed. These results suggest that equations similar to Eq. (5-5) could be used to determine the effective conductivity tensor of fractured rocks at any angle whatever the degree of saturation. As it can be seen in this figure, the off-diagonal terms of the hydraulic conductivity tensor attain their minimum values at approximately the crossover point of suction head. Also, the anisotropy ratio for such fracture systems could be estimated using the equation:

$$\frac{\langle K_{zz}\rangle}{\langle K_{xx}\rangle} = \frac{\langle K_{11}\rangle\ (1 - \cos 2\theta) + \langle K_{22}\rangle\ (1 + \cos 2\theta)}{\langle K_{11}\rangle\ (1 + \cos 2\theta) + \langle K_{22}\rangle\ (1 - \cos 2\theta)} \tag{5-12}$$

Equation (5-12) yields (5-11) for θ=45°. This equation is similar, in some respects, to the formulae by Maini and Hocking (1977) for saturated flow.

The anisotropy ratio for the fractured rock system at different mean suction values and at different angles is shown in Figure 5-22, indicating that the ratio varies with mean suction or moisture content as demonstrated in the result of the stochastic analysis by Yeh et al. (1985 a,b,c). This ratio varies from 0.033 to 33 near saturation for inclination angles ranging from 10 to 80°. However, for the

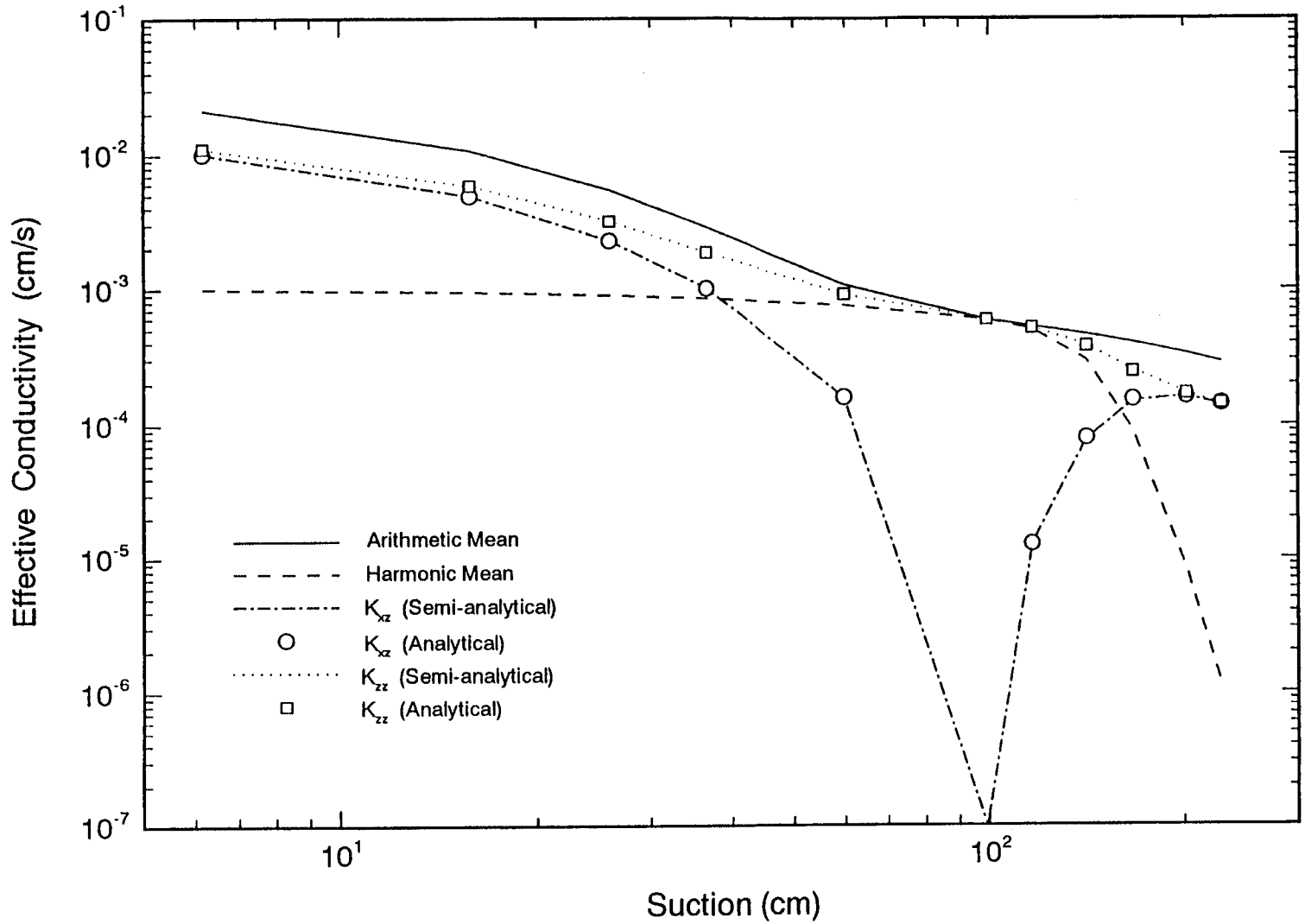

Figure 5-21. Comparison of analytical and semi-analytical solutions for the effective unsaturated conductivity of a 45° inclined set of parallel and infinitely extensive fractures

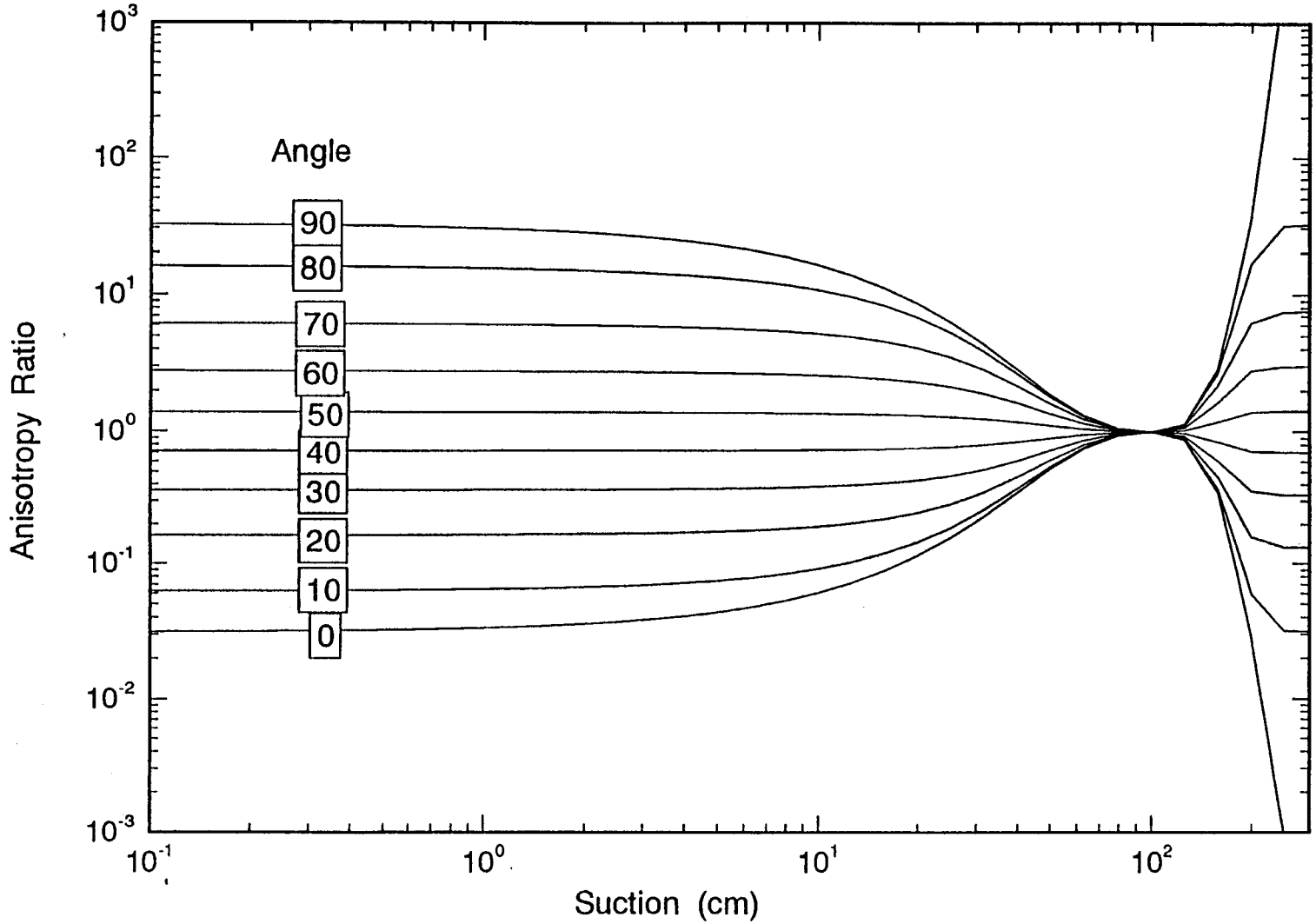

Figure 5-22. Anisotropy ratio (K_{zz}/K_{xx}) as a function of suction head for various angles of inclination

extreme case of θ being equal to 0 and 90° (i.e., horizontal or vertical fractures), this ratio appears to be unbounded at very high suctions. Finally, it should be noted that the anisotropy ratio attains its minimum values around the suction crossover point.

5.4 DISCUSSION

Based on the results of these simulations, the conclusion is reached that the effective unsaturated hydraulic conductivity of the fractured rock mass is strongly controlled by the fracture pattern (i.e., the trace length of the fracture and the orientation of the trace with respect to flow direction). For rock masses with unidirectional fractures, the effective conductivity behaves the same as that of stratified porous media. Therefore, in the case of flow perpendicular to the fractures it can be represented by the harmonic mean, and for flow parallel to the fractures by the arithmetic mean of the fracture and matrix conductivity. These simple averages can be extended to more complicated fracture distributions. For example, in the case of flow through orthogonal fractures, the effective conductivity may be represented by the arithmetic mean of the harmonic means of columns along the flow direction. Similarly, for long fractures embedded in homogeneous and heterogeneous matrices, the flow at small suction values is predominantly along the fractures in the flow direction, resulting in an effective hydraulic conductivity equal to the arithmetic mean. However, at higher suctions (exceeding the crossover point of the fracture and matrix conductivity curves), the horizontal fractures across the domain become less conductive than the matrix resulting in an effective hydraulic conductivity equal to the harmonic mean.

For flow parallel to fractures traversing the entire rock mass, the effective hydraulic conductivity is mainly controlled by the fracture conductivity at suctions smaller than the suction at the crossover point. However, at suctions greater than the crossover point, it is dominated by the conductivity of the rock matrix. Such behavior results in an effective hydraulic conductivity curve characterized by a hump near the crossover point, indicating that the composite model by Peters and Klavetter (1988) may be applicable to flow situations which are more complex than its original confines. However, this statement must be taken cautiously, especially since this behavior is very much dependent on the fracture network topology and other characteristics. On the other hand, when the flow direction is perpendicular to the fractures or if the fractures are short and disconnected, no apparent humps are observed. The heterogeneities in the rock matrix do not strongly influence the effective conductivity for the cases considered in this study.

An important conclusion derived from this study is that the discrete fracture approach, for such sharp contrasts in hydraulic conductivity between the fracture and the matrix, is in many cases, unattainable with the MMOC2 finite element model. The BIGFLOW numerical code demonstrated a higher degree of robustness in terms of the types of properties that it can handle. Furthermore, both numerical codes exemplified the extensive computational resources one may have to rely upon should effective hydraulic properties need to be calculated with direct numerical simulations.

Since the flow domain considered in this study was relatively small and did not contain a large number of fractures, the resulting effective conductivity may not accurately, in a statistical sense, represent the true effective hydraulic conductivity for the fractured rock mass. However, the values of the simulated effective hydraulic conductivity seem physically plausible as discussed before. Monte-Carlo simulations are necessary for assessing the validity and/or reproducibility of these results. A study addressing this very issue is discussed in Chapter 6.

Based on the anisotropy ratio results, we may conclude that the effective unsaturated conductivities in the principal directions for the rock matrix with parallel fractures are bounded, for the majority of suction values, and can thus be represented by the weighted arithmetic and harmonic means. Furthermore, it was found that the effective conductivity is a second rank tensor in agreement with Sagar and Runchal (1982), who obtained symmetric hydraulic conductivity tensors for the case of extensive fractures. It should also be noted that, even though the anisotropy ratio attains its minimum value near the suction crossover point, it is precisely at this suction range that the off-diagonal effective hydraulic conductivity terms attain their minimum value and, therefore, deviate the most from the arithmetic and harmonic mean bounds.

6 PARAMETRIC STUDY FOR THE CALCULATION OF EFFECTIVE PROPERTIES AND LIMITATIONS OF THE REAL SPACE RENORMALIZATION GROUP METHOD

In Chapter 4, the RSRG method was presented, and several verification tests demonstrated its applicability for effective property calculations in fractured rock. However, the range over which this approach provides accurate results has not been investigated. Furthermore, the systems studied in Chapter 4 were of a binary nature, that is the fractures and underlying matrix were assumed to be homogeneous. In Chapter 5, the application of direct numerical simulation for the same purpose was presented for a variety of test cases. Moreover, the two numerical codes used in this work, namely the MMOC2 and BIGFLOW simulators, were verified against each other for some rather complex and computationally challenging cases.

This chapter attempts to provide answers to the following questions. First, how sensitive is the RSRG approach to identifying the effects of various parameters on the effective properties of unsaturated, fractured rock? Second, is there a certain parameter range for which this method does not work? Third, what is the effect of variability in the underlying heterogeneous matrix and the overlying fracture network on the effective hydraulic conductivity? Finally, this chapter attempts to provide some additional verification of the RSRG method for the case of nonbinary systems, that is for systems where the matrix is heterogeneous.

6.1 DESIGN OF EXPERIMENTS

In order to address these issues, 36 experiments were designed to investigate the effect of the following on the effective properties of the combined matrix-fracture system:

- The standard deviation (σ) of the underlying porous medium matrix treated as a spatially correlated random field
- The correlation length of the underlying matrix along the X and Y axis (λ_x, λ_y) of the 2D domain, comprising 64×64 computational cells
- The degree of anisotropy in the correlation length
- The superimposed fracture volume (f) given as a percentage of the total volume
- The length of fractures (i.e., short or long) in the horizontal and vertical directions, as expressed by two inverse length parameters (xlmean, ylmean)
- The contrast between the mean value of the underlying matrix saturated conductivity (K_G^m) and superimposed fracture network (K_s^f), as expressed by the parameter $\omega = \log\ (K_s^f/K_G^m)$.

The range of each of the above parameters is as follows:

$0 \leq \sigma \leq 0.60$
$0 \leq \lambda_x, \lambda_y \leq 64$
$0 \leq f \leq 7$ percent
$K_s^f = 1.0$ cm/s
$K_G^m = 0.01$ or 0.001 cm/s
$0.001 \leq xlmean, ylmean \leq 1.5$

A list of the 36 numerical experiments is presented in Table 6-1. The experiments with a superscript of 1 attempt to determine: (i) the effect of variability in the underlying matrix for a fixed fracture network, and (ii) the effect of variability in the fracture network superimposed on a fixed underlying matrix. The experiments with a superscript of 2 were selected to compare the semi-analytical RSRG solution with BIGFLOW, which is a conventional numerical code that has been successfully tested and verified in the past. The soil properties of the underlying matrix and the assumptions used for all of the above experiments are as follows:

- The Gardner exponential and van Genuchten relationships are used for the description of the hydraulic conductivity versus pressure head and saturation versus pressure head characteristic curves, respectively.
- The van Genuchten parameter n of the soil is homogeneous and equal to 1.51.
- The bubbling pressure or air entry pressure head h_b for both the matrix and fractures is zero.
- The boundary conditions are such that flow is predominantly along the horizontal direction (X axis).
- The 2D domain size is 64 cm along both the X and Y axis.
- The majority of numerical experiments involve short fractures (i.e., $xlmean$, $ylmean = 1.5$). This means that the average fracture length is approximately one computational cell. At the other end of the spectrum, a value of 0.001 means that the fractures extend over the whole domain, that is 64 cells.

The RSRG approach and associated algorithm, presented in Chapter 4, are directly applicable for a binary matrix-fracture system. In order for this algorithm to apply in the case of heterogeneous matrix, the hydraulic properties of computational cells which correspond to the matrix must be inferred from certain *a priori* assumed bounds. Specifically, it is assumed that: (i) the matrix saturated conductivity cannot exceed the fracture saturated conductivity; (ii) all relevant hydraulic properties scale in some proportion to the saturated conductivities; and (iii) several physically based constraints apply, such as that the conductivity cannot become negative, or the slope of the logarithm of unsaturated conductivity versus pressure head curve cannot change sign within the domain.

Therefore, the scaling parameter α_m, (Gardner-α) of the heterogeneous matrix system is based on a linear interpolation (in the semi-log space) from a reference value α_m^* (corresponding to a reference value of saturated conductivity, K_s^{m*}) to α_f based on the following equation:

Table 6-1. List of experiments to study the effect of several parameters on effective conductivity of a stochastic matrix-fracture composite

Expt#	f(%)	xlmean	ylmean	σ	λ_x	λ_y	$\omega=\log(K_s^f/K_G^m)$
1	7	1.5	1.5	0	N/A	N/A	2
2	7	1.5	1.5	0	N/A	N/A	3
3	7	1.5	1.5	0.375	0	0	2
4	7	1.5	1.5	0.375	4	4	2
5	7	1.5	1.5	0.375	64	64	2
6	7	1.5	1.5	0.375	0	0	3
7	7	1.5	1.5	0.375	4	4	3
8	7	1.5	1.5	0.375	64	64	3
9	7	1.5	1.5	0.60	0	0	2
10	7	1.5	1.5	0.60	4	4	2
11(2)	7	1.5	1.5	0.60	64	64	2
12	7	1.5	1.5	0.60	0	0	3
13	7	1.5	1.5	0.60	4	4	3
14(2)	7	1.5	1.5	0.60	64	64	3
15(1)	7	1.5	1.5	0	N/A	N/A	2
16(1)	7	1.5	1.5	0	N/A	N/A	3
17(1)	7	1.5	1.5	0.375	4	4	2
18(1)	7	1.5	1.5	0.375	4	4	3
19	0	N/A	N/A	0.375	0	0	2
20	0	N/A	N/A	0.375	0	0	3
21	0	N/A	N/A	0.375	4	4	2
22	0	N/A	N/A	0.375	4	4	3
23	7	1.5	0.01	0	N/A	N/A	2

Table 6-1. List of experiments to study the effect of several parameters on effective conductivity of a stochastic matrix-fracture composite (cont'd)

Expt#	$f(\%)$	xlmean	ylmean	σ	λ_x	λ_y	$\omega=\log(K_s^f/K_G^m)$
19	0	N/A	N/A	0.375	0	0	2
20	0	N/A	N/A	0.375	0	0	3
21	0	N/A	N/A	0.375	4	4	2
22	0	N/A	N/A	0.375	4	4	3
23	7	1.5	0.01	0	N/A	N/A	2
24	7	1.5	0.01	0	N/A	N/A	3
25(2)	0	N/A	N/A	0.60	64	2	2
26(2)	0	N/A	N/A	0.60	64	2	3
27	0	N/A	N/A	0.60	0	0	2
28	0	N/A	N/A	0.60	0	0	3
29	7	1.5	1.5	0.60	64	2	2
30	7	1.5	1.5	0.60	2	64	2
31	7	1.5	1.5	0.60	2	64	3
32	7	1.5	1.5	0.60	64	2	3
33	0	N/A	N/A	0.60	64	64	2
34	0	N/A	N/A	0.60	64	64	3
35	0	N/A	N/A	0.60	2	64	2
36	0	N/A	N/A	0.60	2	64	3

$$\alpha_m = \alpha_f + \frac{\ln\left(K_s^f/K_s^m\right)}{\ln\left(K_s^f/K_s^{m*}\right)} * \left(\alpha_m^* - \alpha_f\right) \tag{6-1}$$

Thus, when the saturated conductivity K_s^m of a particular cell from the heterogeneous matrix system is K_s^{m*}, Eq. (6-1) yields $\alpha_m=\alpha_m^*$, and when $K_s^m=K_s^f$, Eq. (6-1) yields $\alpha_m=\alpha_f$.

The scaling parameter β_m of the heterogeneous matrix system is based on a linear interpolation from a reference value β_m^* (corresponding to a reference value of saturated conductivity, K_s^{m*}) to β_f based on the following equation:

$$\beta_m = \beta_m^* + \left(\beta_f - \beta_m^*\right) * \frac{K_s^m - K_s^{m*}}{\left(K_s^f - K_s^{m*}\right)} \tag{6-2}$$

From Eq. (6-2) it follows that for $K_s^m=K_s^f$ we get $\beta_m=\beta_f$; and for $K_s^m=K_s^{m*}$ we get $\beta_m=\beta_m^*$. The properties used for performing the scaling described in Eqs. (6-1) and (6-2) are given by:

- The scaling parameter α_m of the matrix for the conductivity-pressure relationship in Eq. (6-1) is 0.025 cm^{-1}.
- The scaling parameter α_f of the superimposed fracture for the conductivity-pressure relationship in Eq. (6-1) is 0.075 cm^{-1}.
- The scaling parameter β_m of the matrix for the van Genuchten moisture retention in Eq. (6-2) is 0.01 cm^{-1}.
- The scaling parameter β_f of the superimposed fracture network for the van Genuchten moisture retention in Eq. (6-2) is 0.05 cm^{-1}.

Finally, the fractures are generated based on the following:

- Fracture centers are exponentially distributed.
- For different realizations, the cluster-of-fractures center is randomly selected.
- For every horizontal fracture, the probability of a vertical fracture is 1.0 (i.e., the fracture network system is isotropic), unless otherwise stated.

6.2 SUMMARY OF PARAMETRIC STUDY RESULTS

In the following section, we summarize the results of the experiments. This section has been subdivided into three main subsections to facilitate understanding of the observations made during the numerical experiments. Each subsection is further subdivided depending on the parameter or variable used to study the sensitivity or variability of the effective conductivity of the combined matrix-fracture system.

6.2.1 Fractured Matrix (f=7 percent)

In the following sections, we discuss those experiments in Table 6-1 that show the effect of the parameters/variables on the effective conductivity of an underlying matrix superimposed with a fracture network of volume 7 percent.

6.2.1.1 Effect of Matrix Standard Deviation σ

Experiments 1, 4, 10 and 2, 7, 13 show the effect of varying the matrix heterogeneity, as expressed by the standard deviation σ, from 0 to 0.60 on the effective conductivity of the combined matrix-fracture system, while the matrix correlation length along the X and Y axis ($\lambda_x = \lambda_y = 4$) as well as the fracture volume (f=7 percent) are kept fixed. Figure 6-1 illustrates the effect of σ on the effective conductivity of the matrix-fracture system for two geometric mean values of the matrix, namely $K_G^{m\,1}$=0.01 cm/s and $K_G^{m\,2}$=0.001 cm/s. As can be seen from Figure 6-1, varying the matrix standard deviation does not have a noticeable effect on the effective conductivity of the matrix-fracture system, except at high suction heads for the case of $K_G^{m\,1}$ = 0.01 cm/s in which a more heterogeneous matrix produces a lower effective conductivity.

6.2.1.2 Effect of Matrix Mean

The experiments described in Table 6-1 serve to confirm that the mean of the underlying matrix conductivity has a direct effect on the effective conductivity of the matrix-fracture system. A high mean value for the matrix conductivity results in a higher effective conductivity of the matrix-fracture system. This is also illustrated in Figure 6-2 for the case of experiments 25 and 26, where the heterogeneity of the matrix is kept fixed (σ=0.60) and a highly anisotropic matrix field is used.

6.2.1.3 Effect of Matrix Correlation Length λ

Experiments 3, 4, 5 and 6, 7, 8 show the effect of varying the matrix correlation length (λ_x=λ_y=0, 4, 64) on the effective conductivity of the combined matrix-fracture system, while the matrix standard deviation (σ=0.375) and fracture volume (f=7 percent) are fixed. Figure 6-3 illustrates the effect of λ on the effective conductivity of the matrix-fracture system for two mean values of the matrix, namely $K_G^{m\,1}$=0.01 cm/s and $K_G^{m\,2}$=0.001 cm/s. As can be seen from Figure 6-3, varying the correlation length of the matrix has, in general, a smaller effect on the effective conductivity than the mean of the matrix conductivity. In the zone close to saturation (low suction head region), a larger correlation length results in lower effective conductivity. The explanation for this observation is that smaller correlation lengths result in shorter pathways which in turn allow more water to flow between these pathways and the more conductive short fractures. In the dry zone (high suction head), varying the correlation length

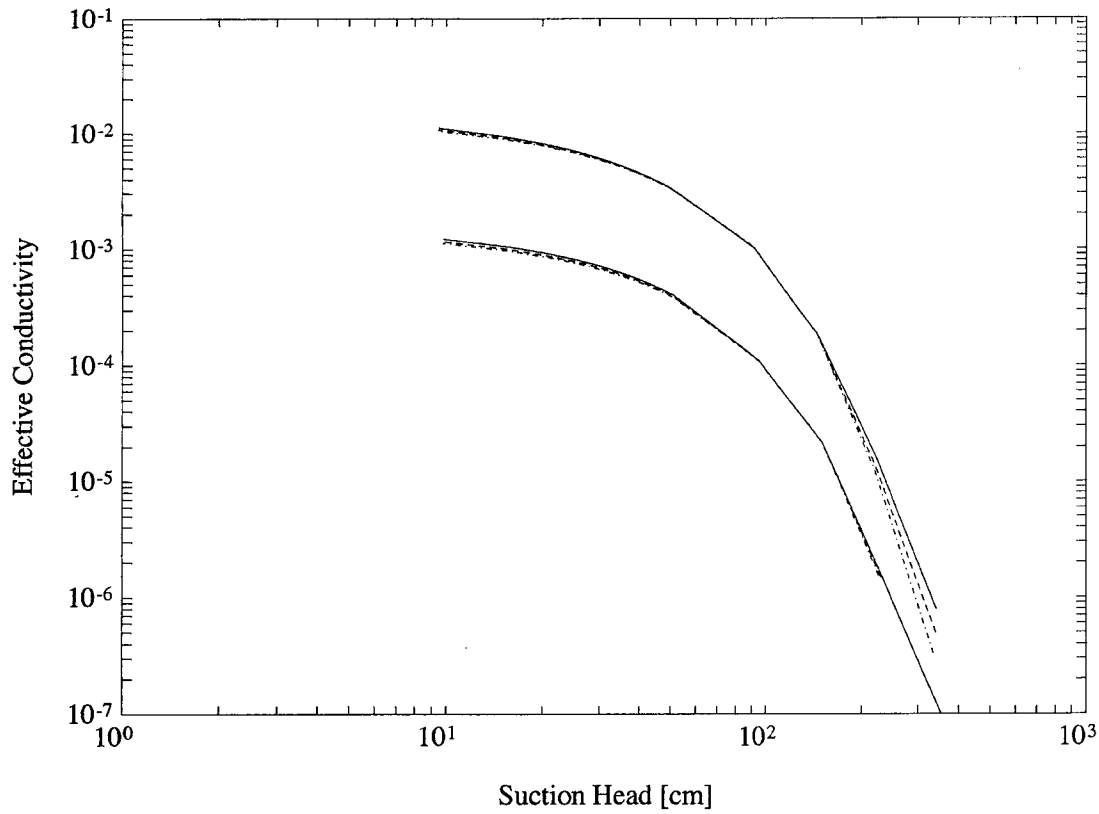

Figure 6-1. Effect of matrix standard deviation on the effective hydraulic conductivity of a fractured medium. Experiments 1 and 2 (σ=0.0; solid), 4 and 7 (σ=0.375; dashed), and 10 and 13 (σ=0.60; dash-dot).

of the matrix has no effect for K_G^m =0.001 cm/s. However, increasing K_G^m to 0.01 cm/s causes a partial reversal of the effect observed at low suction heads, without the results being totally conclusive. Nevertheless, this result is consistent with the observations by Pruess and Tsang (1990) who found that, under capillary-dominated flow regimes, a larger correlation in small apertures yields higher connectivity.

Experiments 9, 10, 11 and 12, 13, 14 show the effect of varying the matrix correlation length (λ_x=λ_y=0, 4, 64) on the effective conductivity of the combined matrix-fracture system, while the matrix standard deviation (σ=0.60) and fracture volume (f=7 percent) are fixed. A comparison of the results of experiments 3, 4, 5, 9, 10, 11 and 6, 7, 8, 12, 13, 17 indicated that the effects of the matrix correlation length are negligible for both levels of matrix heterogeneity. Since the results of experiments 9, 10, 11 and 12, 13, 14 were very similar to experiments 3, 4, 5 and 6, 7, 8 they are not reported here.

6.2.1.4 Effect of Increasing Fracture Volume

Experiments 19, 3, 20, and 6 examine the effect of increasing the fracture volume on the effective conductivity of the combined matrix-fracture system, while fixing the matrix standard deviation (σ = 0.375) and correlation lengths (λ_x=λ_y=0), as shown in Figure 6-4. As expected, increasing the

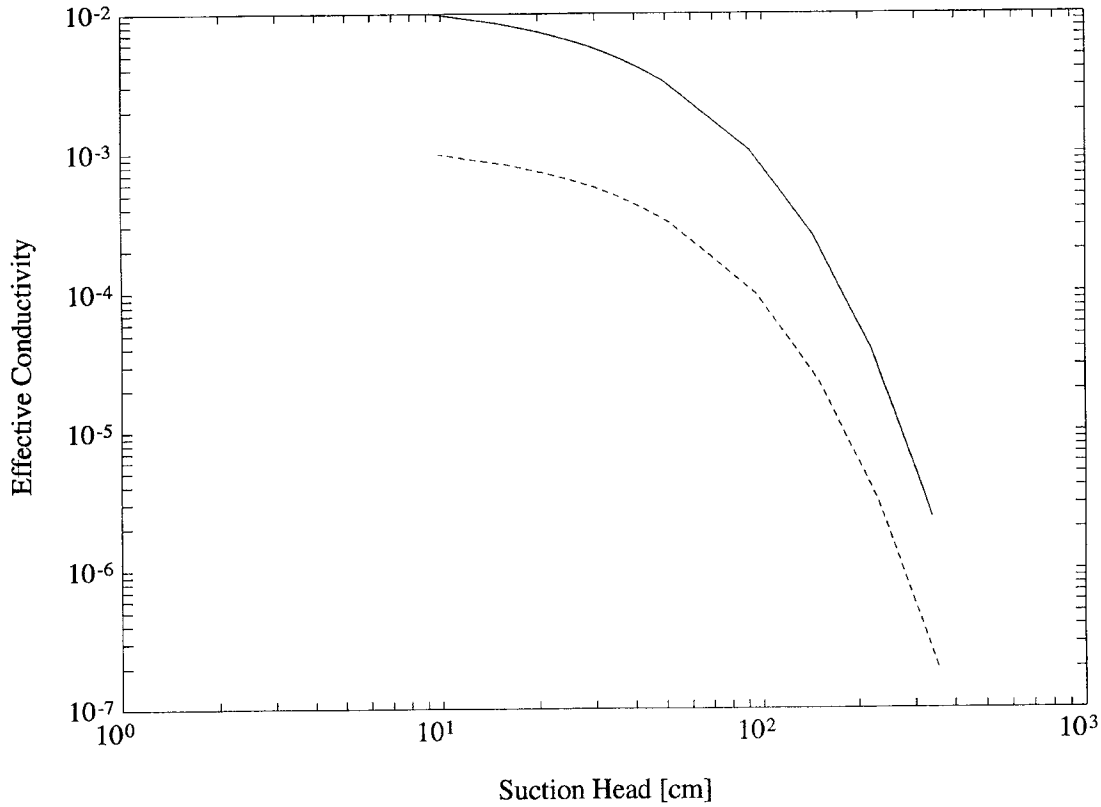

Figure 6-2. Effect of the mean value for the matrix saturated conductivity on the effective conductivity of the combined matrix-fracture system. $K_G^{m^1}$ = 0.01 cm/s (solid), and $K_G^{m^2}$ = 0.001 cm/s (dashed).

fracture volume results in higher effective conductivity for both cases of $K_G^{m\ 1}$ =0.01 cm/s and $K_G^{m\ 2}$ =0.001 cm/s. Moreover, this figure shows that the aforementioned observation is reversed at higher suction heads (dry zone); that is a matrix with no fractures results in a higher effective conductivity compared to one with 7 percent fractures.

The effect of increasing the fracture volume on the effective conductivity of the combined matrix-fracture system for a spatially correlated matrix field was examined with experiments 21, 4, 22, and 7. The results obtained in this case were consistent with the behavior shown in Figure 6-4, and are not reported here.

6.2.1.5 Effect of Anisotropy in Fracture Length, and Matrix Correlation Length

Experiments 23, 1, 24, and 2 show the effect of anisotropy in the fracture length on the effective conductivity, while the matrix is homogeneous (σ=0.0) and the fracture volume (f=7 percent) is fixed. In these experiments, the lengths of vertical fractures were increased to an approximate average length of 20 computational cells. The anisotropy in the fracture length does have a noticeable effect on the effective conductivity of the combined matrix-fracture system. As the fractures along the Y axis

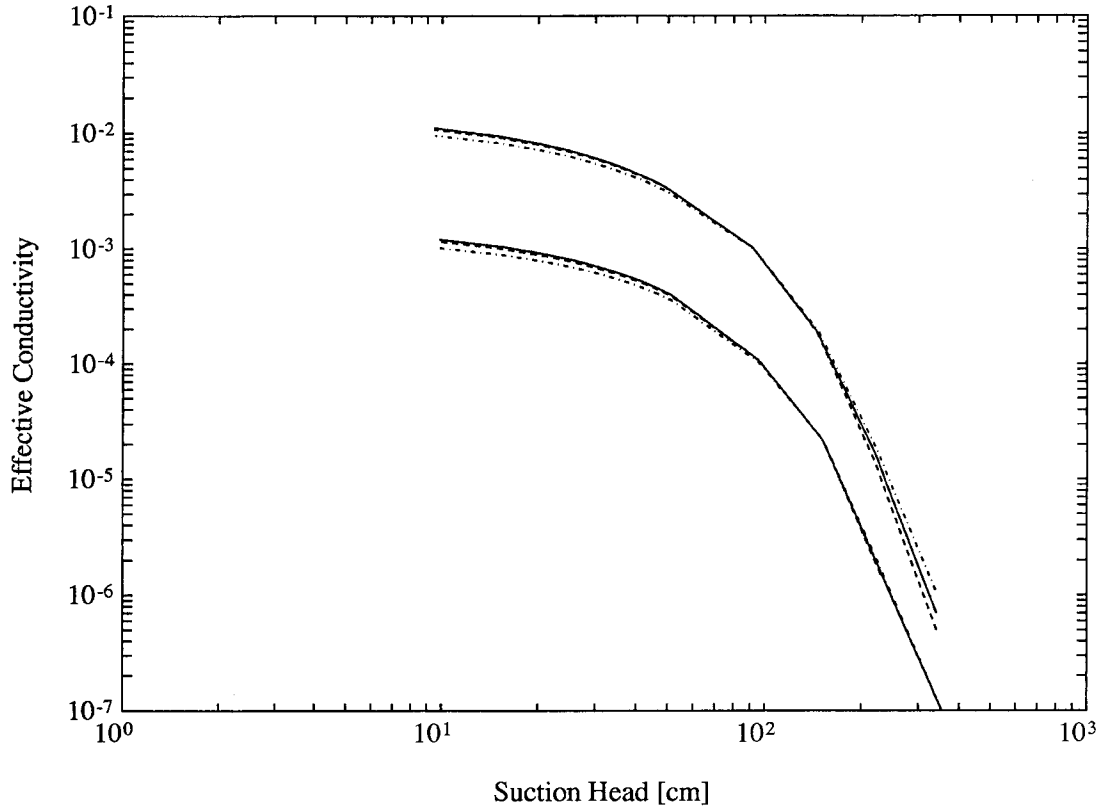

Figure 6-3. Effect of matrix isotropic correlation length on the effective conductivity of a fractured medium. Experiments 3 and 6 (λ=0; solid), 4 and 7 (λ=4; dashed), and 5 and 8 (λ=64; dash-dot).

(vertical direction) get longer, the effective conductivity of the combined matrix-fracture system increases as a consequence of the enhanced cross-flow which allows water to find other highly conductive pathways. Figure 6-5 illustrates the effect of fracture length anisotropy on the effective conductivity of the combined matrix-fracture system.

Experiments 29 and 11 show the effect of varying the matrix correlation λ_y along the Y axis (i.e., varying the lengths of the features along the Y axis) on the effective conductivity of a fractured medium, while fixing the matrix standard deviation σ=0.6, the correlation length λ_x=64 along the X axis, the fracture volume (f=7 percent), and the matrix mean K_G^m=0.01 cm/s. Experiments 31 and 14 vary λ_x (i.e., varying the lengths of the features along the X axis) on the effective conductivity of a fractured medium, while fixing the matrix standard deviation σ=0.6, the Y axis correlation length λ_y=64 and the matrix mean K_G^m=0.001 cm/s. Figure 6-6 shows the effect of each of the correlation lengths along the X and Y axis individually on the effective conductivity of a fractured medium. It is interesting to note that in both cases, the incorporation of anisotropy enhances the effective conductivity near saturation but has relatively little effect at the dry region.

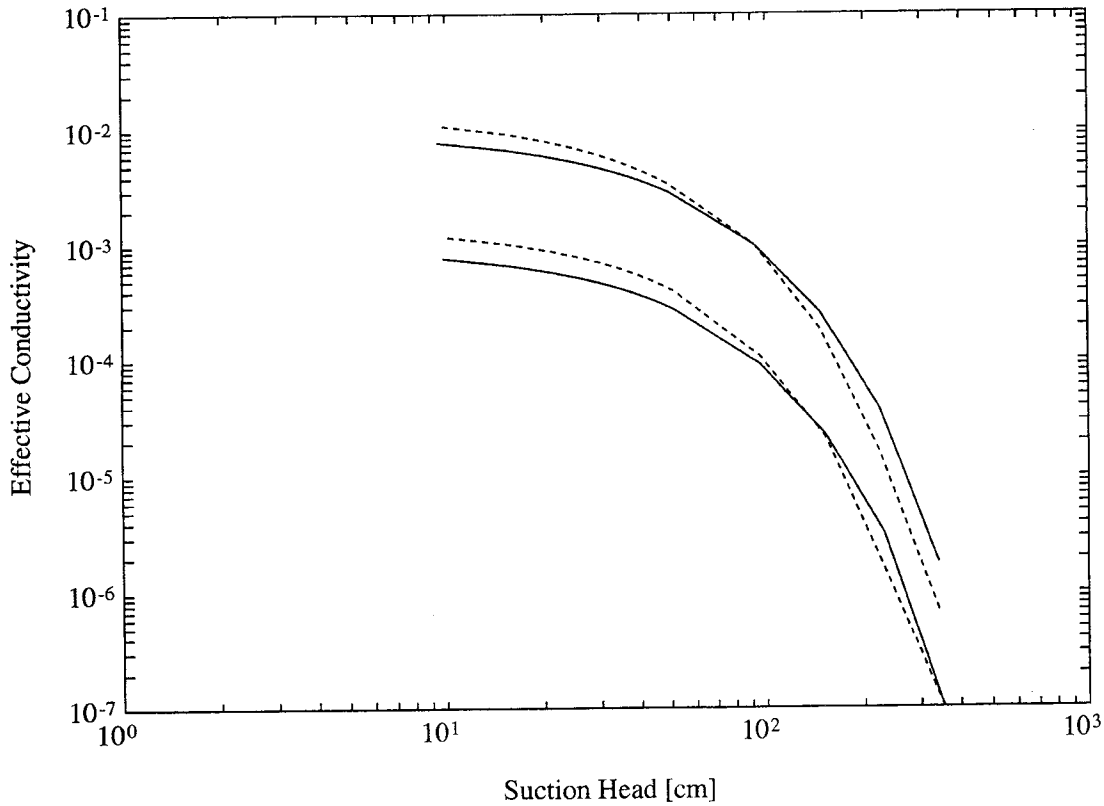

Figure 6-4. Effect of increasing fracture volume on the effective conductivity of a fractured medium. Experiments 19 and 20 (f=0; solid) and 3 and 6 (f=7; dashed).

6.2.2 Nonfractured Matrix

In the following section, those experiments examining the effect of the parameters/variables on the effective conductivity of the underlying matrix alone are discussed. No fractures are considered in this case.

6.2.2.1 Effect of Matrix Spatial Structure

Experiments 19, 20, 21, and 22 show the effect of varying the matrix correlation length ($\lambda_x=\lambda_y=0$, 4) on the effective conductivity of an unfractured matrix, while fixing the matrix standard deviation ($\sigma=0.375$). Figure 6-7 illustrates the effect of the matrix correlation length (λ) on the effective conductivity of a matrix with no fractures. As shown in Figure 6-7, the isotropic matrix correlation length has no effect on the effective conductivity of an nonfractured matrix. This is the case for both $K_G^{m\,1}=0.01$ cm/s and $K_G^{m\,2}=0.001$ cm/s over the entire range of suction heads. Note that the correlation length did not have a noticeable effect on the effective conductivity of a fractured matrix either (see Figure 6-3).

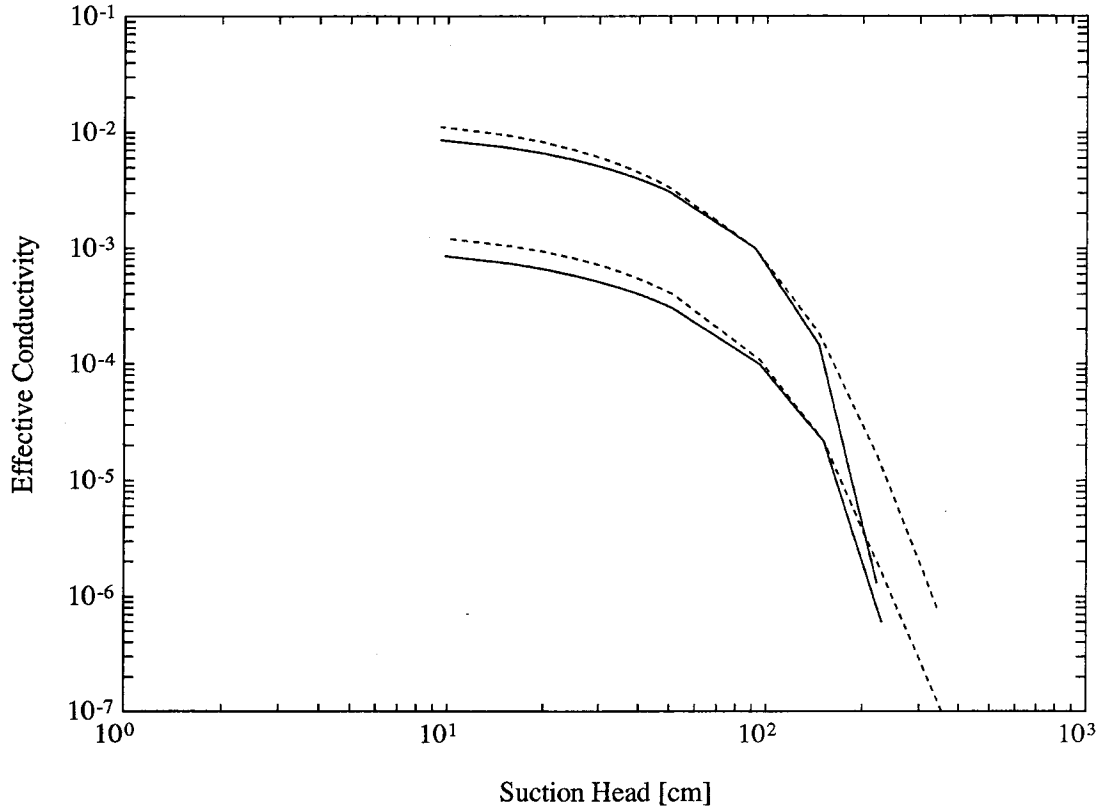

Figure 6-5. Effect of fracture length anisotropy on the effective conductivity of a fractured medium. Experiments 23 and 24 (*yl*mean=0.01; solid), and 1 and 2 (*yl*mean=1.5; dashed).

6.2.2.2 Effect of Anisotropy in Matrix Correlation Length

Experiments 25, 26, 33, and 34 show the effect of varying the correlation λ_y along the *Y* axis (i.e., varying the lengths of the features along the *Y* axis) on the effective conductivity of an unfractured medium, while fixing the matrix standard deviation σ=0.6, the correlation length λ_x=64 along the *X* axis. Figure 6-8 shows the effect of the correlation lengths along the *Y* axis on the effective conductivity of an unfractured medium. Comparing Figure 6-8 to 6-6, we conclude that the effect of correlation length anisotropy is much more pronounced in the case of a fractured medium near saturation. At the dry region there is no noticeable difference. Similar results were observed for experiments 33, 34, 35, and 36 where λ_x was varied (not shown).

6.2.2.3 Effect of Matrix Standard Deviation

Experiments 27, 28, 19, and 20 show the effect of the matrix standard deviation σ on the effective conductivity of an unfractured matrix, while fixing the matrix correlation length (λ_x=λ_y=0). Figure 6-9 illustrates the effect of the spatially uncorrelated matrix standard deviation σ on the effective conductivity of an unfractured matrix. As can be seen from this figure, varying the matrix standard deviation has no effect on the effective conductivity of a nonfractured medium for the whole range of suction, contrary to the case of a fractured medium (Figure 6-1).

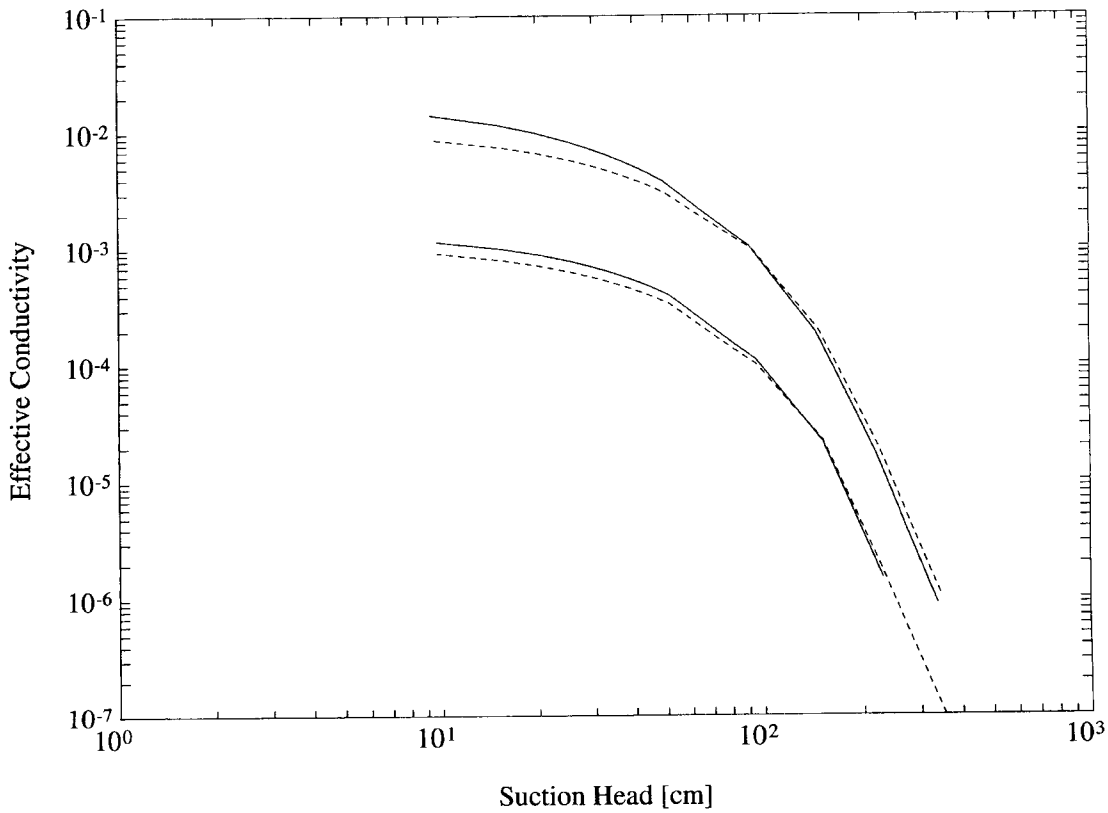

Figure 6-6. Effect of anisotropy in correlation length on the effective conductivity of a fractured medium. Experiments 29 and 31 (λ_x/λ_y=32 and 1/32; solid), and 11 and 14 ($\lambda_x=\lambda_y$=64; dashed).

6.3 SUMMARY OF MULTIPLE REALIZATION STUDY RESULTS

The following section is a study of: (i) the effect of variability in the fracture network for a fixed underlying matrix, and (ii) the effect of variability in the matrix for a fixed fracture network on the effective conductivity of the combined matrix-fracture system.

6.3.1 Effect of Variability in Fracture Network for Fixed Fracture Volume

In experiment 15, the variability in statistically equivalent fracture networks was realized by superimposing 24 random fracture networks with identical fracture volume on a fixed underlying homogeneous matrix with mean saturated conductivity K_G^m=0.01 cm/s. An ensemble mean effective conductivity along with the associated standard deviations was computed from the 24 matrix-fracture realizations. Experiment 16 is very similar to experiment 15 with the difference being that K_G^m=0.001 cm/s. Similar to experiment 15, an ensemble mean effective conductivity along with standard deviations was computed from the 24 matrix-fracture realizations. Figure 6-10 shows the mean effective conductivity of all 24 realizations along with the standard deviation. Figure 6-11 shows the relative variability of the effective conductivity for all 24 realizations, defined as the ratio between the ensemble standard deviation and mean (also known as the coefficient of variation).

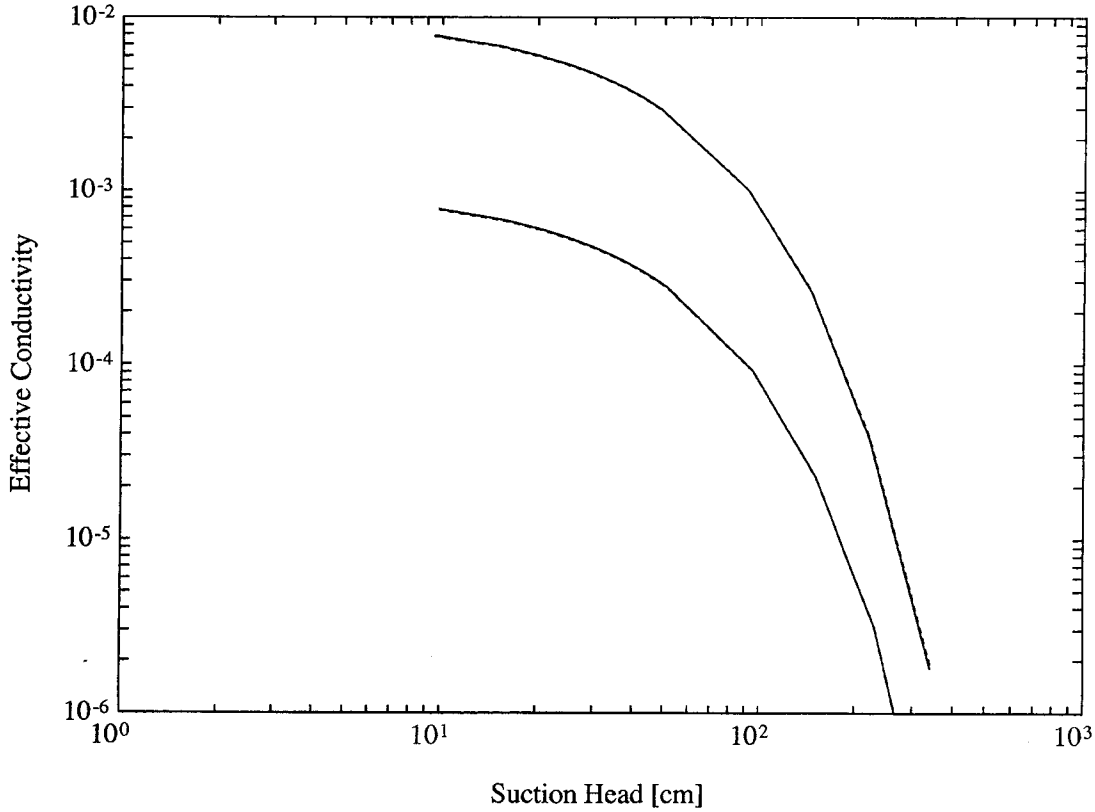

Figure 6-7. Effect of matrix spatial structure on the effective conductivity of an unfractured medium. Experiments 19 and 20 (λ=0; solid) and 21 and 22 (λ=4; dashed).

Figures 6-10 and 6-11 show that the relative variability of the effective conductivity is a minimum in the region of mid-suction head. The variability of the effective conductivity increases at both low and high suction regions. Comparing experiments 15 and 16, it is clear that the effect of fracture network variability is more pronounced for sharper contrast between the matrix and fractures. Thus, the relative variability in the effective conductivity for experiment 16 ranges between 1 and 50 percent; in the case of experiment 15, it ranges between 0.01 and 30 percent.

In experiment 17, the variability in the fracture network was realized by superimposing 24 random fracture networks with identical fracture volume on a fixed underlying heterogeneous matrix with standard deviation σ=0.375, isotropic correlation length λ=4, and mean saturated conductivity K_G^m=0.01 cm/s. The mean effective conductivity along with associated standard deviations were computed from the 24 matrix-fracture realizations. Figure 6-12 shows the mean effective conductivity of all 24 realizations along with the standard deviation, whereas Figure 6-13 shows the relative variability (or coefficient of variation) of the effective conductivity for all 24 realizations. Figures 6-12 and 6-13 also show that the relative variability of the effective conductivity is a minimum in the region of mid-suction head. The variability of the effective conductivity increases at both the low and high suction zones to 10

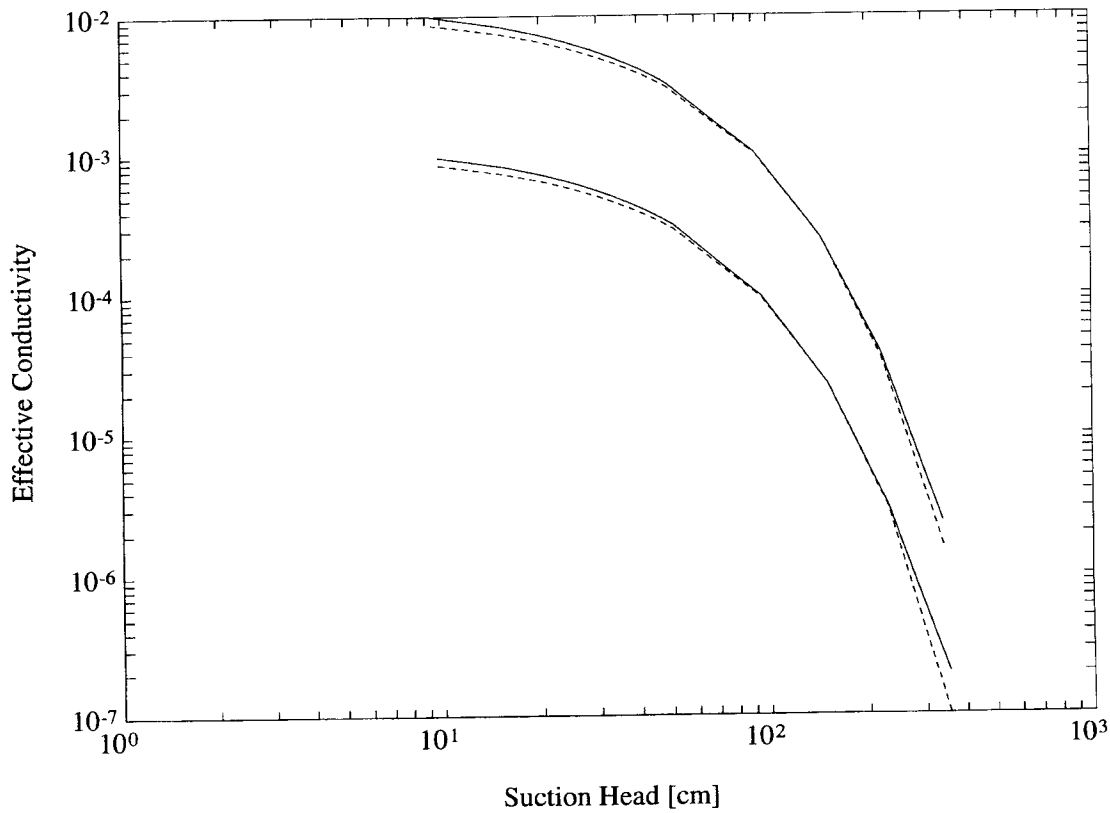

Figure 6-8. Effect of anisotropy in correlation length on the effective conductivity of an unfractured medium. Experiments 25 and 26 ($\lambda_y=2$; solid) and 33 and 34 ($\lambda_y=64$; dashed).

and 50 percent, respectively. Experiment 18 is a repetition of experiment 17 with $K_G^m=0.001$ cm/s. In this case the variability of the effective conductivity at both low and high suction zones is 60 percent, which is consistent with the results obtained for a homogeneous matrix.

6.3.2 Effect of Variability in Matrix for a Fixed Fracture Network

Experiments 17 and 18 were selected to further determine the effect of variability of a heterogeneous matrix with a fixed fracture network on the effective conductivity of the combined matrix-fracture system. In experiment 17, the variability in matrix was realized by superimposing a fixed fracture network on 24, statistically equivalent, realizations of a heterogeneous matrix with standard deviation $\sigma=0.375$, isotropic correlation length $\lambda=4$, and mean saturated conductivity $K_G^m=0.01$ cm/s. Figure 6-14 shows the mean effective conductivity of all 24 realizations along with the standard deviation. Figure 6-15 shows the relative variability of the effective conductivity for all 24 realizations. These figures demonstrate that the effect of variability in a heterogeneous matrix on the relative variability of effective conductivity is, in general, comparable to the relative variability obtained by superimposing 24 fracture network realizations on a fixed matrix.

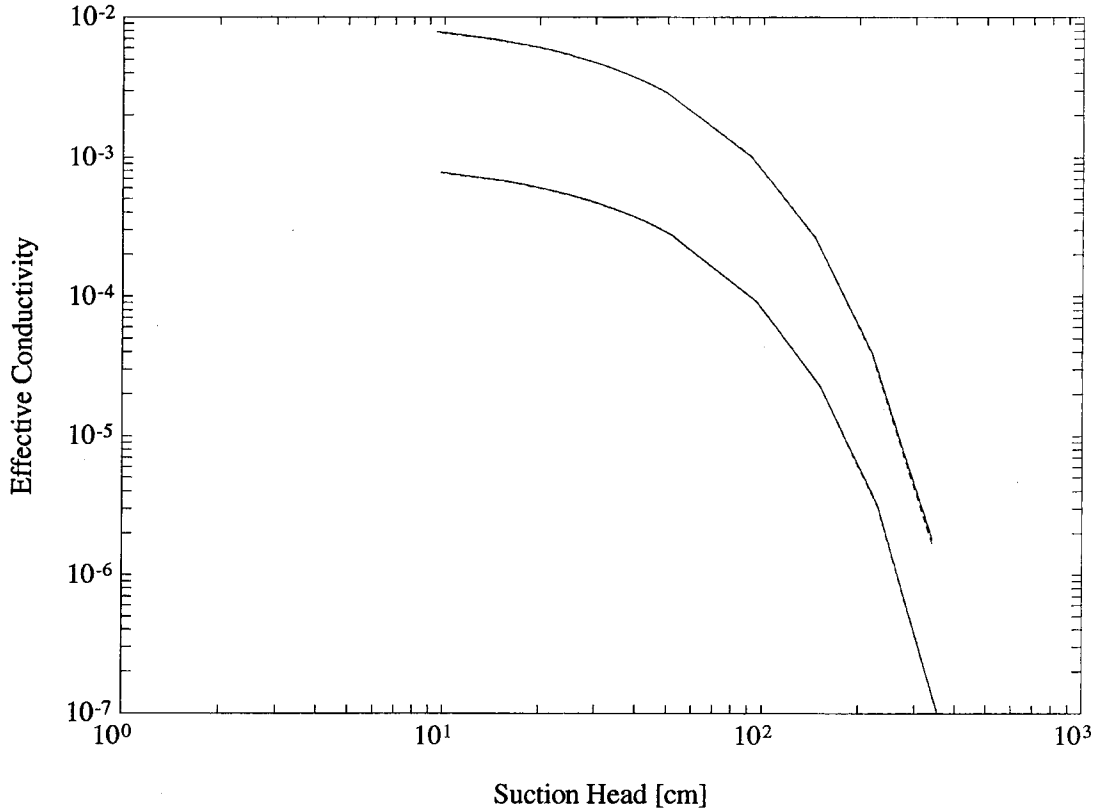

Figure 6-9. Effect of matrix standard deviation on the effective conductivity of an unfractured matrix. Experiments 19 and 20 (σ=0.375; solid) and 27 and 28 (σ=0.60; dashed).

Figure 6-16 shows the mean effective conductivity of all 24 realizations along with the standard deviation for experiment 18, which deals with a K_G^m=0.001 cm/s. Figure 6-17 shows the relative variability of the effective conductivity for all 24 realizations. Figures 6-16 and 6-17 show that the relative variability of the effective conductivity is, in general, comparable to the relative variability obtained by superimposing 24 fracture network realizations on a fixed matrix for all levels of contrast between the mean matrix and fracture conductivities.

6.4 SUMMARY OF REAL SPACE RENORMALIZATION GROUP VERIFICATION RESULTS FOR NONBINARY SYSTEMS

As discussed earlier, four experiments (11, 14, 25, and 26) were reproduced with direct numerical simulations in order to further test the validity of the RSRG approach for the case of nonbinary matrix-fracture systems. Experiments 25 and 26 dealt with a nonbinary fractured, heterogeneous (σ=0.60) matrix, which is characterized by a high level of anisotropy in its correlation length. More specifically, λ_x=64 and λ_y=2, signifying that the system essentially consists of horizontal layers of varying heterogeneous material. An approach similar to the one described in Chapter 5 was followed, using the BIGFLOW numerical code. Figures 6-18 and 6-19 depict the comparison between the RSRG and

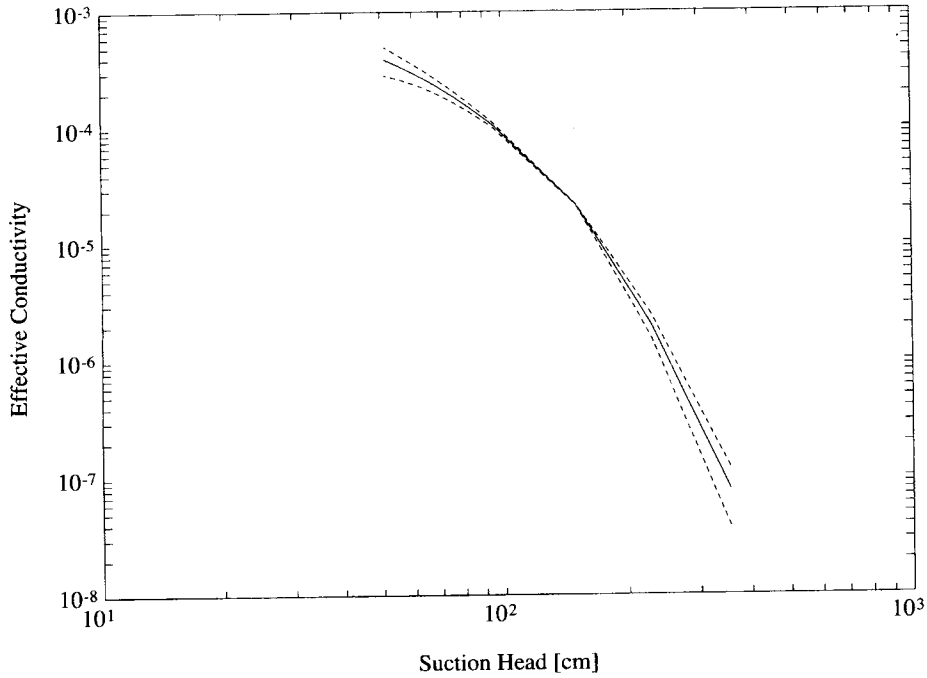

Figure 6-10. Mean (solid) and standard deviation (dashed) of the 24 realizations of fracture networks superimposed on the fixed matrix of experiment 16

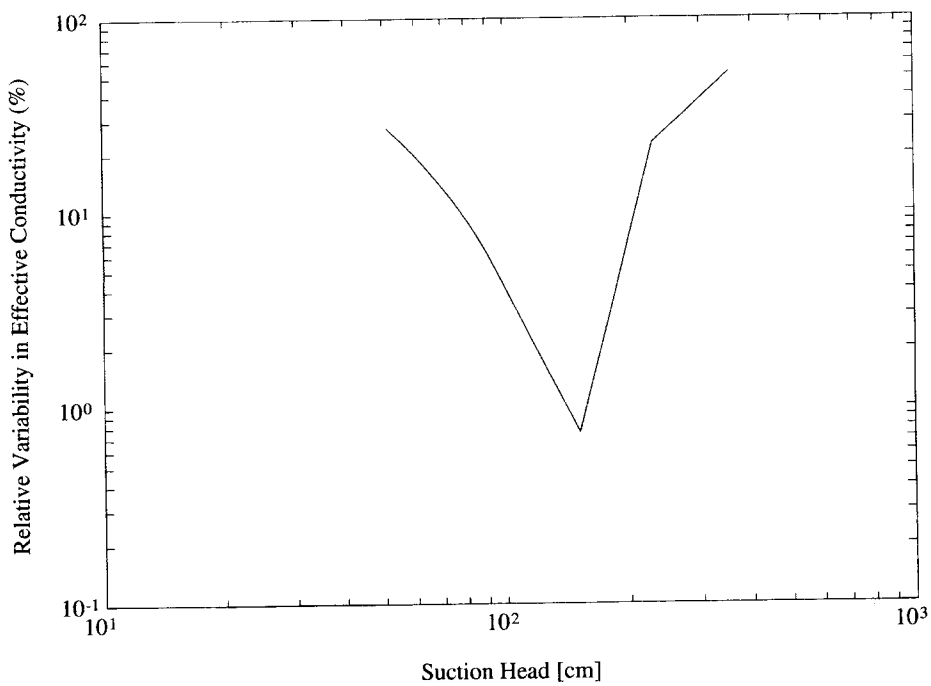

Figure 6-11. Relative variability of the effective conductivity for 24 fracture network realizations on the fixed matrix of experiment 16

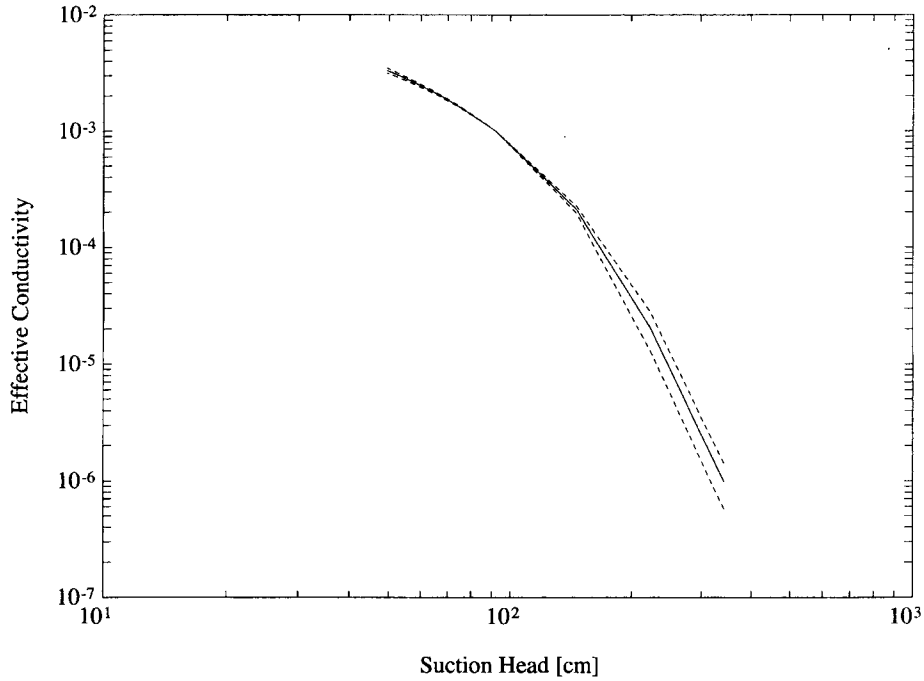

Figure 6-12. Mean (solid) and standard deviation (dashed) of the 24 realizations of fracture networks superimposed on the fixed matrix of experiment 17

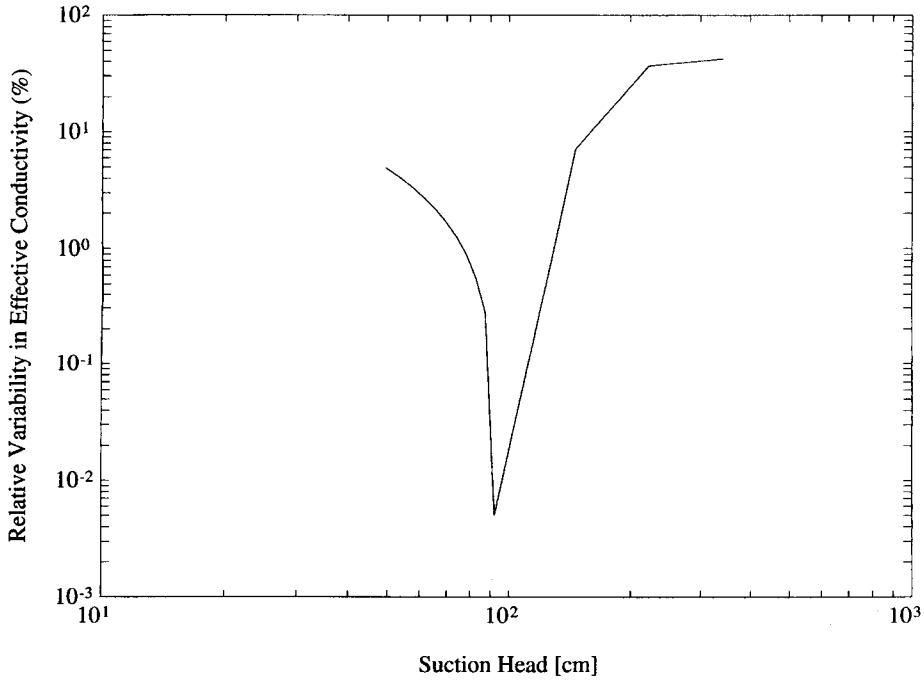

Figure 6-13. Relative variability of the effective conductivity for 24 fracture network realizations on the fixed matrix of experiment 17

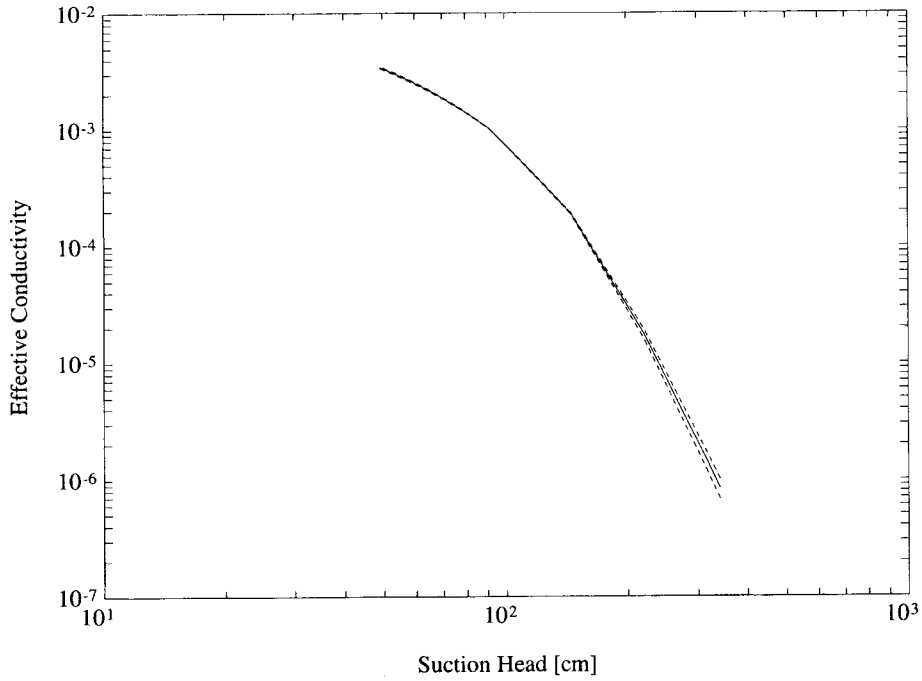

Figure 6-14. Mean (solid) and standard deviation (dashed) of a fixed fracture network superimposed on 24 realizations of the matrix of experiment 17

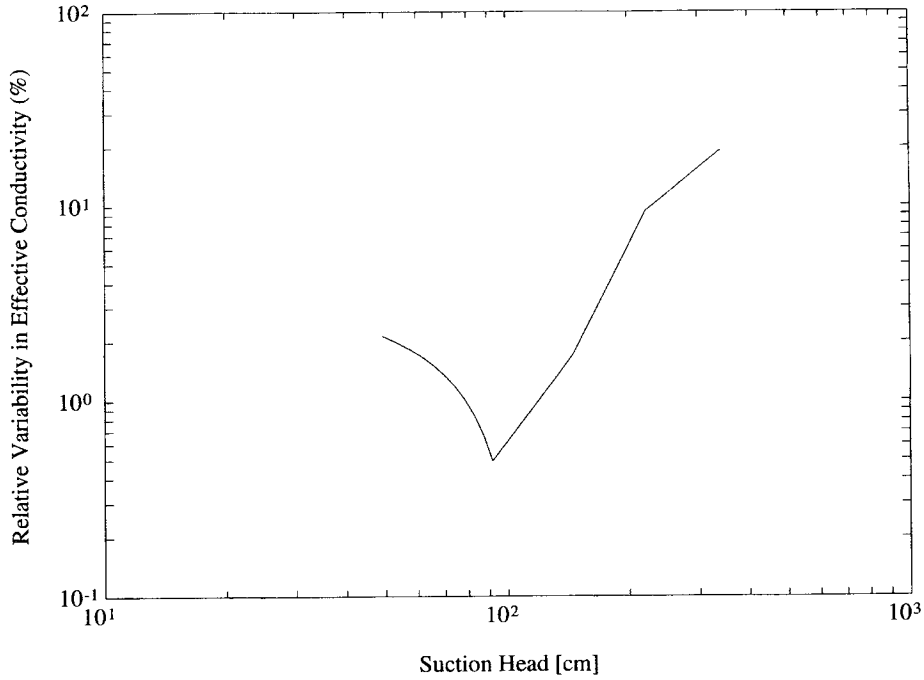

Figure 6-15. Relative variability of the effective conductivity for a single fracture network superimposed on 24 realizations of the matrix of experiment 17

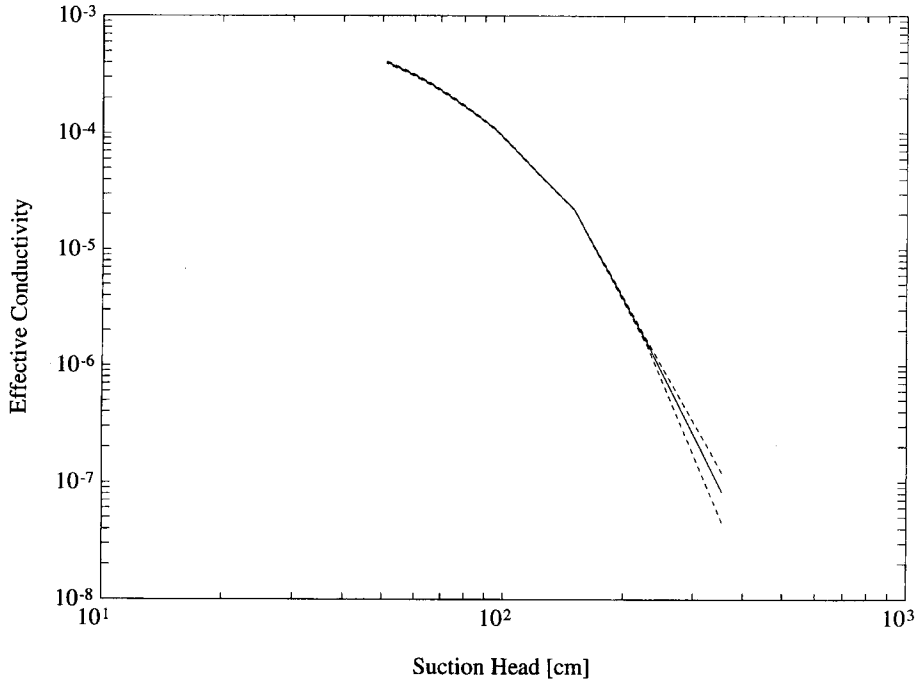

Figure 6-16. Mean (solid) and standard deviation (dashed) of a fixed fracture network superimposed on 24 realizations of the matrix of experiment 18

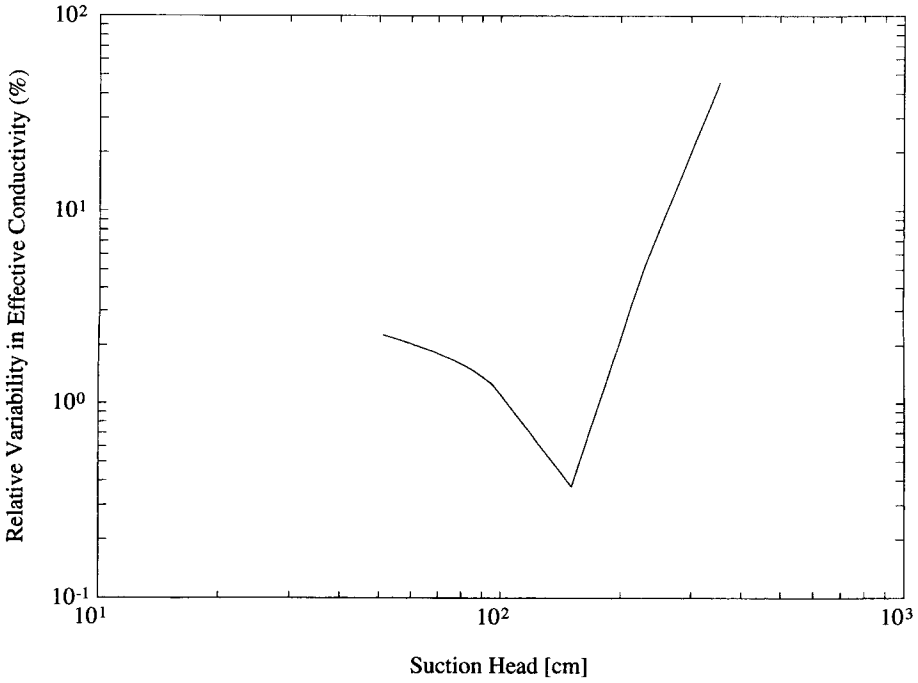

Figure 6-17. Relative variability of the effective conductivity for a single fracture network superimposed on 24 realizations of the matrix of experiment 18

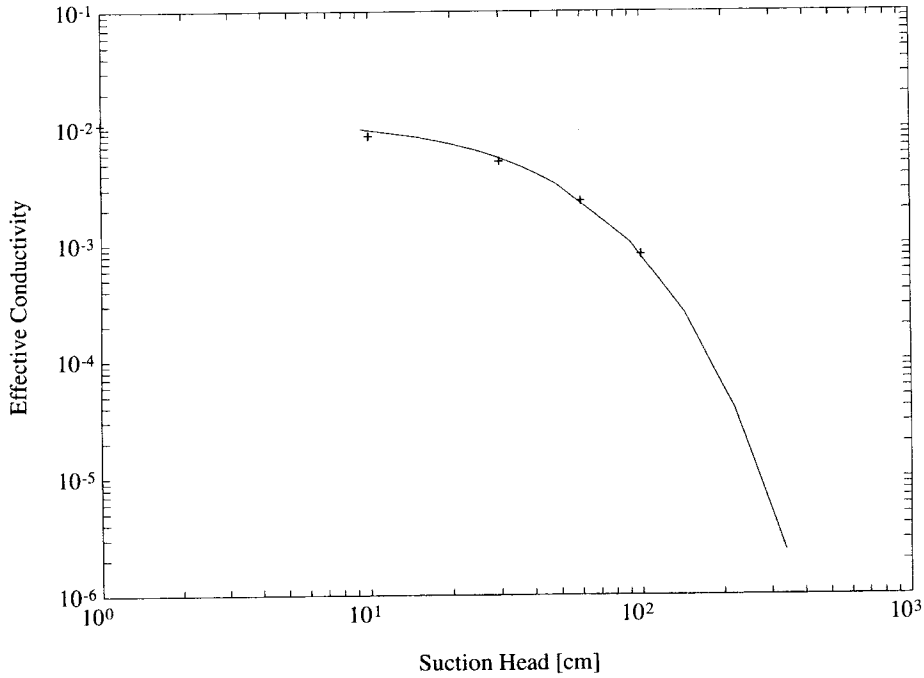

Figure 6-18. Comparison of Real Space Renormalization Group and BIGFLOW results for a heterogeneous, anisotropic, nonfractured matrix field with K_G^m = 0.01 cm/s

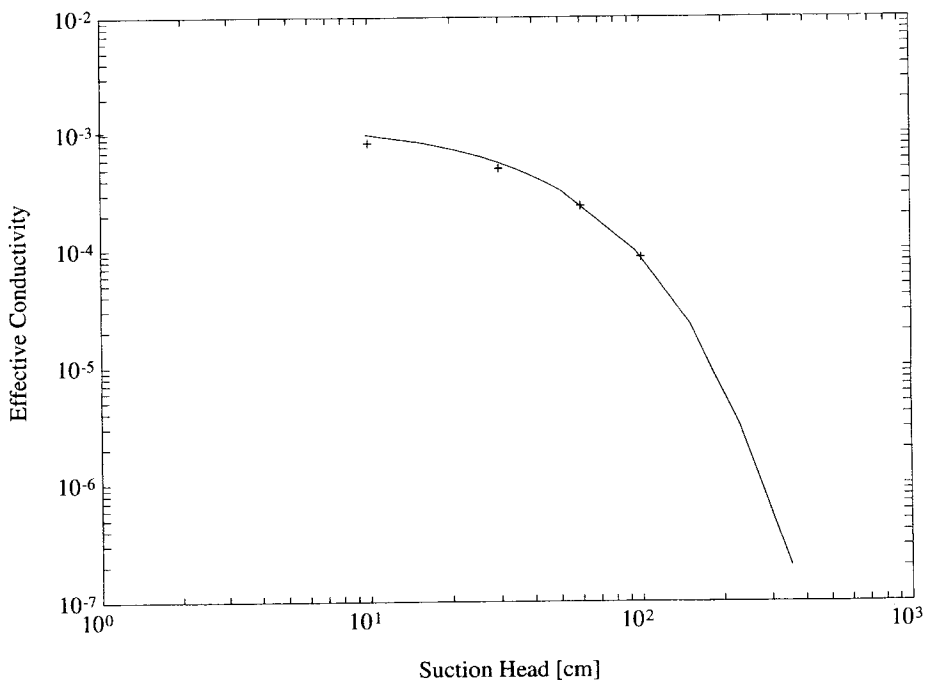

Figure 6-19. Comparison of Real Space Renormalization Group and BIGFLOW results for a heterogeneous, anisotropic, nonfractured matrix field with K_G^m = 0.001 cm/s

BIGFLOW results for $K_G^m = 0.01$ cm/s, and $K_G^m = 0.001$ cm/s, respectively. For both levels of the geometric mean of the heterogeneous matrix field, very good agreement is observed.

Experiments 11 and 14 dealt with a fractured, heterogeneous, isotropic matrix (σ=0.60). However, both experiments imposed an unrealistically large correlation length for the heterogeneous matrix. As a result, the generated matrix field consisted of two or three large-size blocks of homogeneous material. Since these blocks differed in terms of properties, the result was a patch-like heterogeneous material. Figure 6-20 depicts the comparison between the RSRG and BIGFLOW results for $K_G^m = 0.01$ cm/s. It can be seen that the two methods do not compare favorably, especially near saturation. This observation persists in the case of experiment 14. In this experiment, the RSRG method exhibited serious difficulties and produced totally erroneous results. Mohanty (1993) has identified the Simple Recursive Spatial Averaging (SRSA) as a possible explanation for this problem. He points out that the SRSA method could provide incorrect answers because it attempts to apply a statistical method in an absolute sense to lattices with fixed geometry. Therefore, in cases where the correlation length is large, the clusters of heterogeneity grow in size. According to Mohanty (1993), this translates to "[t]he formation of larger, more compact clusters of conducting sites [, and] results in poor connectivity between conducting sites." This explains why the RSRG results, underestimate the effective conductivity, when compared to the direct numerical simulation results.

In order to investigate this limitation of the RSRG further, another numerical experiment was conducted. This experiment corresponds to Figure 5-19, and involves a set of long fractures with an approximate volume fraction of 14 percent. The fracture network is superimposed on a heterogeneous matrix field which is characterized by a correlation length approximately equal to the size of the domain and a $K_G^m = 0.0001$ cm/s. In this case, probably due to the fact that the volume fraction of fractures was 14 percent (as opposed to 7 percent), the RSRG approach produced results even though it was not expected to do so (in light of the findings of experiment 14). However, as demonstrated in Figure 6-21, the comparison between the RSRG and BIGFLOW results is extremely unfavorable for the RSRG method.

6.5 DISCUSSION

A series of 36 numerical experiments was conducted to investigate the effect of: (i) the underlying porous medium matrix heterogeneity; (ii) the spatial structure of the underlying porous medium matrix; (iii) the degree of fracturing, as expressed by the fracture volume fraction; (iv) the length of fractures; and (v) the contrast between the underlying matrix and superimposed fracture saturated conductivity on the effective hydraulic conductivity of the combined matrix-fracture system. Furthermore, some of these experiments served as verification exercises for the RSRG method in the case of nonbinary systems, and indicated some limitations of the method.

Based on the results of these simulations it is concluded, in general, that the RSRG method provides a viable alternative to direct numerical simulation techniques for the calculation of effective hydraulic properties. This was found to be true at two levels of contrast between the saturated hydraulic conductivities of matrix and fractures, and in the case of nonbinary fractured, heterogeneous matrix with high level of anisotropy in its correlation length. The RSRG was found to be limited, in terms of performance against direct numerical techniques, when the underlying matrix is characterized by unrealistically large, isotropic correlation lengths.

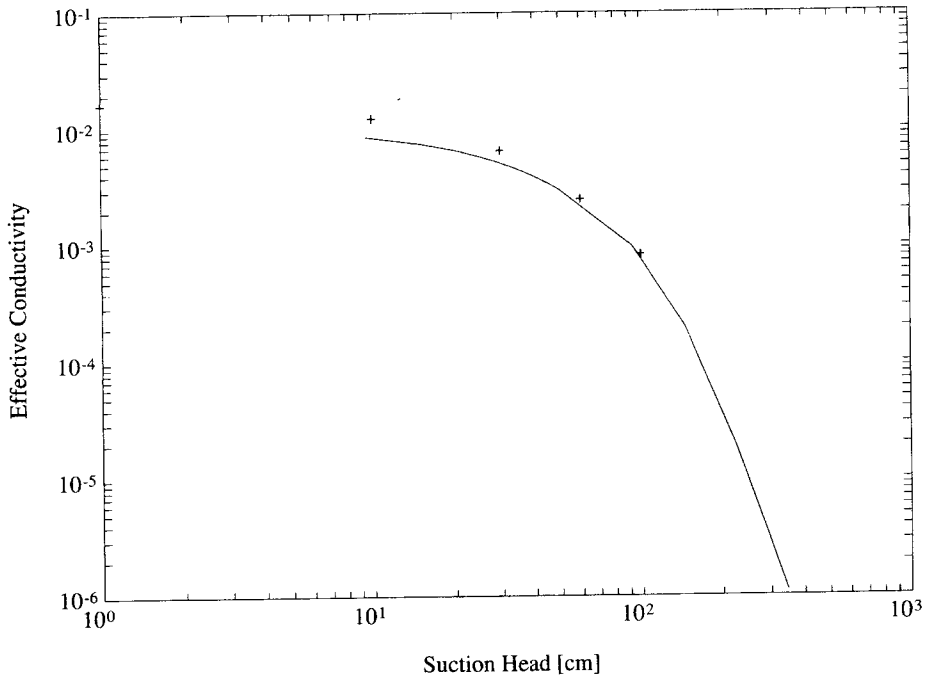

Figure 6-20. Comparison of Real Space Renormalization Group and BIGFLOW results for a heterogeneous, isotropic, fractured matrix field with K_G^m = 0.01 cm/s

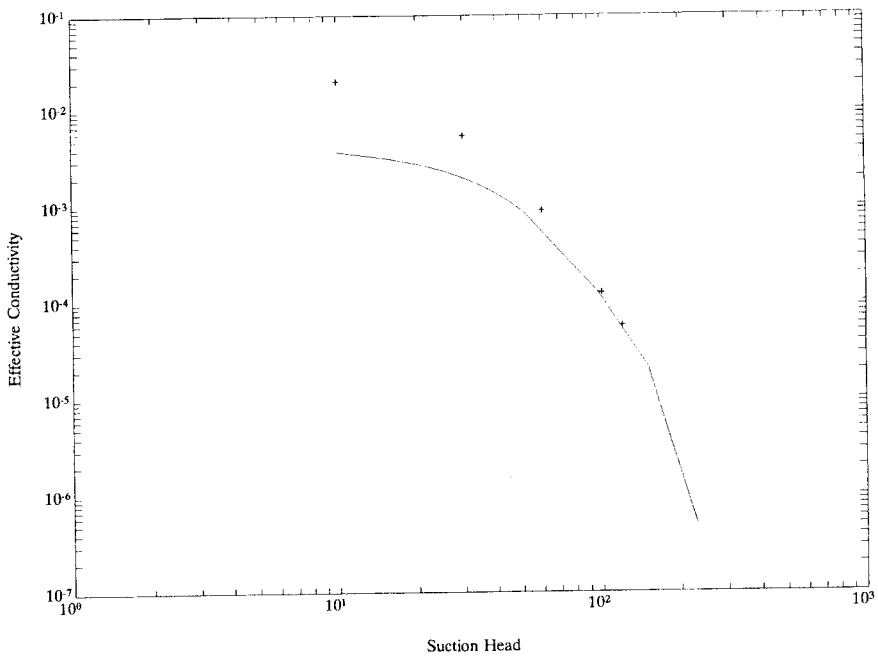

Figure 6-21. Comparison of Real Space Renormalization Group and BIGFLOW results for a heterogeneous, isotropic, fractured matrix field with K_G^m = 0.0001 cm/s

The parametric study indicated the following: (i) the heterogeneity of the underlying matrix has no noticeable effect on the hydraulic conductivity of the matrix-fracture system, except at very high suction heads; (ii) the heterogeneity of the matrix has no effect whatsoever in the case of a nonfractured medium, for the whole range of suction; (iii) the geometric mean of the underlying matrix has a great effect on the effective properties for both fractured and nonfractured media; (iv) the degree of fracturing is affecting greatly the effective hydraulic conductivity; (iv) the anisotropy in the fracture length has a noticeable effect on the effective conductivity of the combined matrix-fracture system, especially near saturation; and (vi) the correlation length of the underlying matrix has little effect on the effective conductivity. However, the effect of anisotropy in the matrix correlation length is much more pronounced in the case of a fractured medium near saturation.

Finally, the multiple realization study concluded the following: (i) the effect of fracture network variability on the relative variability (or coefficient of variation) of the effective conductivity is more pronounced for sharper contrasts between the matrix and fracture properties; (ii) the relative variability of the effective conductivity is a minimum in the region of mid-suction head (near the crossover suction point) (this variability increases at both low and high suction regions); and (iii) the variability of a heterogeneous matrix influence on the effective conductivity is comparable, in general, to that observed due to the fracture network variability.

7 SUMMARY AND CONCLUSIONS

Modeling the flow and transport processes in the vadose zone at Yucca Mountain, Nevada, requires that the effects of various types and levels of heterogeneity be incorporated. Some of the most important geological features are fractures that are hypothesized to play a very significant role in the far-field flow of moisture at a site or subregional scale. It has been postulated (Nitao and Buscheck, 1991) that as water infiltrates down from the surface of the mountain, it first flows mainly through the fractures in the rock. As this process continues, water is hypothesized to imbibe into the matrix, resulting in pure matrix flow. Whether this hypothesis is true or not, one cannot assess the accessibility of the potential repository level to infiltration without studying the effects of various fracture characteristics.

The explicit representation of individual fractures in numerical models on the scale of Yucca Mountain (i.e., subregional scale) is not considered feasible, since it is estimated that in the Topopah Spring welded unit alone over 4×10^{10} discrete fractures are present. Once one recognizes the fact that it is impossible to either characterize every individual fracture, the need for the use of a stochastic representation and effective properties becomes clear.

In this work, a brief but thorough description of fractures and their characteristics has been presented first. Various modeling approaches to study flow in fractured rock were then discussed, and the regionalization of fracture parameters established the ability to model fractured rock as a conglomeration of spatially correlated fracture networks. This in turn provided the necessary platform for the modeling approach advocated in this work. As is shown in the second chapter of this report, where visualization, statistical and connectivity analyses of a realistic fracture data set are conducted, any modeling effort must be site specific. It is shown, for example, that at the ALTS, one of the NRC hydrology research sites, an equivalent continuum approach could be valid for a relatively shallow part of the rock only. At greater depths this approach would most probably neglect the existence of elongated, highly connected features which are classified herein as "persistent discontinuities." Therefore, the approach advocated in this work addresses the issue of modeling flow in fractured rock by: (i) explicitly modeling important geologic features; and (ii) lumping together the remaining heterogeneity, composed either of fractures or matrix heterogeneity, under an effective and/or stochastic continuum approach.

A model is needed to calculate effective hydraulic properties for a variety of conditions and degrees of matrix or fracture network heterogeneity. Moreover, this model must: (i) preserve most of the smaller scale features as is practically possible, and (ii) impose minimal computer space and processing time requirements. This work has reviewed some pertinent literature on methods for effective property calculation, and introduced the RSRG method. In the fourth chapter of this report, a detailed description of the RSRG method together with assumptions and associated algorithms were presented. Then, a verification of the method for binary matrix-fracture systems was presented.

In order to establish a reference point against which one could draw conclusions regarding the suitability of the RSRG method, a detailed direct numerical simulation study was conducted with the help of two numerical codes established in the literature, the MMOC2 (Yeh et al., 1993) and BIGFLOW (Ababou and Bagtzoglou, 1993) codes. A variety of test cases was investigated and comparisons between the two codes and the semi-analytical RSRG solution were made. Inferences about the anisotropic behavior of the effective hydraulic conductivity of fractured rock were also made. Finally, a detailed parametric study of the RSRG method was conducted which showed that it provides a viable alternative to direct numerical

simulation techniques. Some limitations of the method, in cases where the underlying matrix rock is patch-like heterogeneous, that is exhibiting very long correlation structures, were identified.

In summary, this work provided an extensive literature review of: (i) effective property calculations, (ii) fracture network generation with stochastic approaches, and (iii) modeling approaches for simulation of fluid flow in fractured rock. It further presented: (i) visualization, statistical and connectivity analyses of realistic networks; (ii) a simple, yet efficient, fracture network generator and its verification; (iii) the theoretical background, assumptions and algorithm implementation of the RSRG approach; (iv) the verification of the RSRG method for binary and nonbinary matrix-fracture systems; (v) a study of effective property calculations with direct numerical simulations; and (vi) a parametric study and limitations of the RSRG method.

8 REFERENCES

Ababou, R. 1988. *Three-Dimensional Flow in Random Porous Media*. Ph.D. Thesis. Department of Civil Engineering. Cambridge, MA: Massachusetts Institute of Technology.

Ababou, R. 1990. Identification of effective conductivity tensor in randomly heterogeneous and stratified aquifers. *Proceedings 5th Canadian/American Conference on Hydrogeology*. Dublin, OH: National Water Well Association: 155–157.

Ababou, R. 1991. *Approaches to Large Scale Unsaturated Flow in Heterogeneous, Stratified, and Fractured Geologic Media*. NUREG/CR-5743. Washington, DC: Nuclear Regulatory Commission.

Ababou, R. 1993. *Random Porous Media Flow on Large 3-D Grids: Numerics, Performance, and Application to Homogenization*. Preprint Series #1194. Minneapolis, MN: Institute for Mathematics and Applications: 26.

Ababou, R., and A.C. Bagtzoglou. 1993. *BIGFLOW: A Numerical Code for Simulating Flow in Variably Saturated, Heterogeneous Geologic Media (Theory and User's Manual—Version 1.1)*. NUREG/CR-6028. Washington, DC: Nuclear Regulatory Commission.

Ababou, R., and T.-C.J. Yeh. 1992. Random and effective conductivity curves in unsaturated media: Anisotropy, crossing points, and bounds. *EOS Transaction of the American Geophysical Union* 73(43): 196.

Abu-Elbashar, O.B., T.S. Daltaban, C.G. Wall, and J.S. Archer. 1990. Application of analytical method in predicting waterflood performance of reservoirs with stochastic sand bodies. *2nd European Conference on the Mathematics of Oil Recovery*. D. Guerillot and O. Guillon, eds. Paris, France: Editiones Techniques: 65–73.

Aguilera, R. 1980. *Naturally Fractured Reservoirs*. Tulsa, OK: Penn Well Publishing.

Aharony, A., E.L. Hinrichsen, A. Hansen, J. Feder, T. Jossang, and H.H. Hardy. 1991. Effective renormalization group algorithm for transport in oil reservoirs. *Physica A* 177: 260–266.

Ahmadi, A., A. Labastie, and M. Quintard. 1990. Large-scale properties for flow through a stratified medium: A discussion of various approaches. *2nd European Conference on the Mathematics of Oil Recovery*. D. Guerillot and O. Guillon, eds. Paris, France: Editiones Techniques: 91–98.

Ahmed, E., A. Tawansi, and M.A. Soliman. 1991. Grey scaling, a new approximation for random resistor networks. *Physics Letters A* 151(5–6): 301.

Amaziane, B., A. Bourgeat, and J.V. Koebbe. 1990. Numerical simulation and homogenization of diphasic flow in heterogeneous reservoir. *2nd European Conference on the Mathematics of Oil Recovery*. D. Guerillot and O. Guillon, eds. Paris, France: Editiones Techniques: 75–81.

Andersson, J., and B. Dverstorp. 1987. Conditional simulations of fluid flow in three-dimensional networks of discrete fractures. *Water Resources Research* 23(10): 1,876–1,886.

Andersson, J., A.M. Shapiro, and J. Bear. 1984. A stochastic model of a fractured rock conditioned by measured information. *Water Resources Research* 20(1): 79–88.

Auriault, J.L. 1983. Effective macroscopic description for heat conduction in periodic composites. *International Journal of Heat and Mass Transfer* 26: 861–869.

Auriault, J.L. 1991. Heterogeneous medium. Is an equivalent macroscopic description possible? *International Journal of Engineering Science* 29(7): 785–791.

Auriault, J.L., and P. Royer. 1992. Double conductivity media: A comparison between phenomenological and homogenization approaches. *International Journal of Heat and Mass Transfer* 36(10): 2,613–2,621.

Bachu, S., and D. Cuthiell. 1990. Effects of core-scale heterogeneity on steady-state and transient fluid flow in porous media: Numerical analysis. *Water Resources Research* 26: 863–874.

Baecher, G.B. 1983. Statistical analysis of rock mass fracturing. *Mathematical Geology* 15(2): 329–348.

Baecher, G.B., and N.A. Lanney. 1978. Trace length biases in joint surveys. *Proceedings of the 19th U.S. Symposium on Rock Mechanics*. Reno, NV: Published by Conferences and Institutes, Extended Programs and Continuing Education. University of Nevada: 56–65.

Baecher, G.B., N.A. Lanney, and H.H. Einstein. 1977. Statistical description of rock properties and sampling. *Proceedings of the 18th U.S. Symposium on Rock Mechanics*. Golden, CO: Johnson Publishing Company: 5C1–8.

Bagtzoglou, A.C. 1993. Stochastic analysis of unsaturated flow and transport. *NRC High-Level Radioactive Waste Research at CNWRA July 1 Through December 31, 1992*. CNWRA 92-02S. San Antonio, TX: Center for Nuclear Waste Regulatory Analyses: 6-1 to 6-23.

Baker-Jarvis, J., and R. Inguva. 1985. Heat conduction in heterogeneous materials. *Transactions American Society Mechanical Engineers Journal of Heat Transfer* 107: 39–43.

Bakr, A.A., L.W. Gelhar, A.L. Gutjahr, and J. MacMillan. 1978. Stochastic analysis of spatial variability in subsurface flow I. Comparison of one- and three-dimensional flows. *Water Resources Research* 14: 263–271.

Barenblatt, G.E., I.P. Zheltov, and I.N. Kochina. 1960. Basic concepts in the theory of homogeneous liquids in fissured rocks. *Journal of Applied Mathematical Mechanics* 24(5): 1,286–1,303.

Barenblatt, G.I., V.M. Entov, and V.M. Ryzhik. 1990. *Theory of Fluid Flows Through Natural Rocks.* Norwell, MA: Kluwer Academic Publishers.

Barnett, V., and T. Lewis. 1984. *Outliers in Statistical Data*. New York, NY: John Wiley and Sons.

Bartlett, M.S. 1975. *The Statistical Analysis of Spatial Pattern.* New York, NY: John Wiley and Sons.

Barton, C.C., and P.A. Hsieh. 1989. *Physical and Hydrologic-Flow Properties of Fractures.* Washington, DC: 28th International Geological Congress.

Bates, R.L., and J.A. Jackson. 1980. *Glossary of Geology.* 2nd edition. Falls Church, VA: American Geological Institute: 751.

Bear, J. 1993. Modeling flow and contaminant transport in fractured rocks. *Flow and Contaminant Transport in Fractured Rock.* J. Bear, G. de Marsily, and C.-F. Tsang, eds. San Diego, CA: Academic Press: 1–37.

Bear, J., C. Braester, and P.C. Menier. 1987. Effective and relative permeabilities of anisotropic porous media. *Transport in Porous Media* 2: 301–316.

Beckie, R., A.A. Aldama, and E.F. Wood. 1994. The universal structure of the groundwater flow equations. *Water Resources Research.* In press.

Begg, S.H., and P.R. King. 1985. Modeling the effects of shales on reservoir performance: Calculation of effective vertical permeability. *Paper presented at the 8th Symposium on Reservoir Simulation.* Dallas, TX: Society of Petroleum Engineering.

Begg, S.H., R.R. Carter, and P. Dranfield. 1989. Assigning effective values to simulator gridblock parameters for heterogeneous reservoirs. *Society of Petroleum Engineers Research Engineering* 4: 455–463.

Benjamin, J.R., and C.A. Cornell. 1970. *Probability, Statistics, and Decision for Civil Engineers.* New York, NY: McGraw Hill.

Bergman, D.J. 1982. Equivalent conductivity of a heterogeneous medium. *International Journal of Heat and Mass Transfer* 33: 1,759–1,766.

Berkowitz, B., and T. Clemo. 1992. Percolation theory laws for effective parameters in heterogeneous and fractured formations. *EOS Transaction of the American Geophysical Union* 73(43): 214.

Bernasconi, J. 1978. Real space renormalization of bond-disordered conductance lattices. *Physics Review B* 18(5): 2,185–2,191.

Billaux, D., and P. Fuller. 1989. An algorithm for mesh simplification applied to fracture hydrology. *Mathematical Geology* 21(2): 221–231.

Billaux, D., and F. Guérin. 1993. Connectivity and the continuum approximation in fracture flow modelling. *Proceedings of the Fourth Annual International High-Level Radioactive Waste Management Conference.* La Grange Park, IL: American Nuclear Society: 1,118–1,122.

Braester, C., and R. Thunvik. 1987. A study of flow through a fracture network described by statistically distributed properties. *Nuclear Technology* 79: 371–376.

Burganos, V.N., and S.V. Sotirchos. 1987. Diffusion in pore networks: Effective medium theory and smooth field approximation. *American Institute of Chemical Engineering Journal* 33(10): 1,678–1,689.

Chandler, R.J., K. Koplik, K. Lerman, and J.F. Williamson. 1982. Capillary displacement and percolation in porous media. *Journal of Fluid Mechanics* 119: 249–267.

Charlaix, E. 1985. A criterion for percolation threshold in a random array of plates. *Solid State Communications* 50(11): 999–1,002.

Charlaix, E. 1987. *Dispersion en Milieu Poreux: Mise en Evidence de Longueurs Caractéristiques*. Ph.D. Thesis. Paris, France: University of Paris VI.

Chawla, K.K. 1987. *Composite Materials*. New York, NY: Springer Verlag.

Cheeney, R.F. 1983. *Statistical Methods in Geology*. London, United Kingdom: George Allen & Unwin.

Chiles, J.P. 1976. How to adapt kriging to non-classical problems: Three case studies. *Advanced Geostatistics in the Mining Industry*. M. Gaurascio, M. David, and C. Huijbregts, eds. Dordrecht, Netherlands: Dordrecht Reidel Publishing Company: 69–90.

Chiles, J.P. 1989a. Modélisation géostatistique de réseaux de fractures. M. Armstrong, ed. *Geostatistics* 1: 57–76

Chiles, J.P. 1989b. Three-dimensional geometric modelling of a fracture network. *Proceedings from Geostatistical, Sensitivity, and Uncertainty Methods for Ground-Water Flow and Radionuclide Transport Modeling*. B.E. Buxton, ed. New York, NY: Battelle Press: 361–385.

Chiles, J.P, and G. de Marsily. 1993. Stochastic models of fracture systems and their use in flow and transport modeling. *Flow and Contaminant Transport in Fractured Rock*. J.Bear, G. de Marsily, and C.-F. Tsang, eds. San Diego, CA: Academic Press: 169–236.

Clemo, T.M. 1989. Representative elements: A step to large-scale fracture system simulation. *Geostatistical, Sensitivity, and Uncertainty Methods for Ground-Water Flow and Radionuclide Transport Modeling*. Columbus, OH: Battelle Press: 213–227.

Dagan, G. 1979. Models of groundwater flow in statistically homogeneous porous formations. *Water Resources Research* 15: 47–63.

Dagan, G. 1981. Analysis of flow through heterogeneous random aquifers by the method of embedding matrix I. Steady flow. *Water Resources Research* 17: 107–121.

David, C., Y. Guegnen, and A. Pamponkis. 1990. Effective medium theory and network theory applied to the transport properties of rock. *Journal of Geophysical Research* 95(B5): 6,993–7,005.

de Marsily, G. 1985. Flow and transport in fractured rocks: Connectivity and scale effect. *Proceedings International Association of Hydrogeologists: Hydrogeology of Rocks of Low Permeability XVII (Part I)*. Tucson, AZ: International Association of Hydrogeologists: 267–277.

Dershowitz, W.S. 1979. *A Probabilistic Model for the Deformability of Jointed Rock Masses*. M.S. Thesis. Cambridge, MA: Massachusetts Institute of Technology.

Dershowitz, W.S. 1984. *Rock Joint Systems*. Ph.D. Dissertation. Cambridge, MA: Massachusetts Institute of Technology.

Dershowitz, W.S. 1992. Scale effects in fractured and heterogeneous media. *EOS Transaction of the American Geophysical Union* 73(43): 213.

Dershowitz, W.S., B.M. Gordon, and J.C. Kafritsas. 1985. A new three-dimensional model for flow in fractured rock. *International Association of Hydrogeologists: Hydrogeology of Rocks of Low Permeability XVII (Part II)*. International Association of Hydrogeologists: 441–448.

Dershowitz, W.S., P. Wallmann, J.E. Geier, and G. Lee. 1991. *Preliminary Discrete Fracture Network Modeling of Tracer Migration Experiments at the SCV Site*. Stripa Project Technical Report 91-23. Stockholm, Sweden: SKB.

Dershowitz, W.S., G. Lee, J. Geier, S. Hitchcock, and P. LaPointe. 1992. *FracMan Version 2.3 Interactive Discrete Feature Data Analysis, Geometric Modeling, and Exploration Simulation User Documentation*. Redmond, WA: Golder Associates.

Desbarats, A.J. 1987. Numerical estimation of effective permeability in sand-shale formations. *Water Resources Research* 23: 273–286.

Deutsch, C. 1987. Calculating effective absolute permeability in sandstone/shale sequences. *Society Petroleum Engineers* Paper 17246.

Dudley, A.L., R.R. Peters, J.H. Gauthier, M.L. Wilson, M.S. Tierney, and E.A. Klavetter. 1988. *Total System Performance Assessment Code (TOSPAC) Volume 1: Physical and Mathematical Bases*. SAND 85-0002. Albuquerque, NM: Sandia National Laboratories.

Dunne, W.M., and C.P. North. 1990. Orthogonal fracture systems at the limits of thrusting: An example from southwestern Wales. *Journal of Structural Geology* 12(2): 207–215.

Durlofsky, J.L. 1991. Numerical calculation of equivalent grid block permeability tensors for heterogeneous porous media. *Water Resources Research* 27(5): 699–708.

Dverstorp, B., and J. Andersson. 1989. Application of the discrete fracture network concept with field data: Possibilities of model calibration and validation. *Water Resources Research* 25(3): 540–550.

Dykaar, B.B., and P.K. Kitanidis. 1993. Transmissivity of a heterogeneous formation. *Water Resources Research* 29(4): 985–1,001.

Eaton, R.R., R.C. Dykhuizen, and K.M. Hansen. 1991. Flow through nonhomogeneous porous media. *Proceedings of Workshop V: Flow and Transport through Unsaturated Fractured Rock—Related to High-Level Radioactive Waste Disposal*. NUREG/CP-0040. Washington, DC: Nuclear Regulatory Commission.

Engelder, T. 1985. Loading paths to joint propagation during a tectonic cycle: An example from the Appalachian Plateau, U.S.A. *Journal of Structural Geology* 7(3/4): 459–476.

Engelder, T. 1987. Joints and shear fractures in rock. *Fracture Mechanics of Rock*. B.K. Atkinson, ed. London, England: Academic Press: 27–69.

Eshelby, J.D. 1957. The determination of the elastic field of an ellipsoidal inclusion, and related problems. *Proceedings of Royal Society of London*. United Kingdom: A241: 376–396.

Ferrand, L.A., and M.A. Celia. 1992. The effect of heterogeneity on the drainage capillary pressure-saturation relation. *Water Resources Research* 28(3): 859–870.

Ferrand, L.A., M.A. Celia, and W.E. Soll. 1990. Percolation-based models for pore-to-lab scale calculations in multifluid porous media. *Dynamics of Fluids in Hierarchical Porous Media*. J.H. Cushman, ed. San Diego, CA: Academic Press.

Fisher, R.A. 1953. Dispersion on a sphere. *Proceedings of the Royal Society of London Series A*. United Kingdom: 217: 295–306.

Fletcher, C.A.J. 1988. *Computational Techniques for Fluid Dynamics*. New York, NY: Springer-Verlag.

Flint, A., L.E. Flint, and J.A. Havesi. 1993. The influence of long term climate change on net infiltration at Yucca Mountain, Nevada. *Proceedings of Fourth International High-Level Radioactive Waste Management Conference*. La Grange Park, IL: American Nuclear Society and American Society of Civil Engineers: 152–159.

Ford, W. 1991. Groundwater flow through unsaturated fractured rock research needs. *Proceedings of Workshop V: Flow and Transport Through Unsaturated Fractured Rock—Related to High-Level Radioactive Waste Disposal*. D.D. Evans and T.J. Nicholson, eds. NUREG/CP-0040. Washington, DC: Nuclear Regulatory Commission: 116–125.

Furmański, P. 1992. Effective macroscopic description for heat conduction in heterogeneous materials. *International Journal of Heat and Mass Transfer* 35(11): 3,047–3,058.

Garcia, M.H., A.G. Journel, and K. Aziz. 1990. An automatic grid generation and adjustment method for modeling reservoir heterogeneities. *Center for Reservoir Forecasting Report 3*. Palo Alto, CA: Stanford University.

Gary, M., R. McAfee, Jr., and C.L. Wolf. 1972. *Glossary of Geology*. American Geological Institute.

Gates, W.C.B. 1993. New wells safeguard scenic Tahoe. *Civil Engineering*. May Issue: 60–62.

Gelhar, L.W., and C.L. Axness. 1983. Three dimensional stochastic analysis of macrodispersion in aquifers. *Water Resources Research* 19(1): 161–180.

Gentier, S. 1990. Morphological analysis of a natural fracture. *Selected Papers on Hydrogeology from the 28th International Geological Congress, July 9-19, 1989.* E.S. Simpson and J.M. Sharp, Jr., eds. Washington, DC: International Geological Congress: 315–326.

Ghosh, A., and J.J.K. Daemen. 1993. Fractal characteristics of rock discontinuities. *Engineering Geology* 34: 1–9.

Gomez-Hernandez, J.J. 1990. Simulation of block permeabilities conditioned upon data measured at a different scale. *Calibration and Reliability in Groundwater Modelling.* IAHS Publication No. 195. Wallingford, United Kingdom: International Association of Hydrological Sciences: 407–416.

Gomez-Hernandez, J.J., and A.G. Journel. 1990. Stochastic characterization of grid-block permeabilities: From point values to block tensor. *2nd European Conference on the Mathematics of Oil Recovery.* D. Guerillot and O. Guillon, eds. Paris, France: Editiones Techniques: 83–90.

Griggs, D.T. and J. Handin. 1960. Observation on fractures and a hypothesis of earthquakes. *Geological Society of America Memoir* 79: 346–364.

Groshong, R.H., Jr. 1988. Low-temperature deformation mechanisms and their interpretation. *Geological Society of America Bulletin* 100: 1,329–1,360.

Gureghian, A.B. 1975. A study by the finite-element method of the influence of fractures in confined aquifers. *Society of Petroleum Engineers Journal* 15(2): 181–191.

Gureghian, A.B., and B. Sagar. 1991. Evaluation of DCM3D—a dual continuum, 3-D groundwater flow code for unsaturated fractured, porous media, Section 8.2. *Report on Research Activities for Calendar Year 1990, CNWRA 90-01A.* W. Patrick, ed. San Antonio, TX: Center for Nuclear Waste Regulatory Analyses.

Gutjahr, A.L., L.W. Gelhar, A.A. Bakr, and J.R. MacMillan. 1978. Stochastic analysis of spatial variability in subsurface flow 2. Evaluation and application. *Water Resources Research* 14: 953–959.

Hancock, P.L. 1985. Brittle microtectonics: Principles and practice. *Journal of Structural Geology* 7(3/4): 437–457.

Hashin, A., and S. Shtrikman. 1962. A variational approach to the theory of effective magnetic permeability of multiphase materials. *Journal of Applied Physics* 33: 3,125–3,131.

Hatta, H., and M. Taya. 1985. Effective thermal conductivity of a misoriented short fiber composite. *Journal of Applied Physics* 58: 2,478–2,486.

Hestir, K., J. Long, J.P. Chiles, and D. Billaux. 1989. Some techniques for stochastic modeling of three-dimensional fracture networks. *Proceedings from Geostatistical, Sensitivity, and Uncertainty Methods for Ground-Water Flow and Radionuclide Transport Modeling*. B.E. Buxton, ed. New York, NY: Battelle Press: 495–519.

Hestir, K., J.C.S. Long, and S.J. Martel. 1991. *The Use of Iterated Function systems in Fracture Hydrology*. LBL-29700: Berkeley, CA: Lawrence Berkeley Laboratory: 36–40.

Howard, J.H., and R.C. Nolen-Hoeksema. 1990. Description of natural fracture systems for quantitative use in petroleum geology. *Bulletin of American Association of Petroleum Geologists* 74(3): 151–162.

Huppler, J.D. 1970. Numerical investigation of the effects of core heterogeneities on waterflood relative permeabilities. *SPE Journal Forum* 10(4): 381–392.

Jerauld, G.R., and S.J. Salter. 1990. The effect of pore-structure on hysteresis in relative permeability and capillary pressure: Pore-level modeling. *Transport in Porous Media* 5: 103–151.

Johnson, C.R. and R.A. Greenkorn. 1962. Comparison of core analysis and drawdown-test results from a water-bearing upper Pennsylvanian sandstone of central Oklahoma. *Bulletin International Association of Scientific Hydrology* 7: 46–52.

Journel, A.G., C. Deutsch, and A.J. Desbarats. 1986. Power averaging for block effective permeability *Society of Petroleum Engineers* Paper 15128.

Kamb, W.B. 1959. Ice petrofabric observations from Blue Glacier, Washington, in relation to theory and experiment. *Journal of Geophysics Research* 64: 1,891–1,909.

Kasap, E., and L.W. Lake. 1989. An analytical method to calculate the effective permeability tensor of a grid block and its application in an outcrop study. *Proceedings of the Society of Petroleum Engineering Symposium on Reservoir Simulation*. Houston, TX: Society of Petroleum Engineering.

Kasap, E., and W.L. Lake. 1990. Calculating the effective permeability tensor of a gridblock. *Society Petroleum Engineering Formation Evaluation*: 192–200.

King, P.R. 1989. The use of renormalization of calculating effective permeability. *Transport in Porous Media* 4: 37–58.

Kirkpatrick, S. 1973. Percolation and conduction. *Review of Modern Physics* 4: 574–588.

Kitanidis, P.K. 1990. Effective hydraulic conductivity for gradually varying flow. *Water Resources Research* 26: 1,197–1,208.

Klavetter, E.A., and R.R. Peters. 1986a. *Fluid Flow in a Fractured Rock Mass*. SAND85-0855. Albuquerque, NM: Sandia National Laboratories.

Klavetter, E.A., and R.P. Peters. 1986b. *Estimation of Hydrologic Properties of an Unsaturated, Fractured Rock Mass*. SAND84-2642. Albuquerque, NM: Sandia National Laboratories.

Koch, G.S., Jr., and R.F. Link. 1980. *Statistical Analysis of Geological Data*. New York, NY: Dover Publications, Inc.

Kueper, B.H., and D.B. McWhorter. 1992. The use of macroscopic percolation theory to construct large-scale capillary pressure curves. *Water Resources Research* 28(9): 2,425–2,436.

Kumar, S., and G.S. Bodvarsson. 1990. *Fractal Study and Simulation of Fracture Roughness and Apertures*. LBL-27900: Berkeley, CA: Lawrence Berkeley Laboratory: 35–37.

Kwicklis, E.M., and R.W. Healy. 1993. Numerical investigation of steady liquid water flow in a variably saturated fracture network. *Water Resources Research* 29(12): 4,091–4,102.

LaPoint, P.R. 1980. Analysis of the spatial variation in rock mass properties through geostatistics. *Proceedings of the 21st U.S. Symposium on Rock Mechanics*. Rolla, MI: American Institute of Mining Engineers: 570–580.

LaPoint, P.R., and J.A. Hudson. 1981. *Characterization and Interpretation or Rock Mass Jointing Patterns*. Madison, WI: University of Wisconsin: Department of Metallurgical and Mineral Engineering.

Levi, B.G. 1990. Are fractures fractal or quakes chaotic? *Physics Today*: 17–19.

Lin, P., and J.M. Logan. 1991. The interaction of two closely spaced cracks: A rock model study. *Journal of Geophysical Research* 96(B13): 21,667–21,675.

Lobb, C.J., D.J. Frank, and M. Tinkham. 1981. Percolative conduction in anisotropic media: A renormalization-group approach. *Physics Review B* 23(5): 2,262–2,268.

Loeven, C. 1993. *A Summary and Discussion of Hydrologic Data from the Calico Hills Nonwelded Hydrogeologic Unit at Yucca Mountain, Nevada*. LA-12376-MS. Los Alamos, NM: Los Alamos National Laboratory.

Long, J.C.S. 1983. *Investigation of Equivalent Porous Medium Permeability in Networks of Discontinuous Fractures*. Ph.D. Dissertation. Berkeley, CA: University of California.

Long, J.C.S., and D.M. Billaux. 1987. From field data to fracture network modeling: An example incorporating spatial structure. *Water Resources Research* 23(7): 1,201–1,216.

Long, J.C.S., and K. Hestir. 1990. *An Analytical Expression for the Permeability of Random Two-Dimensional Poisson Fracture Networks*. LBL-29700: Berkeley, CA: Lawrence Berkeley Laboratory: 45–48.

Long, J.C.S., P. Gilmour, and P.A. Witherspoon. 1985a. A model for steady fluid flow in random three-dimensional networks of disc-shaped fractures. *Water Resources Research* 21(8): 1,105–1,115.

Long, J.C.S., H.K. Endo, K. Karasaki, L. Pyrak, P. MacLean, and P.A. Witherspoon. 1985b. Hydrologic behavior of fracture networks. *International Association of Hydrogeologists: Hydrogeology of Rocks of Low Permeability XVII (Part II)*. Tucson, AZ: 449–462.

Maini, T., and G. Hocking. 1977. An examination of the feasibility of hydrologic isolation of a high-level waste repository in crystalline rocks. *Annual Meeting of Geological Society of America*. Seattle, WA: Geological Society of America.

Mandelbrot, B.B. 1985. Self-affine fractals and fractal dimension. *Physica Scripta* 32: 257–260.

Mantoglou, A., and L.W. Gelhar. 1987. Effective hydraulic conductivities of transient unsaturated flow in stratified soils. *Water Resources Research* 23(1): 57–67.

Mardia, K.V. 1972. *Statistics of Directional Data*. New York, NY: Academic Press.

Martel, S.J., K. Hestir, and J.C.S. Long. 1991. *Generation of Fracture Patterns Using Self-Similar Iterated Function System Concepts*. LBL-29700. Berkeley, CA: Lawrence Berkeley Laboratory: 52–56.

Martinez, M.J., R.C. Dykhuizen, and R.R. Eaton. 1992. The apparent conductivity for steady unsaturated flow in periodically fractured porous media. *Water Resources Research* 28(11): 2,879–2,887.

Matheron, G. 1967. *Eléments Pour Une Théorie Des Milieux Poreux*. Paris, France: Masson Publishing Company.

Mazurek, M., A. Gautschi, and S. Vomvoris. 1993. Deriving input data for solute transport models from deep borehole investigations: An approach for crystalline rocks. *Geological Disposal of Spent Fuel and High Level and Alpha Bearing Wastes*. Vienna, Austria: International Atomic Energy Agency: 55–67.

Mohanty, S. 1993. *Experimental Determination and Theoretical Prediction of Effective Thermal Conductivity of Porous Media*. Ph.D. Thesis. Austin, TX: University of Texas at Austin.

Mohanty, S., and A.C. Bagtzoglou. 1994. Effective unsaturated hydraulic property determination with the Renormalization Group approach: Methodology. *Proceedings of Fifth International High-Level Radioactive Waste Management Conference*. La Grange Park, IL: American Nuclear Society. In press.

Mohanty, S., and M.M. Sharma. 1990. A recursive method for estimating single and multiphase permeabilities. *Society of Petroleum Engineers* Paper 20477.

Mohanty, S., and M.M. Sharma. 1991. A Monte Carlo RSRG method for the percolation/conduction properties of correlated lattices. *Physics Letters A*: 475–481.

Montazer, P., and P.E. Harrold. 1985. Theoretical calculation of hydraulic properties of unsaturated fractures from roughness profiles. *EOS Transaction of the American Geophysical Union* 66(46): 883.

Muralidhar, K. 1990. Equivalent conductivity of a heterogeneous medium. *International Journal of Heat and Mass Transfer* 33(8): 1,759–1,766.

Neuman, S.P. 1987. Stochastic continuum representation of fractured rock permeability as an alternative to the REV and fracture network concepts. *Proceedings of 28th U.S. Symposium on Rock Mechanics*: Tucson, AZ: Balkema Press: 533–561.

Neuman, S.P., E.S. Simpson, P.A. Hsieh, J.W. Jones, and C.L. Winter. 1985. Statistical analysis of hydraulic test data from fractured crystalline rock near Oracle, Arizona. *International Association of Hydrogeologists: Hydrogeology of Rocks of Low Permeability, XVII (Part I).* Tucson, AZ: 289–300.

Nitao, J.J. 1988. *Numerical Modeling of the Thermal and Hydrological Environment Around a Nuclear Waste Package Using the Equivalent Continuum Approximation: Horizontal Emplacement.* UCID-21444. Livermore, CA: Lawrence Livermore National Laboratory.

Nitao, J.J., and T.A. Buscheck. 1991. Infiltration of a liquid front in an unsaturated, fractured porous medium. *Water Resources Research* 27(8): 2,099–2,112.

Nordqvist, A.W., Y.W. Tsang, C.F. Tsang, B. Dverstorp, and J. Andersson. 1992. A variable aperture fracture network model for flow and transport in fractured rocks. *Water Resources Research* 28(6): 1,703–1,713.

Nuclear Energy Agency. 1993. *The International INTRAVAL Project. Phase 1, Test Cases 10, 11, and 12.* C.F. Voss and T.J. Nicholson, eds. Paris, France: Organization for Economic Co-Operation and Development.

Odling, N.E. 1992. Network properties of a two-dimensional natural fracture pattern. *Pure and Applied Geophysics* 138(1): 95–114.

Parang, M., R.V. Arimilli, and S.P. Ketkar. 1987. Optimal positioning of tubes in arbitrary two dimensional region as using a special boundary integral method. *Transactions American Society of Mechanical Engineers, Journal of Heat Transfer* 109: 826–830.

Peters, R.R., and E.A. Klavetter. 1988. A continuum model for water movement in an unsaturated fractured rock mass. *Water Resources Research* 24(3): 416–430.

Pollard, D.D. 1976. On the form and stability of open hydraulic fractures in the earth's crust. *Geophysical Research Letters* 3(9): 513–516.

Pollard, D.D., and A. Aydin. 1988. Progress in understanding jointing over the past century. *Geological Society of America Bulletin* 100(8): 1,181–1,204.

Pollard, D.D., and P. Segall. 1987. Theoretical displacements and stresses near fractures in rock: With applications to faults, joints, veins, dikes, and solution surfaces. *Fracture Mechanics of Rock.* B.K. Atkinson, ed. London, England: Academic Press: 277–349.

Pruess, K., and Y.W. Tsang. 1990. On two-phase relative permeability and capillary pressure of rough-walled rock fractures. *Water Resources Research* 26(9): 1,915–1,926.

Pruess, K., J.S.Y. Wang, and Y.W. Tsang. 1986. *Effective Continuum Approximation for Modeling Fluid Flow in Fractured Porous Tuff.* SAND86-7000. Albuquerque, NM: Sandia National Laboratories.

Pruess, K., J.S.Y. Wang, and Y.W. Tsang. 1990a. On thermohydrologic conditions near high-level nuclear wastes emplaced in partially saturated fractured tuff. 1. Simulation studies with explicit consideration of fracture effects. *Water Resources Research* 26(6): 1,235–1,248.

Pruess, K., J.S.Y. Wang, and Y.W. Tsang. 1990b. On thermohydrologic conditions near high-level nuclear wastes emplaced in partially saturated fractured tuff. 2. Effective continuum approximation. *Water Resources Research* 26(6): 1,249–1,261.

Pyrak-Nolte, L.J., and N.G.W. Cook. 1988. Fluid percolation through single fractures. *Geophysical Research Letters* 15(11): 1,247–1,250.

Rasmussen, T.C., and D.D. Evans. 1987. *Unsaturated Flow and Transport Through Fractured Rock Related to High-Level Waste Repositories: Final Report, Phase* 2. NUREG/CR-4655. Washington, DC: Nuclear Regulatory Commission.

Rasmussen, T.C., and D.D. Evans. 1989. *Fluid Flow and Solute Transport Modeling Through Three-Dimensional Networks of Variably Saturated Discrete Fractures.* NUREG/CR-5239. Washington, DC: Nuclear Regulatory Commission.

Rasmussen, T.C., C. Huang, and D.D. Evans. 1985. Numerical experiments on artificially-generated, three-dimensional fracture networks: An examination of scale and aggregation effects. *International Association of Hydrogeologists: Hydrogeology of Rocks of Low Permeability XVII (Part II)*: Tucson, AZ: 676–682.

Rasmussen, T.C., T.-C.J. Yeh, and D.D. Evans. 1989. Effect of variable fracture permeability/matrix permeability ratios on three-dimensional fractured rock hydraulic conductivity. *Proceedings from Geostatistical, Sensitivity, and Uncertainty Methods for Ground-Water Flow and Radionuclide Transport Modeling.* B.E. Buxton, ed. New York, NY: Battelle Press: 337–358.

Rasmussen, T.C., D.D. Evans, P.J. Sheets, and J.H. Blanford. 1990. *Unsaturated Fractured Rock Characterization Methods and Data Sets at the Apache Leap Tuff Site.* NUREG/CR-5596. Washington, DC: Nuclear Regulatory Commission.

Rasmussen, T.C., D.D. Evans, P.J. Sheets, and J.H. Blanford. 1993. Permeability of Apache Leap tuff: Borehole and core measurements using water and air. *Water Resources Research* 29(7): 1,997–2,006.

Rautman, C.A., and A. Flint. 1992. Deterministic geologic processes and stochastic modeling. *Proceedings of Third International High-Level Radioactive Waste Management Conference*. La Grange Park, IL: American Nuclear Society: 1,617–1,624.

Rautman, C.A., and T.H. Robey. 1993. Recent developments in stochastic modeling and upscaling of hydrologic properties in tuff. *Proceedings of Fourth International High-Level Radioactive Waste Management Conference*. La Grange Park, IL: American Nuclear Society: 1,437–1,445.

Robertson, A. 1970. The interpretation of geological factors for use in slope stability. *Symposium on the Theoretical Background to the Planning of Open Pit Mines with Special Reference to Slope Stability*. Johannesburg, South Africa: South African Institute of Mining and Metallurgy.

Robinson, P. 1984. *Connectivity, Flow and Transport in Network Models of Fractured Media*. Ph.D. Thesis. Oxford, United Kingdom: Oxford University.

Rockhold, M.L., B. Sagar, and M.P. Connelly. 1992. *Three-Dimensional Modeling of Unsaturated Flow in the Vicinity of Proposed Exploratory Shaft Facilities at Yucca Mountain, Nevada*. PNL-7474. Richland, WA: Pacific Northwest Laboratory.

Ross, B., 1990. The diversion capacity of capillary barriers. *Water Resources Research* 26(10): 2,625–2,629.

Rouleau, A. 1984. *Statistical Characterization and Numerical Simulation of a Fracture System. Application to a Groundwater Flow in the Stripa Granite*. Ph.D. Thesis. Waterloo, Canada: University of Waterloo.

Rubinstein, L.I. 1948. On the question of the process of propagation of heat in heterogeneous media. *Izvestia Akademia Nauk USSR Series in Geography and Geophysics* 12(27).

Rulon, J., S. Bodvarsson, and P. Montazer. 1986. *Preliminary Numerical Simulations of Groundwater Flow in the Unsaturated Zone, Yucca Mountain, Nevada*. LBL-20553. Berkeley, CA: Lawrence Berkeley Laboratory.

Runchal, A.K., and B. Sagar. 1993. *PORFLOW: A Multifluid Multiphase Model for Simulating Flow, Heat Transfer, and Mass Transport in Fractured Porous Media User's Manual—Version 2.41*. NUREG/CR-5991. Washington, DC: Nuclear Regulatory Commission.

Rush, F.E., W. Thordarson, and D.G. Pyles. 1984. *Geohydrology of Test Well USW H-1, Yucca Mountain, Nye County, Nevada*. USGS-WRI-84-4032. Water-Resources Investigations Report. Denver, CO: U.S. Geological Survey.

Saez, A.E., C.J. Otero, and I. Rusinek. 1989. The effective homogeneous behavior of heterogeneous porous media. *Transport in Porous Media* 4: 213–238.

Sagar, B., and A. Runchal. 1982. Permeability of fractured rock: Effect of fracture size and data uncertainties. *Water Resources Research* 18(2): 266–274.

Schwartz, F.W., L. Smith, and A.S. Crowe. 1982. Stochastic analysis of groundwater flow and contaminant transport in a fractured rock system. *The Scientific Basis for Nuclear Waste Management*. Stephen V. Topp, ed. Pittsburgh, PA: Materials Research Society: 457–463.

Scott, R.B., R.W. Spengler, S. Diehl, A.R. Lappin, and M.P. Chornak. 1983. Geologic character of tuffs in the unsaturated zone at Yucca Mountain, southern Nevada. *Role of the Unsaturated Zone in Radioactive and Hazardous Waste Disposal*. J.W. Mercer, P.S.C. Rao, and I.W. Marine, eds. Ann Arbor, MI: Ann Arbor Science Publishers: 289–335.

Shapiro, A.M. 1987. Transport equations for fractured porous media. *Advances in Transport Phenomena in Porous Media*. J. Bear and M.Y. Corapcioglu, eds. NATO Advanced Study Institute Series E(128): 405–471.

Sheridan, M.F. 1992. A Monte Carlo technique to estimate the probability of volcanic dikes. *Proceedings of the Third International Conference on High-Level Radioactive Waste Management*. La Grange Park, IL: American Nuclear Society: 2,033–2,038.

Sibson, R.H. 1986. Brecciation processes in fault zones: Inferences from earthquake rupturing. Basel, Switzerland: Birkhauser Verlag: *PAGEOPH* 124(1/2): 159–175.

Snow, D.T. 1965. *A Parallel Plate Model of Fractured Permeable Media*. Ph.D. Dissertation. Berkeley, CA: University of California.

Snow, D.T. 1968. Rock fractures spacings, openings, and porosities. *Proceedings of the American Society of Civil Engineers, Journal of Soil Mechanics and Foundations*: 73–91.

Snow, D.T. 1969. Anisotropic permeability of fractured media. *Water Resources Research* 5: 1,273–1,289.

Stauffer, D. 1985. *Introduction to Percolation Theory*. London, United Kingdom: Taylor and Francis.

Stinchcombe, R.B., and B.P. Watson. 1976. Renormalization group for percolation conductivity. *Journal of Physics C: Solid State Physics* 9: 3,221-3,247.

Streltsova, T.D. 1976. Hydrodynamics of groundwater flow in a fractured formation. *Water Resources Research* 12(3): 405–414.

Tabatabai-Irani, B. 1989. *Localized Effects of a Single Fracture on the Unsaturated Flow of Water on the Surrounding Porous Medium*. M.S. Thesis. Irvine, CA: University of California.

Thoma, S.G., D.P. Gallegos, and D.M. Smith. 1992. Impact of fracture coatings on fracture/matrix flow interactions in unsaturated, porous media. *Water Resources Research* 28(5): 1,357–1,367.

Thornburg, T.M. 1990. *Electrical Resistivity of Unsaturated, Fractured Tuff: Influence of Moisture Content and Geologic Structure*. M.S. Thesis. University of Arizona: Department of Hydrology and Water Resources.

Tidwell, V.C., J.D. VonDoemming, and K. Martinez. 1993. Scale dependence of effective media properties. *Proceedings of Fourth International High-Level Radioactive Waste Management Conference*. La Grange Park, IL: American Nuclear Society: 1,059–1,065.

Tompson, A.F.B., R. Ababou, L.W. Gelhar. 1987. *Application and use of the Three-Dimensional Turning Bands Random Field Generator: Single Realization Problems*. Report Number 313. Cambridge, MA: Massachusetts Institute of Technology: 1–126.

Torquato, S. 1987. Thermal conductivity of disordered heterogeneous media from the microstructure. *Reviews in Chemical Engineering* 4(3–4): 151–204.

Updegraff, D.C., and C.E. Lee. 1990. *A Dual Continuum, 3-D Groundwater Flow Code for Unsaturated, Fractured, Porous Media*. NUREG/CR-5536. Washington, DC: Nuclear Regulatory Commission.

U.S. Department of Energy. 1988. *Site Characterization Plan, Yucca Mountain Site, Nevada Research and Development Area 2 Part A: Nevada*. Washington, DC: U.S. Department of Energy.

U.S. Geological Survey. 1993. *Site Unsaturated-Zone Modeling and Synthesis*. Study Plan 8.3.1.2.2.9. Denver, CO: U.S. Geological Survey.

van Genuchten, R. 1980. A closed-form equation for predicting the hydraulic conductivity of unsaturated soils. *Soil Science Society of America Journal* 44(4): 892–898.

Veneziano, D. 1978. *Probabilistic Model of Joints in Rock*. Cambridge, MA: Massachusetts Institute of Technology. Unpublished manuscript.

Wang, J.S.Y. 1991. Flow and transport in fractured rocks. *Review of Geophysics Supplement*: 254–262.

Wang, J.S.Y., and T.N. Narasimhan. 1985. Hydrologic mechanisms governing partially saturated fluid flow in fractured porous medium. *Water Resources Research* 21(12): 1,861–1,874.

Wang, J.S.Y., and T.N. Narasimhan. 1986. *Hydrologic Mechanisms Governing Partially Saturated Fluid Flow Fractured Welded Units and Porous Nonwelded Units at Yucca Mountain*. SAND85-7114. Albuquerque, NM: Sandia National Laboratories.

Warren, J.E., and H.S. Price. 1961. Flow in heterogeneous porous media. *Society of Petroleum Engineering Journal*: 153–169.

Warren, J.E., and P.J. Root. 1963. The behavior of naturally fractured reservoirs. *Society of Petroleum Engineers Journal*: 245–255.

Warrick, A.W., and T.-C.J. Yeh. 1990. One-dimensional, steady vertical flow in a layered soil profile, *Advances in Water Resources* 13(4): 207–210.

Wilson, K.G., and J. Kogut. 1974. The renormalization group and the ϵ expansion. *Physics Reports* 12C: 75–200.

Yeh, T.-C.J. 1989. One-dimensional steady-state infiltration in heterogeneous soils. *Water Resources Research* 25(10): 2,149–2,158.

Yeh, T.-C.J., and D.J. Harvey. 1990. Effective unsaturated hydraulic conductivity of layered sands. *Water Resources Research* 26(6): 1,271–1,279.

Yeh, T.-C.J., L.W. Gelhar, and A.L. Gutjahr. 1985a. Stochastic analysis of unsaturated flow in heterogeneous soils: Part 1, statistically isotropic media. *Water Resources Research* 21(4): 447–456.

Yeh, T.-C.J., L.W. Gelhar, and A.L. Gutjahr. 1985b. Stochastic analysis of unsaturated flow in heterogeneous soils: Part 2, statistically anisotropic media. *Water Resources Research* 21(4): 457–464.

Yeh, T.-C.J., L.W. Gelhar, and A.L. Gutjahr. 1985c. Stochastic analysis of unsaturated flow in heterogeneous soils: Part 3, observations and applications. *Water Resources Research* 21(4): 465–471.

Yeh, T.-C.J., T.C. Rasmussen, and D.D. Evans. 1988. *Simulation of Liquid and Vapor Movement in Unsaturated Fractured Rock at the Apache Leap Tuff Site, Models and Strategies.* NUREG/CR-5097. Washington, DC: Nuclear Regulatory Commission.

Yeh, T.-C.J., R. Srivastava, A. Guzman, and T. Harter. 1993. A numerical model for two dimensional flow and chemical transport. *Groundwater* 31(4): 634–644.

Young, A.P., and R.B. Stinchcombe. 1975. A renormalization group theory for percolation problems. *Journal of Physics C: Solid State Physics* 8: L535–540.

Zaslavsky, D., and G. Sinai. 1981. Surface hydrology: IV—Flow in sloping layered soil. *Journal of Hydraulics Division*. American Society of Civil Engineers 107(HY1): 53–64.

Zimmerman, R.W. 1992. Effective hydraulic conductivity of 2-D porous media containing elliptical inhomogeneities. *EOS Transaction of the American Geophysical Union* 73(43): 195–196.

Zimmerman, R.W., and G.S. Bodvarsson. 1992. Semi-analytical treatment of fracture/matrix flow in a dual-porosity simulator for unsaturated fractured rock masses. *Proceedings of Third International High-Level Radioactive Waste Management Conference*. La Grange Park, IL: American Nuclear Society: 272–278.

Zimmerman, R.W., G.S. Bodvarsson, and E.M. Kwicklis. 1990. Absorption of water into porous blocks of various shapes and sizes. *Water Resources Research* 26(11): 2,797–2,806.